2017

Design And Synthesis Of Gold Nanoparticle Contrast Agents For Atherosclerosis Imaging With Computed Tomography

Peter Chhour
University of Pennsylvania, pchhour@gmail.com

Design And Synthesis Of Gold Nanoparticle Contrast Agents For Atherosclerosis Imaging With Computed Tomography

Abstract
Cell tracking offers the opportunity to study migration and localization of cells in vivo, allowing investigations of disease mechanisms and drug efficacy. Monocytes play a key role in the progression of atherosclerotic plaques in the coronary arteries. While x-ray computed tomography (CT) is commonly used to clinically assess coronary plaque burden, cell tracking with CT is mostly unexplored. The establishment of monocyte cell tracking tools would allow for the direct investigation of gene and drug therapies aimed at monocyte recruitment in atherosclerosis. In this thesis, we present the design and optimization of gold nanoparticles as CT contrast agents for cell tracking of monocyte recruitment to atherosclerotic plaques. Gold nanoparticle polymer constructs with controlled localization are evaluated as potential monocyte labels. However, cytotoxic effects were observed at concentrations necessary for cell labeling. Therefore, variations in physical and chemical properties of gold nanoparticles were explored as cell labels for monocyte tracking. Each formulation was screened for effects on cell viability, cell function and uptake in monocytes. The uptake in monocytes revealed a complex relationship with nanoparticle size behavior dependent on the surface ligand used. This led to the selection of an optimal size and coating for monocyte labeling, 11-mercaptoundecanoic acid coated 15 nm gold nanoparticles. This formulation was further investigated for cell viability, function, and uptake with isolated primary monocytes. Moreover, primary monocytes labeled with this formulation were used to observe monocyte recruitment in atherosclerotic mice. Mice with early atherosclerotic plaques received intravenously injections of gold labeled monocytes and their recruitment to plaques were observed over 5 days with CT. Increases in CT attenuation in the plaque and transmission electron microscopy of plaque sections indicated the presence of gold labeled monocytes in the plaque. These results demonstrate the feasibility of using CT to track ex-vivo labeled cells non-invasively with CT and could further be used to investigate drugs aimed at modulating monocyte recruitment in the treatment of atherosclerosis. This work expands the applications of cell tracking and may lead to additional uses in other diseases.

Degree Type
Dissertation

Degree Name
Doctor of Philosophy (PhD)

Graduate Group
Bioengineering

First Advisor
David P. Cormode

Subject Categories
Biomedical | Nanoscience and Nanotechnology

DESIGN AND SYNTHESIS OF GOLD NANOPARTICLE CONTRAST AGENTS FOR ATHEROSCLEROSIS IMAGING WITH COMPUTED TOMOGRAPHY

Peter Chhour

A DISSERTATION

in

Bioengineering

Presented to the Faculties of the University of Pennsylvania

in

Partial Fulfillment of the Requirements for the

Degree of Doctor of Philosophy

2017

_____

Supervisor of Dissertation: David P. Cormode, D.Phil, Assistant Professor of Radiology

_____

Graduate Group Chairperson: Jason A. Burdick, Ph.D, Professor of Bioengineering

Dissertation Committee

Andrew Tsourkas, Ph.D, Professor of Bioengineering - Committee Chair

Victor A. Ferrari, MD, Professor of Medicine

Michael Chorny, Ph.D, Associate Professor of Pediatrics

This is dedicated to my parents for showing me

that with the determination to better oneself

anything is achievable

ACKNOWLEDGEMENTS

I would first like to thank my thesis advisor and mentor, David Cormode for taking me on as his first graduate student. His support and belief in my abilities truly allowed me develop and mature as a scientist. I am grateful for his continual belief that I was capable of handling all the challenges he laid in front of me, even when I felt unsure. I am thankful for the time he dedicates to his mentees, whether it be one on one meetings on short notice, immediately answering emails, or our semi-weekly lab chats. I will always be thankful for being under an advisor with a such passion for mentorship.

I would also like to thank my committee chair Andrew Tsourkas for his support and leadership during my thesis. I would like to thank my committee members Victor Ferrari, Michael Chorny, and Muredach Reilly for providing guidance and advice throughout my time as a graduate student.

Lastly, I would like to thank my family and friends for their continual support and constant inquiries about graduation. I am grateful to my family for always being there to provide a meal or two. I am grateful to have made such wonderful friends here at Penn and at the climbing gym during my Ph.D studies. I am also grateful to my long standing college friends, where I could always go to momentarily forget my daily stresses.

ABSTRACT

DESIGN AND SYNTHESIS OF GOLD NANOPARTICLE CONTRAST AGENTS FOR ATHEROSCLEROSIS IMAGING WITH COMPUTED TOMOGRAPHY

Peter Chhour

David P. Cormode, D.Phil.

Cell tracking offers the opportunity to study migration and localization of cells *in vivo*, allowing investigations of disease mechanisms and drug efficacy. Monocytes play a key role in the progression of atherosclerotic plaques in the coronary arteries. While x-ray computed tomography (CT) is commonly used to clinically assess coronary plaque burden, cell tracking with CT is mostly unexplored. The establishment of monocyte cell tracking tools would allow for the direct investigation of gene and drug therapies aimed at monocyte recruitment in atherosclerosis. In this thesis, we present the design and optimization of gold nanoparticles as CT contrast agents for cell tracking of monocyte recruitment to atherosclerotic plaques. Gold nanoparticle polymer constructs with controlled localization are evaluated as potential monocyte labels. However, cytotoxic effects were observed at concentrations necessary for cell labeling. Therefore, variations in physical and chemical properties of gold nanoparticles were explored as cell labels for monocyte tracking. Each formulation was screened for effects on cell viability, cell function and uptake in monocytes. The uptake in monocytes revealed a complex relationship with nanoparticle size behavior dependent on the surface ligand used. This

led to the selection of an optimal size and coating for monocyte labeling, 11-mercaptoundecanoic acid coated 15 nm gold nanoparticles. This formulation was further investigated for cell viability, function, and uptake with isolated primary monocytes. Moreover, primary monocytes labeled with this formulation were used to observe monocyte recruitment in atherosclerotic mice. Mice with early atherosclerotic plaques received intravenously injections of gold labeled monocytes and their recruitment to plaques were observed over 5 days with CT. Increases in CT attenuation in the plaque and transmission electron microscopy of plaque sections indicated the presence of gold labeled monocytes in the plaque. These results demonstrate the feasibility of using CT to track *ex-vivo* labeled cells non-invasively with CT and could further be used to investigate drugs aimed at modulating monocyte recruitment in the treatment of atherosclerosis. This work expands the applications of cell tracking and may lead to additional uses in other diseases.

TABLE OF CONTENTS

LIST OF TABLES

LIST OF FIGURES

Chapter 1: Introduction to cardiovascular disease, computed tomography and nanoparticle contrast agents

1.1 Introduction

The development of nanotechnology has presented new potential solutions to biomedical problems. Via control over a nanoparticle's physical and chemical properties, it can be specifically tailored to a given biomedical application. These properties influence how the nanoparticles interact with cells and the surrounding biological environment. As a result, nanotechnology has been involved in applications for drug delivery, gene delivery, adjuvants for cancer therapy and medical imaging. In particular, cell tracking has emerged as a methodology to observe cell behavior *in vivo*. The ability to detect migration, viability and localization of nanoparticle labeled cells has become of interest with the emergence of stem cell and immuno-cell therapy. Additionally, cell tracking presents an opportunity to study specific disease mechanisms in conditions such as cardiovascular disease (CVD).

X-ray computed tomography is the most commonly used imaging modality to detect and diagnose CVD in patients due to its high spatial and temporal resolution. However, the current CT contrast agents used for CVD imaging have a number of limitations including fast clearance, potential adverse reactions, and non-specific localization. The use of iodinated nano-structures and inorganic nanocrystals has shown initial success in mitigating the issues mentioned above. Furthermore, the use of CT contrast agents for cell tracking remains largely unexplored, prompting the need to develop cell tracking CT contrast agents for investigating CVD.

Herein, we propose and evaluate the design of gold nanoparticle formulations for optimal labeling of monocytes for non-invasively tracking of their recruitment into atherosclerotic plaques with CT. Complications from atherosclerosis remain the leading cause of death in CVD and monocyte recruitment into plaques plays a large role in the progression of the disease. We hypothesized that large nanoparticles with high payloads would be effective for giving monocytes high loading, to allow their detection with CT. We therefore developed and characterized large (~500 nm) polyphosphazene nanospheres containing high payloads of nanocrystals including gold and iron nanoparticles. We found loading of the nanocrystals could be selectively localized to the core or surface without disrupting the diagnostic function of the nanoparticle (Chapter 2). However at incubation concentrations necessary for sufficient cell loading for *in vivo* detection with CT, cytotoxicity towards monocytes was observed. We next sought to investigate the potential of gold nanoparticles that were not encapsulated in polyphosphazene for labeling monocytes. We studied the effect of gold nanoparticle size and coating on monocyte labeling (Chapter 3). We synthesized particles ranging from 15 to 150 nm and characterized their viability and uptake in monocytes. We found the coating of the gold nanoparticle affected the relationship between size and gold uptake in monocytes suggesting a unique size relationship for each coating examined. Since maximal cell loading could be achieved with 15 nm gold nanoparticles, we chose them for further study. We investigated the biocompatibility of 15 nm gold nanoparticle formulations with both a monocyte cell line and primary monocytes. After selecting an optimal formulation, we were able to detect the recruitment of gold labeled monocytes to atherosclerotic plaques in mice using x-ray computed tomography (Chapter 4). The results indicate the feasibility of non-invasively tracking the localization of gold labeled

cells using computed tomography. In this chapter, we detail the progression of atherosclerosis, the current state of CT technology, and the state of the art use of nanoparticles as CT contrast agents.

1.2 Background

1.2.1 Cardiovascular disease

1.2.1a Overview

Cardiovascular diseases (CVD) are the leading cause of death, accounting for nearly 1 in 3 deaths in the developed world today. Worldwide, CVD accounted for 17.3 million deaths in 2013 which is expected to increase to 23.6 million by 2030.[1] In the United States, approximately 35.1% of adults have at least one cardiovascular disease, and this number is expected to rise to 43.9% by 2030.[2] This rise in prevalence is expected due to increase of factors such as physical inactivity, poor nutrition, and obesity. Cardiovascular disease is a broad definition that covers several pathologies including stroke, high blood pressure, heart failure, and coronary artery disease (CAD). Nearly half of the total deaths from CVD arise from CAD which includes angina pectoris (chest pain), atherosclerosis of the coronary arteries, myocardial infarction, and ischemic heart disease.[3] These underlying causes of these conditions is the development of atherosclerosis in the coronary arteries that lead to narrowing of the arteries and potential blockage from rupture.

1.2.1b Coronary arterial disease

Coronary artery disease is the progression of atherosclerosis in the coronaries such that it leads to clinical manifestations, *i.e.* ischemic heart disease and myocardial infarction. Atherosclerosis is prevalent in areas of high oscillatory flow and low endothelial shear stress, indicating that initiation of atherosclerosis may be due to localized mechanical stresses.[4-5] These local flow conditions allow for the accumulation of circulating low density lipoproteins (LDL) into the intima. Oxidation of these LDL particles leads to the activation of the endothelium, increasing the expression of surface adhesion molecules.[6-7] Increased expression of vascular cell adhesion molecule (VCAM) and intercellular adhesion molecules (ICAM) promote the adherence of circulating leukocytes.[8-10] Subsequently, a chemokine gradient drives the migration of these adhered leukocytes into intima. Inflammatory monocytes play a key role in the progression of atherosclerosis and have been found to be recruited into the intima through chemokine gradients for MCP-1 (CCR2 receptor), fractalkine (CX3CR1 receptor), and CCL5 (CCR5 receptor).[11-13] In the intima, monocytes differentiate into phenotypical macrophages and begin engulfing oxidized LDL particles. These lipid particles accumulate in the macrophages, eventually becoming foam cells, which are thus named due to their appearance under microscopy.[14] Foam cells promote the destabilization of the surrounding extracellular matrix (ECM) through the release of proteolytic enzymes, including matrix metalloproteinases (MMP) and cathepsins.[15] The chronic build up of foam cells and other cells, such as altered smooth muscle cells migrating from the media, increases the chances of plaque rupture.[16]

The development of plaques may eventually lead to their rupture, which releases the contents of the plaque into the circulation as depicted in Figure 1.1. The contents of

the plaque such as necrotic cells and cell debris induce the formation of a thrombus, which can occlude the artery.[17] Such an occlusion occurring in the coronary artery can result in an acute myocardial infarction (MI). The myocardium downstream of the occlusion may become ischemic, which can lead to necrosis. Resolution of the occlusion can lead to increased incidence of a secondary cardiac event for patients resulting from weaken structural integrity of the affected myocardium. Management of wound healing after a MI is critical for improved prognosis for patients.

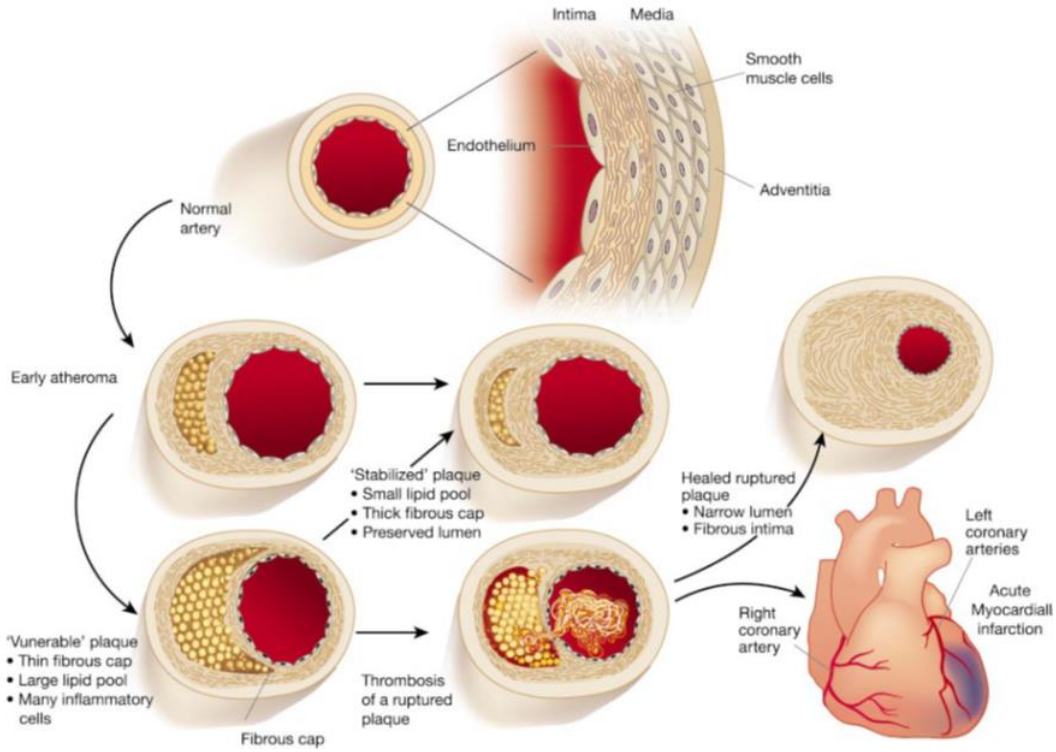

Figure 1.1 Progression of atherosclerosis in artery.

Illustration of plaque build up and progression to stabilized plaque or rupture. Continued accumulation of lipids in the intima can lead to a thin fibrous cap, increasing risk of rupture. Plaque rupture in the coronary artery leads to the formation of thrombus and an

occlusion of the artery *i.e.* myocardial infarction. Reproduced with permission from Libby *et al.* (2002).[15]

1.2.1c The role of monocytes in coronary arterial disease

Monocytes play a central role in both the progression of atherosclerosis in the coronary arteries and wound healing of the myocardium after a MI as shown in Figure 1.2. In both instances, the function of the monocytes depends on their subtype. Monocytes are frequently divided into two subtypes via differential marker expression. In humans, classical inflammatory monocytes are described by the cell surface expression of $CD14^{++}CD16^{-}$ markers.[18] Conversely, resident monocytes are characterized by their expression $CD14^{+}CD16^{+}$.[19] These two distinct monocyte subpopulations have been found to be conserved across species, with $Ly6C^{+}$ and $Ly6C^{-}$ cell surface markers describing inflammatory and resident murine monocyte populations, respectively.[20] These subtypes are also classified by the relative expression of CCR2, a chemokine receptor involved in recruitment of inflammatory cells.[21-22] This receptor plays a prominent role in the migration of inflammatory monocytes to inflamed tissue.

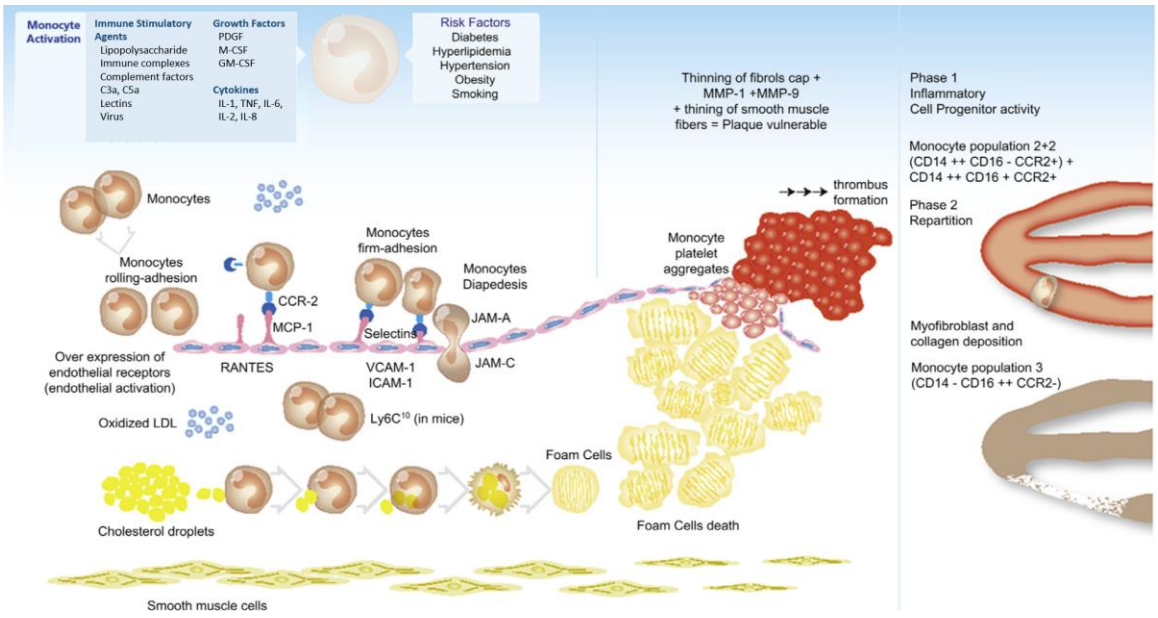

Figure 1.2 The role of monocytes in atherosclerosis progression.

Monocytes are actively recruited into the arterial wall in developing plaques through active chemokine gradients. In the arterial wall, monocytes differentiate in macrophages and engulf LDL, becoming foam cells. Foam cells promote plaque destabilization and rupture. After rupture and occlusion of coronary arteries, monocytes are recruited to injured tissue for repair and wound healing. Reproduced with permission from Ghattas *et al.* (2013).[23]

In the progression of arterial disease, the activation of the endothelium increases the adherence of circulating leukocytes including monocytes. Inflammatory monocytes migrate through the endothelium facilitated by the expression of surface receptors CCR2, CX3CR1 and CCR5.[24-25] The release of chemokines corresponding to these receptors (MCP-1, fractalkine, CCL5) drives the chemokine gradients and subsequent migration. In the intima, monocytes differentiate into macrophages and begin engulfing

oxidized low density lipoproteins.[26-27] The initial recruitment of monocytes populates lesional macrophages early in plaque formation. However in established plaques, the majority of the macrophages are due to local proliferation.[28-29] With the accumulated LDL, the macrophages become phenotypical lipid-laden foam cells releasing cytokines and metalloproteinases that contribute to plaque destabilization.[30-31] The accumulation of foam cells gives rise to lesion formation and eventual plaque rupture.

A plaque rupture in the coronary arteries leads to the formation of a thrombus and potential occlusion of the vessel. The blockage of the coronary arteries is a myocardial infarction also known as a heart attack. The role of monocytes in wound healing after a myocardial infarct is critical to the long term clinical outcome. Monocytes are necessary to clear necrotic tissue from the site as well as promote the repair of the tissue. After an infarct monocytes are recruited from circulation to the injured area for repair for up to two weeks.[32] The recruitment of monocytes has been hypothesized to be a biphasic response with separate monocyte subtypes dominating at each phase. Nahrendorf *et al* proposed that in the first 1-4 days following the infarct, inflammatory Ly-6c^{+} monocytes are the major recruitment subtype, promoting clearance through phagocytosis and enzymatic digestion. Onward from day 4, reparative Ly-6c^{-} monocytes appear to be the actively recruited subtype for wound healing through anti-inflammatory cytokines and growth factors.[33] Similar to the recruitment to plaques, monocyte recruitment to the infarcted area is mediated through the chemokine receptors CCR2, CX3CR1, and CCR5. Moreover, it was proposed that the biphasic recruitment is due to a shift in the expression of ligands specific to these receptors by the infarct tissue. The production of MCP-1 (CCR2 ligand) promotes Ly-6c^{+} recruitment during “phase 1,” and fractalkine (CX3CR1 ligand) expression promotes Ly-6c^{-} recruitment during “phase 2.”[33]

Studies have shown that increased recruitment of Ly6c^{+} can lead to improper healing outcomes such as left ventricular dilation that can manifest into future clinical cardiovascular events.[34-36] Therefore, proper accumulation of monocyte population in each phase after a myocardial infarct is critical to understanding infarct healing.

1.2.2 Imaging of coronary arteries

1.2.2a Introduction

Coronary artery disease is a chronic condition, typically developing for decades before becoming symptomatic. While symptoms may differ in patients, a common early indicator for CAD is chest pain *i.e.* angina pectoris. Risk factors such as age, sex, weight, smoking, and hypertension are used to determine the risk of CAD for patients with chest pain.[37] Patients with high risk undergo electrocardiography for evidence of ST-T wave changes or LV hypertrophy. If abnormalities are present, further evaluation is necessary to determine extent of the CAD and risk of a cardiac event.[38-39] A coronary angiogram is a commonly used method to assess the location and severity of the arterial plaques. To perform a coronary angiogram, a catheter is fed to the coronary arteries and an iodinated dye is released. X-ray is used to observed the location and extent of stenosis in the coronary arteries. Coronary angiography also allows for stent and angioplasty intervention in the cases that call for revascularization. There is interest in developing imaging tools to non-invasively characterize plaque severity where magnetic resonance imaging (MRI), positron emission tomography (PET), and x-ray computed tomography (CT) are utilized.

MRI provides excellent soft tissue contrast, but suffers from long image acquisition times, preventing imaging of the coronary arteries from being performed in a single breath hold (which is needed to limit the impact of respiratory motion). Moreover, MRI of the coronary arteries lacks information on plaque calcification and cannot quantify the extent of the disease.[40] MRI is not routinely used for coronary artery imaging in clinical practice. PET can provide functional cardiac information with the use of radioisotope contrast agents.[41] Radiolabeled contrast agents typically have short-half-lives, which increases the complexity of their distribution from production centers. The use of PET for coronary artery disease in the research field continues to expand, but still remains extremely limited clinically.[42] 18F-fluorodeoxyglucose (18F-FDG) has been used as a macrophage marker and subsequent marker of inflammation in atherosclerosis.[43] However, the low spatial resolution of PET has caused concern about reliability when quantifying 18F-FDG uptake in the coronary plaque.[44] 18F-sodium fluoride has also been explored as a PET marker for arterial calcification.[45] For both contrast agents, low spatial resolution, motion and off-target uptake typically limits PET studies to evaluation of plaque only in larger arteries such as the carotids or thoracic aorta. As we will explain below, the modality of choice for clinical imaging of coronary artery disease is CT.

1.2.2b CT principles

CT has unique advantages for visualizing the coronary arteries that make it an excellent modality for this application. CT relies on x-rays that are produced by accelerating electrons from a cathode towards an anode, which is typically made of tungsten. The impact of the electrons, depending on their energy, produces x-rays in the

form of bremsstrahlung and characteristic radiation. In bremsstrahlung radiation, the incoming electron path is diverted by interaction with the nuclei, converting lost kinetic energy into an x-ray. In the case of characteristic radiation, the incoming electron ejects an inner-orbital electron of the atom. An electron from an outer orbital fills the vacancy while releasing a characteristic x-ray. For imaging applications, x-rays from the generating source interact with the object of interest in two primary mechanisms, Compton scattering and the photoelectric effect (Figure 1.3a). For Compton scattering, the incoming x-ray transfers a portion of its energy to an outer shell electron which causes the x-ray to scatter in a different direction. For CT energy levels, the primary form of interaction between x-rays and the subject is the photoelectric effect. The incoming x-ray ejects an inner shell electron of the atom, typically of the k or l shell. An outer shell electron fills the inner-shell vacancy and produces a characteristic x-ray. The photoelectric effect occurs when the energy of the incoming x-ray is higher than the binding energy of the inner-shell electron, also known as the k-edge or l-edge energy. The photoelectric effect produces a significant jump in mass attenuation, improving contrast for imaging (Figure 1.3b). For CT contrast agents, imaging with peak voltages higher than the k-edge energy of the x-ray attenuating agent improves contrast enhancement between the agent and surrounding tissue. X-ray attenuation is quantified by the Hounsfield scale which defines Hounsfield units (HU) = 1000 * (μ- μ_{water})/(μ_{water} - μ_{air}), where μ is the linear attenuation coefficient of the corresponding material. The Hounsfield scale standardizes the attenuation of a material in reference to the attenuation of water (HU= 0) and air (HU= -1000).

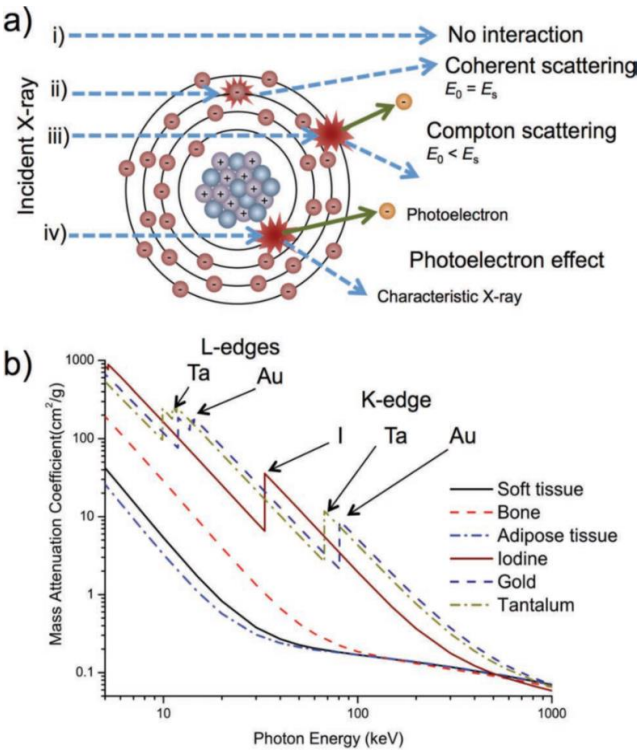

Figure 1.3 X-ray interaction with materials.

(a) Incoming x-rays interact with matter via coherent scattering, Compton scattering, and photoelectron effect depending on the energy of the incident x-ray. At CT energy levels, the primary interaction is the photoelectron effect, where inner shell electrons are ejected and characteristic x-rays are produced. (b) For high Z-elements, ejection of inner shell (k or l shells) electron produces a spike in attenuation of x-ray, allowing for strong discrepancy between materials. Reproduced from with permission from Lee *et al.* (2013).[46]

1.2.2c Current CT technologies

Due to its non-invasive qualities and comparable effectiveness in predicting CAD in patients, the use of CT angiography has begun to rival coronary angiography in the

emergency room.[47-48] The coronary arteries in humans are approximately 4-5 mm in diameter proximally, tapering rapidly to less than 1 mm, mandating high spatial resolution for imaging. A variety of adjustable factors, including slice thickness, reconstruction parameters, and field of view can affect spatial resolution in CT; most modern scanners are capable of producing resolution of 0.5 mm or less in each dimension.[49] Moreover, cardiac and respiratory motion can be overcome by the fast temporal resolution of CT and a volume coverage allowing imaging of the entire heart to be acquired in a single breath hold. Increases in the number of detectors and improvement in gantry rotation speed in CT scanners has considerably improved the temporal resolution over the past two decades. Modern clinical 64-detector CT systems are capable of sub-200 ms resolution,[50] while the newest CT scanners are capable of sub-100 ms temporal resolution.[51] Synchronization of the acquisition to the electrocardiogram (ECG) signal can be used to reduce artifacts from heart motion.[52] ECG synchronization can be performed using two methods, prospective triggering and retrospective gating. Prospective triggering acquires images at a pre-defined portion of the R-R interval, while retrospective gating acquires images throughout the cardiac cycle, allowing for image reconstruction at any phase of the heartbeat, but at the cost of a higher radiation dose.

CT can quickly image the coronary arteries and exclude coronary artery disease from patients presenting with chest pain.[53-55] CT allows for post-processing of cross-sectional scans to create improved visual information, such as 3D renderings of coronary arteries.[56] The applications of cardiac CT for plaque characterization include calcium scoring, determination of non-calcified plaque volume and extent of stenosis.[57] These parameters can be assessed with CT angiography (CTA), a non-invasive CT

scan using contrast agents to visualize arterial flow. The plaque characteristics that can be derived from CTA can be used to identify patients at high risk of a significant cardiac event. High risk plaque features that can be visualized with CTA include stenosis ≥ 50%, positive remodeling, low HU, napkin ring sign, and spotty calcium.[58] A novel application of cardiac CT angiography is noninvasive determination of the hemodynamic significance of an observed stenosis. Fractional flow reserve (FFR) describes the pressure difference across an arterial stenosis as compared to the pressure in the absence of a stenosis and can be measured directly with catheter angiography.[59] However, advancements in computer modeling has allowed calculations of fluid dynamics from CTA scans for accurate determination of coronary flow and pressure without the need for an invasive procedure. CTA-derived computational models of FFR have been shown to have higher accuracy of determining the impact of stenoses than CTA based measurements of stenosis dimensions alone.[60] The myocardium can also be visualized with high resolution allowing for detection of abnormal morphology in the chambers of the heart and valves.[61] Moreover, the degree of injured myocardium after an infarct can be determined due to the changes in the thickness and/or scar formation of the myocardium.[62]

1.2.2d Developing CT technologies

Advancements in x-ray CT technology are allowing for new potential clinical indications. Most commonly, CT images have been reconstructed using back filtered projection to create 3D datasets. With increases in computing power, iterative reconstruction methods have become available, allowing for improved signal to noise

ratios (SNR) as compared to current reconstruction methods *i.e*. back filtered projection.[63] With improved SNR, similar image quality compared to back filtered projection reconstructions are achievable with less radiation dose.[64] Various models of iterative reconstruction have been compared to filtered back projection, and lower image noise was consistently observed for identical CT imaging parameters.[65] Iterative reconstruction could therefore be a boon for cardiothoracic imaging where image quality can suffer from motion artifacts, obese patients, calcium artifacts, and blooming from stents.[66] Researchers have found that the improved image quality leads to more accurate diagnoses with iterative reconstruction compared to filtered back projection for coronary CT angiography.[67-68] While various iterative reconstruction models are available, further experimental validation is needed before wider adoption. There is also current exploration for the use of iterative reconstruction methods to improve CT sensitivity towards contrast agents.[69] Improving CT sensitivity to contrast agents may further enable CT applications such as cell tracking.

Multi-color or spectral computed tomography is an emerging CT technology capable of distinguishing different elements based on their x-ray absorption at different energies. This technology works by exploiting the x-ray absorption at the k-edge of high Z-elements and creating discrete photon energy bins.[70] By separating the incoming photons by energy, multiple materials can distinguished in a single scan.[71] This technology allows for material decomposition which results in material-specific images, providing additional information compared with current CT scanners. Additionally, spectral CT can offer new benefits for CT contrast agents due to material discrimination.[72-73] Specifically, this technology allows for quantification of localized contrast agents and the possibility of discriminating multiple contrast agents in a single

scan.[74-75] The use of contrast agents for CT can benefit from both of these emerging technologies, with the aim to improve CT sensitivity for contrast agents and expand detection capabilities of current CT scanners.

1.2.3 CT cardiovascular contrast agents

1.2.3a Introduction

CT contrast agents play a key role in cardiovascular CT scans; the use of contrast agents in CT can improve the delineation between different soft tissues and is critical for highlighting blood vessels. The primary mechanism for x-ray attenuation in CT is the photoelectric effect. At CT energy levels (25-140 keV), incoming x-rays have enough energy to interact and eject inter-shell electrons (k or l shell) of the atom. Ejection of a k-shell electron produces a significant increase in x-ray attenuation and allows for increased separation between tissue and contrast media. For this reason, CT contrast agents are typically high atomic number elements such as iodine, barium, gold, bismuth, and lanthanides that have l and/or k edges that are at much higher energies than tissue and are closer to diagnostic x-ray energies (Table 1.1). However, CT suffers from low sensitivity to contrast agents, typically requiring millimolar local concentrations to produce contrast that can be distinguished from the background.[76]

Table 1.1 Characteristics of elements commonly used to form CT contrast agents.

Element	Atomic Number	l-edge (keV)	k-edge (keV)
Ag	47	3.35	25.5
I	53	4.55	33.2
Ba	56	5.25	37.4
La	57	5.48	38.9
Gd	64	7.24	50.2
Yb	70	8.94	61.3
Ta	73	9.88	67.4
Au	79	11.9	80.7
Bi	83	13.4	90.5

Clinically, iodinated contrast agents (ICA) can be used to visualize the vasculature as well as organs such as the brain, heart, liver, and kidneys.[77-79] Clinical ICA are small molecules that are based on a tri-iodinated benzene ring (Figure 1.4). These types of structures have reduced osmolality and toxicity compared with iodide ion based agents. These iodinated rings are typically functionalized with amides and alcohol groups to provide water solubility, and can be monomers or dimers. These agents can be further categorized into ionic and non-ionic formulations which yield different properties in terms of toxicity and clearance from the blood stream. Regardless of the molecular structure of these agents, clinically approved ICA suffer from rapid renal clearance from the circulation after intravenous injection, on the order of minutes.[80] Given this rapid clearance, large amounts of contrast agent are often used for prolonged or multiple CT scans, with doses of 150 ml being used routinely.[811] Injecting large volumes of ICA increases the chance of severe renal impairment, known as contrast induced nephropathy, in specific patient populations.[82] Contrast-induced nephropathy is more likely in patients with pre-existing renal dysfunction,[83] who now compose 26% of

the US population over 65.[84] This proportion is expected to increase in the coming years, since renal dysfunction is common in diabetics and the prevalence of diabetes is predicted to rapidly rise.[85-86] Iodinated contrast agents also can commonly cause adverse reactions in patients ranging from mild symptoms including nausea and vomiting to severe reactions such as anaphylaxis.[87]

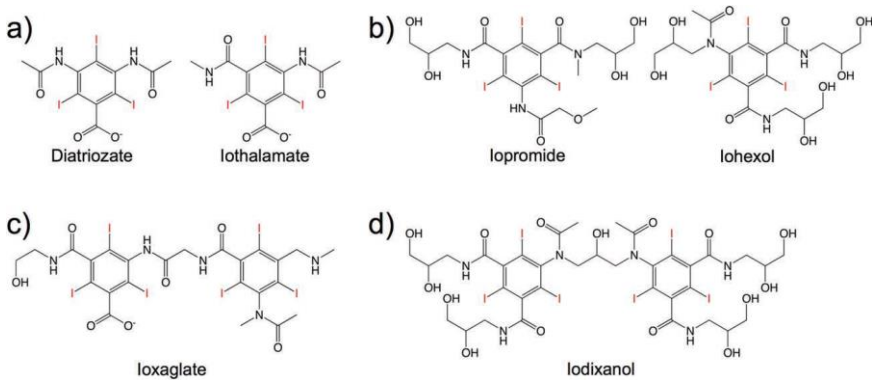

Figure 1.4 Common used iodinated small molecules.
Tri-iodinated benzene ring based compounds that are clinically used as CT contrast agents. Variations include (a) ionic monomers, (b) non-ionic monomers, (c) ionic dimers and (d) non-ionic dimer. Reproduced from with permission from Lee *et al* (2013).[46]

As mentioned, iodinated small molecule contrast agents are the most widely used class of agent in clinical CT scanning. While different formulations (ionic vs non-ionic, dimer vs monomer) have slightly differing biocompatibility properties, they continue to suffer from rapid clearance and the risk of adverse reactions.[87] Researchers have turned to nanotechnology to improve the properties of iodine-based agents. Incorporation of iodinated agents into nanoparticles such as nano-emulsions, micelles, liposomes, dendrimers have resulted in improvements in circulation time and

biocompatibility. The structures of some of the nanoparticle agents used as CT contrast agents are displayed in Figure 1.5. Long blood circulation times of contrast agents may help to improve the assessment of cardiovascular health. A long circulating agent can also decrease the total dose necessary for an imaging procedure, potentially reducing the burden of the agent on the patient. The use of a blood pool contrast agent for CT may provide information about coronary artery disease and progression, allowing visualization of the extent of stenosis in an artery as well as calcified and non-calcified plaques.[88] Use of a contrast agent also allows for assessment of cardiac functions such as ejection fraction and stroke volume.[49] In addition, contrast agents are needed to highlight blood vessels during stent placement procedures. Below, we further explore the current state of CT contrast agents including iodinated nanotechnologies and inorganic nanoparticles.

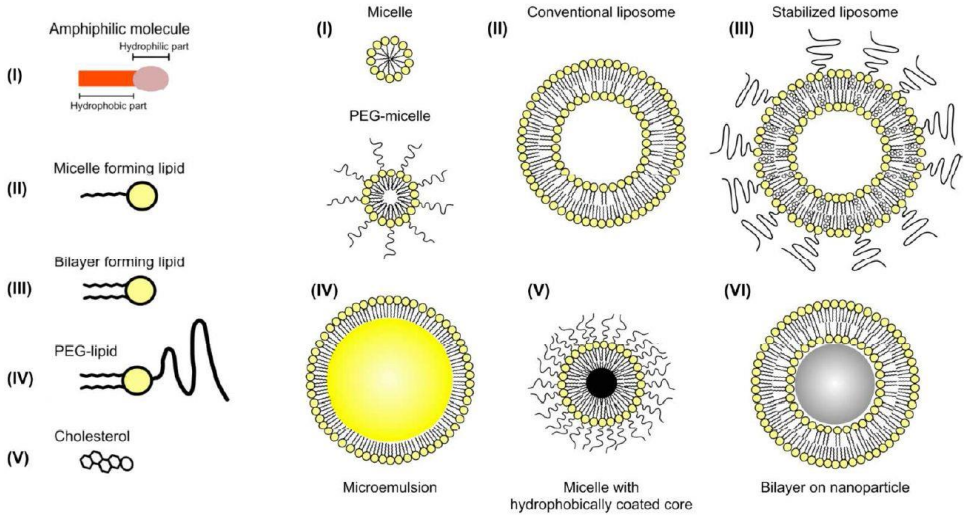

Figure 1.5 Nanotechnologies used for contrast agent development.

Schematic representations of some of the nanoparticle platforms used to incorporate iodinated agents and inorganic nanocrystals for improved biocompatibility and biological function. Reproduced with permission from Mulder *et al* (2005).[89]

1.2.3b Iodinated nanoparticle contrast agents

To incorporate iodinated agents into nanoparticles, researchers have turned to a number of different nanotechnology platforms, each with their own advantages. Predominately, iodinated agents have been encapsulated or conjugated to oils and lipids to form these nanoparticles. One such platform is nano-emulsions, where the core of the particle contains iodinated oils. Nano-emulsions can be formed via simple methods that produce stable iodinated particles and have been an attractive choice for iodinated contrast agents. An emulsion is formed with a suitable amphiphilic surfactant encapsulating an iodinated oil core. An iodinated oil called Lipiodol (also known as Ethiodol) is FDA approved and consists of iodine combined with ethyl esters of poppy seed oil.[90] Because Lipiodol is hydrophobic, it has limited clinical uses (it is used as an agent for lymphangiography and trans-arterial chemoembolization).[91-92] To expand the applications of Lipiodol as a blood pool agent, Pluronic F127 and a polyethylene glycol (PEG) diamine was used to encapsulate Lipiodol into a nano-emulsion.[93] These particles, 150 nm in diameter, were shown to be thermodynamically stable and produce vascular CT contrast in the ventricles and major arteries for up to 4 hours.

Nano-emulsions have also been reported where a mixture of phospholipids and cholesterol was used to surround the hydrophobic core, which consisted of iodinated triglycerides. A nano-emulsion formed with endogenous oils and lipids was

demonstrated as an effective contrast agent for hepatic imaging and is available as a commercial product known as Fenestra LC®.[94-95] The iodinated triglycerides making up the core of this nano-emulsion are rapidly metabolized by the liver.[96] To provide longer circulation as a blood pool contrast agent, the agent has been reformulated with PEG included at the surface of the particle to reduce uptake by hepatocytes, which is known as Fenestra VC®.[97-98] As a blood pool agent, Fenestra VC® has been used to study cardiac function in mice, quantifying ejection fraction, stroke volume, and cardiac output.[99] In this study, Fenestra VC® provided vascular contrast for 3 hours with a nearly 500 HU value difference between the blood and myocardium. Moreover, with the use of Fenestra VC®, Detombe *et al.,* studied cardiac function and ventricular remodeling in a mouse model of myocardial infarction. The group was able to assess systolic and diastolic volumes and ejection fraction non-invasively over the course of 4 weeks after myocardial infarction.[100] Both studies utilized cardiac gating with micro-CT to quantify cardiac function accurately.

While Fenestra formulations have been used successfully for cardiac applications, relatively poor inclusion of iodine by weight means that very large volume administrations of the agent are required (up to 40% of total blood volume). To overcome this issue, researchers have used denser iodinated oils to improve iodine content in the formulations. Using, a dense, tri-iodinated oil, de Vries *et al.,* formed nano-emulsions using the amphiphilic polymer, poly(butadiene)-b-poly(ethylene oxide) (PBD-PEO).[101] The agent was able to provide strong vascular contrast in the chambers of the heart of up to 220 HU directly after administration. Attenuation of the liver and spleen remained at high levels over the three hour observation period suggesting the mononuclear phagocytic system as the main clearance pathway for the agent. Novel

approaches to increasing the density of iodinated oils continue to be explored.[102-103] For instance, Attia *et al.* reported agents that contain up to 65% wt. of iodine via use of a hexa-iodinated monoglyceride and a PEGylated nonionic surfactant.[98] This formulation showed clear delineation of the major arteries and heart chambers post-injection with a long circulation half-life of 6.1 hours.

Micelles are similar to nano-emulsions, in that they are self-assemblies of amphiphilic molecules where the hydrophilic head groups point outwards and the hydrophobic tails point inwards (Figure 1.5). The main difference between emulsions and micelles is that there is not an oil core for micelles. Therefore, to form micelle-based CT contrast agents, iodinated molecules are typically linked to the hydrophobic tails of the amphiphiles, concentrating the iodinated moieties into the center of the micelle. This allows for high iodine payloads.[104] There have been several reports of iodinated micelles used as blood pool contrast agents.[105] Torchilin *et al.* reported the synthesis of micelles using iodine containing poly-l-lysine (MPEG-iodolysine). The micelles were approximately 80 nm in diameter with 33.8% iodine content. The agent was injected intravenously and allowed for CT imaging of the aorta, heart, liver and spleen for up to 3 hours post-injection in rats.[106]

While nano-emulsions and micelles can carry hydrophobic contrast media, liposomes are versatile platforms that can carry both aqueous and hydrophobic payloads. Liposomes are synthesized through the use of amphiphilic lipids or polymers that self-assemble into bilayers. This architecture allows for encapsulation of hydrophilic agents in the core as well as hydrophobic agents in the bilayer. One of the first liposomal iodinated contrast agents was synthesized using L-α-phosphatidylcholine and was loaded with a number of different aqueous iodinated agents.[107] The agent was injected

intravenously as a blood pool contrast agent. Uptake of the liposome was seen in the liver and spleen in a dose dependent manner with maximum attenuation of 240 HU seen at 1 hour. Because these early liposomes provided strong contrast of the liver and spleen, it was primarily used to visualize tumors in these organs.[108-109]

With improvements to liposome design, most notably the modification of amphiphilic lipids/polymers with PEG, the diagnostic applications of liposomal contrast agents expanded. The addition of PEG to liposomal formulations allows for significantly increased blood circulation times improving their utility as blood pool agents.[110-111] One of the earliest reports of PEGylated liposomes, PEG-phosphatidylethanolamine (PEG-PE) liposomes, found that the addition of PEG increased the blood circulation time to up to 5 hours as compared to 30 minutes for non-PEGylated formulations.[112] Iodinated PEGylated liposomes have been successful in providing strong vascular contrast of up to 900 HU in the aorta, as reported in a study by Mukundan *et al.*[113]

With the use of liposomes, a significant issue is the leakage of internal payloads through the lipid bilayer. Hydrophilic payloads have been found to diffuse through bilayers due to chemical gradients. To overcome this issue, some groups have added cholesterol to liposome formulations, which reduces the permeability of the liposome and thereby decreases payload leakage.[114-115] Additionally, direct iodination of the lipids used to form the liposome can be used to prevent internal leakage, since covalently binding iodine onto lipid constrains the contrast generating material in the bilayer.[116]

Moreover by incorporating iodinated molecules into the lipid bilayer, the aqueous core can carry a separate payload including drugs for theranostics applications, another imaging agent for multi-modal imaging, or more of the same agent for increased payload delivery. A study by Kweon *et al.,* reported liposomes that were simultaneously loaded

with iodinated contrast into both the core and lipid bilayer.[117] 1,2-dimyristoyl-sn-glycero-3phosphocholine (DMPC), cholesterol, and Lipiodol were mixed together, freeze-dried and resuspended with a solution containing iopamidol to form the liposomes. As mentioned above, cholesterol increases the rigidity of the lipid membrane decreasing leakiness of the liposomes. This dual loading procedure produced particles about 280 nm in diameter, and a solution whose iodine concentration was 49.2 mg/ml. Inclusion of both Lipiodol and iopamidol was found to improve iodine content in the nanoparticle solution over either payload alone. Intravenous injection of the liposome produced strong contrast in the aorta after injection and was observed for up to 2.5 hr. Because of the lack of PEG in the formulation, high uptake was seen in the liver and spleen, resulting in attenuation values of up to 684 HU for the spleen. This study demonstrates the versatility of liposomes for contrast agent delivery.

Dendrimers are another platform that has been used to develop contrast agents for computed tomography. Dendrimers are polymeric molecules formed through sequential branched growth steps termed “generations”. Each generation exponentially increases the number of branches, isolating the core from the external environment. Additionally, the last generation of the branched sequence can be functionalized to confer specific properties to the dendrimer. The branched structure provides excellent molecular stability and can provide many sites for functionalization at the ends of the branches.[118] Dendrimers synthesized using poly(amido amine) (PAMAM) allow for functionalization through amine groups at the available termini of the molecule. By conjugating triiodobenzenepropanoic acid (DMAA-IPA) onto a PAMAM dendrimer, Yordanov *et al.* were able to incorporate up to 33% iodine content by weight.[119] Large dendrimers are often quickly cleared through the mononuclear phagocytic system,

however Fu *et al.* reported dendrimer-based CT contrast agents with improved circulation times. These dendrimers were formed via the use of a large PEG core (6000-12000 MW) and poly-L-lysine for branch generation.[120] The amine termini of these dendrimers were functionalized with triiodophthalamide molecules to provide CT contrast.

Nanotechnology offers several platforms upon which to develop contrast agents for CT as outlined above. Blood pool agents are useful to help visualize several pathologies in coronary artery disease and myocardial infarction, however specific targeting of contrast agents can allow single mechanisms or processes in cardiovascular disease to be probed. The progression of coronary artery disease occurs in many stages, providing numerous targets to study. Targeting can be accomplished by attaching ligands such as antibodies or peptides to the surface of the particle. Moreover, the use of native biological material such as lipoproteins (e.g LDL or high density lipoprotein) can provide targeting for cardiovascular disease.

Pan *et al.,* used poly(styrene-b-acrylic acid) to produce nano-emulsions with high payloads of Lipiodol (up to 37% wt of iodine) under 100 nm in diameter.[121] Furthermore, the authors conjugated an anti-fibrin monoclonal antibody onto the particle using a modified avidin-biotin linker. Fibrin is generated during the coagulation cascade and is a key element in thrombus formation. It is a very high density target and therefore suitable for molecular imaging via CT (high density targets are needed due to the low sensitivity of CT). A fibrin targeted agent may reveal information on plaque rupture and subsequent thrombus formation. Using a fibrin clot phantom, the agent found a CNR value of 98 ± 12 compared to the surrounding water. From rat experiments, the blood half-life of the

agent was found to be 56 minutes, although *in vivo* thrombus targeting experiments were not reported.

LDL is an attractive platform for targeted imaging due to its evasion of the immune system, biocompatibility, biodegradability, defined size and innate targeting. LDL infiltration in leaky endothelium is a key stage in early atherosclerosis development. A number of studies have attempted to use LDL as nanoparticle platform to carry imaging agents for detection of plaque for multi-modalities.[122-124] For iodinated contrast agents, a study by Hill *et al.* demonstrated the feasibility of using LDL containing iodinated tri-glycerides to target liver cells (HepG2) that over express the LDL-receptor.[125] This *in vitro* study resulted in contrast enhancement of the cells, but would require further testing *in vivo.*

1.2.3c Inorganic nanoparticle contrast agents

While iodinated small molecules are the contrast agents used for x-ray computed tomography clinically, there has been significant pre-clinical interest in the development of inorganic nanoparticles as imaging agents. Inorganic nanoparticles can provide improved x-ray attenuation at CT energy ranges due to higher k-edge energy levels as compared to iodinated agents. Furthermore, the payloads of inorganic nanoparticles can be much higher than for iodine based agents, since the density of inorganic materials is often very high. For example, Brown *et al.,* reported a solid bismuth core CT contrast agent (core density 9.8 g/ml) whose 76 nm cores carried a payload of 6 million Bi atoms each.[126] Additionally, the use of inorganic nanocrystals may alleviate biocompatibility complications associated with iodinated agents as outlined above.

Of the various types of inorganic nanocrystals that have been proposed as CT contrast agents, gold nanoparticles (AuNP) have been the focus of most work. Gold nanoparticle syntheses allow for control of size, shape, and functionality of the particles. This precise control allows for specific tailoring of these particles for a given application. AuNP can be included in various nanotechnology platforms, i.e. micelles, liposomes, dendrimers, and as ligand stabilized crystalline nanoparticles.[127-128] Gold nanoparticles are also well known for their biocompatible properties and have been used in a variety of biomedical applications such as drug delivery, imaging, biosensors, and photothermal ablation (Figure 1.6).[129-133]

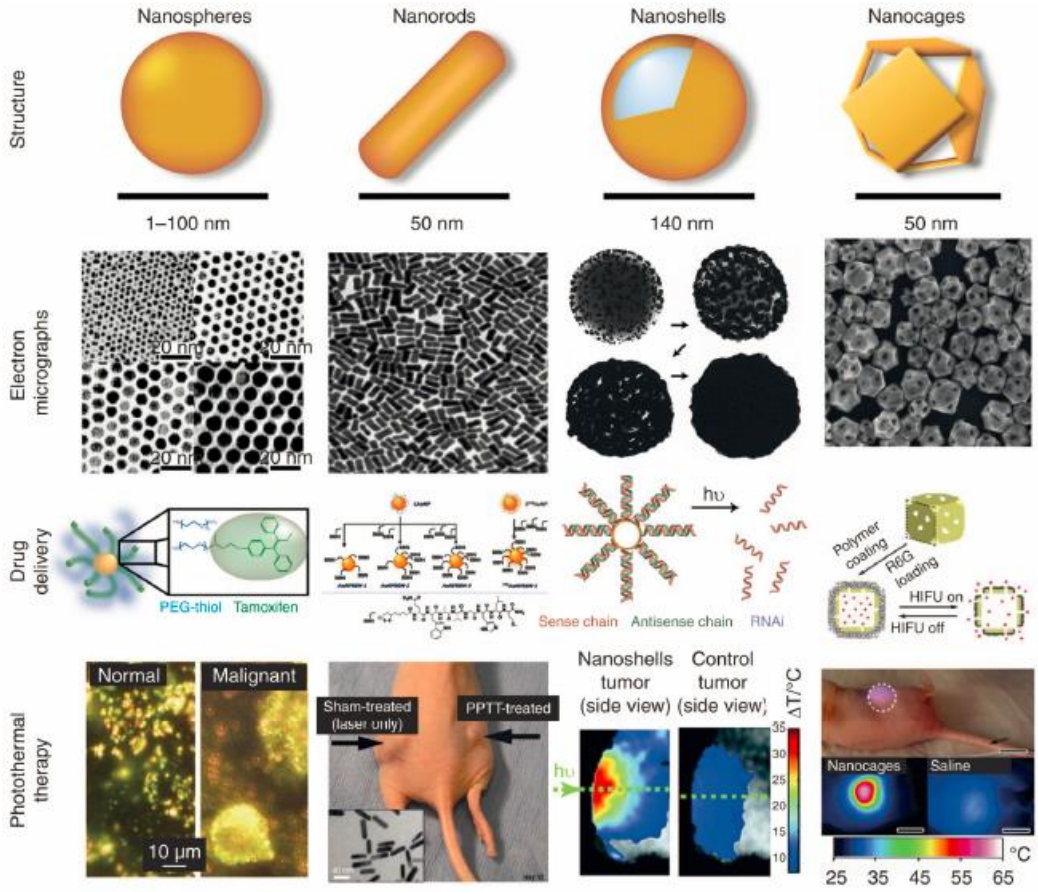

Figure 1.6 Biomedical applications of gold nanoparticles.

Gold nanoparticles can be synthesized in various shapes and sizes. Control over these properties in addition to control over chemical functionalization allow for tailoring of nanoparticles to specific biomedical applications. Reproduced with permission from Dreaden *et al* (2012).[134]

As a CT contrast agent, the physical parameters of the particle as well as its chemical properties can drastically influence the particle's biological properties in terms of clearance and biocompatibility. One of the first AuNP developed as an x-ray contrast agent was a 1.9 nm spherical formulation, and was shown to provide strong enhancement of the major vessels. However, due to the small size of the agent, the particles were rapidly cleared through the renal system as evidenced by high attenuation in the bladder in images acquired 10 mins after injection.[135] Increasing the size and/or modifying the surface functionality of AuNP has been shown to improve circulation time, as found in studies of AuNP whose core size was around 10 nm. After coating with PEG, the nanoparticles had an overall size of 38 nm. These nanoparticles were not renally cleared and provided vascular contrast over a period of 12-24 hours.[136]

A study by Kim *et al.,* examined the effectiveness of AuNP as blood pool contrast agents after surface modification with PEG.[137] AuNP 30 nm in diameter were synthesized through the reduction of gold chloride by sodium citrate using a modified Turkevich method.[138-139] Ligand exchange was performed with 5000 molecular weight methoxy-PEG-thiol for stabilization and to provide a long circulation half-life. Cytotoxicity of the AuNP-PEG particles were evaluated in HepG2 (epithelial liver cell line). The particles were well tolerated up to 1000 µg/ml of Au. After intravenous injection of AuNP-PEG, the agent yielded strong contrast in the heart and major arterial vessels (>100

HU). An increase in attenuation of roughly 100 HU in the heart and blood vessels was sustained for 4 hours post-injection. The attenuation of the liver and spleen was found to increase over the 24 hour period, indicating the major clearance pathways for the PEG coated AuNP. Due to the uptake of the particles by Kupffer cells and hepatocytes, the authors demonstrated visualization of a hepatoma *in vivo* in a rat model. In scans, 12 hours post-injection, strong attenuation in the aorta was seen with clear delineation of the hepatoma. Other studies have focused on different AuNP structures (e.g. nanorods[140-141]), coatings (such as gum-arabic[142-143]) or incorporated gold into other platforms such as dendrimers.[144-147] While AuNP have desirable properties for x-ray imaging, the cost of gold may be an issue for widespread adoption and scale up. Other high atomic number elements have been explored as CT contrast agents. For example, studies have shown bismuth nanoparticles as a possible CT blood pool contrast agent.[148] Naha *et al.,* reported the development of dextran coated bismuth-iron nanoparticles for *in vivo* blood contrast imaging with both CT and MRI.[149]

Tantalum is another element that has been recently explored as a candidate for CT contrast agents due to the low toxicity of its oxide and strong x-ray absorption.[150-151] A group from General Electric have published on several tantalum oxide formulations where the overall nanoparticle size is below 5 nm, thus allowing for swift renal excretion. Due to the relative natural abundance of tantalum compared to gold, tantalum is an order of magnitude cheaper, which may facilitate widespread use. In another study, tantalum oxide nanocrystals were prepared using reverse emulsions and then surface functionalized with PEG and a fluorophore tag.[152] This synthesis can be done on a bulk scale and allows the core size to be controlled in the 6-15 nm diameter range. As a blood pool agent, strong contrast enhancement of the heart and major blood vessels

could be seen for up to 3 hours post-injection, with eventual accumulation in the spleen and liver.

Gadolinium chelates serve as MRI contrast agents for several biomedical applications including cancer and vascular imaging.[153-154] Despite the toxicity concerns over non-chelated gadolinium and tissue retention, several studies have evaluated gadolinium as a potential CT contrast agent.[155-156] Due to its unique properties for MRI, researchers have developed gadolinium nanoparticles for dual mode imaging with CT and MRI. The addition of gadolinium chelates to gold nanoparticles has been shown to provide significant contrast for both modalities.[157-159]

A number of other high atomic number elements have shown promise as effective CT contrast agents. Gold and silver core-shell nanoparticles have been shown to produce stronger CT contrast than iodinated agents.[160-162] A report by Chou *et al.,* demonstrated the use of iron/platinum nanoparticles for dual CT and MRI molecular imaging after intravenous injection.[163] Several studies have reported the use of tungsten nanoparticles as CT contrast agents that provide better enhancement compared to traditional iodinated agents.[164-166] Moreover, ytterbium based nanoparticles have received attention as potential CT agents due to favorable x-ray absorption spectra and relative natural abundance compared to other potential elements mentioned.[167-168] Ytterbium based nanoparticles also present multi-modal opportunities through upconversion fluorescence imaging. Upconverting fluorescent probes allow for excitation at NIR-wavelengths for deep tissue penetration with reduced background tissue absorption. Liu *et al.*, synthesized ytterbium based particles coated in PEG for use as a CT contrast agent.[169] Xing *et al.*, synthesized tri-modal nanoparticles for upconversion fluorescence, MR and CT imaging.[170] The group synthesized gadolinium-based

upconverting nanoparticles (doped with yttrium, ytterbium, erbium, and thulium) that were also surface coated with gold nanoparticles. *In vivo* imaging of these trimodal particles was demonstrated with subcutaneous injection of the particles at tumor bearing locations in mice.

1.2.3c Cell tracking agents

The use of nanoparticles as contrast agents provides unique advantages that can be exploited for specific biomedical applications. One such application is *in vivo* cell tracking, where a population of specific cells can be monitored in real time via imaging. Cell tracking offers the possibility of non-invasively observing cell behaviors such as migration, localization, and viability over a period of time.[171] This technology has emerged as a particular area of interest since the development of adoptive cell therapy and stem cell transplantations.[172] Both therapies involve the transplantation of endogenous cells that have been modified *ex vivo*. The fate of these transplanted cells is of high interest as it may provide information on the effectiveness of the therapies and the conditions that predict a successful treatment. Cell tracking has been explored with several imaging modalities including MRI, ultrasound, PET and optical imaging.[173-174] Contrast agents have developed for in a variety of cell tracking applications including neural stem cells,[175] mesenchymal stem cells,[176] hematopoietic progenitor cells,[177] and cardiac applications.[178-179]

In cell tracking, coronary artery disease is of high interest due to the cells involved in the disease progression and regenerative opportunities after myocardial infarction. With injection of stem cells after myocardial infarction, there have been clinical

reports of improved left ventricle remodeling and function.[180] However, concerns about cell fate, localization and safety need to resolved before further adoption of the therapy. Clinical imaging modalities are currently being explored as a method to address these issues.[181] The use of MRI and MRI contrast agents have been the main focus due to high spatial resolution and reasonable contrast agent sensitivity. MRI contrast agents for cell tracking typically contain superparamagnetic (SPION) or ultra small paramagnetic (USPION) iron oxide particles.[182] These agents primarily work by shortening T2 relaxation (iron oxide) to produce hypo-contrast in the images (i.e. image darkening). There has a been a number of pre-clinical studies demonstrating success stem cell tracking in infarct models.[183-185] A study Bulte *et al.*, labeled autologous mesenchymal stem cells with Feridex (SPION) and directly injected the cells intra-myocardial into the infarct border zone in a canine model.[186] The cells could be detected for up to 8 weeks post-injection with MRI and histology showed that the transplanted cells were indeed in the infarct region. While tracking stem cells with MRI can provide information about migration and localization, cell functionality can be difficult to assess. In a study by Chapon *et al.*, the study utilized both MRI and FDG-PET to evaluate the localization and metabolic activity of the transplanted cells.[187] FDG is a glucose analog with a fluorine-18 radionuclide substituted for a hydroxyl group. Its uptake in cells is closely correlated to metabolic activity and viability. In a rat infarct model, bone marrow derived stem cells were labeled with SPION and injected directly into infarct zone. The stem cells could be detected for up to 6 weeks with MRI. With PET, an increase in FDG uptake was noticeable in the first week in infarct animals with the labeled stem cells as compared to infarct animals that did not receive stem cells. However, the increase in FDG did not persist the duration of the 6 weeks, potentially indicating death of the injected stem cells

providing valuable information about cell viability that could not be determined through MRI alone.

While PET can be used to assess function of the injected cells, a number of studies have sought to use radiolabeled tracers to track transplanted stem cells with PET/SPECT. Because of short half-lives of radionuclides, ^{111}In is the most commonly explored agent (half-live 2.8 days) with most studies lasting one week.[188-189] With SPECT, Mitchel *et al.* were able to observe 57% retention of ^{111}In-tropolone labeled endothelial progenitor cells in the infarct border zone in a canine infarct model. The study observed that the cells could be detected after 15 days. Clinically, some studies have used PET to determine the engraftment of stem cells after delivery in short term cases of acute myocardial infarction.[190-191] A study by Penicka *et al.* compared the engraftment of ^{99m}Tc labeled bone marrow derived mononuclear cells in acute (AMI) versus chronic myocardial infarction (CMI) patients. At 2 hours, myocardial activity from the transplanted cells could be seen in all five patients with AMI and 4 out of 5 CMI patients. However, after 20 hours, only 3 of the AMI patients had detection of the labeled cells. These results demonstrate that engraftment of cells for myocardial infarction may be limited to only acute cases. For cell tracking, PET/SPECT offers high sensitivity for cell detection but is limited by poor spatial resolution and short half-lives of agents.

There has been in interest in developing cell tracking agents for ultrasound (US) due to its low cost, non-invasiveness and real time imaging capabilities. Typical US agents are based on inert gases trapped inside a microparticle for detection. For cell labeling, long term stability of the agent within the cell remains a problem in addition to poor spatial resolution. Most studies for cell tracking with US have been limited to *in vitro* studies with polymer microbubbles as cell labels.[192] A study by Toma *et al.* used lipid

microbubbles to label mesenchymal stem cells and deliver these cells via an intra-aortic injection to plaque rupture models in rabbits.[193] After 24 hours, labeled cells could be detected on the lumen surface at the delivery site but did not show migration towards injury location.

Progress with CT cell tracking has been limited due to the low CT sensitivity towards contrast agents requiring relatively large payloads of agent for detection. Despite this limitation, researchers have developed cell tracking with CT, demonstrating feasibility in a number of applications.[96, 194] Barnett *et al.* have demonstrated the use of perfluoroctylbromide (PFOB) nanoparticles (conjugated to rhodamine) to label and track exogenous cells non-invasively over time. The PFOB acted as a multimodal label allowing for CT and US imaging. Pancreatic islets were co-encapsulated with PFOB in alginate-based capsules, which allowed their visualization in vivo.[195]

Several cell tracking applications with CT have found success in using AuNP to label cells. For instance, Betzer *et al.* utilized 20 nm AuNP surface functionalized with glucose to label mesenchymal stem cells.[196] These gold labeled cells were injected directly into the left ventricle in the brain and monitored over 21 days. The authors were able to observe the migration of gold labeled cells over the 21 days to a specific region of injury. The authors were able to non-invasively quantify the number of AuNP labeled cells in particular regions, since x-ray attenuation is linearly proportional to the concentration of contrast agent, allowing for quantification of cell number from CT scans. This group has performed similar studies such as tracking the migration of AuNP labeled T-cells to xenograft tumors.[197]

With AuNP and the use of synchrotron x-ray radiation sources, super high resolution of in vivo cells have been demonstrated.[198] Astolfo *et al.* demonstrated the

feasibility of detecting engrafted rat F98 glioma cells in a mice model. The cells were labeled with 50 nm citrate coated spherical AuNP and 200,000 cells were injected into the striatum. The cells could be detected for the duration of the experiment, 7.5 days, using CT synchrotron radiation.[198] While synchrotron radiation imaging remains experimental, researchers have been able to reach single cell resolution with AuNP labeled cells, opening new possibilities of future CT applications.[199]

1.3 Conclusion

For medical imaging, contrast agents are able to provide additional anatomical and functional information that can help assess the health of the patient. The development of contrast agents continues to improve, further expanding their applications and capabilities. As discussed previously for CT, contrast agents have evolved from simple iodinated molecules to complex nanotechnologies with purposeful design. However, expanding the breadth of these nanotechnologies into specialized biomedical applications requires individual investigation to assess the effectiveness of the nanoparticles in that application.

Interest in cell tracking continues to grow with the advancement in cell-based therapies. While exploration of cell tracking contrast agents have been mostly limited to MRI (clinical) and optical (pre-clinical), CT's spatial and temporal resolution make it a promising cell tracking modality for cardiovascular applications. Specifically, the development of atherosclerosis in the coronary arteries, subsequent rupture, and myocardial infarction present several stages where cell tracking technology is of high need. Monocytes are a cell type that plays a role in each stage, infiltrating developing plaques, promoting eventual plaque rupture, and participating in wound healing after an

infarct. The labeling and tracking of these monocytes can lead to more in-depth investigation of each stage, elucidating mechanisms in the disease. In the following chapters we present the development and assessment of nanotechnologies designed for labeling of monocytes for detection with CT. We investigate the parameters of the nano-complexes that optimize the labeling and biocompatibility with monocytes. Lastly, we explore the use of the nanotechnologies in tracking monocytes during the progression of atherosclerosis in mice models.

1.4 References

1. Writing Group, M.; Mozaffarian, D.; Benjamin, E. J.; Go, A. S.; Arnett, D. K.; Blaha, M. J.; Cushman, M.; Das, S. R.; de Ferranti, S.; Despres, J. P., et al., Heart Disease and Stroke Statistics-2016 Update: A Report From the American Heart Association. *Circulation* **2016,** *133* (4), e38-360.

2. Mozaffarian, D.; Benjamin, E. J.; Go, A. S.; Arnett, D. K.; Blaha, M. J.; Cushman, M.; de Ferranti, S.; Despres, J.; Fullerton, H. J.; Howard, V. J., et al., Heart Disease and Stroke Statistics-2015 Update: A Report From the American Heart Association. *Circulation* **2014**.

3. Go, A. S.; Mozaffarian, D.; Roger, V. L.; Benjamin, E. J.; Berry, J. D.; Blaha, M. J.; Dai, S.; Ford, E. S.; Fox, C. S.; Franco, S., et al., Heart disease and stroke statistics--2014 update: a report from the American Heart Association. *Circulation* **2014,** *129* (3), e28-e292.

4. Chatzizisis, Y. S.; Coskun, A. U.; Jonas, M.; Edelman, E. R.; Feldman, C. L.; Stone, P. H., Role of endothelial shear stress in the natural history of coronary atherosclerosis and vascular remodeling: molecular, cellular, and vascular behavior. *J Am Coll Cardiol* **2007,** *49* (25), 2379-2393.

5. Stone, P. H.; Coskun, A. U.; Yeghiazarians, Y.; Kinlay, S.; Popma, J. J.; Kuntz, R. E.; Feldman, C. L., Prediction of sites of coronary atherosclerosis progression: In vivo profiling of endothelial shear stress, lumen, and outer vessel wall characteristics to predict vascular behavior. *Curr Opin Cardiol* **2003,** *18* (6), 458-470.

6. Skalen, K.; Gustafsson, M.; Rydberg, E. K.; Hulten, L. M.; Wiklund, O.; Innerarity, T. L.; Boren, J., Subendothelial retention of atherogenic lipoproteins in early atherosclerosis. *Nature* **2002,** *417* (6890), 750-754.

7. Srinivasan, S. R.; Vijayagopal, P.; Dalferes, E. R., Jr.; Abbate, B.; Radhakrishnamurthy, B.; Berenson, G. S., Low density lipoprotein retention by aortic tissue. Contribution of extracellular matrix. *Atherosclerosis* **1986,** *62* (3), 201-208.

8. Cybulsky, M. I.; Iiyama, K.; Li, H.; Zhu, S.; Chen, M.; Iiyama, M.; Davis, V.; Gutierrez-Ramos, J. C.; Connelly, P. W.; Milstone, D. S., A major role for VCAM-1, but not ICAM-1, in early atherosclerosis. *J Clin Invest* **2001,** *107* (10), 1255-1262.

9. Huo, Y.; Hafezi-Moghadam, A.; Ley, K., Role of vascular cell adhesion molecule-1 and fibronectin connecting segment-1 in monocyte rolling and adhesion on early atherosclerotic lesions. *Circ Res* **2000,** *87* (2), 153-159.

10. Ramos, C. L.; Huo, Y.; Jung, U.; Ghosh, S.; Manka, D. R.; Sarembock, I. J.; Ley, K., Direct demonstration of P-selectin- and VCAM-1-dependent mononuclear cell rolling in early atherosclerotic lesions of apolipoprotein E-deficient mice. *Circ Res* **1999,** *84* (11), 1237-1244.

11. Boisvert, W. A.; Rose, D. M.; Johnson, K. A.; Fuentes, M. E.; Lira, S. A.; Curtiss, L. K.; Terkeltaub, R. A., Up-regulated expression of the CXCR2 ligand KC/GRO-alpha in atherosclerotic lesions plays a central role in macrophage accumulation and lesion progression. *Am J Pathol* **2006,** *168* (4), 1385-1395.

12. Boring, L.; Gosling, J.; Cleary, M.; Charo, I. F., Decreased lesion formation in CCR2-/- mice reveals a role for chemokines in the initiation of atherosclerosis. *Nature* **1998,** *394* (6696), 894-897.

13. Combadiere, C.; Potteaux, S.; Rodero, M.; Simon, T.; Pezard, A.; Esposito, B.; Merval, R.; Proudfoot, A.; Tedgui, A.; Mallat, Z., Combined inhibition of CCL2, CX3CR1, and CCR5 abrogates Ly6C(hi) and Ly6C(lo) monocytosis and almost abolishes atherosclerosis in hypercholesterolemic mice. *Circulation* **2008,** *117* (13), 1649-1657.

14. Shashkin, P.; Dragulev, B.; Ley, K., Macrophage differentiation to foam cells. *Curr Pharm Des* **2005,** *11* (23), 3061-3072.

15. Libby, P., Inflammation in atherosclerosis. *Nature* **2002,** *420* (6917), 868-874.

16. Moreno, P. R.; Falk, E.; Palacios, I. F.; Newell, J. B.; Fuster, V.; Fallon, J. T., Macrophage infiltration in acute coronary syndromes. Implications for plaque rupture. *Circulation* **1994,** *90* (2), 775-778.

17. Galis, Z. S.; Sukhova, G. K.; Lark, M. W.; Libby, P., Increased expression of matrix metalloproteinases and matrix degrading activity in vulnerable regions of human atherosclerotic plaques. *J Clin Invest* **1994,** *94* (6), 2493-2503.

18. Weber, C.; Belge, K. U.; von Hundelshausen, P.; Draude, G.; Steppich, B.; Mack, M.; Frankenberger, M.; Weber, K. S.; Ziegler-Heitbrock, H. W., Differential chemokine receptor expression and function in human monocyte subpopulations. *J Leukoc Biol* **2000,** *67* (5), 699-704.

19. Passlick, B.; Flieger, D.; Ziegler-Heitbrock, H. W., Identification and characterization of a novel monocyte subpopulation in human peripheral blood. *Blood* **1989,** *74* (7), 2527-2534.

20. Geissmann, F.; Jung, S.; Littman, D. R., Blood monocytes consist of two principal subsets with distinct migratory properties. *Immunity* **2003,** *19* (1), 71-82.

21. Kurihara, T.; Warr, G.; Loy, J.; Bravo, R., Defects in macrophage recruitment and host defense in mice lacking the CCR2 chemokine receptor. *J Exp Med* **1997,** *186* (10), 1757-1762.

22. Kuziel, W. A.; Morgan, S. J.; Dawson, T. C.; Griffin, S.; Smithies, O.; Ley, K.; Maeda, N., Severe reduction in leukocyte adhesion and monocyte extravasation in mice

deficient in CC chemokine receptor 2. *Proc Natl Acad Sci U S A* **1997,** *94* (22), 12053-12058.

23. Ghattas, A.; Griffiths, H. R.; Devitt, A.; Lip, G. Y.; Shantsila, E., Monocytes in coronary artery disease and atherosclerosis: where are we now? *J Am Coll Cardiol* **2013,** *62* (17), 1541-1551.

24. Combadiere, C.; Potteaux, S.; Gao, J. L.; Esposito, B.; Casanova, S.; Lee, E. J.; Debre, P.; Tedgui, A.; Murphy, P. M.; Mallat, Z., Decreased atherosclerotic lesion formation in CX3CR1/apolipoprotein E double knockout mice. *Circulation* **2003,** *107* (7), 1009-1016.

25. Tacke, F.; Alvarez, D.; Kaplan, T. J.; Jakubzick, C.; Spanbroek, R.; Llodra, J.; Garin, A.; Liu, J.; Mack, M.; van Rooijen, N., et al., Monocyte subsets differentially employ CCR2, CCR5, and CX3CR1 to accumulate within atherosclerotic plaques. *J Clin Invest* **2007,** *117* (1), 185-194.

26. Libby, P.; Ridker, P. M.; Maseri, A., Inflammation and atherosclerosis. *Circulation* **2002,** *105* (9), 1135-1143.

27. Lusis, A. J., Atherosclerosis. *Nature* **2000,** *407* (6801), 233-241.

28. Zhu, S. N.; Chen, M.; Jongstra-Bilen, J.; Cybulsky, M. I., GM-CSF regulates intimal cell proliferation in nascent atherosclerotic lesions. *J Exp Med* **2009,** *206* (10), 2141-2149.

29. Robbins, C. S.; Hilgendorf, I.; Weber, G. F.; Theurl, I.; Iwamoto, Y.; Figueiredo, J. L.; Gorbatov, R.; Sukhova, G. K.; Gerhardt, L. M.; Smyth, D., et al., Local proliferation dominates lesional macrophage accumulation in atherosclerosis. *Nat Med* **2013,** *19* (9), 1166-1172.

30. Gerrity, R. G., The role of the monocyte in atherogenesis: I. Transition of blood-borne monocytes into foam cells in fatty lesions. *Am J Pathol* **1981,** *103* (2), 181-190.

31. Newby, A. C.; George, S. J.; Ismail, Y.; Johnson, J. L.; Sala-Newby, G. B.; Thomas, A. C., Vulnerable atherosclerotic plaque metalloproteinases and foam cell phenotypes. *Thromb Haemost* **2009,** *101* (6), 1006-1011.

32. Frangogiannis, N. G.; Mendoza, L. H.; Ren, G.; Akrivakis, S.; Jackson, P. L.; Michael, L. H.; Smith, C. W.; Entman, M. L., MCSF expression is induced in healing myocardial infarcts and may regulate monocyte and endothelial cell phenotype. *Am J Physiol Heart Circ Physiol* **2003,** *285* (2), H483-492.

33. Nahrendorf, M.; Swirski, F. K.; Aikawa, E.; Stangenberg, L.; Wurdinger, T.; Figueiredo, J. L.; Libby, P.; Weissleder, R.; Pittet, M. J., The healing myocardium sequentially mobilizes two monocyte subsets with divergent and complementary functions. *J Exp Med* **2007,** *204* (12), 3037-3047.

34. Bouchentouf, M.; Paradis, P.; Forner, K. A.; Cuerquis, J.; Boivin, M. N.; Zheng, J.; Boulassel, M. R.; Routy, J. P.; Schiffrin, E. L.; Galipeau, J., Monocyte derivatives promote angiogenesis and myocyte survival in a model of myocardial infarction. *Cell Transplant* **2010,** *19* (4), 369-386.

35. Panizzi, P.; Swirski, F. K.; Figueiredo, J. L.; Waterman, P.; Sosnovik, D. E.; Aikawa, E.; Libby, P.; Pittet, M.; Weissleder, R.; Nahrendorf, M., Impaired infarct healing in atherosclerotic mice with Ly-6C(hi) monocytosis. *J Am Coll Cardiol* **2010,** *55* (15), 1629-1638.

36. van Amerongen, M. J.; Harmsen, M. C.; van Rooijen, N.; Petersen, A. H.; van Luyn, M. J., Macrophage depletion impairs wound healing and increases left ventricular remodeling after myocardial injury in mice. *Am J Pathol* **2007,** *170* (3), 818-829.

37. Pryor, D. B.; Shaw, L.; Harrell, F. E., Jr.; Lee, K. L.; Hlatky, M. A.; Mark, D. B.; Muhlbaier, L. H.; Califf, R. M., Estimating the likelihood of severe coronary artery disease. *Am J Med* **1991,** *90* (5), 553-562.

38. Cassar, A.; Holmes, D. R., Jr.; Rihal, C. S.; Gersh, B. J., Chronic coronary artery disease: diagnosis and management. *Mayo Clin Proc* **2009,** *84* (12), 1130-1146.

39. Rihal, C. S.; Davis, K. B.; Kennedy, J. W.; Gersh, B. J., The utility of clinical, electrocardiographic, and roentgenographic variables in the prediction of left ventricular function. *Am J Cardiol* **1995,** *75* (4), 220-223.

40. Yonezawa, M.; Nagata, M.; Kitagawa, K.; Kato, S.; Yoon, Y.; Nakajima, H.; Nakamori, S.; Sakuma, H.; Hatakenaka, M.; Honda, H., Quantitative analysis of 1.5-T whole-heart coronary MR angiograms obtained with 32-channel cardiac coils: a comparison with conventional quantitative coronary angiography. *Radiology* **2014,** *271* (2), 356-364.

41. Health Quality, O., Positron emission tomography for the assessment of myocardial viability: an evidence-based analysis. *Ont Health Technol Assess Ser* **2010,** *10* (16), 1-80.

42. Sarikaya, I., Cardiac applications of PET. *Nucl Med Commun* **2015,** *36* (10), 971-985.

43. Mehta, N. N.; Torigian, D. A.; Gelfand, J. M.; Saboury, B.; Alavi, A., Quantification of atherosclerotic plaque activity and vascular inflammation using [18-F] fluorodeoxyglucose positron emission tomography/computed tomography (FDG-PET/CT). *J Vis Exp* **2012,** (63), e3777.

44. Huet, P.; Burg, S.; Le Guludec, D.; Hyafil, F.; Buvat, I., Variability and uncertainty of 18F-FDG PET imaging protocols for assessing inflammation in atherosclerosis: suggestions for improvement. *J Nucl Med* **2015,** *56* (4), 552-559.

45. Derlin, T.; Richter, U.; Bannas, P.; Begemann, P.; Buchert, R.; Mester, J.; Klutmann, S., Feasibility of 18F-sodium fluoride PET/CT for imaging of atherosclerotic plaque. *J Nucl Med* **2010,** *51* (6), 862-865.

46. Lee, N.; Choi, S. H.; Hyeon, T., Nano-sized CT contrast agents. *Adv Mater* **2013,** *25* (19), 2641-2660.

47. Gorenoi, V.; Schonermark, M. P.; Hagen, A., CT coronary angiography vs. invasive coronary angiography in CHD. *GMS Health Technol Assess* **2012,** *8*, Doc02.

48. Litt, H. I.; Gatsonis, C.; Snyder, B.; Singh, H.; Miller, C. D.; Entrikin, D. W.; Leaming, J. M.; Gavin, L. J.; Pacella, C. B.; Hollander, J. E., CT angiography for safe discharge of patients with possible acute coronary syndromes. *N Engl J Med* **2012,** *366* (15), 1393-1403.

49. Bardo, D. M.; Brown, P., Cardiac multidetector computed tomography: basic physics of image acquisition and clinical applications. *Curr Cardiol Rev* **2008,** *4* (3), 231-243.

50. Otero, H. J.; Steigner, M. L.; Rybicki, F. J., The "post-64" era of coronary CT angiography: understanding new technology from physical principles. *Radiol Clin North Am* **2009,** *47* (1), 79-90.

51. Flohr, T. G.; McCollough, C. H.; Bruder, H.; Petersilka, M.; Gruber, K.; Suss, C.; Grasruck, M.; Stierstorfer, K.; Krauss, B.; Raupach, R., et al., First performance evaluation of a dual-source CT (DSCT) system. *Eur Radiol* **2006,** *16* (2), 256-268.

52. Dewey, M.; Teige, F.; Laule, M.; Hamm, B., Influence of heart rate on diagnostic accuracy and image quality of 16-slice CT coronary angiography: comparison of multisegment and halfscan reconstruction approaches. *Eur Radiol* **2007,** *17* (11), 2829-2837.

53. Hoffmann, U.; Pena, A. J.; Cury, R. C.; Abbara, S.; Ferencik, M.; Moselewski, F.; Siebert, U.; Brady, T. J.; Nagurney, J. T., Cardiac CT in emergency department patients with acute chest pain. *Radiographics* **2006,** *26* (4), 963-978; discussion 979-980.

54. Lee, N. J.; Litt, H., Cardiac CT angiography for evaluation of acute chest pain. *Int J Cardiovasc Imaging* **2015**.

55. Goldberg, A.; Litt, H. I., Evaluation of the patient with acute chest pain. *Radiol Clin North Am* **2010,** *48* (4), 745-755.

56. Achenbach, S.; Daniel, W. G., Cardiac imaging in the patient with chest pain: coronary CT angiography. *Heart* **2010,** *96* (15), 1241-1246.

57. Nasis, A.; Mottram, P. M.; Cameron, J. D.; Seneviratne, S. K., Current and evolving clinical applications of multidetector cardiac CT in assessment of structural heart disease. *Radiology* **2013,** *267* (1), 11-25.

58. Puchner, S. B.; Liu, T.; Mayrhofer, T.; Truong, Q. A.; Lee, H.; Fleg, J. L.; Nagurney, J. T.; Udelson, J. E.; Hoffmann, U.; Ferencik, M., High-risk plaque detected on coronary CT angiography predicts acute coronary syndromes independent of significant stenosis in acute chest pain: results from the ROMICAT-II trial. *J Am Coll Cardiol* **2014,** *64* (7), 684-692.

59. Pijls, N. H.; De Bruyne, B.; Peels, K.; Van Der Voort, P. H.; Bonnier, H. J.; Bartunek, J. K. J. J.; Koolen, J. J., Measurement of fractional flow reserve to assess the

functional severity of coronary-artery stenoses. *N Engl J Med* **1996,** *334* (26), 1703-1708.

60. Taylor, C. A.; Fonte, T. A.; Min, J. K., Computational Fluid Dynamics Applied to Cardiac Computed Tomography for Noninvasive Quantification of Fractional Flow Reserve Scientific Basis. *J Am Coll Cardiol* **2013,** *61* (22), 2233-2241.

61. Bittencourt, M. S.; Achenbach, S.; Marwan, M.; Seltmann, M.; Muschiol, G.; Ropers, D.; Daniel, W. G.; Pflederer, T., Left ventricular thrombus attenuation characterization in cardiac computed tomography angiography. *J Cardiovasc Comput Tomogr* **2012,** *6* (2), 121-126.

62. Grude, M.; Juergens, K. U.; Wichter, T.; Paul, M.; Fallenberg, E. M.; Muller, J. G.; Heindel, W.; Breithardt, G.; Fischbach, R., Evaluation of global left ventricular myocardial function with electrocardiogram-gated multidetector computed tomography: comparison with magnetic resonance imaging. *Invest Radiol* **2003,** *38* (10), 653-661.

63. Singh, S.; Khawaja, R. D.; Pourjabbar, S.; Padole, A.; Lira, D.; Kalra, M. K., Iterative image reconstruction and its role in cardiothoracic computed tomography. *J Thorac Imaging* **2013,** *28* (6), 355-367.

64. Renker, M.; Geyer, L. L.; Krazinski, A. W.; Silverman, J. R.; Ebersberger, U.; Schoepf, U. J., Iterative image reconstruction: a realistic dose-saving method in cardiac CT imaging? *Expert Rev Cardiovasc Ther* **2013,** *11* (4), 403-409.

65. Halpern, E. J.; Gingold, E. L.; White, H.; Read, K., Evaluation of coronary artery image quality with knowledge-based iterative model reconstruction. *Acad Radiol* **2014,** *21* (6), 805-811.

66. Cho, Y. J.; Schoepf, U. J.; Silverman, J. R.; Krazinski, A. W.; Canstein, C.; Deak, Z.; Grimm, J.; Geyer, L. L., Iterative image reconstruction techniques: cardiothoracic computed tomography applications. *J Thorac Imaging* **2014,** *29* (4), 198-208.

67. Renker, M.; Nance, J. W., Jr.; Schoepf, U. J.; O'Brien, T. X.; Zwerner, P. L.; Meyer, M.; Kerl, J. M.; Bauer, R. W.; Fink, C.; Vogl, T. J., et al., Evaluation of heavily calcified vessels with coronary CT angiography: comparison of iterative and filtered back projection image reconstruction. *Radiology* **2011,** *260* (2), 390-399.

68. Wang, R.; Schoepf, U. J.; Wu, R.; Nance, J. W., Jr.; Lv, B.; Yang, H.; Li, F.; Lu, D.; Zhang, Z., Diagnostic accuracy of coronary CT angiography: comparison of filtered back projection and iterative reconstruction with different strengths. *J Comput Assist Tomogr* **2014,** *38* (2), 179-184.

69. Bernstein, A. L.; Dhanantwari, A.; Jurcova, M.; Cheheltani, R.; Naha, P. C.; Ivanc, T.; Shefer, E.; Cormode, D. P., Improved sensitivity of computed tomography towards iodine and gold nanoparticle contrast agents via iterative reconstruction methods. *Sci Rep* **2016,** *6*, 26177.

70. Shikhaliev, P. M., Photon counting spectral CT: improved material decomposition with K-edge-filtered x-rays. *Phys Med Biol* **2012,** *57* (6), 1595-1615.

71. Roessl, E.; Brendel, B.; Engel, K. J.; Schlomka, J. P.; Thran, A.; Proksa, R., Sensitivity of photon-counting based K-edge imaging in X-ray computed tomography. *IEEE Trans Med Imaging* **2011,** *30* (9), 1678-1690.

72. Feuerlein, S.; Roessl, E.; Proksa, R.; Martens, G.; Klass, O.; Jeltsch, M.; Rasche, V.; Brambs, H. J.; Hoffmann, M. H.; Schlomka, J. P., Multienergy photon-counting K-edge imaging: potential for improved luminal depiction in vascular imaging. *Radiology* **2008,** *249* (3), 1010-1016.

73. Schirra, C. O.; Brendel, B.; Anastasio, M. A.; Roessl, E., Spectral CT: a technology primer for contrast agent development. *Contrast Media Mol Imaging* **2014,** *9* (1), 62-70.

74. Cormode, D. P.; Roessl, E.; Thran, A.; Skajaa, T.; Gordon, R. E.; Schlomka, J. P.; Fuster, V.; Fisher, E. A.; Mulder, W. J.; Proksa, R., et al., Atherosclerotic plaque composition: analysis with multicolor CT and targeted gold nanoparticles. *Radiology* **2010,** *256* (3), 774-782.

75. Schlomka, J. P.; Roessl, E.; Dorscheid, R.; Dill, S.; Martens, G.; Istel, T.; Baumer, C.; Herrmann, C.; Steadman, R.; Zeitler, G., et al., Experimental feasibility of multi-energy photon-counting K-edge imaging in pre-clinical computed tomography. *Phys Med Biol* **2008,** *53* (15), 4031-4047.

76. Galper, M. W.; Saung, M. T.; Fuster, V.; Roessl, E.; Thran, A.; Proksa, R.; Fayad, Z. A.; Cormode, D. P., Effect of computed tomography scanning parameters on gold nanoparticle and iodine contrast. *Invest Radiol* **2012,** *47* (8), 475-481.

77. Bae, K. T., Intravenous contrast medium administration and scan timing at CT: considerations and approaches. *Radiology* **2010,** *256* (1), 32-61.

78. Weininger, M.; Barraza, J. M.; Kemper, C. A.; Kalafut, J. F.; Costello, P.; Schoepf, U. J., Cardiothoracic CT angiography: current contrast medium delivery strategies. *AJR Am J Roentgenol* **2011,** *196* (3), W260-272.

79. Fleischmann, D.; Kamaya, A., Optimal vascular and parenchymal contrast enhancement: the current state of the art. *Radiol Clin North Am* **2009,** *47* (1), 13-26.

80. Bourin, M.; Jolliet, P.; Ballereau, F., An overview of the clinical pharmacokinetics of x-ray contrast media. *Clin Pharmacokinet* **1997,** *32* (3), 180-193.

81. Watchorn, J.; Miles, R.; Moore, N., The role of CT angiography in military trauma. *Clin Radiol* **2013,** *68* (1), 39-46.

82. Goldenberg, I.; Matetzky, S., Nephropathy induced by contrast media: pathogenesis, risk factors and preventive strategies. *CMAJ* **2005,** *172* (11), 1461-1471.

83. Thomsen, H. S.; Morcos, S. K., Contrast media and the kidney: European Society of Urogenital Radiology (ESUR) guidelines. *Br J Radiol* **2003,** *76* (908), 513-518.

84. Jun, Y. W.; Choi, J. S.; Cheon, J., Shape control of semiconductor and metal oxide nanocrystals through nonhydrolytic colloidal routes. *Angew Chem Int Ed Engl* **2006,** *45* (21), 3414-3439.

85. Boyle, J. P.; Thompson, T. J.; Gregg, E. W.; Barker, L. E.; Williamson, D. F., Projection of the year 2050 burden of diabetes in the US adult population: dynamic modeling of incidence, mortality, and prediabetes prevalence. *Popul Health Metr* **2010,** *8*, 29.

86. Ritz, E.; Orth, S. R., Nephropathy in patients with type 2 diabetes mellitus. *N Engl J Med* **1999,** *341* (15), 1127-1133.

87. Pasternak, J. J.; Williamson, E. E., Clinical pharmacology, uses, and adverse reactions of iodinated contrast agents: a primer for the non-radiologist. *Mayo Clin Proc* **2012,** *87* (4), 390-402.

88. Hou, Z. H.; Lu, B.; Gao, Y.; Jiang, S. L.; Wang, Y.; Li, W.; Budoff, M. J., Prognostic value of coronary CT angiography and calcium score for major adverse cardiac events in outpatients. *JACC Cardiovasc Imaging* **2012,** *5* (10), 990-999.

89. Mulder, W. J.; Strijkers, G. J.; van Tilborg, G. A.; Griffioen, A. W.; Nicolay, K., Lipid-based nanoparticles for contrast-enhanced MRI and molecular imaging. *NMR Biomed* **2006,** *19* (1), 142-164.

90. Bhattacharya, S.; Novell, J. R.; Winslet, M. C.; Hobbs, K. E., Iodized oil in the treatment of hepatocellular carcinoma. *Br J Surg* **1994,** *81* (11), 1563-1571.

91. Lim, J. S.; Choi, J.; Song, J.; Chung, Y. E.; Lim, S. J.; Lee, S. K.; Hyung, W. J., Nanoscale iodized oil emulsion: a useful tracer for pretreatment sentinel node detection using CT lymphography in a normal canine gastric model. *Surg Endosc* **2012,** *26* (8), 2267-2274.

92. Ahrar, K.; Gupta, S., Hepatic artery embolization for hepatocellular carcinoma: technique, patient selection, and outcomes. *Surg Oncol Clin N Am* **2003,** *12* (1), 105-126.

93. Kong, W. H.; Lee, W. J.; Cui, Z. Y.; Bae, K. H.; Park, T. G.; Kim, J. H.; Park, K.; Seo, S. W., Nanoparticulate carrier containing water-insoluble iodinated oil as a multifunctional contrast agent for computed tomography imaging. *Biomaterials* **2007,** *28* (36), 5555-5561.

94. Weichert, J. P.; Longino, M. A.; Bakan, D. A.; Spigarelli, M. G.; Chou, T. S.; Schwendner, S. W.; Counsell, R. E., Polyiodinated triglyceride analogs as potential computed tomography imaging agents for the liver. *J Med Chem* **1995,** *38* (4), 636-646.

95. Henning, T.; Weber, A. W.; Bauer, J. S.; Meier, R.; Carlsen, J. M.; Sutton, E. J.; Prevrhal, S.; Ziegler, S. I.; Feussner, H.; Daldrup-Link, H. E., et al., Imaging characteristics of DHOG, a hepatobiliary contrast agent for preclinical microCT in mice. *Acad Radiol* **2008,** *15* (3), 342-349.

96. Weber, S. M.; Peterson, K. A.; Durkee, B.; Qi, C.; Longino, M.; Warner, T.; Lee, F. T., Jr.; Weichert, J. P., Imaging of murine liver tumor using microCT with a hepatocyte-selective contrast agent: accuracy is dependent on adequate contrast enhancement. *J Surg Res* **2004,** *119* (1), 41-45.

97. Willekens, I.; Lahoutte, T.; Buls, N.; Vanhove, C.; Deklerck, R.; Bossuyt, A.; de Mey, J., Time-course of contrast enhancement in spleen and liver with Exia 160, Fenestra LC, and VC. *Mol Imaging Biol* **2009,** *11* (2), 128-135.

98. Attia, M. F.; Anton, N.; Chiper, M.; Akasov, R.; Anton, H.; Messaddeq, N.; Fournel, S.; Klymchenko, A. S.; Mely, Y.; Vandamme, T. F., Biodistribution of X-ray iodinated contrast agent in nano-emulsions is controlled by the chemical nature of the oily core. *ACS Nano* **2014,** *8* (10), 10537-10550.

99. Badea, C. T.; Fubara, B.; Hedlund, L. W.; Johnson, G. A., 4-D micro-CT of the mouse heart. *Mol Imaging* **2005,** *4* (2), 110-116.

100. Detombe, S. A.; Ford, N. L.; Xiang, F.; Lu, X.; Feng, Q.; Drangova, M., Longitudinal follow-up of cardiac structure and functional changes in an infarct mouse model using retrospectively gated micro-computed tomography. *Invest Radiol* **2008,** *43* (7), 520-529.

101. de Vries, A.; Custers, E.; Lub, J.; van den Bosch, S.; Nicolay, K.; Grull, H., Block-copolymer-stabilized iodinated emulsions for use as CT contrast agents. *Biomaterials* **2010,** *31* (25), 6537-6544.

102. Hallouard, F.; Briancon, S.; Anton, N.; Li, X.; Vandamme, T.; Fessi, H., Iodinated nano-emulsions as contrast agents for preclinical X-ray imaging: Impact of the free surfactants on the pharmacokinetics. *Eur J Pharm Biopharm* **2013,** *83* (1), 54-62.

103. Li, X.; Anton, N.; Zuber, G.; Zhao, M.; Messaddeq, N.; Hallouard, F.; Fessi, H.; Vandamme, T. F., Iodinated alpha-tocopherol nano-emulsions as non-toxic contrast agents for preclinical X-ray imaging. *Biomaterials* **2013,** *34* (2), 481-491.

104. Trubetskoy, V. S., Polymeric micelles as carriers of diagnostic agents. *Adv Drug Deliv Rev* **1999,** *37* (1-3), 81-88.

105. Trubetskoy, V. S.; Gazelle, G. S.; Wolf, G. L.; Torchilin, V. P., Block-copolymer of polyethylene glycol and polylysine as a carrier of organic iodine: design of long-circulating particulate contrast medium for X-ray computed tomography. *J Drug Target* **1997,** *4* (6), 381-388.

106. Torchilin, V. P.; Frank-Kamenetsky, M. D.; Wolf, G. L., CT visualization of blood pool in rats by using long-circulating, iodine-containing micelles. *Acad Radiol* **1999,** *6* (1), 61-65.

107. Ryan, P. J.; Davis, M. A.; DeGaeta, L. R.; Woda, B.; Melchior, D. L., Liposomes loaded with contrast material for image enhancement in computed tomography. Work in progress. *Radiology* **1984,** *152* (3), 759-762.

108. Havron, A.; Seltzer, S. E.; Davis, M. A.; Shulkin, P., Radiopaque liposomes: a promising new contrast material for computed tomography of the spleen. *Radiology* **1981,** *140* (2), 507-511.

109. Seltzer, S. E.; Davis, M. A.; Adams, D. F.; Shulkin, P. M.; Landis, W. J.; Havron, A., Liposomes carrying diatrizoate. Characterization of biophysical properties and imaging applications. *Invest Radiol* **1984,** *19* (2), 142-151.

110. Kao, C. Y.; Hoffman, E. A.; Beck, K. C.; Bellamkonda, R. V.; Annapragada, A. V., Long-residence-time nano-scale liposomal iohexol for X-ray-based blood pool imaging. *Acad Radiol* **2003,** *10* (5), 475-483.

111. Pannu, H. K.; Thompson, R. E.; Phelps, J.; Magee, C. A.; Fishman, E. K., Optimal contrast agents for vascular imaging on computed tomography: iodixanol versus iohexol. *Acad Radiol* **2005,** *12* (5), 576-584.

112. Klibanov, A. L.; Maruyama, K.; Torchilin, V. P.; Huang, L., Amphipathic polyethyleneglycols effectively prolong the circulation time of liposomes. *FEBS Lett* **1990,** *268* (1), 235-237.

113. Mukundan, S., Jr.; Ghaghada, K. B.; Badea, C. T.; Kao, C. Y.; Hedlund, L. W.; Provenzale, J. M.; Johnson, G. A.; Chen, E.; Bellamkonda, R. V.; Annapragada, A., A liposomal nanoscale contrast agent for preclinical CT in mice. *AJR Am J Roentgenol* **2006,** *186* (2), 300-307.

114. Carruthers, A.; Melchior, D. L., Studies of the Relationship between Bilayer Water Permeability and Bilayer Physical State. *Biochemistry* **1983,** *22* (25), 5797-5807.

115. Seltzer, S. E.; Blau, M.; Herman, L. W.; Hooshmand, R. L.; Herman, L. A.; Adams, D. F.; Minchey, S. R.; Janoff, A. S., Contrast material-carrying liposomes: biodistribution, clearance, and imaging characteristics. *Radiology* **1995,** *194* (3), 775-781.

116. Elrod, D. B.; Partha, R.; Danila, D.; Casscells, S. W.; Conyers, J. L., An iodinated liposomal computed tomographic contrast agent prepared from a diiodophosphatidylcholine lipid. *Nanomedicine* **2009,** *5* (1), 42-45.

117. Kweon, S.; Lee, H. J.; Hyung, W. J.; Suh, J.; Lim, J. S.; Lim, S. J., Liposomes coloaded with iopamidol/lipiodol as a RES-targeted contrast agent for computed tomography imaging. *Pharm Res* **2010,** *27* (7), 1408-1415.

118. Simon, G. H.; Fu, Y.; Berejnoi, K.; Fournier, L. S.; Lucidi, V.; Yeh, B.; Shames, D. M.; Brasch, R. C., Initial computed tomography imaging experience using a new macromolecular iodinated contrast medium in experimental breast cancer. *Invest Radiol* **2005,** *40* (9), 614-620.

119. Yordanov, A. T.; Lodder, A. L.; Woller, E. K.; Cloninger, M. J.; Patronas, N.; Milenic, D.; Brechbiel, M. W., Novel iodinated dendritic nanoparticles for computed tomography (CT) imaging. *Nano Letters* **2002,** *2* (6), 595-599.

120. Fu, Y.; Nitecki, D. E.; Maltby, D.; Simon, G. H.; Berejnoi, K.; Raatschen, H. J.; Yeh, B. M.; Shames, D. M.; Brasch, R. C., Dendritic iodinated contrast agents with PEG-cores for CT imaging: synthesis and preliminary characterization. *Bioconjug Chem* **2006,** *17* (4), 1043-1056.

121. Pan, D.; Williams, T. A.; Senpan, A.; Allen, J. S.; Scott, M. J.; Gaffney, P. J.; Wickline, S. A.; Lanza, G. M., Detecting vascular biosignatures with a colloidal, radio-opaque polymeric nanoparticle. *J Am Chem Soc* **2009,** *131* (42), 15522-15527.

122. Glickson, J. D.; Lund-Katz, S.; Zhou, R.; Choi, H.; Chen, I. W.; Li, H.; Corbin, I.; Popov, A. V.; Cao, W.; Song, L., et al., Lipoprotein nanoplatform for targeted delivery of diagnostic and therapeutic agents. *Mol Imaging* **2008,** *7* (2), 101-110.

123. Song, L.; Li, H.; Sunar, U.; Chen, J.; Corbin, I.; Yodh, A. G.; Zheng, G., Naphthalocyanine-reconstituted LDL nanoparticles for in vivo cancer imaging and treatment. *Int J Nanomedicine* **2007,** *2* (4), 767-774.

124. Allijn, I. E.; Leong, W.; Tang, J.; Gianella, A.; Mieszawska, A. J.; Fay, F.; Ma, G.; Russell, S.; Callo, C. B.; Gordon, R. E., et al., Gold Nanocrystal Labeling Allows Low-Density Lipoprotein Imaging from the Subcellular to Macroscopic Level. *Acs Nano* **2013,** *7* (11), 9761-9770.

125. Hill, M. L.; Corbin, I. R.; Levitin, R. B.; Cao, W.; Mainprize, J. G.; Yaffe, M. J.; Zheng, G., In vitro assessment of poly-iodinated triglyceride reconstituted low-density lipoprotein: initial steps toward CT molecular imaging. *Acad Radiol* **2010,** *17* (11), 1359-1365.

126. Brown, A. L.; Naha, P. C.; Benavides-Montes, V.; Litt, H. I.; Goforth, A. M.; Cormode, D. P., Synthesis, X-ray Opacity, and Biological Compatibility of Ultra-High Payload Elemental Bismuth Nanoparticle X-ray Contrast Agents. *Chem Mater* **2014,** *26* (7), 2266-2274.

127. Mieszawska, A. J.; Mulder, W. J.; Fayad, Z. A.; Cormode, D. P., Multifunctional gold nanoparticles for diagnosis and therapy of disease. *Mol Pharm* **2013,** *10* (3), 831-847.

128. Thakor, A. S.; Jokerst, J.; Zavaleta, C.; Massoud, T. F.; Gambhir, S. S., Gold nanoparticles: a revival in precious metal administration to patients. *Nano Lett* **2011,** *11* (10), 4029-4036.

129. Wang, B.; Yantsen, E.; Larson, T.; Karpiouk, A. B.; Sethuraman, S.; Su, J. L.; Sokolov, K.; Emelianov, S. Y., Plasmonic intravascular photoacoustic imaging for detection of macrophages in atherosclerotic plaques. *Nano Lett* **2009,** *9* (6), 2212-2217.

130. von Maltzahn, G.; Park, J. H.; Agrawal, A.; Bandaru, N. K.; Das, S. K.; Sailor, M. J.; Bhatia, S. N., Computationally guided photothermal tumor therapy using long-circulating gold nanorod antennas. *Cancer Res* **2009,** *69* (9), 3892-3900.

131. Qian, X.; Peng, X. H.; Ansari, D. O.; Yin-Goen, Q.; Chen, G. Z.; Shin, D. M.; Yang, L.; Young, A. N.; Wang, M. D.; Nie, S., In vivo tumor targeting and spectroscopic detection with surface-enhanced Raman nanoparticle tags. *Nat Biotechnol* **2008,** *26* (1), 83-90.

132. Lee, S. E.; Sasaki, D. Y.; Park, Y.; Xu, R.; Brennan, J. S.; Bissell, M. J.; Lee, L. P., Photonic gene circuits by optically addressable siRNA-Au nanoantennas. *ACS Nano* **2012,** *6* (9), 7770-7780.

133. Naha, P. C.; Chhour, P.; Cormode, D. P., Systematic in vitro toxicological screening of gold nanoparticles designed for nanomedicine applications. *Toxicol In Vitro* **2015,** *29* (7), 1445-1453.

134. Dreaden, E. C.; Austin, L. A.; Mackey, M. A.; El-Sayed, M. A., Size matters: gold nanoparticles in targeted cancer drug delivery. *Ther Deliv* **2012,** *3* (4), 457-478.

135. Hainfeld, J. F.; Slatkin, D. N.; Focella, T. M.; Smilowitz, H. M., Gold nanoparticles: a new X-ray contrast agent. *Br J Radiol* **2006,** *79* (939), 248-253.

136. Cai, Q. Y.; Kim, S. H.; Choi, K. S.; Kim, S. Y.; Byun, S. J.; Kim, K. W.; Park, S. H.; Juhng, S. K.; Yoon, K. H., Colloidal gold nanoparticles as a blood-pool contrast agent for X-ray computed tomography in mice. *Invest Radiol* **2007,** *42* (12), 797-806.

137. Kim, D.; Park, S.; Lee, J. H.; Jeong, Y. Y.; Jon, S., Antibiofouling polymer-coated gold nanoparticles as a contrast agent for in vivo X-ray computed tomography imaging. *J Am Chem Soc* **2007,** *129* (24), 7661-7665.

138. Jana, N. R.; Gearheart, L.; Murphy, C. J., Evidence for seed-mediated nucleation in the chemical reduction of gold salts to gold nanoparticles. *Chem Mater* **2001,** *13* (7), 2313-2322.

139. Turkevich, J.; Stevenson, P.; Hillier, J., A study of the nucleation and growth processes in the synthesis of colloidal gold. *Discuss. Faraday Soc.* **1951,** *11*, 55-75.

140. Popovtzer, R.; Agrawal, A.; Kotov, N. A.; Popovtzer, A.; Balter, J.; Carey, T. E.; Kopelman, R., Targeted gold nanoparticles enable molecular CT imaging of cancer. *Nano Lett* **2008,** *8* (12), 4593-4596.

141. Huang, P.; Bao, L.; Zhang, C.; Lin, J.; Luo, T.; Yang, D.; He, M.; Li, Z.; Gao, G.; Gao, B., et al., Folic acid-conjugated silica-modified gold nanorods for X-ray/CT imaging-

guided dual-mode radiation and photo-thermal therapy. *Biomaterials* **2011,** *32* (36), 9796-9809.

142. Kattumuri, V.; Katti, K.; Bhaskaran, S.; Boote, E. J.; Casteel, S. W.; Fent, G. M.; Robertson, D. J.; Chandrasekhar, M.; Kannan, R.; Katti, K. V., Gum arabic as a phytochemical construct for the stabilization of gold nanoparticles: in vivo pharmacokinetics and X-ray-contrast-imaging studies. *Small* **2007,** *3* (2), 333-341.

143. Chanda, N.; Upendran, A.; Boote, E. J.; Zambre, A.; Axiak, S.; Selting, K.; Katti, K. V.; Leevy, W. M.; Afrasiabi, Z.; Vimal, J., et al., Gold nanoparticle based X-ray contrast agent for tumor imaging in mice and dog: a potential nano-platform for computer tomography theranostics. *J Biomed Nanotechnol* **2014,** *10* (3), 383-392.

144. Peng, C.; Li, K.; Cao, X.; Xiao, T.; Hou, W.; Zheng, L.; Guo, R.; Shen, M.; Zhang, G.; Shi, X., Facile formation of dendrimer-stabilized gold nanoparticles modified with diatrizoic acid for enhanced computed tomography imaging applications. *Nanoscale* **2012,** *4* (21), 6768-6778.

145. Guo, R.; Wang, H.; Peng, C.; Shen, M. W.; Pan, M. J.; Cao, X. Y.; Zhang, G. X.; Shi, X. Y., X-ray Attenuation Property of Dendrimer-Entrapped Gold Nanoparticles. *J Phys Chem C* **2010,** *114* (1), 50-56.

146. Liu, H.; Xu, Y.; Wen, S.; Chen, Q.; Zheng, L.; Shen, M.; Zhao, J.; Zhang, G.; Shi, X., Targeted tumor computed tomography imaging using low-generation dendrimer-stabilized gold nanoparticles. *Chemistry* **2013,** *19* (20), 6409-6416.

147. Ye, K.; Qin, J.; Peng, Z.; Yang, X.; Huang, L.; Yuan, F.; Peng, C.; Jiang, M.; Lu, X., Polyethylene glycol-modified dendrimer-entrapped gold nanoparticles enhance CT imaging of blood pool in atherosclerotic mice. *Nanoscale Res Lett* **2014,** *9* (1), 529.

148. Rabin, O.; Manuel Perez, J.; Grimm, J.; Wojtkiewicz, G.; Weissleder, R., An X-ray computed tomography imaging agent based on long-circulating bismuth sulphide nanoparticles. *Nat Mater* **2006,** *5* (2), 118-122.

149. Naha, P. C.; Zaki, A. A.; Hecht, E.; Chorny, M.; Chhour, P.; Blankemeyer, E.; Yates, D. M.; Witschey, W. R.; Litt, H. I.; Tsourkas, A., et al., Dextran coated bismuth-iron oxide nanohybrid contrast agents for computed tomography and magnetic resonance imaging. *J Mater Chem B Mater Biol Med* **2014,** *2* (46), 8239-8248.

150. Bonitatibus, P. J., Jr.; Torres, A. S.; Goddard, G. D.; FitzGerald, P. F.; Kulkarni, A. M., Synthesis, characterization, and computed tomography imaging of a tantalum oxide nanoparticle imaging agent. *Chem Commun (Camb)* **2010,** *46* (47), 8956-8958.

151. Bonitatibus, P. J., Jr.; Torres, A. S.; Kandapallil, B.; Lee, B. D.; Goddard, G. D.; Colborn, R. E.; Marino, M. E., Preclinical assessment of a zwitterionic tantalum oxide nanoparticle X-ray contrast agent. *ACS Nano* **2012,** *6* (8), 6650-6658.

152. Oh, M. H.; Lee, N.; Kim, H.; Park, S. P.; Piao, Y.; Lee, J.; Jun, S. W.; Moon, W. K.; Choi, S. H.; Hyeon, T., Large-scale synthesis of bioinert tantalum oxide nanoparticles for X-ray computed tomography imaging and bimodal image-guided sentinel lymph node mapping. *J Am Chem Soc* **2011,** *133* (14), 5508-5515.

153. Zhou, Z.; Lu, Z. R., Gadolinium-based contrast agents for magnetic resonance cancer imaging. *Wiley Interdiscip Rev Nanomed Nanobiotechnol* **2013,** *5* (1), 1-18.

154. Mohs, A. M.; Lu, Z. R., Gadolinium(III)-based blood-pool contrast agents for magnetic resonance imaging: status and clinical potential. *Expert Opin Drug Deliv* **2007,** *4* (2), 149-164.

155. Karagiannis, P.; Niumsawatt, V.; Rozen, W. M., An alternative contrast medium for computed tomographic angiography: gadolinium. *Plast Reconstr Surg* **2014,** *133* (6), 900e-901e.

156. Gierada, D. S.; Bae, K. T., Gadolinium as a CT contrast agent: assessment in a porcine model. *Radiology* **1999,** *210* (3), 829-834.

157. Zeng, C.; Shi, X.; Wu, B.; Zhang, D.; Zhang, W., Colloids containing gadolinium-capped gold nanoparticles as high relaxivity dual-modality contrast agents for CT and MRI. *Colloids Surf B Biointerfaces* **2014,** *123*, 130-135.

158. Alric, C.; Taleb, J.; Le Duc, G.; Mandon, C.; Billotey, C.; Le Meur-Herland, A.; Brochard, T.; Vocanson, F.; Janier, M.; Perriat, P., et al., Gadolinium chelate coated gold nanoparticles as contrast agents for both X-ray computed tomography and magnetic resonance imaging. *J Am Chem Soc* **2008,** *130* (18), 5908-5915.

159. van Schooneveld, M. M.; Cormode, D. P.; Koole, R.; van Wijngaarden, J. T.; Calcagno, C.; Skajaa, T.; Hilhorst, J.; t Hart, D. C.; Fayad, Z. A.; Mulder, W. J., et al., A fluorescent, paramagnetic and PEGylated gold/silica nanoparticle for MRI, CT and fluorescence imaging. *Contrast Media Mol Imaging* **2010,** *5* (4), 231-236.

160. Huo, D.; He, J.; Li, H.; Yu, H.; Shi, T.; Feng, Y.; Zhou, Z.; Hu, Y., Fabrication of Au@Ag core-shell NPs as enhanced CT contrast agents with broad antibacterial properties. *Colloids Surf B Biointerfaces* **2014,** *117*, 29-35.

161. Huo, D.; Ding, J.; Cui, Y. X.; Xia, L. Y.; Li, H.; He, J.; Zhou, Z. Y.; Wang, H. W.; Hu, Y., X-ray CT and pneumonia inhibition properties of gold-silver nanoparticles for targeting MRSA induced pneumonia. *Biomaterials* **2014,** *35* (25), 7032-7041.

162. Naha, P. C.; Lau, K. C.; Hsu, J. C.; Hajfathalian, M.; Mian, S.; Chhour, P.; Uppuluri, L.; McDonald, E. S.; Maidment, A. D.; Cormode, D. P., Gold silver alloy

nanoparticles (GSAN): an imaging probe for breast cancer screening with dual-energy mammography or computed tomography. *Nanoscale* **2016,** *8* (28), 13740-13754.

163. Chou, S. W.; Shau, Y. H.; Wu, P. C.; Yang, Y. S.; Shieh, D. B.; Chen, C. C., In vitro and in vivo studies of FePt nanoparticles for dual modal CT/MRI molecular imaging. *J Am Chem Soc* **2010,** *132* (38), 13270-13278.

164. Zhou, Z.; Kong, B.; Yu, C.; Shi, X.; Wang, M.; Liu, W.; Sun, Y.; Zhang, Y.; Yang, H.; Yang, S., Tungsten oxide nanorods: an efficient nanoplatform for tumor CT imaging and photothermal therapy. *Sci Rep* **2014,** *4*, 3653.

165. Jakhmola, A.; Anton, N.; Anton, H.; Messaddeq, N.; Hallouard, F.; Klymchenko, A.; Mely, Y.; Vandamme, T. F., Poly-epsilon-caprolactone tungsten oxide nanoparticles as a contrast agent for X-ray computed tomography. *Biomaterials* **2014,** *35* (9), 2981-2986.

166. Mongan, J.; Rathnayake, S.; Fu, Y.; Wang, R.; Jones, E. F.; Gao, D. W.; Yeh, B. M., In vivo differentiation of complementary contrast media at dual-energy CT. *Radiology* **2012,** *265* (1), 267-272.

167. Xing, H.; Bu, W.; Ren, Q.; Zheng, X.; Li, M.; Zhang, S.; Qu, H.; Wang, Z.; Hua, Y.; Zhao, K., et al., A NaYbF4: Tm3+ nanoprobe for CT and NIR-to-NIR fluorescent bimodal imaging. *Biomaterials* **2012,** *33* (21), 5384-5393.

168. Liu, Y.; Liu, J.; Ai, K.; Yuan, Q.; Lu, L., Recent advances in ytterbium-based contrast agents for in vivo X-ray computed tomography imaging: promises and prospects. *Contrast Media Mol Imaging* **2014,** *9* (1), 26-36.

169. Liu, Y.; Ai, K.; Liu, J.; Yuan, Q.; He, Y.; Lu, L., A high-performance ytterbium-based nanoparticulate contrast agent for in vivo X-ray computed tomography imaging. *Angew Chem Int Ed Engl* **2012,** *51* (6), 1437-1442.

170. Xing, H.; Bu, W.; Zhang, S.; Zheng, X.; Li, M.; Chen, F.; He, Q.; Zhou, L.; Peng, W.; Hua, Y., et al., Multifunctional nanoprobes for upconversion fluorescence, MR and CT trimodal imaging. *Biomaterials* **2012,** *33* (4), 1079-1089.

171. Bernsen, M. R.; Guenoun, J.; van Tiel, S. T.; Krestin, G. P., Nanoparticles and clinically applicable cell tracking. *Br J Radiol* **2015,** *88* (1054), 20150375.

172. Taylor, A.; Wilson, K. M.; Murray, P.; Fernig, D. G.; Levy, R., Long-term tracking of cells using inorganic nanoparticles as contrast agents: are we there yet? *Chem Soc Rev* **2012,** *41* (7), 2707-2717.

173. Azene, N.; Fu, Y.; Maurer, J.; Kraitchman, D. L., Tracking of stem cells in vivo for cardiovascular applications. *J Cardiovasc Magn Reson* **2014,** *16*, 7.

174. Mathiasen, A. B.; Kastrup, J., Non-invasive in-vivo imaging of stem cells after transplantation in cardiovascular tissue. *Theranostics* **2013,** *3* (8), 561-572.

175. Modo, M.; Beech, J. S.; Meade, T. J.; Williams, S. C.; Price, J., A chronic 1 year assessment of MRI contrast agent-labelled neural stem cell transplants in stroke. *Neuroimage* **2009,** *47 Suppl 2*, T133-142.

176. Karussis, D.; Karageorgiou, C.; Vaknin-Dembinsky, A.; Gowda-Kurkalli, B.; Gomori, J. M.; Kassis, I.; Bulte, J. W.; Petrou, P.; Ben-Hur, T.; Abramsky, O., et al., Safety and immunological effects of mesenchymal stem cell transplantation in patients with multiple sclerosis and amyotrophic lateral sclerosis. *Arch Neurol* **2010,** *67* (10), 1187-1194.

177. Agudelo, C. A.; Tachibana, Y.; Hurtado, A. F.; Ose, T.; Iida, H.; Yamaoka, T., The use of magnetic resonance cell tracking to monitor endothelial progenitor cells in a rat hindlimb ischemic model. *Biomaterials* **2012,** *33* (8), 2439-2448.

178. Frangioni, J. V.; Hajjar, R. J., In vivo tracking of stem cells for clinical trials in cardiovascular disease. *Circulation* **2004,** *110* (21), 3378-3383.

179. Hoshino, K.; Ly, H. Q.; Frangioni, J. V.; Hajjar, R. J., In vivo tracking in cardiac stem cell-based therapy. *Prog Cardiovasc Dis* **2007,** *49* (6), 414-420.

180. Britten, M. B.; Abolmaali, N. D.; Assmus, B.; Lehmann, R.; Honold, J.; Schmitt, J.; Vogl, T. J.; Martin, H.; Schachinger, V.; Dimmeler, S., et al., Infarct remodeling after intracoronary progenitor cell treatment in patients with acute myocardial infarction (TOPCARE-AMI): mechanistic insights from serial contrast-enhanced magnetic resonance imaging. *Circulation* **2003,** *108* (18), 2212-2218.

181. Wei, H.; Ooi, T. H.; Tan, G.; Lim, S. Y.; Qian, L.; Wong, P.; Shim, W., Cell delivery and tracking in post-myocardial infarction cardiac stem cell therapy: an introduction for clinical researchers. *Heart Fail Rev* **2010,** *15* (1), 1-14.

182. Bulte, J. W.; Kraitchman, D. L., Iron oxide MR contrast agents for molecular and cellular imaging. *NMR Biomed* **2004,** *17* (7), 484-499.

183. Kraitchman, D. L.; Heldman, A. W.; Atalar, E.; Amado, L. C.; Martin, B. J.; Pittenger, M. F.; Hare, J. M.; Bulte, J. W., In vivo magnetic resonance imaging of mesenchymal stem cells in myocardial infarction. *Circulation* **2003,** *107* (18), 2290-2293.

184. Stuckey, D. J.; Carr, C. A.; Martin-Rendon, E.; Tyler, D. J.; Willmott, C.; Cassidy, P. J.; Hale, S. J.; Schneider, J. E.; Tatton, L.; Harding, S. E., et al., Iron particles for noninvasive monitoring of bone marrow stromal cell engraftment into, and isolation of viable engrafted donor cells from, the heart. *Stem Cells* **2006,** *24* (8), 1968-1975.

185. Weber, A.; Pedrosa, I.; Kawamoto, A.; Himes, N.; Munasinghe, J.; Asahara, T.; Rofsky, N. M.; Losordo, D. W., Magnetic resonance mapping of transplanted endothelial

progenitor cells for therapeutic neovascularization in ischemic heart disease. *Eur J Cardiothorac Surg* **2004,** *26* (1), 137-143.

186. Bulte, J. W.; Kostura, L.; Mackay, A.; Karmarkar, P. V.; Izbudak, I.; Atalar, E.; Fritzges, D.; Rodriguez, E. R.; Young, R. G.; Marcelino, M., et al., Feridex-labeled mesenchymal stem cells: cellular differentiation and MR assessment in a canine myocardial infarction model. *Acad Radiol* **2005,** *12 Suppl 1*, S2-6.

187. Chapon, C.; Jackson, J. S.; Aboagye, E. O.; Herlihy, A. H.; Jones, W. A.; Bhakoo, K. K., An in vivo multimodal imaging study using MRI and PET of stem cell transplantation after myocardial infarction in rats. *Mol Imaging Biol* **2009,** *11* (1), 31-38.

188. Terrovitis, J.; Lautamaki, R.; Bonios, M.; Fox, J.; Engles, J. M.; Yu, J.; Leppo, M. K.; Pomper, M. G.; Wahl, R. L.; Seidel, J., et al., Noninvasive quantification and optimization of acute cell retention by in vivo positron emission tomography after intramyocardial cardiac-derived stem cell delivery. *J Am Coll Cardiol* **2009,** *54* (17), 1619-1626.

189. Tran, N.; Li, Y.; Maskali, F.; Antunes, L.; Maureira, P.; Laurens, M. H.; Marie, P. Y.; Karcher, G.; Groubatch, F.; Stoltz, J. F., et al., Short-term heart retention and distribution of intramyocardial delivered mesenchymal cells within necrotic or intact myocardium. *Cell Transplant* **2006,** *15* (4), 351-358.

190. Hofmann, M.; Wollert, K. C.; Meyer, G. P.; Menke, A.; Arseniev, L.; Hertenstein, B.; Ganser, A.; Knapp, W. H.; Drexler, H., Monitoring of bone marrow cell homing into the infarcted human myocardium. *Circulation* **2005,** *111* (17), 2198-2202.

191. Kang, W. J.; Kang, H. J.; Kim, H. S.; Chung, J. K.; Lee, M. C.; Lee, D. S., Tissue distribution of 18F-FDG-labeled peripheral hematopoietic stem cells after intracoronary

administration in patients with myocardial infarction. *J Nucl Med* **2006,** *47* (8), 1295-1301.

192. Herbst, S. M.; Klegerman, M. E.; Kim, H.; Qi, J.; Shelat, H.; Wassler, M.; Moody, M. R.; Yang, C. M.; Ge, X.; Zou, Y., et al., Delivery of stem cells to porcine arterial wall with echogenic liposomes conjugated to antibodies against CD34 and intercellular adhesion molecule-1. *Mol Pharm* **2010,** *7* (1), 3-11.

193. Toma, C.; Fisher, A.; Wang, J.; Chen, X.; Grata, M.; Leeman, J.; Winston, B.; Kaya, M.; Fu, H.; Lavery, L., et al., Vascular endoluminal delivery of mesenchymal stem cells using acoustic radiation force. *Tissue Eng Part A* **2011,** *17* (9-10), 1457-1464.

194. Arifin, D. R.; Manek, S.; Call, E.; Arepally, A.; Bulte, J. W., Microcapsules with intrinsic barium radiopacity for immunoprotection and X-ray/CT imaging of pancreatic islet cells. *Biomaterials* **2012,** *33* (18), 4681-4689.

195. Barnett, B. P.; Ruiz-Cabello, J.; Hota, P.; Ouwerkerk, R.; Shamblott, M. J.; Lauzon, C.; Walczak, P.; Gilson, W. D.; Chacko, V. P.; Kraitchman, D. L., et al., Use of perfluorocarbon nanoparticles for non-invasive multimodal cell tracking of human pancreatic islets. *Contrast Media Mol Imaging* **2011,** *6* (4), 251-259.

196. Betzer, O.; Shwartz, A.; Motiei, M.; Kazimirsky, G.; Gispan, I.; Damti, E.; Brodie, C.; Yadid, G.; Popovtzer, R., Nanoparticle-based CT imaging technique for longitudinal and quantitative stem cell tracking within the brain: application in neuropsychiatric disorders. *ACS Nano* **2014,** *8* (9), 9274-9285.

197. Meir, R.; Shamalov, K.; Betzer, O.; Motiei, M.; Horovitz-Fried, M.; Yehuda, R.; Popovtzer, A.; Popovtzer, R.; Cohen, C. J., Nanomedicine for Cancer Immunotherapy: Tracking Cancer-Specific T-Cells in Vivo with Gold Nanoparticles and CT Imaging. *ACS Nano* **2015,** *9* (6), 6363-6372.

198. Astolfo, A.; Schultke, E.; Menk, R. H.; Kirch, R. D.; Juurlink, B. H.; Hall, C.; Harsan, L. A.; Stebel, M.; Barbetta, D.; Tromba, G., et al., In vivo visualization of gold-loaded cells in mice using x-ray computed tomography. *Nanomedicine* **2013,** *9* (2), 284-292.

199. Schultke, E.; Menk, R.; Pinzer, B.; Astolfo, A.; Stampanoni, M.; Arfelli, F.; Harsan, L. A.; Nikkhah, G., Single-cell resolution in high-resolution synchrotron X-ray CT imaging with gold nanoparticles. *J Synchrotron Radiat* **2014,** *21* (Pt 1), 242-250.

Chapter 2: Design of polymer nanoparticle constructs as CT contrast agents

2.1 Abstract

Nanoparticles of complex architectures can have unique properties. Self-assembly of spherical nanocrystals is a high yielding route to such systems. In this study, we report the self-assembly of a polymer and nanocrystals into aggregates, where the location of the nanocrystals can be controlled to be either at the surface or in the core. These nanospheres, when surface decorated with nanocrystals, resemble disco balls thus the term nano-disco balls. We studied the mechanism of this surface loading phenomenon and found it to be Ca^{2+} dependent. We also investigated whether excess phospholipids could prevent nanocrystal adherence. We found surface loading to occur with a variety of nanocrystal types including iron oxide nanoparticles, quantum dots, and nanophosphors, as well as sizes (10-30 nm) and shapes. Additionally, surface loading occurred over a range of polymer molecular weights (~30-3,000 kDa) and phospholipid carbon tail length. We also show that nanocrystals remain diagnostically active after loading onto the polymer nanospheres *i.e.* providing contrast in the case of magnetic resonance imaging for iron oxide nanoparticles and fluorescence for quantum dots. Hypothesizing that large, high payload nanoparticles would allow high cell loading, we investigated the labeling of monocytes with core loaded nanospheres for CT cell tracking applications.

2.2 Introduction

Methods to create complex nanoparticle architectures such as stars, shells, cubes and frames have led to structures with unique properties.[1-4] However, direct syntheses of such structures are frequently low yielding and difficult to scale up. An alternative approach is to form complex architectures from self-assembly of simpler, high-yielding components. One such route is incorporation of inorganic nanocrystals into polymeric nanoparticles. Such assemblies have a wide range of applications including uses in catalysis,[5] energy,[6] drug delivery,[7-8] and medical imaging.[9] Often the structural organization of these nanoparticles will dictate its function and behavior in a given application. For example, previous research has shown that gold nanoparticles are capable of quenching the emission of nearby fluorescent sources when closely arranged. Jennings *et al* showed that fluorescence could be recovered by separating the 1.5 nm gold nanoparticles and fluorophore a distance as little as 15 nm.[10] Hence, separate core and surface loading of gold cores and fluorophores could maintain fluorophore fluorescence. Therefore, the ability to control localization of nanocrystals *via* self-assembly would be a valuable tool in the synthesis of nanocrystal/polymer composite particles. Control over nanocrystal distribution within the core of polymer constructs has previously been demonstrated.[11-17] For instance, Luo *et al* found that by modifying the surface ligands of gold nanoparticles, their incorporation could be focused to specific regions (*i.e*. the core center or at the edge of the core) within nanoparticles formed from amphiphilic co-polymers of polystyrene and poly(acrylic acid).[18]

In this chapter, we report the serendipitous discovery of a system where nanocrystals can be selectively loaded onto the *surface* of polymer nanospheres, as opposed to the core. This forms a structure reminiscent of a disco ball, which we term a

nano-disco ball. We have found that phospholipid coated inorganic nanoparticles can be used to surface decorate a polymer nanosphere formed from poly(bis(4-carboxyphenoxy)phosphazene), or PCPP, whereas carboxylic acid coated nanocrystals localize to the core. PCPP is a part of a larger class of phosphorous-nitrogen backbone based polymers called polyphosphazenes.[19] These polymers have drawn interest for use in biomedical applications due to their tunable functionality and biocompatibility.[20-22] By modifying the polyphosphazene side chains and molecular weight, the biodegradation rate of polymers can be controlled, making this a promising platform for drug and contrast agent delivery.[23-24] Specifically, PCPP has been used to form ionically cross-linked hydrogels,[25-26] polymer films,[27] and more recently microencapsulating spheres.[23, 28-29] This is the first report of a system that integrates polyphosphazenes and nanocrystals. Furthermore, this is a rare instance of a system where nanocrystals can be preferentially loaded onto the surface of a particle as opposed to internal loading. We believe that this novel system has excellent potential as a contrast agent or theranostic delivery platform.

Herein, we selectively incorporate nanocrystals into the core or surface of the nanospheres synthesized with PCPP. We investigate the conditions for surface localization of nanocrystals onto PCPP nanospheres (Figure 2.1). We report the synthesis of these nano-disco balls and their characterization *via* transmission electron microscopy, scanning electron microscopy and electron microscopy tomography. They can be loaded with separate core and surface payloads, maximizing contrast for two imaging methods. We have probed the synthetic process for the key steps in the formation of the nano-disco balls. We evaluated the effects of varying the physical and chemical properties of the nanocrystals used on surface loading. We also varied

phospholipid tail length for micelle formation and PCPP molecular weights for synthesis. In addition, we have investigated how competing micelles might affect the adherence of nanocrystals. Lastly, we assessed the biocompatibility and effectiveness of core loaded nanospheres and nano-disco balls as cell tracking contrast agents for monocyte labeling. Since CT is limited by low sensitivity, we hypothesized that large, ultra-high payload nanoparticles would be effective for creating high intra-cellular contrast agent loading. We therefore evaluated CT contrast generation, viability, and cytokine release for gold core loaded PCPP nanospheres. We also examined stability in serum and applications as a dual cell tracking and drug delivery agent for nano-disco balls.

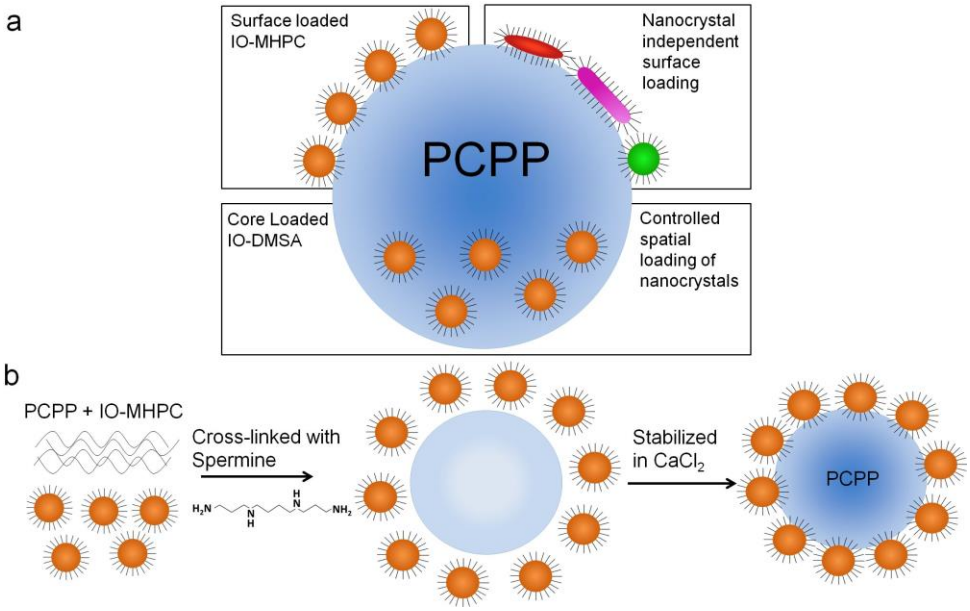

Figure 2.1 Schematic depictions of the PCPP nanosphere platform.

(a) Versatility of PCPP platform for nanocrystal type and loading location. (b) Schematic of PCPP nanosphere synthesis.

Table 2.1: Definitions for abbreviations in PCPP study

Abbreviation	Definition
PCPP	poly(bis(4-carboxyphenoxy)phosphazene)
MHPC	1-myristoyl-2-hydroxy-sn-glycero-3-phosphocholine
AuNP	Gold nanoparticles coated in 11-MUA
Au-PCPP	PCPP nanospheres core loaded with AuNP
IONP	oleic acid coated iron oxide nanoparticles
IO-DMSA	dimercaptosuccinic acid coated iron oxide nanoparticles
IO-MHPC	MHPC micelle encapsulated iron oxide nanoparticles
IO-NB	PCPP nanospheres surfaced loaded with IO-MHPC
IO-DMSA-PCPP	PCPP nanospheres core loaded with IO-DMSA
FITC-BSA	bovine serum albumin conjugated with fluorescein isothiocyanate
FITC-PCPP	FITC-BSA loaded PCPP nanospheres
FITC-NB	FITC-BSA loaded IO-NB

2.3 Materials and methods

2.3.1 Materials

Poly(bis(4-carboxyphenoxy)phosphazene) disodium salt (PCPP, 1 MDa) was purchased from Sigma-Aldrich (St. Louis, MO). PCPP polymers of 3.8 MDa and 36.4 kDa molecular weight were synthesized at The Pennsylvania State University. All phospholipids including 1-myristoyl-2-hydroxy-sn-glycero-3-phosphocholine (MHPC) and chain length variants were purchased from Avanti Polar Lipids (Alabaster, AL). Oleic acid capped cadmium sulfide quantum dots were purchased from NN-Labs, LLC (Fayettville, AR). Oleic acid capped iron oxide nanoparticles (IONP) of various sizes (10, 15, 20, 25, 30 nm) were purchased from Ocean NanoTech (Springdale, AR) and some IONP were synthesized at University of Pennsylvania (vide infra). All other chemicals of analytical grade were purchased through Sigma Aldrich (St. Louis, MO) with the exceptions of sodium fluoride (Acros Organics, NJ), trifluoroacetic acid (Alfa Aesar, MA), Tetrahydrofuran (EMD, PA), dichloromethane (EMD, PA), and ethyl ether (EMD, PA).

Gadolinium or lanthanum trifluoroacetate precursors were prepared using a literature method by refluxing gadolinium or lanthanum oxide in trifluoroacetic acid/water mixture (50 vol%).[30] A monocyte cell line, RAW 264.7, was purchased from ATCC. Cells were cultured in Dubecco's Modified Eagle Medium supplemented with 10% fetal bovine serum and 1% penicillin/streptomycin (10,000 units/mL, 10,000 μg/mL) from Life Technologies Invitrogen (Grand Island, NY).

2.3.2 Polyphosphazene synthesis

For 35.6 kDa PCPP preparation, PCl_5 (0.11 g) was dissolved in 50 mL anhydrous dicholormethane (DCM) for 10 min. Chlorophosphoranimine (6.00 g) prepared by a previous report,[30] was added to the solution rapidly, and the mixture was stirred at room temperature for 4 hr. DCM was then removed under reduced pressure to give colorless viscous living oligo(dichlorophosphazene). The polymer was re-dissolved in anhydrous tetrahydrofuran (THF), and propyl 4-hydroxybenzoate (14.43 g) and $CsCO_3$ (26.00 g) was added to the solution. The mixture was stirred at room temperature for 2 days. Afterwards, the reaction medium was concentrated and precipitated into water (300 mL×3). The precipitate was isolated by centrifugation. Then, the crude product was re-dissolved in DCM, and dialyzed *versus* methanol/DCM (1:4) for 3 days (Spectra/Por dialysis membrane, MWCO: 1,000). The solvent was removed under vacuum to give a white adhesive polymer. (Molecular weight: 35.6 g/mol; PDI: 1.07; repeat units: 82) For the deprotection reaction, the above 1.00 g of polymer was dissolved in 100 mL anhydrous THF. Potassium *tert*-butoxide (2.50 g) and water (0.45 g) were added to the polymer solution. The mixture was stirred at room temperature for 3 days. Then, the

reaction medium was dialyzed *versus* water for 1 day, water/methanol (1:1) for 2 days, and then methanol for 2 days (Spectra/Por dialysis membrane, MWCO: 1,000). Poly(bis(4-carboxylatophenoxy)phosphazene) dipotassium was obtained by the removal of all solvent under vacuum at 35 °C (overall yield: 46%). ^{31}P NMR (D_2O): δ -18.75 (s). ^{1}H NMR (D_2O): δ 7.31 (d, 2H), 6.50 (d, 2H).

A high molecular weight (MW) PCPP (3.8 MDa) was synthesized by first dissolving poly(dichlorophophazene) (2.00 g) in 200 mL of THF. Poly(dichlorophosphazene) was prepared by the thermal ring-opening polymerization of recrystallized and sublimed hexachlorocyclotriphosphazene (Fushimi Chemical Co., Japan) in evacuated Pyrex tubes at 250 °C. Propyl-4-hydroxy-benzoate (9.33 g) was dissolved in THF (100 mL) then added to the polymer solution. Solid cesium carbonate (16.9 g) was then immediately added to the reaction mixture. The reaction proceeded at room temperature for 3 days. Afterward, the solution was concentrated, and precipitated into water 3 times and hexane once. The solvent was removed under reduced pressure to yield a white solid that was obtained in an 80% yield (molecular weight: 3,882,000 g/mol; PDI: 1.62; repeat units: 9,600). For the de-protection reaction, the polymer (3.00 g) was re-dissolved in anhydrous THF (300 mL). Potassium tert-butoxide (7.51 g) and water (1.34 g) were added to the polymer solution. The reaction was stirred at room temperature for 3 days and was then concentrated. This was dialyzed *versus* water for 2 days, (1:1) methanol/water for 2 days, and then (4:1) methanol/water for 1 day. The solvent was then removed under reduced pressure to yield the product with an 81% yield. ^{31}P NMR (D2O): δ -18.53 (s). ^{1}H NMR (D2O): 7.16 (s, 2H), 6.36 (s, 2H).

2.3.3 Iron oxide synthesis

Iron oxide nanoparticles (IONP) were synthesized using oleic acid as the capping ligand following a modified literature method.[31] Typically, 1.5 g of iron chloride and 5.2 g of sodium oleate were first added in a 100 mL flask. Subsequently, 20 mL of hexane, 11.5 mL of ethanol, and 8.8 mL of distilled water were added to the flask and the mixture was sonicated. The two-phase mixture was heated to reflux (~70 °C) for four hours, which produced iron-oleate in the organic layer. The upper organic layer was washed three times with 30 mL of water and separated by centrifugation (5,000 rpm, 10 min). After washing, the hexane was evaporated from the dark brown organic layer and stored under vacuum. The synthesis of 15.6 nm iron oxide nanoparticles was carried out by reacting 5.5 g of iron-oleate and 1.5 g of oleic acid in 31 g of 1-octadecene in a 250 mL round-bottom flask. The reaction mixture was heated to 320 °C at a rate of 200 °C/hour, and kept at that temperature for 30 minutes. The color of the solution turned from dark brown to black upon the formation of nanoparticles. The resulting solution was cooled to room temperature and nanoparticles were precipitated by adding ethanol (35 mL). The precipitated nanoparticles were collected by centrifugation (5,000 rpm, 10 mins) and then redispersed in hexane (10 mL). The nanoparticles were further purified by precipitation with acetone (35 mL), centrifuging at 5,000 rpm for 10 min, and redispersing the collected nanoparticles in hexane (10 mL). This washing step was repeated two more times. After the final washing step, the IONP were redissolved in chloroform (10 mL) and centrifuged at low speed (3,000 rpm, 5 min) to remove aggregates. A sample of these IONP was rendered water soluble through encapsulation with dimercaptosuccinic acid (Figure 2.2) following previous literature methods (IO-DMSA).[32]

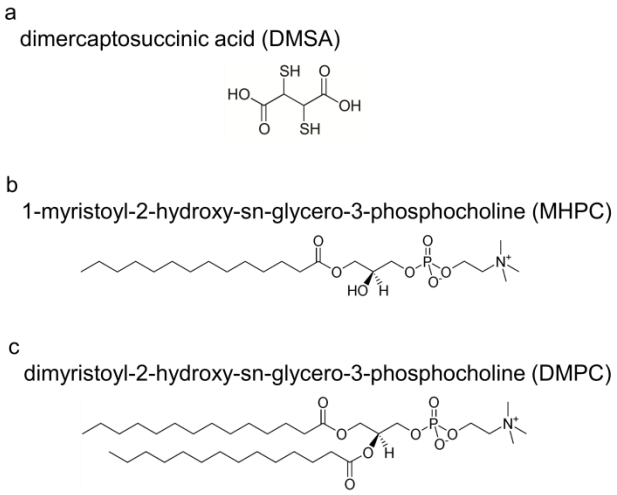

Figure 2.2 Chemical structures.

Chemical structures of iron oxide coatings (DMSA), and phospholipids used for micelle formation (MHPC, DMPC).

2.3.4 Gold nanoparticle synthesis

Carboxylic-acid coated gold nanoparticles (AuNP) were synthesized using the Turkevich method with slight modifications.[33] Briefly, 85 mg of chloroauric acid ($HAuCl_3$) was dissolved in 250ml of Milli-Q water for a final concentration of 1 mM. After heating to a boil, a 38.8 mM solution of sodium citrate (285 mg in 25 ml Milli-Q water) was added, causing the color of the solution to become dark red. The solution was heated for another 15 minutes and then allowed to cool to room temperature. For carboxylic-acid ligand exchange, an 11.9 mM solution of 11-mercaptoundecanoic acid (11-MUA, 2.6 mg in 1 ml of EtOH) was added to the citrate AuNP as prepared above. The solution was stirred for 24 hours. Afterwards, the AuNP were purified and collected by centrifuging at 12.5 krcf for 45 minutes. The pellet was resuspended with Milli-Q water and repeated

two times. The AuNP solution was finally resuspended in 1 ml of Milli-Q water and filtered through a 0.45 µm syringe filter.

2.3.5 Nanophosphor synthesis

Hexagonal phase sodium gadolinium tetrafluoride nanospheres (β-$NaGdF_4$) were synthesized according to a previously reported procedure with slight modification.[34] Briefly, gadolinium trifluoroacetate (2 mmol) and sodium fluoride (5 mmol) were added into a 125 mL three-neck flask containing 60 mL of 1-octadecene/oleic acid solvent mixture (50% by volume). The solution was then degassed under vacuum at 125 ^oC for an hour to remove water. For nanocrystal growth, the solution was heated to 290 ^oC under N_2 environment at a rate of 10 ^oC/min and maintained at this temperature for 5 hours. Purification was performed twice by washing with ethanol and then centrifuging at 6000 rpm for 2 min The nanocrystals were redissolved in hexane (10 mL) and residual sodium fluoride were removed by centrifugation at 3000 rpm for 2 min. β-$NaGdF_4$ nanorods were synthesized by using 2.5 mmol of sodium fluoride in the same method to synthesize nanospheres. Lanthanum trifluoride (LaF_3) discs were synthesized using similar methods as β-$NaGdF_4$ nanospheres while substituting lanthanum trifluoroacetate for gadolinium trifluoracetate The reaction were conducted at 290 ^oC for 5 hours under N_2 environment. LaF_3 nanoplates were redissolved in hexane and centrifuged at 3000 rpm for 2 min to remove lithium fluoride salts.

2.3.6 Nanocrystal micelle synthesis

IONP, quantum dots, and nanophosphors were rendered water soluble through encapsulation in phospholipid micelles. In a typical preparation, 50 mg of MHPC (Figure 2.2) was dissolved in a 1 mL chloroform/methanol mixture (4:1). Oleic acid coated IONP (5.00 mg in 0.5 mL chloroform) were added to the MHPC solution. This mixture was then added to heated Milli-Q water (10 mL) in a slow, drop-wise fashion. The resulting solution was heated for an additional 10 min to ensure organic solvent evaporation and then cooled to room temperature. Afterwards, the aqueous solution was centrifuged at 800 g for 10 min to remove precipitates and multi-cored micelles. The supernatant was collected and centrifuged at 20,000 g for 90 min. The pellet was redispersed in Milli-Q water (~15 mL). These washes were performed three times to ensure purification. Finally, the sample was resuspended in approximately 1 mL of Mill-Q water yielding IONP encapsulated in MHPC micelles (IO-MHPC). Quantum dots and nanophosphors were encapsulated using similar methods as the IONP. Iron oxide encapsulation was also performed using the following additional lipids: 1-lauroyl-2-hydroxy-sn-glycero-3-phosphocholine (IO-LHPC), 1-palmitoyl-2-hydroxy-sn-glycero-3-phosphocholine (IO-PHPC), and 1-stearoyl-2-hydroxy-sn-glycero-3-phosphocholine (IO-SHPC). Additionally, MHPC micelles were formed in the absence of any nanocrystals to obtain samples of empty MHPC micelles. Mixed phospholipid micelles encapsulating IONP (10, 15, 20, 25, and 30 nm diameter) were formed with a 1:1 mixture of MHPC and dimyristoyl-2-hydroxy-sn-glycero-3-phosphocholine (DMPC, Figure 2.2).

2.3.7 PCPP sphere synthesis

Formation of polyphosphazene polymer nanospheres was performed using modified literature methods.[28, 35] A typical synthesis was performed as follows, 40.0 mg of PCPP (1.0 MDa MW) was dissolved in 20 mL of Dulbecco's phosphate buffered saline (DPBS, pH 7.4). IO-MHPC (0.15 mg, 200 µL) were added into 1 mL of this PCPP solution. Then 16.8 µL of a 70.0 mg/mL spermine solution (DPBS, pH 7.4) was added to the PCPP/IO-MHPC solution (0.98% spermine). The mixture was immediately added into a beaker of 88.0 mg/mL $CaCl_2$ buffer (~100 mL) and incubated at room temperature for 30 minutes while stirring. This suspension was purified through centrifugation (800 g, 10 min) and washed three times with Milli-Q water. The resulting IO-MHPC surface loaded nanospheres (IO-NB) were resuspended in 1 mL of Milli-Q water. This process is depicted schematically in Figure 1b. Synthesis of non-loaded PCPP nanospheres were formed similarly, except without the addition of IO-MHPC. PCPP nanospheres (AuIO-NB) were formed, for example, by mixing IO-MHPC (0.15mg, 42 ul) and AuNP (1 mg, 32 ul) together. Afterwards this solution was added to 1 mL of previously described PCPP solution. The synthesis followed as described above. Nanocrystal variants such as CdS quantum dots, nanophosphors (β-$NaGdF_4$ spheres, rods, LaF_3 discs), or iron oxides of varying cores sizes and coatings were substituted for IO-MHPC for inclusion in the PCPP nanosphere synthesis. PCPP of additional molecular weights (35.6 kDa and 3.88 MDa) were also used to form surface loaded nanospheres. Additionally, FITC-BSA (0.1, 0.25 mg) was core loaded into PCPP nanospheres using the standard synthesis method with and without the simultaneous surface loading of IO-MHPC (0.15 mg) to form FITC-PCPP and FITC-IO, respectively.

2.3.8 Polymer and particle characterization

^{1}H and ^{31}P NMR spectra were recorded on a Bruker WM–360 NMR spectrometer operated at 360 and 145 MHz, respectively. ^{1}H NMR spectra were referenced to solvent signals while ^{31}P NMR chemical shifts were relative to 85% phosphoric acid as an external reference, with positive shift values downfield from the reference. Molecular weights were estimated using a Hewlett–Packard HP 1090 gel permeation chromatograph (GPC) equipped with an HP-1047A refractive index detector, American Polymer Standards AM gel 10 mm and AM gel 10 mm 104 Å columns, and calibrated *versus* polystyrene standards.

Transmission electron microscopy images were acquired on a FEI Tecnai T12 microscope at 120 kV. Scanning electron microscopy was performed with a Philips XL20 at 10 kV. Fluorescent imaging for both the quantum dots and the FITC-BSA was performed with an IVIS Spectrum system using 465 nm excitation and 520 nm emission filters. Relaxivities were measured using a Bruker Minispec mq relaxometer at 1.41 T (60 MHz) and 40°C. Freely suspended IO-MHPC were prepared in DPBS for measurements. PCPP samples were prepared in a 1% agar gel in DPBS to prevent sedimentation of nanospheres. Iron oxide concentrations were determined through inductively coupled plasma-optical emission spectroscopy (ICP-OES) on a Spectro Genesis system.

Magnetic hysteresis measurements were performed on a MicroMag Magnetometer (Westerville, OH) at in field range of 10 kOe. Samples (5 µl) were prepared on a coverglass for measurements. Magnetic resonance imaging (MRI) was used to evaluate IO-NB contrast generating properties. IO-NB were prepared in a 1% agar gel at concentrations of 0.05 mM and 0.16 mM of Fe. Additionally, control samples

of DPBS, non loaded PCPP, and 0.16 mM of Fe IO-MHPC in 1% agar gel were scanned. For MRI phantom preparation, samples were placed in a 2% agar gel doped with 0.35 mM manganese chloride. The samples were scanned using a head coil on a Siemens Magnetom Trio with a 3 T magnet. A 2D spin echo sequence was used. Relevant imaging parameters were: echo time (TE), 15 ms; repetition time (TR), 10 s; 1 slice with thickness 3mm, 1 average, flip angle (FA), 90 degrees; acquisition matrix, 184x256; in-plane spatial resolution 0.546 mm^2, field of view (FOV) 140 mm^2. The resulting images were processed using Osirix v.3.0.1 32-bit (Geneva, Switzerland; www.osirix-viewer.com). CT images were acquired with a Siemens Definition DS 64-slice clinical CT scanner at 140 kV (245 mA) with a matrix size of 512x512, field of view 37x37 cm, reconstruction kernel B30f and slice thickness of 0.6 cm. Images were analyzed using Osirix 64 bit (v3.7.1).

2.3.9 In vitro incubations

RAW 264.7 cells were cultured on 6-well plates at a concentration of 2 million cells/mL at 37° C. After 24 hours, the cells were treated with IO-NB at a concentration of 50 µg Fe/mL (0.89 mM) for 4 hours. The cells were washed 3 times with DPBS and then collected by gentle scraping. The cells were fixed in a solution of 2% glutaraldehyde and 5% paraformaldehyde in DPBS. Fixed cells were embedded in resin and prepared for TEM using standard methods.[36] Cell sections were imaged using a FEI Tecnai T12 electron microscope.

For cytotoxicity, Au-PCPP5 (AuNP core loaded in PCPP nanospheres at 5:1 mass ratio, 10 mg gold to 2 mg PCPP) was incubated with monocytes for 24 hours at

37˚C on 20 mm glass bottom dishes at 7.5 x 10^4 cells per dish. Afterwards, the media was washed with DPBS and LIVE/DEAD cocktail was added (2 mL DPBS, 2 µL stock Ethidium-1 homodimer, 0.5 µL stock Calcein AM, and 0.5 µL 3.2 mM Hoechst 33342). The cocktail was left on for 20 mins before imaging with Nikon Eclipse Ti-U fluorescent microscope. Filters for DAPI (Ex. 359, Em. 461 nm), FITC (Ex. 495, Em. 519 nm), and Texas Red (Ex. 595, Em. 613 nm) were used to visualize cell nuclei, living cells and dead cells respectively. Four fields were taken per dish and analyzed with a custom written MATLAB (MathWorks, Natick MA) program for cell counting. The values for each field were averaged for cytotoxicity results. Viability % is expressed as living cells/total cells *100.

To evaluate cytokine expression, ELISA was used to measure TNF-α from media collected following treatment of monocytes with Au-PCPP5. Monocytes were cultured in 96 well plates at 1.0 x10^5 cells per well for 24 hours. Afterwards, cells were treated with increasing concentrations of Au-PCPP5 for 24 hours. Cells were washed twice with DPBS and the media was replaced with or without lipopolysaccharide (LPS) for 3 hours. The media was collected and ELISA was performed according to kit instructions (Life Technologies Invitrogen, Grand Island, NY).

For fluorescent microscopy, RAW 264.7 cells were cultured on glass-bottomed well dishes (20 mm diameter) at a concentration of 800k cells per well. After 24 hours, the cells were treated with 50 ug Fe/ml (0.89 mM) of FITC-NB or FITC-PCPP for 4 hours. The cells were then washed with DPBS 3 times and stained with DAPI. Imaging was performed on a Nikon Eclipse fluorescence microscope (Nikon Eclipse Ti-U, Melville, NY). The DAPI stain was imaged using a 358 nm excitation filter and a 461 nm

emission filter. FITC was imaged using a 494 nm excitation filter and a 516 nm emission filter.

2.4 Results

2.4.1 Core loading of PCPP nanopsheres

Gold nanoparticles of 15 nm in diameter were synthesized and coated in small chain carboxylic acid (11-mercaptoundecanoic acid). Inclusion of these particles into the one pot synthesis with PCPP, formed AuNP core-loaded PCPP nanospheres (AuPCPP). The core loading of AuNP into the PCPP nanospheres increased with higher starting concentrations of gold (Figure 2.3). The internal loading of the AuNP was confirmed with 3D tomographic reconstruction, showing aggregation of AuNP into clusters within the core of the nanosphere (Figure 2.3d). At the highest ratio examined (10 mg Au to 2 mg PCPP), the incorporation of AuNP into the core distorted the morphological sphere shape of the nanosphere.

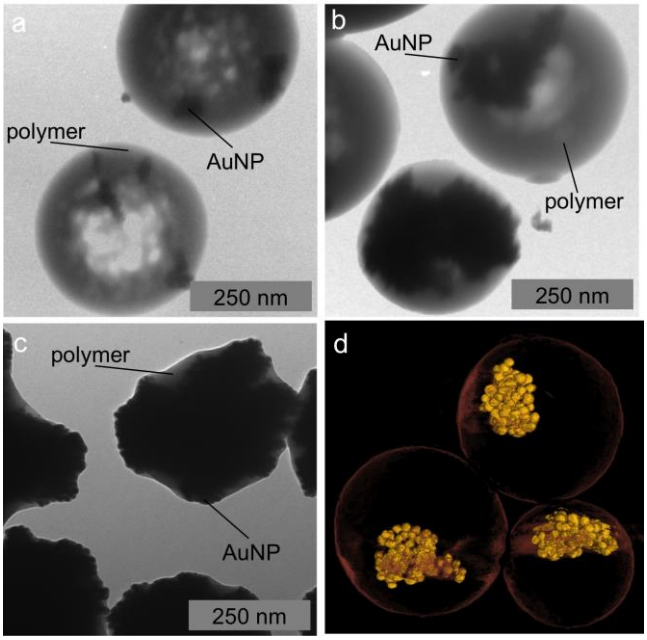

Figure 2.3 AuNP loaded PCPP nanospheres.

TEM of PCPP nanoparticles loaded with varying amounts of carboxylic acid coated gold nanoparticles. A) 1:5, B) 1:1 and C) 5:1 mass ratios. D) 3D reconstruction of sample in B).

2.4.2 Surface decoration of PCPP nanospheres

PCPP is a biocompatible polymer, which we have used to create a novel platform to exploit for nanocrystal delivery in biomedical applications. PCPP nanospheres were synthesized using a modified method that was previously developed to make microspheres.[28] The polycarboxylate PCPP is cross-linked with the polycation spermine to form polymer spheres. The self-assembled nanospheres were dispersed in $CaCl_2$, which we found necessary to halt nanoparticle growth.[35] This process resulted in polymer nanoparticles of 508 ± 185 nm (Figure 2.4a). With loading of these polymer

nanoparticles, we added dimercaptosuccinic acid coated iron oxides (IO-DMSA) to the synthesis prior to adding the spermine cross-linker. We found that IO-DMSA were included in the core of the polymer spheres (Figure 2.4b) similar to our findings with AuNP. We then decided to explore the incorporation of iron oxide nanoparticles with alternative coatings.

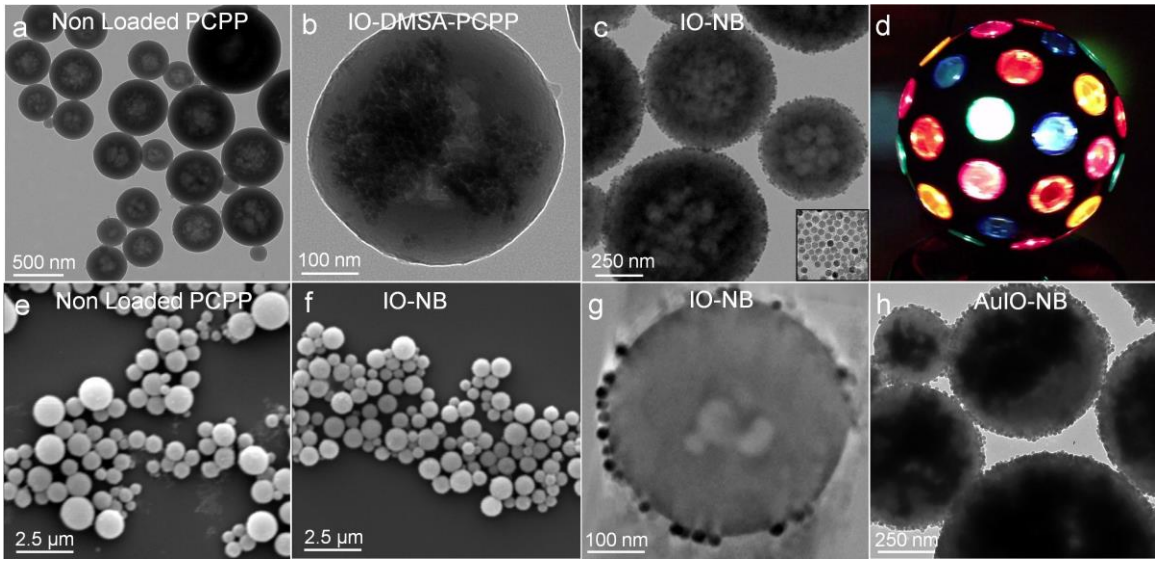

Figure 2.4 Surface loaded PCPP nanospheres.

Electron microscopy images of PCPP nanospheres. TEM images of (a) non loaded PCPP nanospheres, (b) IO-DMSA core loaded into PCPP nanospheres, (c) IO-MHPC surface loaded PCPP nanospheres (IO-NB). (d) Image of disco ball. SEM images of (e) non loaded PCPP and (f) IO-NB. (g) z-slice of tomographic reconstruction of IO-NB. (h) Localization control of IO-MHPC and AuNP with PCPP nanospheres.

Lipid coatings are a common method used to make nanocrystals biocompatible.[37] Oleic acid coated nanocrystals were rendered water soluble through encapsulation in micelles formed by MHPC.[38-39] We mixed these phospholipids coated nanocrystals with PCPP before the addition of spermine. In the final product, we found

that surprisingly, the nanocrystals were exclusively localized to the surface of the nanospheres, in a structure we found reminiscent of a disco ball (Figure 2.4c, d). Electron microscopy images of these IO-MHPC surface loaded PCPP nanoparticles, or iron oxide loaded nano-disco balls (IO-NB), can be seen in Figure 2.4c. The average diameter of IO-NB was found to be 384 ± 127 nm (from analysis of 100+ nanoparticles in TEM images). SEM images revealed IO-NB to be an average diameter of 473.7 ± 125.9 nm and non loaded PCPP nanospheres to be 548.7 ± 200.8 nm. (Figure 2.4e,f). Three dimensional tomographic reconstructions were performed to confirm the localization of IO-MHPC within PCPP nanoparticles. The reconstructions proved exclusive loading of IO-MHPC on the surface of PCPP nanospheres (Figure 2.4g). The total surface area available for IO-MHPC binding was calculated using the average size of PCPP nanospheres and found to be 123.2 cm^2/mg polymer. The total occupied binding space of IO-MHPC was found to be 96.96 cm^2, *i.e.* 78.7%. This coverage corresponds to 609 IO-MHPC particles per PCPP nanosphere. However, we found that the coating density could be tuned, depending on the amount of IO-MHPC added in the synthesis procedure. These calculations can be found in the Appendix.

Next, we studied whether two types of nanocrystal could be loaded into the PCPP nanoparticles. We added both carboxylic acid coated gold nanoparticles and IO-MHPC to the synthesis at the same time. As can be seen in Fig. 2.4h, the gold nanoparticles could be selectively localized to the core, while the IO-MHPC were localized to the particle surface. Gold nanoparticles produce computed tomography (CT) contrast in high concentrations, with no access to water needed,[40-41] therefore core loading is best for gold nanoparticles. On the other hand, less iron oxide is needed to produce MRI contrast and access to water is needed, which surface loading provides.

This formulation demonstrates the benefits of selective nanocrystal localization *via* optimization of the contrast properties for each technique.

Having made the surprising observation of surface loading of PCPP nanospheres with IO-MHPC, we probed the role of different steps in the synthesis, the flexibility of the process, examined the contrast generating potential of the nano-disco balls, evaluated whether the surface attachment of the IO-MHPC was robust to biological conditions *in vitro* and demonstrated the theranostic potential of the nanoparticles.

2.4.3 Surface adhesion occurs during stabilization with $CaCl_2$

The surface loading of PCPP nanospheres occurs *via* self-assembly during synthesis. To investigate the crucial step in the formation of surface loaded nanospheres, we added IO-MHPC at different points in the process. Initially, we formed IO-NB by mixing IO-MHPC with a PCPP solution and then immediately adding spermine as schematically outlined in Figure 1b. The mixture was quickly transferred to a $CaCl_2$ solution and incubated at room temperature for 30 minutes. Afterwards the solution was washed through centrifugation and resuspended in water. To determine if longer incubations of IO-MHPC and PCPP solution together would result in internal loading of IO-MHPC, the reagents were incubated together at room temperature for 30 minutes and 24 hours before the addition of spermine. Results in Figure 2.5a-c, show no visible differences between our standard synthesis, 30 minute pre-incubation, or 24 hour pre-incubation, indicating that longer incubation times did not affect spatial distribution of IO-MHPC in PCPP nanospheres (Fig. 2.5c).

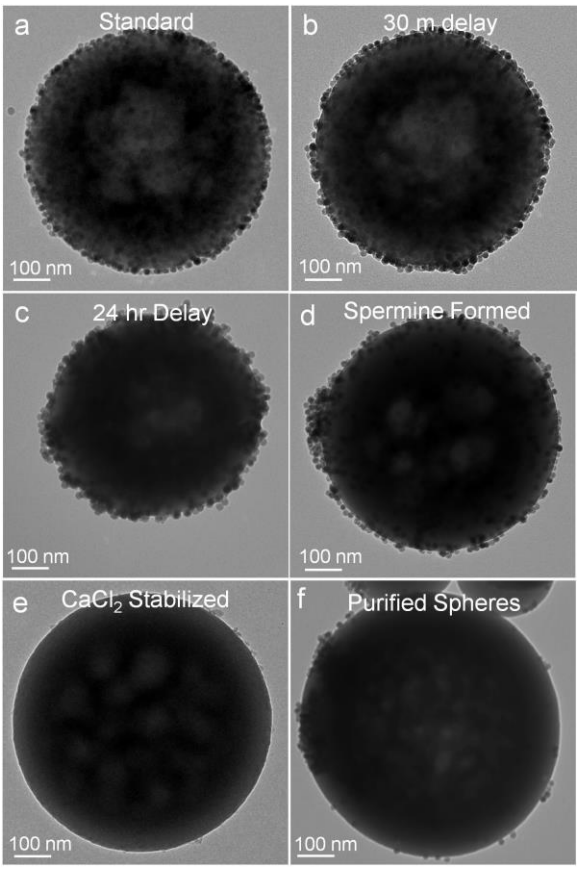

Figure 2.5 Probing synthesis steps of IO-PCPP.

TEM images of synthesis variations: (a) standard synthesis, (b) 30 minute and (c) 24 hr pre-incubation of PCPP and IO-MHPC before spermine addition. TEM of (d) PCPP spheres formed with spermine and then incubated with IO-MHPC, (e) PCPP spheres formed with spermine, stabilized in $CaCl_2$ and then incubated with IO-MHPC, (f) purified non loaded nanospheres re-synthesized with surface loading

Next we examined the effect of mixing PCPP with spermine before the addition of IO-MHPC. As shown in Figure 2.5d, IO-MHPC surface adherence was unaffected when added after spermine addition, demonstrating that surface loading does not occur during the PCPP and spermine cross-linking process. To further explore the mechanism

of surface loading, non loaded spheres were completely formed before the addition of IO-MHPC. The PCPP solution and spermine were first mixed and then transferred to $CaCl_2$ for 30 minutes at room temperature. Afterwards, IO-MHPC were added into the solution and stirred for an additional 30 minutes. The results seen in Figure 2.5e showed no surface loading of IO-MHPC in the sample. These data demonstrate that surface loading of MHPC lipid coated IONP (IO-MHPC) is achievable at any stage before $CaCl_2$ stabilization. We also found fully synthesized non loaded nanospheres (nanospheres formed in the absence IO-MHPC) could be surface loaded by incubating the non loaded spheres with IO-MHPC and then transferring to 0.88% $CaCl_2$ solution for 30 minutes Figure 2.5f). This data suggests a calcium dependent mechanism for surface loading. Presumably there is some form of calcium-mediated binding between the PCPP and phospholipid head group (Ca^{2+} binding to phospholipids is well known).[42] Other divalent cations could likely produce similar phenomenon as Ca^{2+}.

With our standard synthesis method, we studied the IO-NB stability over time when stored in Milli-q water at room temperature. After 24 hours, the IO-NB were found to loosely settle, but could easily be re-dispersed with gently mixing. The surface loading and structure of these nanospheres was unaffected over the observed time frame of 7 months as determined by TEM (Figure 2.6). These data indicate that the particles are robustly stable when stored at room temperature for extended periods of time.

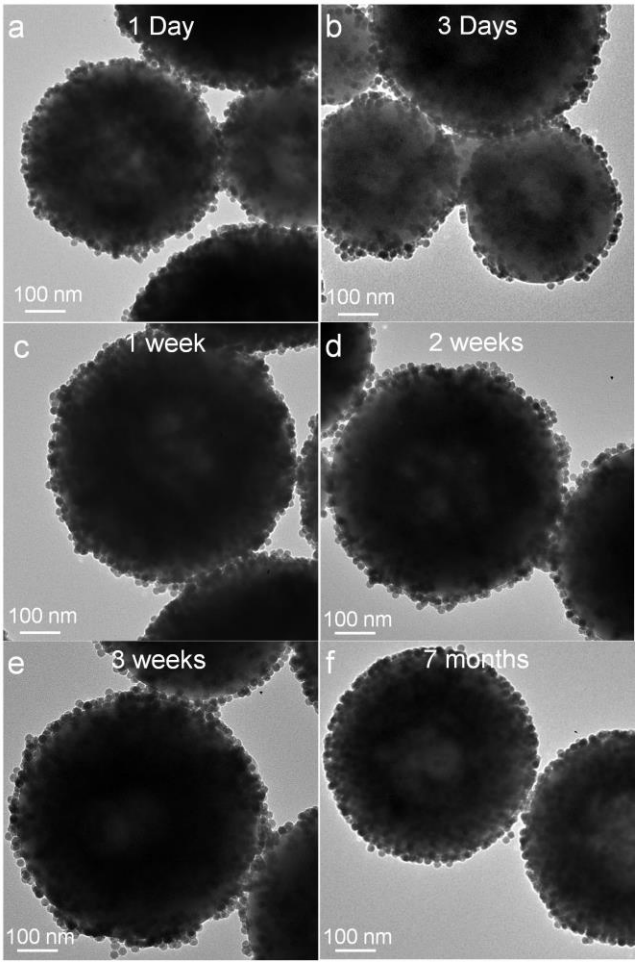

Figure 2.6 Shelf life of IO-PCPP.

TEM of IO-NB stored at room temperature for (a) 1 day, (b) 3 days, (c) 1 week, (d) 2 weeks, (e) 3 weeks, and (f) 7 months.

2.4.4 Surface loading is independent of polymer size, lipid length, core size, and core type

Exclusive surface loading was found with the use of MHPC lipids encapsulating 15.6 nm diameter iron nanoparticles. We examined the flexibility of the reaction by

varying parameters such as PCPP molecular weight, phospholipid length, and nanocrystal core size and type. Surface loaded nanospheres were synthesized using our standard method with PCPP in a range of molecular weights (35.6 kDa, 1.0 MDa, 3.8 MDa MW). Surface loading of IO-MHPC was found with each PCPP MW, demonstrating that the process is independent of polymer size (Figure 2.7). The effect of phospholipid tail length was studied by encapsulating 15.6 nm diameter IONP with 12 (LHPC), 14 (MHPC), 16 (PHPC), and 18 (SHPC) carbon tail chain length phospholipids. PCPP nanospheres were successfully synthesized and surface loaded with each micelle formation (Figure 2.8). Note that LHPC is a relatively poor amphiphile and therefore formed aggregates as opposed to individually dispersed nanocrystals). Additionally, oleate-coated IONP of increasing sizes (10, 15, 20, 25, 30 nm diameters) were encapsulated in micelles using MHPC/DMPC mixtures (IO-MHPC-DMPC). Micelles synthesized using only MHPC to encapsulate the larger 25 and 30 nm IONP were not stable, however, we found that they could be stably coated with a 1:1 mixture of MHPC/DMPC and that nanoparticles with such coatings adhered to PCPP nanospheres also. The PCPP nanospheres were synthesized using our standard method with the various IONP core sizes. TEM revealed surface loading occurred for each core size (Figure 2.9).

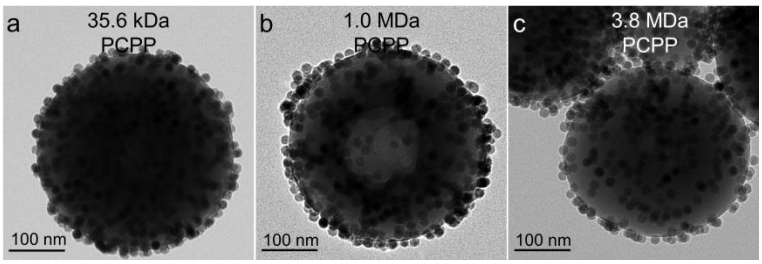

Figure 2.7 IO-PCPP molecular weight.

Surface loading using increasing PCPP MW polymer: (a) 35.6 kDa PCPP, (b) 1.0 MDa PCPP, (c) 3.8 MDa PCPP

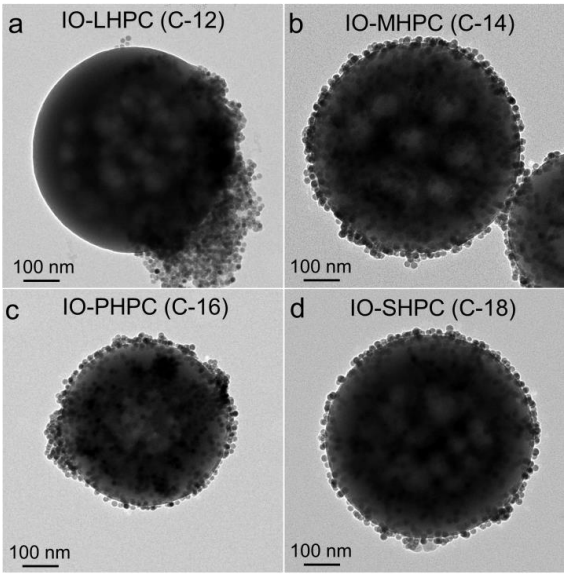

Figure 2.8 Loading with varying micelle phospholipid length.

Surface loading of IONPs with increasing carbon tail lengths. (a) IO-LHPCs (12 carbon tail length) (b) IO-MHPCs (14 carbon tail length), (c) IO-PHPC (16 carbon tail length), and (d) IO-SHPC (18 carbon tail length) loaded onto PCPP nanospheres.

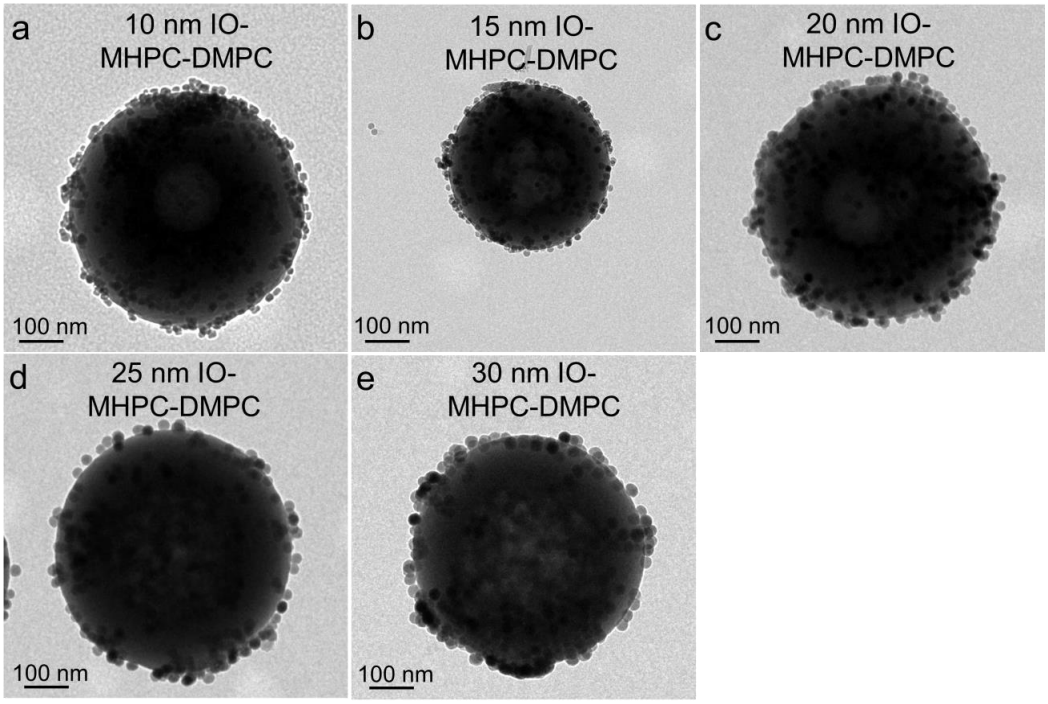

Figure 2.9 Size variants of IONPs formed in phospholipid micelles.
TEM images of PCPP nanosphere phospholipid mixture micelles: (a) 10 nm IO-MHPC-DMPC, (b) 15 nm IO-MHPC-DMPC, (c) 20 nm IO-MHPC-DMPC, (d) 25 nm IO-MHPC-DMPC, (e) 30 nm IO-MHPC-DMPC particles.

To further explore the breadth of applicability of this surface loading process, a variety of diagnostically active nanocrystals were investigated for adherence to PCPP nanospheres. Oleic acid coated quantum dots (CdS spheres) and nanophosphors (β-$NaGdF_4$ spheres, rods, LaF_3 discs) were all found to incorporate into MHPC micelles using the same procedure as for IONP. Surface loading of each core variant was achieved through our standard method of PCPP nanosphere synthesis. TEM verified surface adsorption to be present in each sample (Figure 2.10). From these data, nanocrystals encapsulated into phosphocholine head group lipid micelles can be

successfully surface adsorbed onto PCPP nanospheres regardless of the core type, size, or shape.

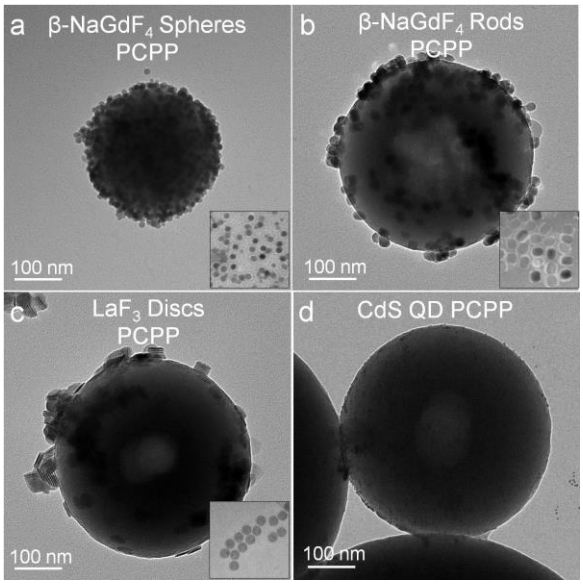

Figure 2.10 Surface loaded nanocrystals variants.

TEM images of PCPP nanosphere surface loaded with various nanocrystals. (a) β-$NaGdF_4$ spheres, (b) β-$NaGdF_4$ rods, (c) LaF_3 discs, and (d) CdS quantum dots surface loaded onto PCPP nanospheres (QD-NB).

2.4.5 Excess empty micelles disrupt nanosphere formation but not surface adherence

We examined whether an excess of empty micelles would reduce surface adsorption of IO-MHPC on PCPP nanospheres. Empty MHPC micelles were mixed together with IO-MHPC at increasing ratios (1:1, 5:1, 10:1, 25:1, based on phospholipid content). PCPP nanosphere synthesis was performed using our standard method with these empty micelles:IO-MHPC ratios. From TEM, lower ratio mixtures did not appear to

affect surface adsorption of IO-MHPC onto the PCPP nanospheres (Figure 2.11). However, at larger ratios of 10:1 and 25:1, disruption of nanosphere formation was observed. These particles appeared amorphous but the surface adsorption of the IO-MHPC was still present. The increased concentration of empty micelles appeared to interfere with the spermine-PCPP cross-linking. We hypothesized that performing the cross linking before the addition of IO-MHPC and empty micelles would allow for the observation of competition without disrupting the PCPP nanosphere formation. We found that by adding the spermine before the IO-MHPC, we were able to surface load IO-MHPC in the presence of high concentrations of empty micelles. Ratios of 10:1, 15:1, 20:1, 25:1 were used in the synthesis, and surface loading of IO-MHPC appeared similar in all samples (Figure 2.12). This phenomenon could be due to the larger area of interaction for the IO-MHPC with the PCPP nanospheres creating stronger attachments, therefore preferentially binding IO-MHPC as compared to empty MHPC micelles.

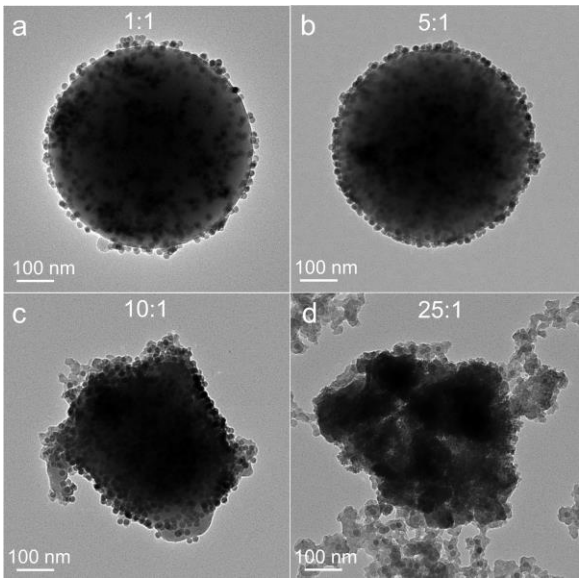

Figure 2.11 Empty micelle inhibition of PCPP formation.

TEM images of PCPP nanosphere standard synthesis with increasing ratios of empty MHPC-micelles to IO-MHPC: (a) 1:1 (b) 5:1 (c) 10:1 (d) 25:1

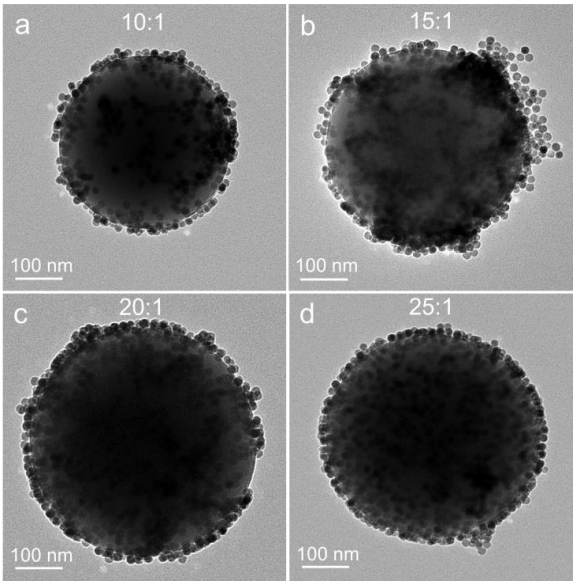

Figure 2.12 Competitive inhibition with cross-linking before surface loading.
TEM images of PCPP nanospheres formed with increasing ratios of empty MHPC-micelles to IO-MHPCs: (a) 10:1 (b) 15:1 (c) 20:1 (d) 25:1. Samples synthesized with spermine addition preceding addition of IO-MHPCs and empty MHPC-micelles mixture.

2.4.6 Particles remain diagnostically active after surface loading

With the ability to load a variety of diagnostically active nanoparticles, we evaluated the contrast generating properties of nanocrystal loaded polymer particles. Magnetic moment curves measured for IO-MHPC and IO-NB did not indicate magnetic hysteresis (Figure 2.13). IO-MHPC and IO-NB had almost identical magnetization saturation values of 67.81 and 65.01 emu/g, respectively. The longitudinal and transverse relaxivity (measures of MRI contrast) of surface loaded IO-NB were examined (Table 2.2) at 1.41 T and 37 °C. Surface loaded particles, IO-NB were found to have a lower transverse (r_2) relaxivity than free IO-MHPC, although still at a

substantial value of 68.2 $mM^{-1}s^{-1}$. The decreased relaxivity could be caused by some loss of interaction between the surrounding water due to the absorption of IO-MHPC to the PCPP nanospheres.[43]

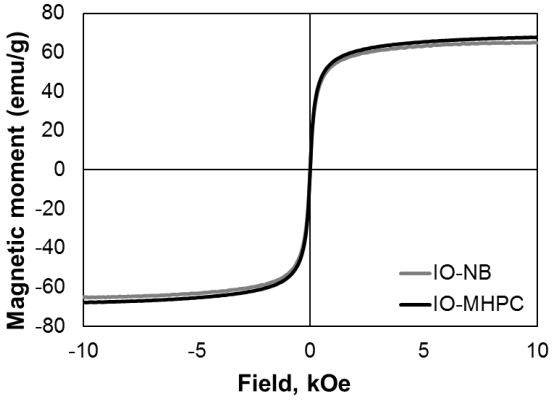

Figure 2.13 Magnetic hysteresis curves for IO-NB and IO-MHPC.
Measured magnetic saturation values were IO-MHPC, 67.81 and IO-NB, 65.01 emu/g.

However, the ratio of transverse to longitudinal relaxivity (r_2/r_1) was higher for IO-NB indicating good properties for T_2-weighted imaging. Additionally for further evaluation, contrast generation for IO-NB was evaluated with a MRI scan. Iron oxide increases the rate of transverse relaxation therefore leading to a decrease in signal intensity, or darkening in T_2/T_2*-weighted MR images. An MR image of a phantom containing IO-NB (0.05 and 0.16 mM Fe), DPBS, free IO-MHPC (0.16 mM Fe) and non loaded PCPP spheres are displayed in Figure 2.14a. The DPBS and non loaded PCPP nanospheres were of relatively similar signal intensity. As expected, the IO-NB were much darker, with a concentration dependent intensity. Although, the IO-NB and IO-MHPC samples were at the same concentration, the IO-NB produced less signal. This

effect could be due to the increased relaxivity (r_2/r_1) ratio seen in the relaxation measurements, or perhaps is due to the different field strengths used for imaging and to determine relaxivities. Overall, IO-NB retained relaxation properties that allow for contrast generation in MRI. Moreover, PCPP nanospheres loaded with quantum dots (QD-NB) exhibit similar fluorescent properties as free quantum dots (QD-MHPC). The fluorescence of the quantum dots persisted after encapsulation in micelles and PCPP surface loading (Figure 2.14). The phantom image in Figure 2.14 indicates the strong CT contrast produced by gold loaded PCPP particles.

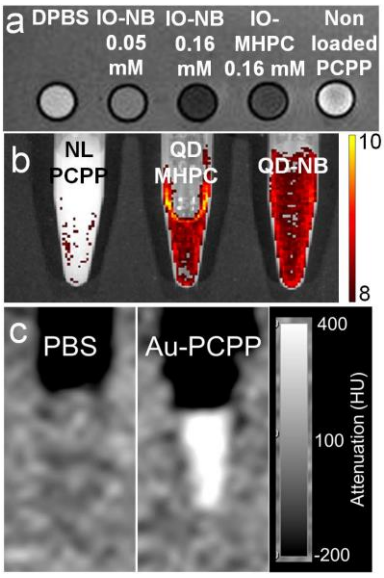

Figure 2.14 Applications of surface loaded PCPP nanospheres.

(a) MRI phantom image. (b) fluorescence image of non loaded PCPP particles, QD-MHPC micelles and QD-NB. Scale bar in units of radiant efficiency (*10^7 (p/s/cm^2/sr)/μW/cm^2) (c) CT phantom image of gold loaded PCPP particles (17 mg/ml).

Table 2.2: Relaxation measurements for free IO-MHPC and IO-NB at 1.41 T.

	r_1 ($mM^{-1}s^{-1}$)	r_2 ($mM^{-1}s^{-1}$)	r_2/r_1
IO-MHPC	3.95	107.66	27.3
IO-NB	1.81	68.22	37.6

2.4.7 In vitro evaluation of core loaded nanospheres for monocyte labeling

With confirmation of diagnostic activity of core and surface loaded PCPP nanospheres, their effectiveness in biomedical applications were assessed. PCPP nanospheres core-loaded with AuNP were investigated for cell viability and function.

Monocytes were incubated with Au-PCPP for 24 hours for all studies. Uptake of these particles (5:1 ratio of gold to PCPP by mass, Au-PCPP5) were assessed with CT scans demonstrating an increase in x-ray attenuation with increased incubation concentrations (Figure 2.15a). Cytotoxicity across different gold concentrations were assessed with both Au-PCPP1 (1:1 mass ratio) and Au-PCPP5 (5:1 mass ratio). Cytotoxicity was observed with increasing concentration for both formulations, but was more pronounced for the Au-PCPP1 formulation (Figure 2.15b). We also sought to investigate the release of TNF-α, an inflammatory cytokine released during activation of the monocytes. Monocytes were incubated with Au-PCPP5 at increasing concentrations with and without lipopolysaccharides (LPS). LPS causes the activation of the monocytes and subsequent release of TNF-α. At the highest concentrations examined (0.25 and 0.5 mg/ml), the difference between LPS and non LPS groups were non-significant indicating that the Au-PCPP5 at those concentrations were activating the monocytes (Figure 2.15c).

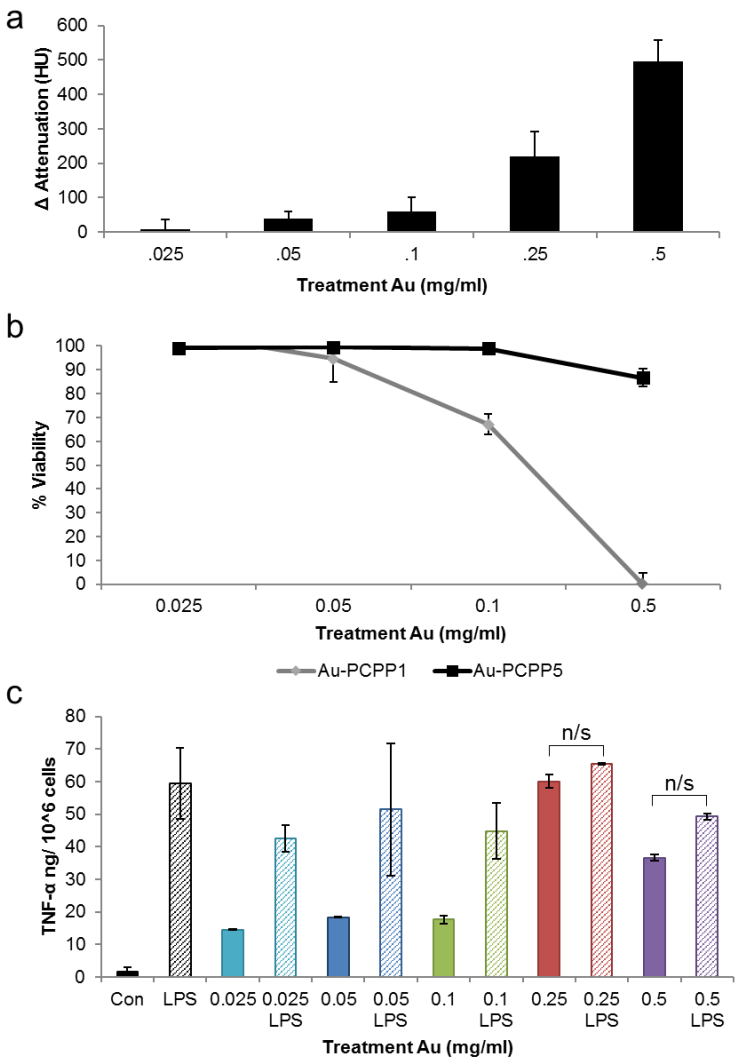

Figure 2.15 In vitro assessment of AuNP core loaded in PCPP nanospheres.

PCPP nanospheres loaded with AuNP (5:1 ratio gold to PCPP) incubated with a monocyte cell line for 24 hours. (a) X-ray attenuation measured at different treatment concentrations of Au-PCPP5. (b) (1:1, Au-PCPP1 and 5:1, Au-PCPP5) viability assessed at increasing concentrations after 24 hour treatment. (c) TNF-α release of monocytes treated with Au-PCPP5 for 24 hours with and without LPS activation. Student

t-test used to compare significance between groups with and without LPS at identical concentrations ($p<0.05$ for significance). Non-significance represented by n/s.

2.4.8 In vitro evaluation of surface loaded nanospheres

The robustness of surface attachment of IO-MHPC to PCPP nanospheres was briefly evaluated for potential biological applications. We incubated nano-disco balls (IO-NB) for 1, 4, 24 hr in cell culture media at 37 °C. IO-NB were then collected through centrifugation and iron oxide content was measured through ICP-OES (Figure 2.16a). The loss of iron content in the samples appeared similar at each time point suggesting that after some initial IO-MHPC release, the remainder was retained over the timeframe tested. TEM performed on these nanoparticles revealed that many IO-MHPC were still attached to the surface of PCPP nanospheres after 4 hr incubation (Figure 2.16b). Next we incubated IO-NB with RAW 264.7 monocytes for 4 hr. Remarkably, TEM performed on these cells revealed IO-MHPC organized in ring shapes located within endosomes (Figure 2.16c). We believe this demonstrates that the IO-MHPC still remain surface bound to PCPP nanospheres after undergoing cellular uptake.

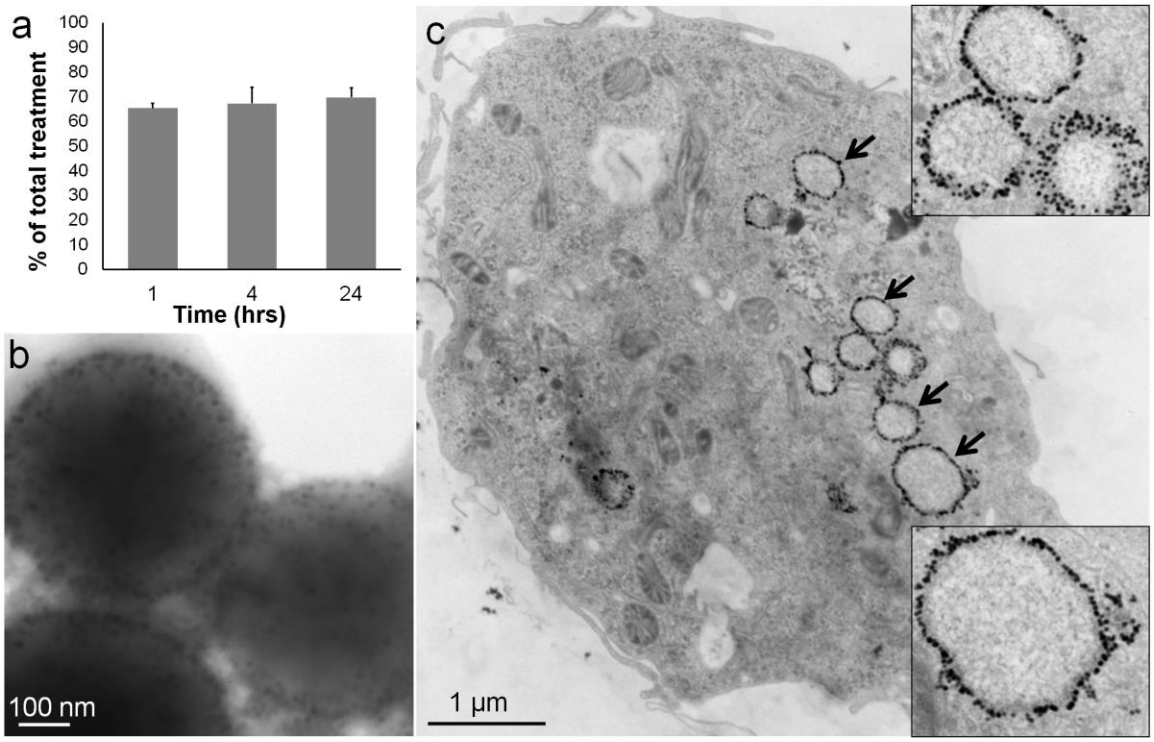

Figure 2.16 IO-NB stability and uptake for cell studies.

(a) Remaining iron oxide concentration after incubation in serum for 1, 4, and 24 hrs. (b) TEM image of IO-NB incubated for 4 hours in cell culture media. (c) TEM images of macrophages that have been incubated with IO-NB. Arrows indicate areas of IO-NB uptake.

2.4.9 Delivery of protein loaded IO-NB

With exclusive surface loading of polymer nanospheres, the internal core of the nanospheres can be used for drug loading. We used bovine serum albumin conjugated with fluorescein isothiocyanate (FITC-BSA, 0.25 mg) as a model drug. This was loaded into PCPP nanospheres (FITC-PCPP). Additionally, FITC-BSA was loaded into the core of nanospheres with simultaneous surface loading of IO-MHPC (FITC-NB, 0.1, 0.25 mg).

TEM and fluorescence imaging were used to characterize FITC-PCPP and FITC-NB. Both particles demonstrated successful loading of FITC-BSA into the PCPP nanosphere as evident from the fluorescence of the purified material. TEM of FITC-NB revealed that IO-MHPC were surface loaded in the presence of the additional FITC-BSA payload, without alteration of the NB structure (Figure 2.17).

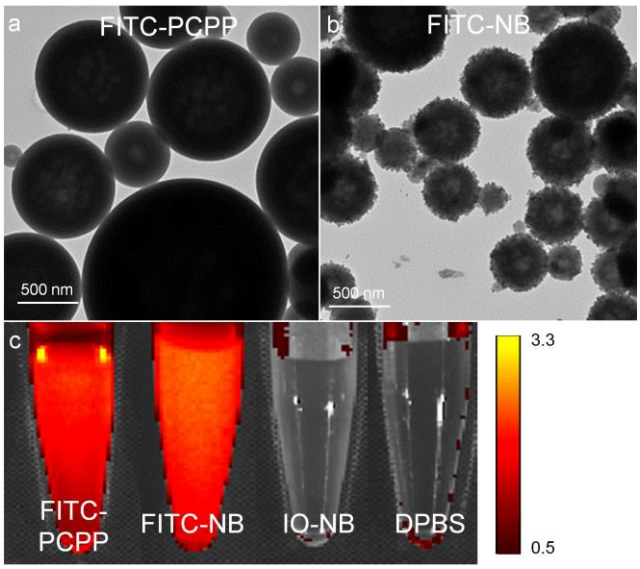

Figure 2.17 FITC-BSA loaded PCPP.

Characterization of PCPP nanospheres with core loaded FITC-BSA. TEM images of (a) FITC-PCPP particles and (b) FITC-NB particles. Image of fluorescent intensity of FITC-PCPP, FITC-NB, IO-NB, and DPBS. Scale bar in units of radiant efficiency (*10^8 (p/s/cm^2/sr)/µW/cm^2).

To evaluate the ability of these particles to deliver FITC-BSA to cells, they were incubated with monocytes for 4 hours. Afterwards the cells were stained with DAPI and imaged with fluorescence microscopy. Phase images of treated cells reveal areas of

particle uptake within the cells (Figure 2.18). Additionally, FITC can be seen within the cells as defined by DAPI (nuclei stain). The added surface loaded IO-MHPC did not prevent the delivery of FITC-BSA to the cells. These data demonstrate that “drug” (FITC-BSA) loading can be achieved with additional exclusive surface loading. Furthermore, the loaded nanospheres remained stable for *in vitro* tracking of delivery into cells.

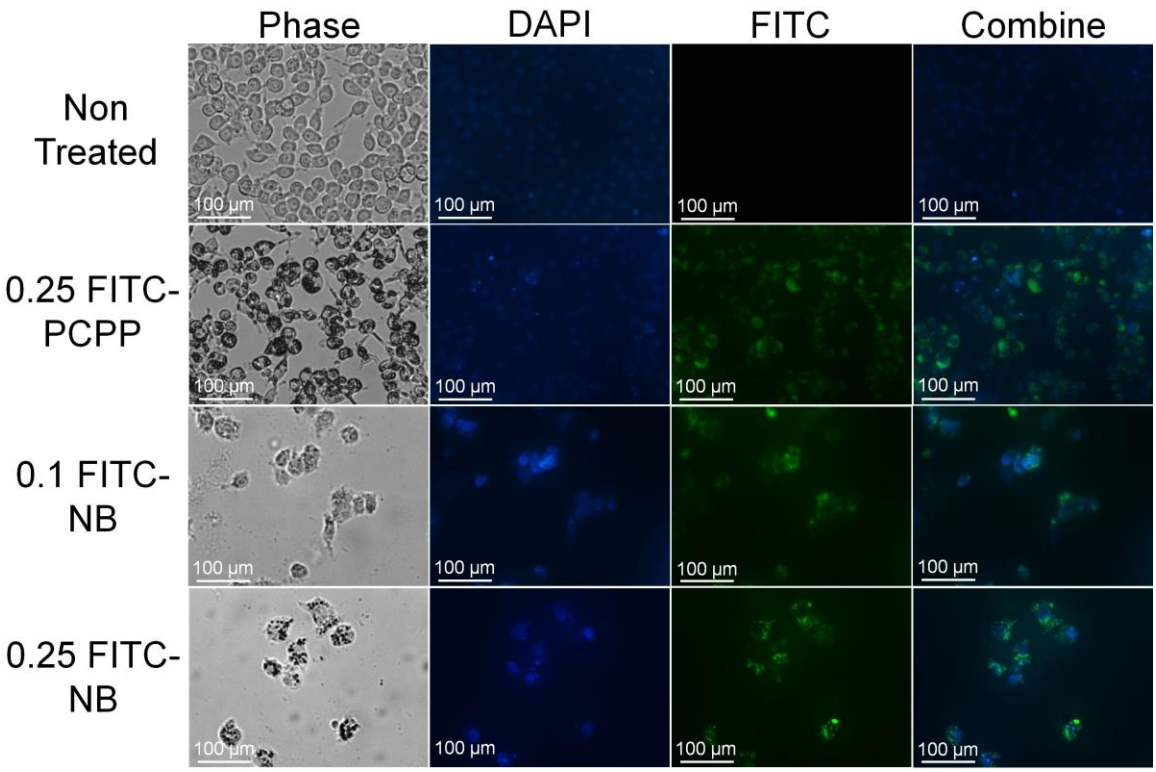

Figure 2.18 Delivery of FITC-BSA in PCPP nanospheres.

Fluorescence of monocytes treated with FITC-BSA encapsulated PCPP nanospheres. Images of phase, DAPI (blue), FITC (green), and the combination of DAPI and FITC for the conditions indicated after 4 hours.

2.5 Discussion

In this study, we have examined the PCPP nanosphere platform, investigating the ability to load nanocrystals both internally and externally. With polymer nano-carriers, drugs and/or nanocrystals are incorporated into the core of the complex and have been explored with several biomedical applications.[44-45] Similarly in our study, inclusion of 11-MUA AuNP aggregated into the core of the PCPP-nanospheres. These Au-PCPP particles were able to incorporate up to a 5:1 mass ratio between gold and PCPP, albeit with a morphological distortion (Figure 2.3). However, with the use of MHPC coated nanocrystals, we found selective loading onto the surface of the PCPP nanospheres.

The controlled localization of nanocrystals to the surface opens opportunities in various delivery and imaging applications. In the study, the robustness of the synthesis and its steps were probed, demonstrating that many parameters (lipid coating, PCPP MW, nanocrystals) can be varied and still achieve selective surface loading of those particles. As shown in Figure 2.6, the IO-NB remain stable for prolonged periods at room temperature, demonstrating an overall stability. Additionally, the ability to load many different types of nanocrystals regardless of size, shape, or elemental composition (Figure 2.10) opens a number of interesting avenues for the platform. In the single pot synthesis, particles can be controlled to localize on the surface or core allowing for multimodal applications carrying different agents. In Figure 2.18, FITC-BSA was core loaded into PCPP with IO-MHPC localized to the surface of the platform. We demonstrated that the FITC-NB could be internalized by monocytes with the structure remaining intact. Both agents could be delivered simultaneously while remaining separated.

Gold nanoparticles loaded into the PCPP nanospheres can be used as CT contrast agents due to gold's x-ray attenuation. We investigated this potential application by evaluating 5:1 mass ratio (Gold to PCPP) Au-PCPP5. The Au-PCPP were able to generate CT contrast, as demonstrated by the phantom images shown in Figure 2.14. Additionally, when incubated with monocytes, high uptake was observed in the cells by measuring the x-ray attenuation in cell pellets (Figure 2.15). For biocompatibility, Au-PCPP5 incubated with monocytes showed some cytotoxicity at the highest concentration of 0.5 mg/ml. At the same concentration, Au-PCPP1 showed nearly 100% cytotoxicity. These results demonstrated, that at high concentrations, Au-PCPP may be affecting cell behavior. To further investigate, the release of TNF-α from monocytes after incubation with Au-PCPP5 was measured. In Figure 2.15, high treatment concentrations of Au-PCPP5 resulted in comparable releases of TNF-α to LPS activated monocytes. LPS is an activator of monocytes, causing monocytes to release TNF-α and other inflammatory cytokines.[46] Ideally, the uptake of Au-PCPP5 should not affect the normal function of monocytes for cell tracking applications. For CT applications, high concentrations of gold are required for imaging, however at high concentrations of Au-PCPP5, some cytotoxic and activation effects were seen. For these reasons, Au-PCPP is not ideal for monocyte labeling and we therefore examined alternative nanoparticles for this application, as described in subsequent chapters.

2.6 Conclusion

As we have described above, PCPP nanospheres can be loaded with nanocrystals in a controlled fashion to result in exclusive localization of the nanocrystals to the surface of the sphere rather than the typically observed core loading of polymer

nanoparticles. We found that simultaneous surface and core loading is possible. A range of diagnostically active nanocrystals could be surface loaded onto the PCPP nanospheres regardless of their individual core size, shape, or chemical composition. The nanocrystals loaded on the spheres retained their contrast generating properties, *i.e.* MR contrast in respect to relaxation for iron oxide particles and fluorescence for quantum dots. The point of nanocrystal attachment was also probed through the investigation of each synthesis step. We observed that surface loading was successful prior to $CaCl_2$ addition. In addition, we found that surface loading was achievable using a variation of polymer sizes and phospholipid tail lengths, demonstrating multiple feasible approaches to surface loading. We showed the stability of the nano-disco balls in cell culture media and the potential for drug delivery and cell tracking. However, labeling of monocytes with AuNP core-loaded PCPP nanospheres showed adverse effects on viability and cytokine expression, despite the excellent x-ray attenuation results. For monocyte tracking, the contrast generation of gold nanoparticles is promising, but further refinement of nanoparticle parameters to improve biocompatibility is necessary. We explore the physical and chemical properties for gold nanoparticles as optimized monocyte labeling in the following chapters.

2.7 Appendix

Determination of IO-MHPC coverage on PCPP particles

PCPP Available Surface Area

Average diameter of sphere (from TEM): 487 nm

Surface area of one sphere: $4\pi r^2$

$4\pi*((4.87e\text{-}5)/2)^2) = 7.45e\text{-}9\ cm^2$

Volume of one sphere: $4/3\pi r^3$

$(4/3)\ \pi*(4.87e\text{-}5)/2)^3) = 6.04e\text{-}14\ cm^3$

Assume density of PCPP = 1000 mg/ml,

PCPP mass in one sphere: Vol of one sphere*density

(6.04e-14)*(1000) = 6.04e-11 mg

Assume 50% PCPP use in batch, total mass = 1mg

Total number of PCPP spheres in batch: Total mass/mass of one sphere

1/(6.04e-11) = 1.65e10 spheres

Total available surface area for binding in one batch: SA for one sphere *total spheres

(7.45e-9)*(1.65e10) = **123.2 cm^2**

Binding Space of Iron Oxide Nanoparticle

Average diameter of IONP (from TEM): 15.6 nm

Volume of one particle: $4/3\pi r^3$

$(4/3)\ \pi*(1.56e\text{-}5)/2)^3) = 1.98e\text{-}18\ cm^3$

Density of IO = 5175 mg/ml

IO mass of nanoparticle: Vol of IONP*density

(1.98e-18)*(5175) = 1.03e-14 mg

Average iron content in one batch (from ICP) = 0.075mg

% iron in IO particle (Fe_3O_4):

(3*55.6)/((3*55.6)+(4*15.9))*100 = 72.34%

Total IO mass in one batch: (ICP mass)/(% iron in IO)

0.075/(72.34/100) = 0.104 mg

Total number of IONP particles in batch: (total IO mass)/(mass IO sphere)

0.104/(1.03e-14) = 1.00e13 particles

Hydrodynamic diameter of IONP =35 nm

Binding area of IONP (area of circle) = $2\pi r^2$

$2\pi((3.5e-6)/2)^2$ = 9.63e-12 cm^2

Total binding area occupied by IONP in one batch: Binding Area*total IONP particles

(9.63e-12)*(1.00e13) = **96.96 cm^2**

Coverage of PCPP nanosphere

Total binding area of IONP/Total available surface area of PCPP:

(96.96/123.2) = **78.7%**

# of IONPs per PCPP sphere

SA of one PCPP sphere *Coverage / Binding area of one IONP

(7.45e-9)*(78.7/100) / (9.63e-12) = **609.49 IONPs per PCPP sphere**

2.8 References

1. Li, N.; Zhao, P.; Astruc, D., Anisotropic gold nanoparticles: synthesis, properties, applications, and toxicity. *Angew. Chem.* **2014,** *53*, 1756-1789.

2. Nehl, C. L.; Liao, H.; Hafner, J. H., Optical properties of star-shaped gold nanoparticles. *Nano Lett.* **2006,** *6* (4), 683-688.

3. Kim, J.; Park, S.; Lee, J. E.; Jin, S. M.; Lee, J. H.; Lee, I. S.; Yang, I.; Kim, J.-S.; Kim, S. K.; Cho, M.-H., et al., Designed Fabrication of Multifunctional Magnetic Gold Nanoshells and Their Application to Magnetic Resonance Imaging and Photothermal Therapy. *Angew. Chem. Int. Ed.* **2006,** *45*, 7754-7758.

4. Skrabalak, S. E.; Chen, J.; Sun, Y.; Lu, X.; Au, L.; Cobley, C. M.; Xia, Y., Gold nanocages: synthesis, properties, and applications. *Acc Chem Res* **2008,** *41* (12), 1587-1595.

5. Liu, P.; Hensen, E. J., Highly efficient and robust Au/MgCuCr2O4 catalyst for gas-phase oxidation of ethanol to acetaldehyde. *J Am Chem Soc* **2013,** *135* (38), 14032-14035.

6. Wu, Z.; Song, T.; Xia, Z.; Wei, H.; Sun, B., Enhanced performance of polymer solar cell with ZnO nanoparticle electron transporting layer passivated by in situ cross-linked three-dimensional polymer network. *Nanotechnology* **2013,** *24* (48), 484012.

7. Zhou, W.; Gao, P.; Shao, L.; Caruntu, D.; Yu, M.; Chen, J.; O'Connor, C. J., Drug-loaded, magnetic, hollow silica nanocomposites for nanomedicine. *Nanomedicine* **2005,** *1* (3), 233-237.

8. Mieszawska, A. J.; Kim, Y.; Gianella, A.; van Rooy, I.; Priem, B.; Labarre, M. P.; Ozcan, C.; Cormode, D. P.; Petrov, A.; Langer, R., et al., Synthesis of polymer-lipid

nanoparticles for image-guided delivery of dual modality therapy. *Bioconjug Chem* **2013,** *24* (9), 1429-1434.

9. Mieszawska, A. J.; Gianella, A.; Cormode, D. P.; Zhao, Y. M.; Meijerink, A.; Langer, R.; Farokhzad, O. C.; Fayad, Z. A.; Mulder, W. J. M., Engineering of lipid-coated PLGA nanoparticles with a tunable payload of diagnostically active nanocrystals for medical imaging. *Chem Commun* **2012,** *48* (47), 5835-5837.

10. Jennings, T. L.; Singh, M. P.; Strouse, G. F., Fluorescent lifetime quenching near d = 1.5 nm gold nanoparticles: probing NSET validity. *J Am Chem Soc* **2006,** *128* (16), 5462-5467.

11. Binder, W. H.; Sachsenhofer, R.; Farnik, D.; Blaas, D., Guiding the location of nanoparticles into vesicular structures: a morphological study. *Phys Chem Chem Phys* **2007,** *9* (48), 6435-6441.

12. Kalra, V.; Lee, J.; Lee, J. H.; Lee, S. G.; Marquez, M.; Wiesner, U.; Joo, Y. L., Controlling nanoparticle location via confined assembly in electrospun block copolymer nanofibers. *Small* **2008,** *4* (11), 2067-2073.

13. Mai, Y.; Eisenberg, A., Controlled incorporation of particles into the central portion of vesicle walls. *J Am Chem Soc* **2010,** *132* (29), 10078-10084.

14. Krack, M.; Hohenberg, H.; Kornowski, A.; Lindner, P.; Weller, H.; Forster, S., Nanoparticle-loaded magnetophoretic vesicles. *J Am Chem Soc* **2008,** *130* (23), 7315-7320.

15. Pinho, S. L. C.; Laurent, S.; Rocha, J.; Roch, A.; Delville, M. H.; Mornet, S.; Carlos, L. D.; Vander Elst, L.; Muller, R. N.; Geraldes, C. F. G. C., Relaxometric Studies of gamma-Fe2O3@SiO2 Core Shell Nanoparticles: When the Coating Matters. *J. Phys. Chem. C.* **2012,** *116* (3), 2285-2291.

16. van Schooneveld, M. M.; Gloter, A.; Stephan, O.; Zagonel, L. F.; Koole, R.; Meijerink, A.; Mulder, W. J.; de Groot, F. M., Imaging and quantifying the morphology of an organic-inorganic nanoparticle at the sub-nanometre level. *Nat. Nanotechnol.* **2010,** *5* (7), 538-544.

17. Wijaya, A.; Hamad-Schifferli, K., High-density encapsulation of Fe3O4 nanoparticles in lipid vesicles. *Langmuir* **2007,** *23* (19), 9546-9550.

18. Luo, Q. J.; Hickey, R. J.; Park, S. J., Controlling the Location of Nanoparticles in Colloidal Assemblies of Amphiphilic Polymers by Tuning Nanoparticle Surface Chemistry. *ACS Macro Letters* **2013,** *2* (2), 107-111.

19. Allcock, H. R., *Chemistry and applications of polyphosphazenes*. Wiley-Interscience: Hoboken, N.J., 2003; p xi, 725 p.

20. Kumbar, S. G.; Bhattacharyya, S.; Nukavarapu, S. P.; Khan, Y. M.; Nair, L. S.; Laurencin, C. T., In vitro and in vivo characterization of biodegradable poly(organophosphazenes) for biomedical applications. *J. Inorg. Organomet. P.* **2006,** *16* (4), 365-385.

21. Allcock, H. R.; Morozowich, N. L., Bioerodible polyphosphazenes and their medical potential. *Polym. Chem.* **2012,** *3* (3), 578-590.

22. Lakshmi, S.; Katti, D. S.; Laurencin, C. T., Biodegradable polyphosphazenes for drug delivery applications. *Adv. Drug. Deliv. Rev.* **2003,** *55* (4), 467-482.

23. Andrianov, A. K.; Payne, L. G.; Visscher, K. B.; Allcock, H. R.; Langer, R., Hydrolytic Degradation of Ionically Cross-Linked Polyphosphazene Microspheres. *J Appl Polym Sci* **1994,** *53* (12), 1573-1578.

24. Singh, A.; Krogman, N. R.; Sethuraman, S.; Nair, L. S.; Sturgeon, J. L.; Brown, P. W.; Laurencin, C. T.; Allcock, H. R., Effect of side group chemistry on the properties of

biodegradable L-alanine cosubstituted polyphosphazenes. *Biomacromolecules* **2006,** *7* (3), 914-918.

25. Allcock, H. R.; Kwon, S., An Ionically Cross-Linkable Polyphosphazene - Poly[Bis(Carboxylatophenoxy)Phosphazene] and Its Hydrogels and Membranes .8. *Macromolecules* **1989,** *22* (1), 75-79.

26. Allcock, H. R.; Kwon, S.; Riding, G. H.; Fitzpatrick, R. J.; Bennett, J. L., Hydrophilic polyphosphazenes as hydrogels: radiation cross-linking and hydrogel characteristics of poly[bis(methoxyethoxyethoxy)phosphazene]. *Biomaterials* **1988,** *9* (6), 509-513.

27. Andrianov, A. K.; DeCollibus, D. P.; Gillis, H. A.; Kha, H. H.; Marin, A.; Prausnitz, M. R.; Babiuk, L. A.; Townsend, H.; Mutwiri, G., Poly[di(carboxylatophenoxy)phosphazene] is a potent adjuvant for intradermal immunization. *Proc Natl Acad Sci USA* **2009,** *106* (45), 18936-18941.

28. Andrianov, A. K.; Chen, J. P., Polyphosphazene microspheres: Preparation by ionic complexation of phosphazene polyacids with spermine. *J Appl Polym Sci* **2006,** *101* (1), 414-419.

29. Garlapati, S.; Eng, N. F.; Wilson, H. L.; Buchanan, R.; Mutwiri, G. K.; Babiuk, L. A.; Gerdts, V., PCPP (poly[di(carboxylatophenoxy)-phosphazene]) microparticles co-encapsulating ovalbumin and CpG oligo-deoxynucleotides are potent enhancers of antigen specific Th1 immune responses in mice. *Vaccine* **2010,** *28* (52), 8306-8314.

30. Wang, B.; Rivard, E.; Manners, I., A new high-yield synthesis of Cl(3)P=NSiMe(3), a monomeric precursor for the controlled preparation of high molecular weight polyphosphazenes. *Inorg Chem* **2002,** *41* (7), 1690-1691.

31. Park, J.; An, K.; Hwang, Y.; Park, J. G.; Noh, H. J.; Kim, J. Y.; Park, J. H.; Hwang, N. M.; Hyeon, T., Ultra-large-scale syntheses of monodisperse nanocrystals. *Nat. Mater.* **2004,** *3* (12), 891-895.

32. Jun, Y. W.; Huh, Y. M.; Choi, J. S.; Lee, J. H.; Song, H. T.; Kim, S.; Yoon, S.; Kim, K. S.; Shin, J. S.; Suh, J. S., et al., Nanoscale size effect of magnetic nanocrystals and their utilization for cancer diagnosis via magnetic resonance imaging. *J Am Chem Soc* **2005,** *127* (16), 5732-5733.

33. Turkevich, J.; Stevenson, P.; Hillier, J., A study of the nucleation and growth processes in the synthesis of colloidal gold. *Discuss. Faraday Soc.* **1951,** *11*, 55-75.

34. Paik, T.; Ko, D. K.; Gordon, T. R.; Doan-Nguyen, V.; Murray, C. B., Studies of liquid crystalline self-assembly of GdF(3) nanoplates by in-plane, out-of-plane SAXS. *ACS Nano* **2011,** *5* (10), 8322-8330.

35. Andrianov, A. K.; Chen, J.; Payne, L. G., Preparation of hydrogel microspheres by coacervation of aqueous polyphosphazene solutions. *Biomaterials* **1998,** *19* (1-3), 109-115.

36. Horak, D.; Babic, M.; Jendelova, P.; Herynek, V.; Trchova, M.; Pientka, Z.; Pollert, E.; Hajek, M.; Sykova, E., D-Mannose-modified iron oxide nanoparticles for stem cell labeling. *Bioconjug Chem* **2007,** *18* (3), 635-644.

37. Cormode, D. P.; Sanchez-Gaytan, B. L.; Mieszawska, A. J.; Fayad, Z. A.; Mulder, W. J. M., Inorganic nanocrystals as contrast agents in MRI: synthesis, coating and introduction of multifunctionality. *Nmr in Biomedicine* **2013,** *26* (7), 766-780.

38. Skajaa, T.; Cormode, D. P.; Jarzyna, P. A.; Delshad, A.; Blachford, C.; Barazza, A.; Fisher, E. A.; Gordon, R. E.; Fayad, Z. A.; Mulder, W. J., The biological properties of

iron oxide core high-density lipoprotein in experimental atherosclerosis. *Biomaterials* **2011,** *32* (1), 206-213.

39. van Schooneveld, M. M.; Vucic, E.; Koole, R.; Zhou, Y.; Stocks, J.; Cormode, D. P.; Tang, C. Y.; Gordon, R. E.; Nicolay, K.; Meijerink, A., et al., Improved biocompatibility and pharmacokinetics of silica nanoparticles by means of a lipid coating: a multimodality investigation. *Nano Lett* **2008,** *8* (8), 2517-2525.

40. Cormode, D. P.; Naha, P. C.; Fayad, Z. A., Nanoparticle contrast agents for computed tomography: a focus on micelles. *Contrast Media Mol Imaging* **2014,** *9* (1), 37-52.

41. Galper, M. W.; Saung, M. T.; Fuster, V.; Roessl, E.; Thran, A.; Proksa, R.; Fayad, Z. A.; Cormode, D. P., Effect of Computed Tomography Scanning Parameters on Gold Nanoparticle and Iodine Contrast. *Invest Radiol* **2012,** *47* (8), 475-481.

42. Macdonald, P. M.; Seelig, J., Calcium-Binding to Mixed Phosphatidylglycerol-Phosphatidylcholine Bilayers as Studied by Deuterium Nuclear-Magnetic-Resonance. *Biochemistry* **1987,** *26* (5), 1231-1240.

43. Bjornerud, A.; Johansson, L., The utility of superparamagnetic contrast agents in MRI: theoretical consideration and applications in the cardiovascular system. *Nmr in Biomedicine* **2004,** *17* (7), 465-477.

44. Kore, G.; Kolate, A.; Nej, A.; Misra, A., Polymeric micelle as multifunctional pharmaceutical carriers. *J Nanosci Nanotechnol* **2014,** *14* (1), 288-307.

45. Tran, P. H.; Tran, T. T.; Vo, T. V., Polymer conjugate-based nanomaterials for drug delivery. *J Nanosci Nanotechnol* **2014,** *14* (1), 815-827.

46. Ghattas, A.; Griffiths, H. R.; Devitt, A.; Lip, G. Y.; Shantsila, E., Monocytes in coronary artery disease and atherosclerosis: where are we now? *J Am Coll Cardiol* **2013,** *62* (17), 1541-1551.

Chapter 3: Effect of size and surface functionality of AuNP for monocyte labeling

3.1 Abstract

With advances in cell therapies, interest in cell tracking techniques to monitor the migration, localization and viability of these cells continues to grow. X-ray computed tomography (CT) is a cornerstone of medical imaging but has been limited in cell tracking applications due to its low sensitivity towards contrast media. In this study, we investigate the role of size and surface functionality of gold nanoparticles for monocyte uptake to optimize the labeling of these cells for tracking in CT. We synthesized gold nanoparticles (AuNP) that range from 15 to 150 nm in diameter and examined several capping ligands, generating 44 distinct AuNP formulations. *In vitro* cytotoxicity and uptake experiments were performed with the RAW 264.7 monocyte cell line. The majority of formulations at each size were found to be biocompatible, with only certain 150 nm PEG functionalized particles reducing viability at high concentrations. High uptake of AuNP was found using small capping ligands with distal carboxylic acids (11-MUA and 16-MHA). Similar uptake values were found with intermediate sizes (50 and 75 nm) of AuNP when coated with 2000 MW poly(ethylene-glycol) carboxylic acid ligands (PCOOH). Low uptake values were observed with 15, 25, 100, and 150 nm PCOOH AuNP, revealing interplay between size and surface functionality. TEM and CT performed on cells revealed similar patterns of high gold uptake for 50 nm PCOOH and 75 nm PCOOH AuNP. These results demonstrate that highly negatively charged carboxylic acid coatings for AuNP provide the greatest internalization of AuNP in monocytes, with a complex dependency on size.

3.2 Introduction

The ability to track specific cells non-invasively in biological systems is of growing importance.[1] With surging interest in adoptive cell therapies for cancer treatment and the promise of stem cell therapy, techniques to monitor the behavior of transferred cells are becoming increasingly valuable tools.[2-4] Labeling and tracking of transferred cells can be uniquely informative, revealing insights about cell migration, differentiation and viability without invasive procedures.[3, 5] A number of studies have explored the potential benefits of cell tracking for cellular therapies including applications for stem cell implantations, T-cell immunotherapy, and myeloid cells for treatment of myocardial infarction.[6-10]

Only a few groups have attempted to use the advantages of x-ray computed tomography (CT) for the purpose of cell tracking.[11-13] CT is a whole body imaging technique that has high spatial and temporal resolution, which has led it to become one of the foremost clinical imaging methodologies, with more than 70 million scans performed annually in the USA alone.[14-15] CT is therefore the first-in-line imaging modality for a number of conditions, such as cardiovascular disease, lung cancer and trauma.[15-16] The development of cell tracking for CT is therefore of considerable interest. For CT, attenuation from contrast agents is linearly proportional to the concentration of the agent allowing for quantification opportunities in cell tracking. For instance, Betzer *et al.,* were able to estimate the number of gold labeled cells *in vivo* in a region of the brain non-invasively using CT scans.[17] Quantifying cell numbers can reveal vital information for cell tracking studies including cell migration and viability. Advances in emerging CT technology continue to open new possibilities for cell tracking; e.g., with the use of x-ray synchrotron beams, some groups were able to achieve single cell resolution for cell

tracking.[18-19] Additionally, with the emergence of spectral CT for specific differentiation of contrast agents from tissue, opportunities for cell tracking with CT continue to grow.[14, 20]

Cell tracking requires the labeling of specific cells of interest with a reporter for imaging. The challenge for CT is its low sensitivity towards contrast agents, which demands efficient methods for labeling cells with high payloads. Gold nanoparticles (AuNP) are an attractive platform upon which to base CT contrast agents due to being biologically inert, providing strong attenuation for CT and their high density, which allows efficient payload delivery.[21-22] Moreover, developments in AuNP chemistry have allowed for control over their size, shape and chemical functionality allowing the nanoparticle properties to be tailored for specific biomedical applications.[23-24] Previous investigations have shown that these nanoparticle properties can affect cytotoxicity, cell uptake and serum protein interactions in biological systems.[25-27] However, the interaction of the nanoparticles appears to be dependent on the surrounding biological environment and system of interest, so the optimal nanoparticle properties for desired interactions (*i.e.* cell avoidance or uptake) must be determined for each specific case.[28]

Monocytes play a critical role in the progression of plaques and other diseases, with monocyte recruitment being prominent in early stages of disease development.[29-32] Imaging recruitment of these monocytes can reveal information about the disease state and allow further investigation of factors that may affect this behavior. In this study, we sought to optimize the uptake of AuNP by monocytes via examining in depth, the effects of size and chemical functionality on AuNP uptake. We synthesized and characterized a library of particles ranging from 15 nm to 150 nm in diameter, each coated with several functionally distinct ligands, totaling 44 unique formulations. We sought to explore short carbon chain carboxylic acid and poly(ethylene) glycol ligands with carboxyl acid end

groups. Additionally, we explored poly(ethylene) glycol ligands with alternate end groups to explore how differences in surface properties affect interactions with monocytes. The interactions of these nanoparticles with monocytes were assessed via viability and uptake studies. Moreover, parameters of incubation time were explored to optimize cell uptake. CT contrast generation of AuNP labeled monocytes was examined with CT scans and intracellular localization studied with TEM.

3.3 Materials and methods

3.3.1 Materials

Chemicals of analytical grade were purchased from Sigma-Aldrich (St. Louis, MI) unless specified elsewhere. The monocyte cell line used for cell studies, RAW 264.7, was purchased from ATCC (Manassas, VA). Cells were cultured with Dubecco's Modified Eagle Medium (DMEM) supplemented with 10% fetal bovine serum (FBS) and 1% penicillin/streptomycin (10000 units/MI, 10000 µg/mL), purchased from Cellgro, Corning (Manassas, VA).

3.3.2 AuNP synthesis

Spherical AuNP of 15 nm and 25 nm in diameter were synthesized using a modified Frens/Turkevich method.[33-34] For 15 nm AuNP, 600 µl of 1% gold(III) chloride ($HAuCl_3$) was dissolved in 60 mL of ultrapure water (Milli-Q, EMD Millipore, Billerica MA). The solution was brought to a boil before 1.8 mL of 1% sodium citrate dihydrate was added to the mixture. The solution was left to reflux for 15 min before cooling to room

temperature. Similarly, 25 nm AuNP were synthesized by adding 1 mL of 1% sodium citrate dihydrate to the boiling gold solution.

AuNP ranging from 50 nm to 150 nm in diameter were synthesized using the seeded growth method described by Perrault *et al*.[35] Briefly, 15 nm spherical AuNP were used as seeds in this method and were produced as outlined above. For the synthesis, 1 mL of 1% $HAuCl_3$ was added to 100 mL of ultrapure water at room temperature. A number of gold "seeds" were added to the solution to create nanoparticles 50, 75, 100 or 150 nm in diameter. The number of seeds needed for each size was empirically determined (Figure 3.1). A typical solution of seeds contained 1.54 $x10^{12}$ seeds/mL. For example, 50 nm AuNP were synthesized by adding 3 mL of seed solution (as made in the above method) to $HAuCl_3$ solution. To initiate the AuNP growth reaction, 220 µL sodium citrate dihydrate (1% weight/volume) and 1 mL of 0.03 M hydroquinone solution were added quickly in succession to the seed/$HAuCl_3$ solution. The solution was allowed to stir for an hour before performing ligand exchange.

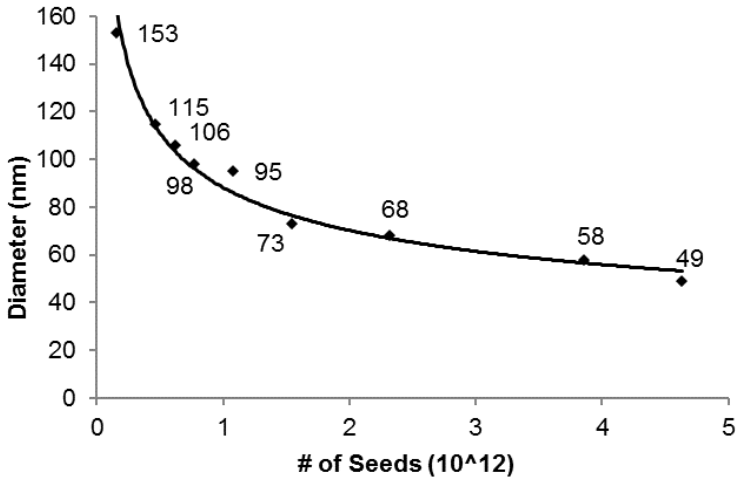

Figure 3.1 Seed number vs gold size diameter.

Effect of seed number (15 nm seeds) on gold nanoparticle diameter in the seeded growth method used in this study.

After AuNP core synthesis, ligand exchange was performed with a library of ligands to stabilize the AuNP for biomedical applications and provide differing chemical functionalities to explore their effect on cell uptake. AuNP that did not undergo ligand exchange remained coated with citrate and were also used in the study. Short carbon chain carboxylic acid ligands 11-mercaptoundecanoic acid (11-MUA) and 16-mercaptohexadecanoic acid (16-MHA) were examined. Additionally, 2000 MW poly(ethylene-gycol) with methoxy (MPEG), carboxylic acid (PCOOH), and amine functional groups were examined. AuNP synthesized with PEG-amine were found to aggregate during ligand exchange, however, amine containing coatings were achieved by using 1:4 ratio of PEG-amine to MPEG (2N8M) or PCOOH (2N8C). Each nanoparticle size was capped with a ligand amount that we estimated based on the total nanoparticle surface area for that size. A ratio of 1.35 x 10^6 mmol/cm^2 was used to

determine the amount of ligand to use (Table 3.1). Each ligand was dissolved at 5 mg/mL concentration before addition to the gold solutions. 11-MUA and 16-MHA ligands were dissolved in ethanol and all PEG functionalized ligands were dissolved in water. For example, for 100 nm PCOOH, 85 µL (0.421 mg) of 5 mg/mL PCOOH solution was added to a typical 100 nm seeded growth solution (100 mL) for exchange. Gold solutions were allowed to stir overnight for complete ligand exchange. Afterwards, the nanoparticles were washed twice by centrifugation and then purified through a 0.45 µm syringe filter (EMD Millipore, Billerica MA). The parameters for centrifugation were specific to each size and can be found in Table 3.2.

Table 3.1 Ligand determination for each size of AuNP.

Size (nm)	15	25	50	75	100	150
Surface area of single particle (cm^2)	7.07E-12	1.96E-11	7.85E-11	1.77E-10	3.14E-10	7.07E-10
Volume of single particle (cm^3)	1.77E-18	8.18E-18	6.54E-17	2.21E-16	5.24E-16	1.77E-15
Mass of Single Particle (mg)	3.41E-14	1.58E-13	1.26E-12	4.27E-12	1.01E-11	6.41E-11
Mass of Au in synthesis (mg)	3	3	5.186	5.0465	5.0186	5.0062
Total # Particles in batch	8.79E+13	1.90E+13	4.10E+12	1.18E+12	4.96E+11	1.47E+11
Total Surface Area (cm^2)	621.12	372.67	322.11	208.96	155.86	103.65
mmol/cm^2 ratio	1.35E-06	1.35E-06	1.35E-06	1.35E-06	1.35E-06	1.35E-06
Ligand Necessary for batch (mmol)	8.40E-04	5.04E-04	4.36E-04	2.83E-04	2.11E-04	1.40E-04
Volume added to each batch (5 mg/ml concentration)						
11-MUA (µL)	36.71	22.02	19.04	12.35	9.21	6.13
16-MHA (µL)	48.49	29.10	25.15	16.32	12.17	8.09
MPEG (µL)	341.41	204.84	177.05	114.86	85.67	56.97
PCOOH (µL)	343.76	206.26	178.27	115.65	86.26	57.36
2N8M (µL)	68.3/273.1	41/163.9	35.4/141.6	22.9/91.9	17.1/68.5	11.4/45.6
2N8C (µL)	68.8/275	41.25/165	35.7/142.6	23.1/92.5	17.3/69	11.5/45.9

Table 3.2 Centrifuge parameters for gold nanoparticles.

	Centrifuge	Speed (rcf)	Time (mins)	Initial Volume (mL)	Resuspension Volume (mL)
15	Sorvall RC 5c Plus	11000	150	40	20
25	Sorvall RC 5c Plus	10500	45	40	20
50	Eppendorf 5810 R	3200	10	45	20
75	Eppendorf 5810 R	1400	12	45	20
100	Eppendorf 5810 R	650	12	45	20
150	Eppendorf 5810 R	250	10	45	20

3.3.3 Particle characterization

The AuNP concentration after purification was determined through inductively coupled plasma – optical emission spectroscopy (ICP-OES). Samples (typically around 10 µL) were dissolved in 1 mL aqua regia (3 parts HCl:1 part HNO_3) for 30 mins before making the final volume of the sample to 3 mL with ultrapure water. The resulting solutions were analyzed with a Spectro-Genesis ICP (Spectro Analytical Instruments GmbH, Kleve, Germany) for gold content. Transmission electron microscopy (TEM) was used to visualize the AuNP and evaluate core size and was performed on a JEOL 1010 (JEOL USA Inc., Peabody MA) at 80 kV. Over 200 AuNP in the TEM images were measured with ImageJ (National Institutes of Health) to determine the average diameter for each core size. UV/Vis spectra were recorded using an Evolution 201 UV-Visible Spectrophotometer (Thermo Scientific, Waltham, MA) scanning from wavelengths of 700 to 300 nm. Typically, 10 µL of sample was added to a cuvette and diluted to 1 mL with ultrapure water. The hydrodynamic diameters (dynamic light scattering) and zeta potentials of the AuNP were evaluated using a Nano ZS-90 Zetasizer (Malvern Instruments, Worcestershire, UK). AuNP samples were diluted to 1 mL with ultrapure water for analysis with these techniques.

3.3.4 In vitro studies

The effects of AuNP size and coating were studied using a monocyte cell line, RAW 264.7. The LIVE/DEAD assay (Life Technologies, Frederick, MD) was used to study cytotoxicity. Monocytes were cultured in 20 mm glass bottom dishes at 7.5 x 10^4 cells per dish for 24 hours at 37˚C, 5% CO_2 with DMEM (10% FBS, 1%

streptomycin/penicillin). After this time, the media was removed and fresh media containing AuNP at 0.1, 0.5, 1.0 mg/ml or without AuNP was added. The cells were incubated with the AuNP for 24 hours before performing analyses, unless specified otherwise. After incubation, cells were washed twice with DPBS before 400 µL of LIVE/DEAD cocktail (2 mL DPBS, 2 µL stock Ethidium-1 homodimer, 0.5 µL stock Calcein AM, 0.5 µL 3.2 mM Hoechst 33342) was gently added to the cells. The cells were incubated for 20 mins with the LIVE/DEAD cocktail. Afterwards, the cells were imaged with Nikon Eclipse Ti-U fluorescence microscope. Filters for DAPI (Ex. 359, Em. 461 nm), FITC (Ex. 495, Em. 519 nm), and Texas Red (Ex. 595, Em. 613 nm) were used to visualize cell nuclei, living cells and dead cells respectively. Four separate fields were taken for each dish for each filter channel. The images were analyzed by a custom MATLAB (MathWorks, Natick MA) program to count the number of stained cells in each field. The viability percent is expressed as number of living cells divided by total number of cells present in each field of view. Viability experiments were repeated 3 times (n=3).

3.3.5 Cell uptake studies

For uptake studies, monocytes were cultured in 12 well plates, 8.0×10^5 cells per well for 24 hours at 37˚C, 5% CO_2 with DMEM (10% FBS, 1% streptomycin/penicillin). At this point, the media was removed and replaced with fresh media containing AuNP. Various concentrations, formulations and timeframes were used, see results for details. After incubation with AuNP, the media was removed and the cells were washed twice with DPBS and then scraped for collection in 1 mL of DPBS. The cells were counted with a hemocytometer and centrifuged at 200 g for 5 mins to form a pellet. The supernatant was discarded and the cells were re-suspended in 200 µL of 4% paraformaldehyde

(PFA) until preparation for ICP-OES. Cells were dissolved in 1 mL of aqua regia (3 parts HCl:1 parts HNO_3) for 30 mins and then centrifuged at 200 g for 5 mins to pellet and discard cell debris. The supernatant was collected and diluted to 3 mL with ultrapure water and analyzed with ICP-OES.

Cells treated with AuNP for 24 hours were also collected and fixed in 2% PFA/2.5% glutaraldehyde, cut into 60 nm sections and prepared using standard techniques for examination with TEM.[36] Sections were viewed with a JEOL 1010 Electron Microscope at 80 kV. For CT scans, after treating cells with AuNP, monocytes were collected and fixed with 200 µL 4% PFA. The cells were allowed to loosely settle into pellets in 250 µl tubes before scanning with a small animal MicroCAT II scanner (Imtek Inc., Knoxville, TN). The parameters used for the scan were 100 µm slice thickness (100 x 100 µm in-plane spatial resolution), 51.2 mm x 76.8 mm field of view, 80 kVp tube voltage, and tube current of 500 µA. The microCT contains a 1.0 mm aluminum beam filter. Image reconstruction was done using a Feldkamp cone beam correction and a Shepp-Logan filter, which produced images scaled in Hounsfield units (HU). Images were analyzed with OsiriX v3.7.1 64-bit software. Identical regions of interest (1.5 mm^2) were drawn on 3 sequential slices in the cell pellets and the recorded attenuation values averaged. The ΔHU was defined as the difference in attenuation between non treated cell pellets and samples treated with AuNP.

3.3.6 Statistical methods

All error bars shown on figures are standard errors of means. Statistical analysis was performed using Stata-14 (64-bit, College Station, Texas). For viability of 150 nm PCOOH, 2N8M, and 2N8C, a one-way ANOVA was used to determine significance

among concentrations. Post-hoc, Tukey pairwise mean comparison was used to compare the interactions between each concentration. For our time course experiment, a one-way ANOVA was used to analyze significance for cell numbers and AuNP uptake. Tukey pairwise mean comparison was used to compare interactions between each time point for both cell number and uptake. For uptake experiments, a two-way ANOVA was used to analyze significance differences caused by both size and coating on uptake. Afterwards, a post-hoc Tukey pairwise mean comparison was used to analyze differences between coatings at each size. For CT attenuation experiments, a one-way ANOVA was performed to determine significant differences at each concentration examined. A post-hoc Tukey pairwise comparison was used for the coatings at each concentration examined.

3.4 Results

3.4.1 AuNP synthesis

Spherical AuNP of approximately 15, 25, 50, 75, 100, and 150 nm in diameter were synthesized to examine the effect of size on cellular uptake. AuNP of 15 and 25 nm were synthesized using the Turkevich method.[33-34] Diameters of 50 nm and above were synthesized using a modified seeded growth method described by Perrault *et al*.[35] This method utilized 15 nm AuNP synthesized via the Turkevich method as nucleation points to further "grow" gold around these "seeds." We used the seeded growth method for these larger diameter nanoparticles, since we found that the Turkevich method resulted in highly heterogeneous sizes and shapes when forming nanoparticles 50 nm or above. The number of seeds added to the synthesis dictated the final size of the AuNP. We

empirically determined the number of seeds needed to form nanoparticles of a range of sizes with this synthesis (Figure 3.1). TEM images in Figure 3.2 were analyzed to determine core sizes of the AuNP. The distributions for each nanoparticle size can be seen in Figure 3.3. A Shapiro-Wilk test was used to test for normality. Each nanoparticle formulation was found to be normally distributed except the 15 nm particles ($p<0.05$).

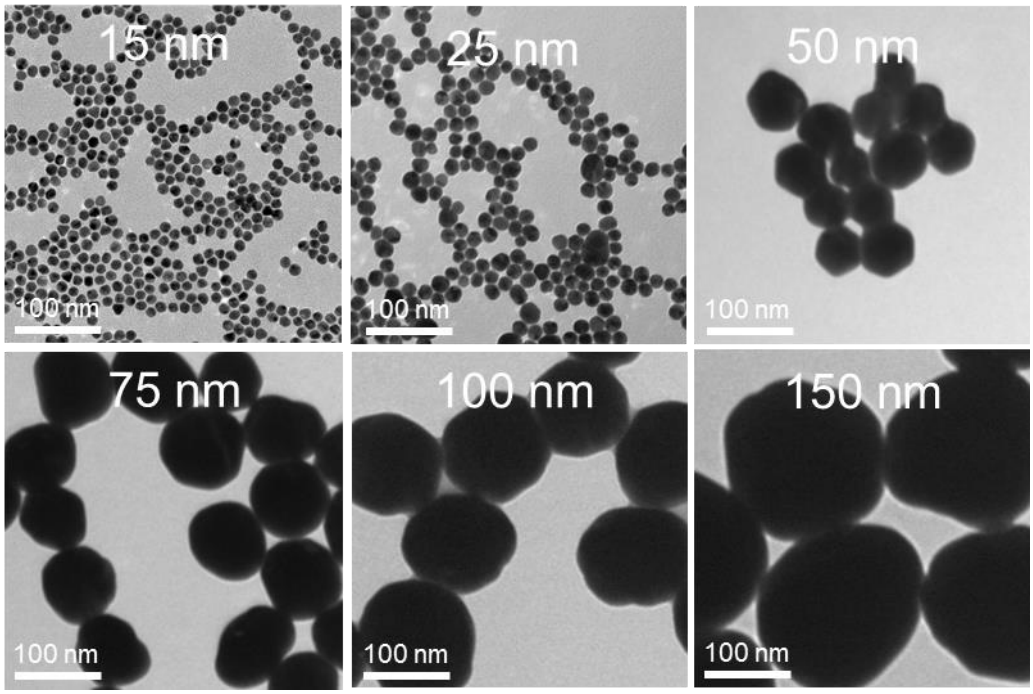

Figure 3.2 TEM of AuNP from 15 to 150 nm.

TEM images of spherical gold nanoparticle of increasing size from 15 to 150 nm. 15 and 25 nm AuNP were synthesized through the Turkevich method. 50, 75, 100, and 150 nm AuNP were synthesized through a seeded growth method.

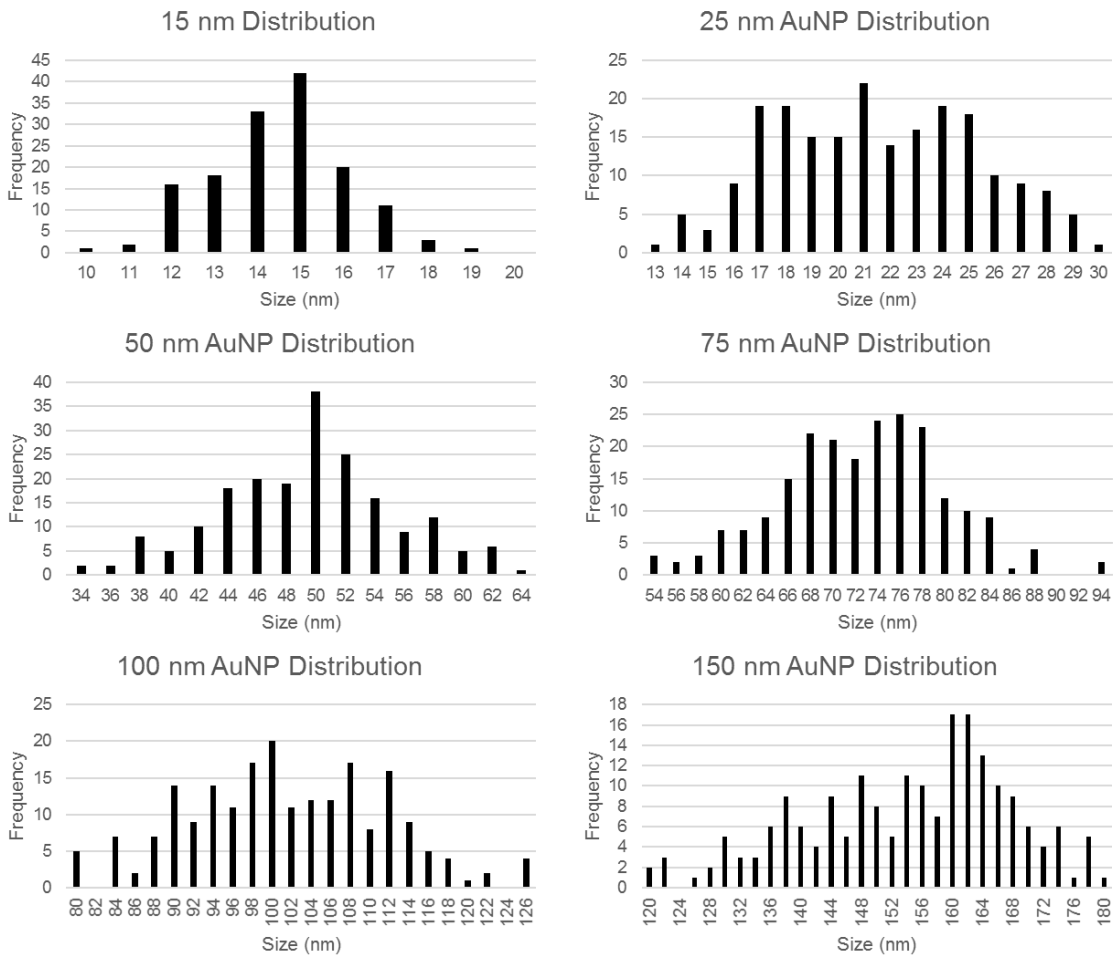

Figure 3.3 AuNP synthesis size distributions.

Histogram plots of size distributions for each AuNP size. Sizes are measured nanoparticle core diameters from TEM images (>200 particles surveyed). Shapiro-Wilk test was used to test for normality. Normality was rejected for only 15 nm size particles ($p<0.5$).

In addition to forming nanoparticles of a range of sizes, several different coatings were used for each nanoparticle size. With the use of thiol ligands, the surface coating of AuNP was exchanged to produce particles with various chemical functionalities. We

examined seven different coatings for each size of AuNP (including citrate) and each formulation was characterized for UV/Vis absorption, hydrodynamic diameter (dynamic light scattering) and overall surface charge (zeta potential) (Table 3.3). The chemical structure for each ligand is shown in Figure 3.4. Straight-chain hydrocarbon ligands with distal carboxylic acid functional groups (11-MUA and 16-MHA) were used as they demonstrate high uptake in monocytes without affecting viability as shown in our previous work with 15 nm AuNP.[13] In addition, a variety of thiol-poly(ethylene-glycol) (PEG) based coatings were examined. PEG with a distal methoxy group (MPEG) is widely used to coat nanoparticles, typically providing high stability and resulting in low cell uptake.[37-38] We used this coating as a control.

Table 3.3 Surface characterization of AuNP formulations

Size	Coating	Abs (nm)	Hydrodynamic diameter (nm)	PDI	Zeta (mV)
15 nm	Citrate	518.2	25.20	0.180	-38.4 ± 1.6
	11 MUA	525.9	23.39	0.207	-45.9 ± 1.8
	16 MHA	521.1	18.59	0.420	-48.8 ± 0.7
	mPEG	522.3	28.46	0.115	-18.0 ± 0.7
	PCOOH	520.2	31.89	0.164	-36.5 ± 3.0
	2N8M	521.9	27.91	0.100	-14.6 ± 0.4
	2N8C	519.6	29.54	0.092	-30.0 ± 3.5
25 nm	Citrate	530.36	45.23	0.671	-42.8 ± 0.9
	11 MUA	527.1	49.86	0.484	-47.3 ± 0.1
	16 MHA	539.1	31.51	0.511	-49.0 ± 0.4
	mPEG	532.95	45.46	0.68	-30.4 ± 1.1
	PCOOH	532.69	43.6	0.688	-39.7 ± 1.1
	2N8M	531.91	43.58	0.588	-21.4 ± 0.2
	2N8C	532.65	44.99	0.678	-41.6 ± 0.6
50 nm	Citrate	529.5	51.96	0.206	-48.3 ± 1.9
	16 MHA	529.7	54.56	0.147	-54.8 ± 0.8
	mPEG	529.2	53.26	0.236	-55.4 ± 0
	PCOOH	535.11	57.37	0.14	-41.5 ± 0.3
	2N8M	534.6	60.48	0.088	-35.0 ± 0.2
	2N8C	533.7	44.51	0.337	-49.5 ± 1.9
75 nm	Citrate	548.3	79.69	0.11	-53.6 ± 1.4
	16 MHA	562.7	99.72	0.187	-49.2 ± 0
	mPEG	544.8	82.5	0.177	-48.0 ± 0.8
	PCOOH	554.1	96.24	0.178	-37.4 ± 1.4
	2N8M	557.3	93.96	0.153	-49.4 ± 1.8
	2N8C	552.2	86.81	0.155	-54.0 ± 0.3
100 nm	Citrate	583.3	122.7	0.131	-41.2 ± 0.3
	16 MHA	566.2	125.8	0.113	-46.0 ± 0.6
	mPEG	569.8	107.4	0.151	-40.0 ± 0.6
	PCOOH	559.8	110.5	0.163	-55.1 ± 1.2
	2N8M	572	110.2	0.163	-44.1 ± 0.1
	2N8C	587.0	123.0	0.143	-51.5 ± 1.5
150 nm	Citrate	546.4	153.5	0.193	-45.2 ± 2.8
	16 MHA	565.11	174.9	0.115	-47.8 ± 2.1
	mPEG	550.95	167	0.168	-30.5 ± 0.8
	PCOOH	550.79	169.9	0.281	-45.6 ± 1.6
	2N8M	554.26	175.1	0.139	-43.0 ± 2.0
	2N8C	554.71	154.8	0.218	-32 ± 0.8

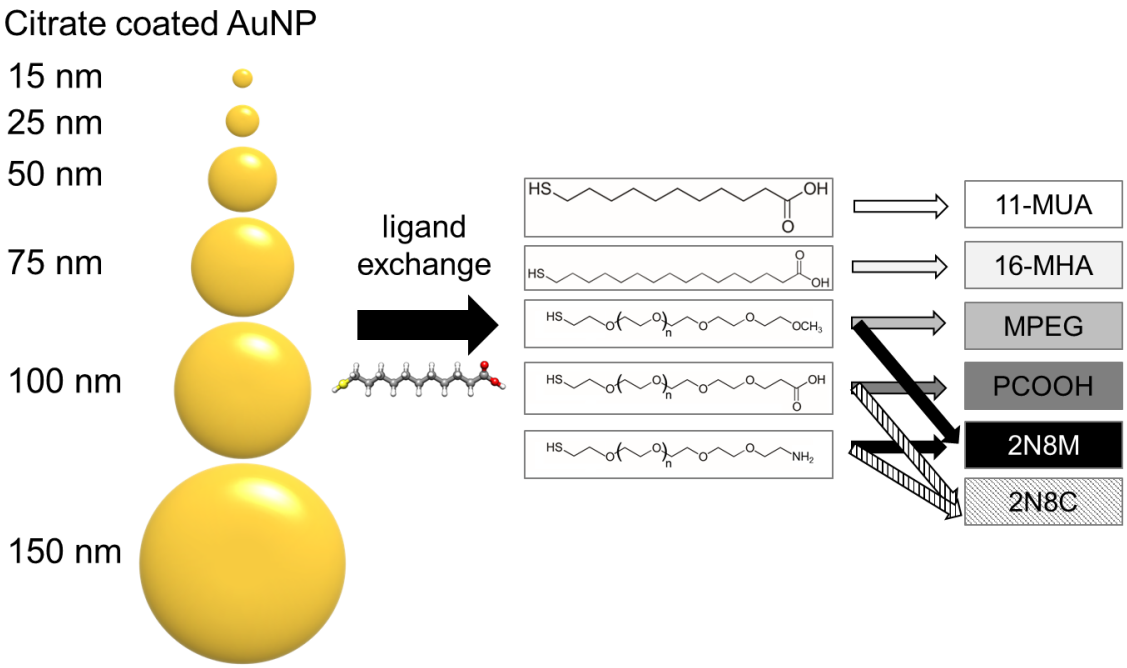

Figure 3.4 Schematic of gold ligand exchange.

Schematic depiction of the range of AuNP sizes used in this study and the chemical structures of the ligands used as coatings. PEG-amine coatings were mixed in 1:4 ratios with MPEG and PCOOH to provide particle stability. Ligands examined represent different functionalities and charges.

For this study, we sought to improve AuNP uptake by monocytes, therefore we investigated PEG coatings with charged distal end groups such as carboxylic acid (PCOOH) and PEG-amine. The bulky PEG coating should help to provide AuNP stability, while we hypothesized that the charged surfaces may increase cell uptake.[39] We found that 100% PEG-amine coated AuNP aggregated after 24 hours (data not shown). However, we found that AuNP coated with PEG-amine mixed in a 1:4 ratio with MPEG (2N8M) or with PCOOH (2N8C) were stable, and therefore were used in this

study. Characterization data for each AuNP core size coated are shown in Table 3.3. As the core diameter of the AuNP increases, the UV/Vis absorbance maxima increase in wavelength, in agreement with previously published results.[40] The surface potential of PCOOH coated particles for each size is highly negative as expected due to the carboxylic acid functional end group. Measurements of hydrodynamic diameters were larger than core diameters measured by TEM as expected due to the ligands attached to the nanoparticle surfaces. Large PDI values were seen for 25 nm formulations indicating some heterogeneity for these particles (Table 3.3). With the 11-MUA ligand, 50, 75, 100, and 150 nm particles were not stable and aggregated during ligand exchange (Figure 3.5) and therefore were not used in the study.

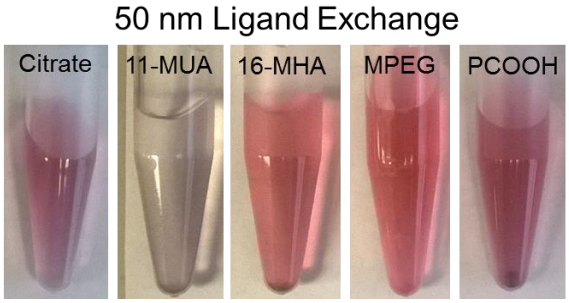

Figure 3.5 Stability of 50 nm AuNP after 24-hour incubation with various ligands. Aggregation seen for short carboxylic acid coated 50 nm AuNP as compared to other coatings

3.4.2 Cytotoxicity

As an initial screen for suitability for cell labeling purposes, the effect on cell viability of each AuNP formulation was examined. The cells were treated with AuNP for 24 hours at concentrations of 0.1, 0.5, and 1.0 mg Au/ml to examine the effect of each size and surface functionality over a large concentration range (Figure 3.6). The majority

of formulations studied in the 15-100 nm diameter range were found to be biocompatible for the concentrations tested. However, significant reductions in cell viability were observed for several 150 nm AuNP that had PEG-based coatings. For 150 nm PCOOH AuNP, significant ($p<0.05$) cytotoxicity was only observed at the highest concentration tested (1.0 mg Au/ml). In the case of 150 nm 2N8M AuNP, 0.5 and 1.0 mg Au/ml concentrations resulted in cell viability of approximately 60% but only 0.5 Au/ml was found to be statistically significant. Lastly, 150 nm 2N8C AuNP caused significant reductions in cell viability at all concentrations examined.

Formulations that did not cause adverse effects on cell viability were studied for their uptake by monocytes, as detailed in the next section. However, we found that some formulations aggregated under the conditions used for cell culture (i.e. 50 nm 2N8C, 75 nm 16-MHA, 75 nm 2N8C, 100 nm 16-MHA, 100 nm 2N8M, 100 nm 2N8C, 150 nm 16-MHA, 150 nm 2N8M and 150 nm 2N8C) likely due to a combination of particle instability and sedimentation. Since co-injection of free nanoparticles with labeled cells would result in erroneous conclusions in cell tracking experiments, these formulations were excluded from cell uptake experiments. Notably, this effect was seen in all citrate formulations regardless of size. This effect was also more common for larger size AuNP formulations such as 100 nm and 150 nm, for which only MPEG and PCOOH were found to be stable. This is likely due to the higher van der Waals interactions for these larger AuNP overcoming the steric/charge-based repulsion of the ligands. Additionally, formulations that resulted in toxicity at 0.5 mg/ml were excluded from uptake studies.

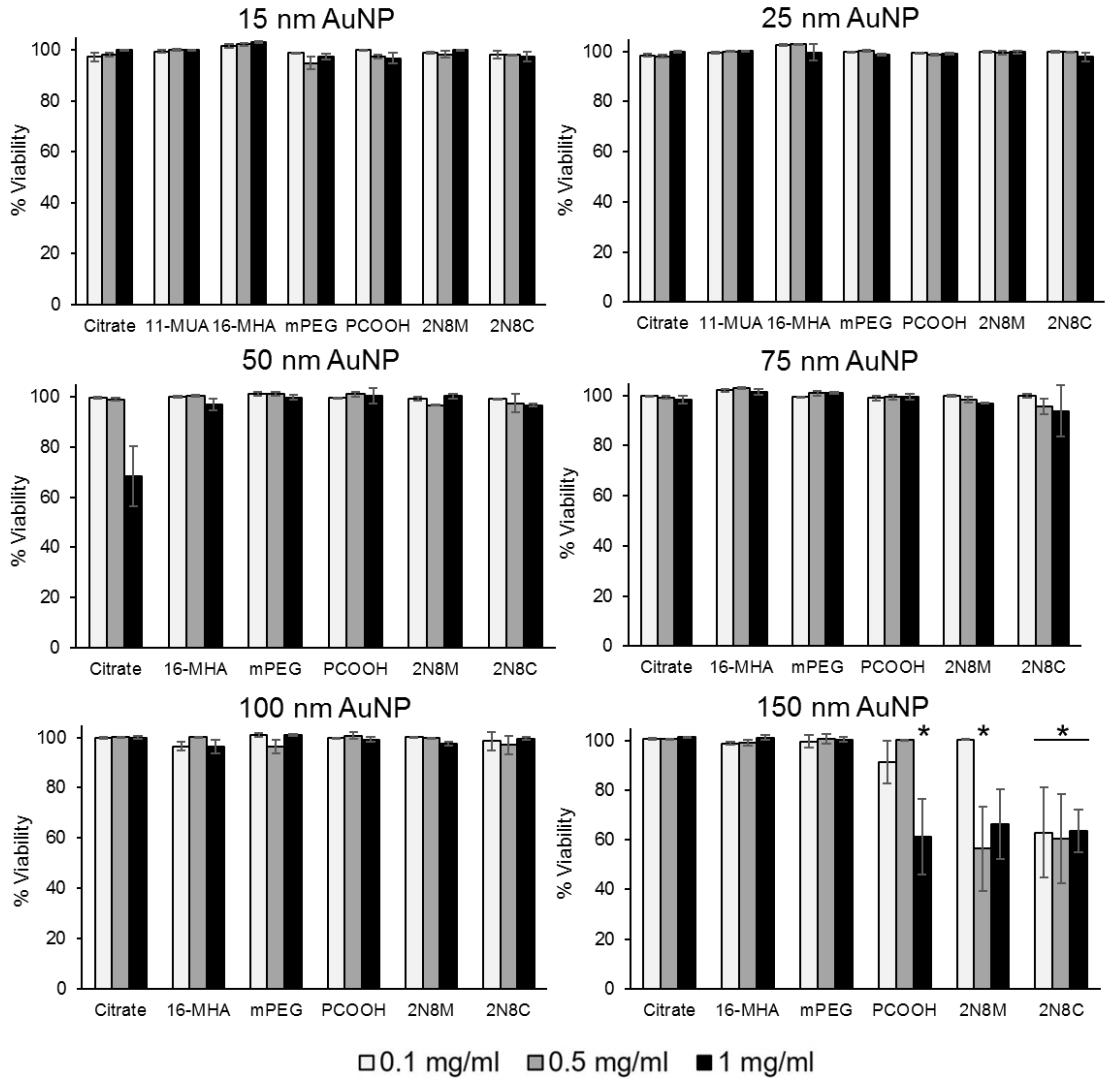

Figure 3.6 Cell viability with AuNP formulations.

Cell viability of monocytes incubated with AuNP of a range of diameters and coatings. Cells were incubated with AuNP for 24 hours at 0.1, 0.5, 1.0 mg Au/ml. Viability was assessed with the LIVE/DEAD assay. Values are normalized to those for untreated monocytes. Values represent the mean of 3 replicates (n=3) and error bars represent standard error of mean. Significance for 150 nm AuNP was examined with one-way

ANOVA and post hoc Tukey pairwise comparisons. * indicates significance of treated groups compared to non-treated group ($p<0.05$).

3.4.3 AuNP uptake by monocytes

We first investigated the optimal incubation time to yield high AuNP uptake. Figure 3.7 shows the results of experiments where monocytes were incubated with 15 nm 11-MUA AuNP (0.5 mg Au/ml) for several different durations, ranging from 2 to 48 hours. From 2 to 24 hours, AuNP uptake in the cells increased with increasing time in addition to the number of cells rising. However, there was no significant difference ($p>0.05$) in gold uptake between 24 and 48-hour incubations suggesting that the maximum limit of AuNP uptake had been reached at 24 hours. Additionally, when the cells were incubated with these AuNP for 48 hours, fewer cells were present after culture than at 24 hours ($p<0.05$). From these data, we concluded that 24 hours was the best duration over which to incubate monocytes with AuNP for both maximum uptake and number of cells. We therefore used 24 hours incubation time in all subsequent experiments.

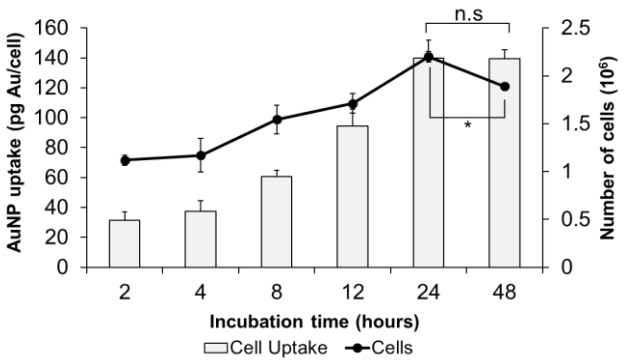

Figure 3.7 Optimization of AuNP incubation time.

Evaluation of gold content in monocytes incubated with 15 nm 11-MUA AuNP (0.5 mg Au/ml) for up to 48 hours. In addition, the total number cells at each time point is displayed. Values represent mean of 3 replicates (n=3) and error bars are standard error of mean. A one-way ANOVA was used to determine significance for both uptake and number of cells. Post-hoc Tukey pairwise comparison was used to compare significance between time points ($p<0.05$). Results for statistical comparisons between 24 and 48 hours shown only.

For the investigation of cell uptake, all sizes and formulations were incubated with monocytes at a concentration of 0.5 mg/ml for 24 hours. In Figure 3.8, a number of distinct relationships between size of nanoparticle and coating ligand on uptake can be observed. Particles coated with small molecule functionalized carboxylic acids (11-MUA and 16-MHA) show high uptake with smaller size particles between 15 nm and 50 nm. However, these ligands were increasingly unstable at larger sizes, preventing experimental measurements being acquired. MPEG AuNP exhibited low gold uptake in cells with slightly increasing values at larger sizes. We suspect this result was due to these larger AuNP settling in the cell culture media, resulting in increased cell contact

and uptake. Most notably, PCOOH AuNP exhibited a complex relationship between uptake and particle size. Minimal uptake was found at 15 and 25 nm while the highest uptake values were observed at 50 and 75 nm. Interestingly, cell uptake for 100 and 150 nm PCOOH AuNP was significantly less than for 50 and 75 nm AuNP. The uptake for 50, 75, and 100 nm PCOOH AuNP was found to be significantly different than all other coatings at that size ($p<0.05$). Similar uptake values for 150 nm PCOOH and MPEG AuNP suggests that for both these nanoparticles uptake may be largely due to particle settling (non-significant, $p>0.05$). Low uptake was observed for 15 and 25 nm 2N8C and were found to aggregate at 50 nm and above.

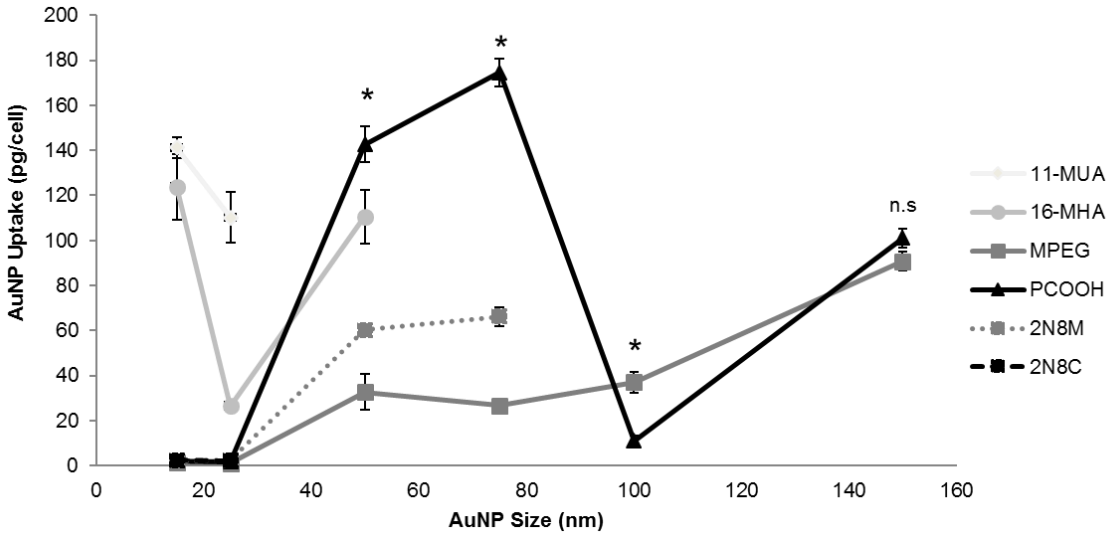

Figure 3.8 Uptake of gold nanoparticles in monocytes.

Gold uptake in monocytes incubated with AuNP of a variety of sizes and coatings. Formulations exhibiting particle instability (significant aggregation and sedimentation) or cytotoxicity were excluded from the study. The cells were treated for 24 hours at 0.5 mg Au/ml and evaluated for gold content with ICP-OES. Values represent mean of typically

six replicates (n=6) and error bars are standard error of mean. A two-way ANOVA was used to determine significance of AuNP uptake for size and coating. A Tukey pairwise mean comparison was used to determine significance between coatings at each size. * indicates significance of PCOOH compared to all other coatings at that size.

Monocytes incubated with selected AuNP formulations were additionally examined with TEM to observe the intra-cellular localization of AuNP. Cells were treated for 24 hours with 0.5 mg/ml of 15, 75, 100, and 150 nm PCOOH AuNP. The results in Figure 3.8 show AuNP aggregated into intercellular vesicles located in the cytoplasm of the monocytes. With monocytes, the uptake of AuNP is likely through phagocytosis with particles concentrated into lysosomes. Further investigation would be required to confirm the route of uptake, but other researchers have shown that the major route of uptake of nanoparticles in monocytes and macrophages is phagocytosis.[41-42] More AuNP were seen more frequently in 75 nm PCOOH AuNP treated monocytes as compared to other sizes, in agreement with the results observed from ICP-OES measurements (Figure 3.9).

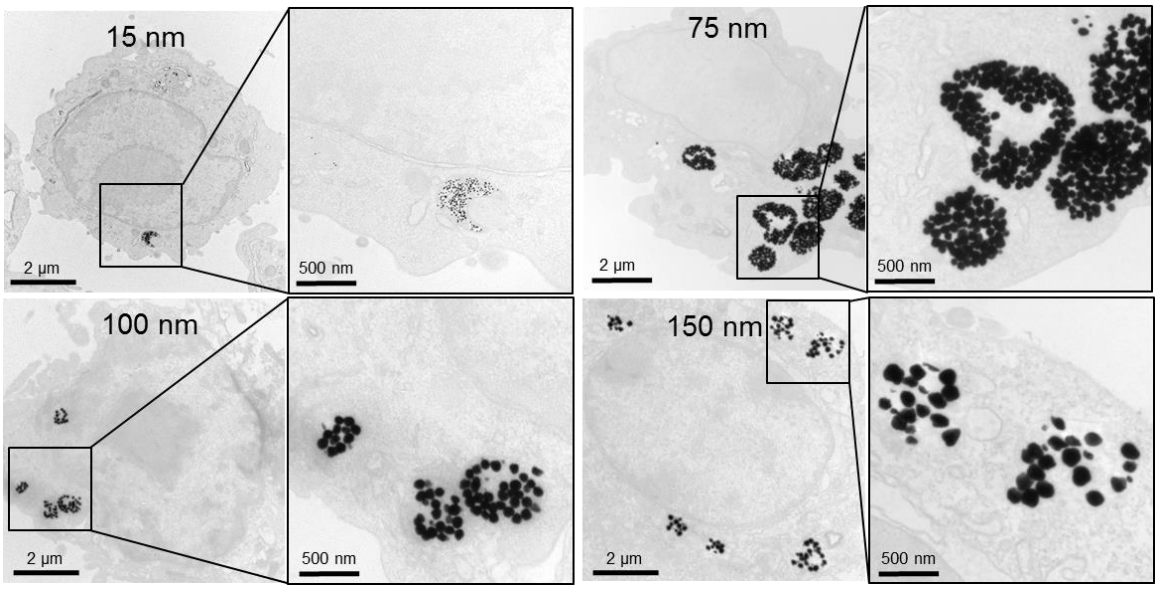

Figure 3.9 TEM of cells after treatment with AuNP.

TEM of monocytes treated with 15, 75, 100, and 150 nm PCOOH AuNP. Cells were treated at 0.5 mg/ml for 24 hours before being harvested and fixed for TEM.

3.4.4 CT imaging

To demonstrate the contrast generating properties of the AuNP taken up in monocytes, cells were scanned with a microCT scanner at 80 kVp. Monocytes were treated with 50, 75, 100 and 150 nm PCOOH AuNP for 24 hours at 0, 0.1, 0.25, and 0.5 mg/ml. Afterwards, cells were collected in 4% PFA and allowed to settle into loose pellets before scanning (Figure 3.10). Figure 3.10A shows CT scans of cells treated at increasing concentrations for 75 and 150 nm AuNP. The contrast generated from the AuNP increases as treatment concentration increases for these formulations. Quantitative analysis of the attenuation of these cell pellets is shown in Figure 3.10B, and revealed that the highest contrast enhancement arose for 50 and 75 nm AuNP. This

size dependent attenuation for the PCOOH AuNP closely matches the AuNP uptake results in Figure 3.8, signifying that the observed attenuation is due to the internalized AuNP. The change in attenuation was measured by normalizing to values obtained from untreated monocytes. A one-way ANOVA and post-hoc tukey pairwise mean comparison was used to determine significance between sizes at each concentration group. At each treatment concentration, the quantified attenuation was found to be significant between all sizes for PCOOH ($p<0.05$). To explore the relationship between gold uptake and CT attenuation, the attenuation of cell pellets (HU) was plotted against gold uptake (pg/cell). Figure 3.11 shows that there is a linear relationship ($R^2 = 0.89$) between attenuation and gold uptake.

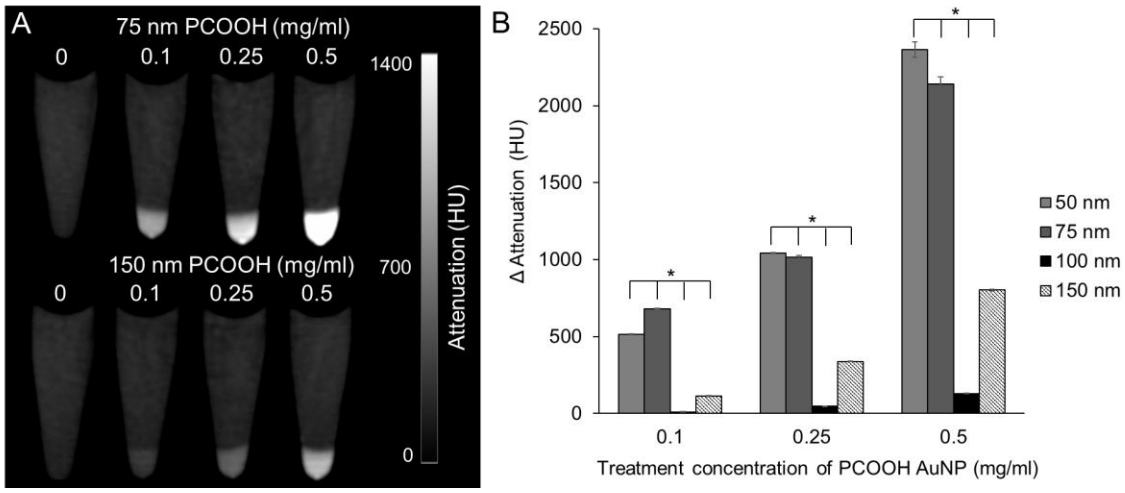

Figure 3.10 CT attenuation of monocytes labeled with AuNP of each size.

A) CT scans of monocytes settled into pellets after treatment with 75 and 150 nm PCOOH AuNP for 24 hours at 0, 0.1, 0.25 and 0.5 mg/ml. Cells were collected in 4% PFA solution after treatment. Scans performed on small animal microCT scanner with 100 µm spatial resolution at 80 kVP and 500 µA. (B) Quantification of attenuation in

Figure 3.10A of monocytes incubated with PCOOH AuNP of various sizes. Values normalized to untreated cells. Error bars are standard error of the mean with (n=3 for each data point). A one-way ANOVA and post-hoc Tukey pairwise mean comparison used to compare different sizes at each concentration group. * indicates significance between all sizes at that concentration ($p<0.05$).

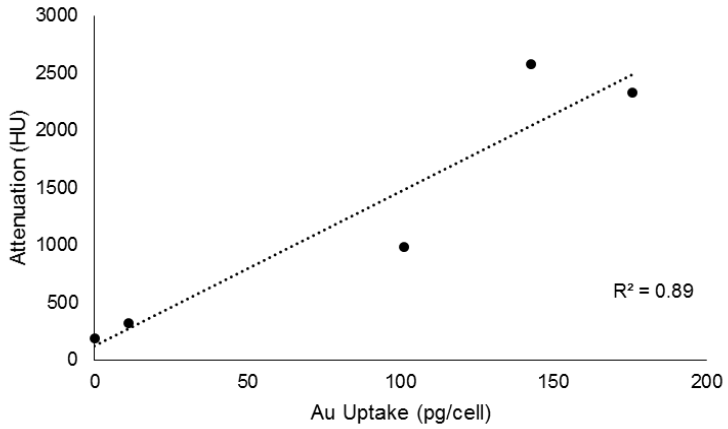

Figure 3.11 Correlation of uptake and attenuation for PCOOH AuNP**.**
Attenuation of cell pellets plotted against cell uptake for PCOOH coatings. Attenuation of untreated cell pellets used for zero uptake. The dotted line is the line of best fit for this data, assuming linearity.

3.5 Discussion

We studied a total of 44 AuNP formulations with a range of diameters and diverse capping ligands as potential labels for monocyte cell tracking. While the majority of the formulations studied did not affect cell viability, we observed that 150 nm AuNP with PEG-amine as part of the coating (2N8M, 2N8C) resulted in significant reductions in

cell viability (Figure 3.6). This toxicity is likely due to the presence of the positively charged amine groups in combination with increased AuNP-cell interactions due to these large nanoparticles settling in the cell culture media. Researchers have hypothesized that cytotoxicity from cationic surface coatings could be due to increased diffusion of nanoparticles through the cell membrane, disrupting the lipid bilayer.[43] Formation of protein coronas adsorbed onto the AuNP from the serum in the cell culture media during the incubation is also likely to play a role in their monocyte interactions.[44] The protein corona formed would be unique to each AuNP formulation and some speculate these adsorbed proteins are highly influential in the interactions between cells and nanoparticles.[45]

The small animal microCT scanner used in the study was limited to 80 kVp as the maximum x-ray tube voltage. At 80 kVp the photons produced are below the k-edge (80.7 keV) of Au. However, at 80 kVp, the attenuation difference between Au and tissue remains substantial, allowing for strong contrast in our study. With the higher voltages typically available on clinical scanners (100-140 kVp), we would likely see greater contrast between Au and controls than seen in this study.

In the uptake experiments, high uptake of AuNP was found with short carbon chain carboxylic acid ligands, consistent with those of others.[7, 46] It may be the case that upon incubation in serum, formation of protein coronas or aggregation of these AuNP with proteins cause changes in size. The resulting nanoparticles may be highly taken up by monocytes due to their size or due to settling. Future experiments will probe the structure of these nanoparticles in serum to answer these questions. For AuNP coated with these short carboxylic acid ligands, uptake was greater for 15 nm particles than 25 nm particles, however a size trend could not be discerned due to a lack of stability of

larger diameter AuNP with these coatings. 11-MUA particles were unstable during ligand exchange for particles larger than 25 nm, while 16-MHA coated were stable during synthesis but produced significant aggregation artifacts in uptake studies with particles larger than 50 nm (Figure 3.8). These results indicate that larger AuNP may require larger ligands for robust stability. For increased stability at larger AuNP diameters, we explored a variety of PEG-2000 ligands. PEG-2000 is well known to provide nanoparticle stability in serum as well as 'stealth' properties.[47] As expected, MPEG coated AuNP were taken up at low levels for all particle sizes, although slightly increased uptake was seen at the largest sizes, i.e. 100 and 150 nm (Figure 3.8). This uptake is likely a function of the increased settling rates for larger nanoparticles rather than due to the particle's surface properties. Due to the lack of uptake with methoxy-PEG coating, we explored PEG coating ligands that possessed carboxyl and amine functional groups at their distal ends.

PEG functionalized carboxylic acids coated particles (PCOOH) were stable for each diameter of AuNP studied. The monocyte uptake of AuNP coated with this ligand demonstrated a complex relationship with size (Figure 3.8). The highest gold uptake values were seen with 50 and 75 nm PCOOH AuNP. Other researchers have suggested 50 nm as optimal uptake size for AuNP in other cell lines.[48] For instance, Chithrani *et al.,* observed the highest accumulation for 50 nm citrate coated AuNP in HeLa cells after 24 hours.[49] While the data for PCOOH AuNP from our experiments are in agreement with these prior studies, maximal uptake for 50 nm AuNP was not common to all coatings, demonstrating that uptake is dependent on both size and surface functionality. The PCOOH ligand and citrate both expose carboxylic acid groups to the surrounding milieu

and may therefore form similar protein coronas around them, which may explain the similarity between our results and those of Chithrani *et al*.

Several studies have reported favorable nanoparticle uptake with amine based coatings.[50-51] Therefore for this study, we incorporated PEG-amine ligands into MPEG (2N8M) and PCOOH (2N8C) at a 1:4 ratio (AuNP coated with 100% PEG-amine were not stable). Low uptake values with both coatings at 15 and 25 nm suggest similar properties to MPEG and PCOOH coated AuNP. However, for larger core sizes only 50 and 75 nm 2N8M AuNP were found to be without stability issues, limiting the extent to which these coatings could be explored. The gold uptake values of 50 and 75 nm 2N8M AuNP are similar to those of MPEG of the same sizes, suggesting the observed behavior is dominated by the presence of MPEG and that the availability of the amine groups was limited. A higher ratio of PEG-amine to MPEG may be necessary to fully explore the effect of size with PEG-amine coated AuNP.

In CT imaging of cell pellets, the uptake of PCOOH coated AuNP resulted in large attenuation values, <2000 HU for the formulations with the highest uptake. These values are dependent on the amount of gold present in the volume of the cell pellet. For 75 nm PCOOH, we calculated the total mass of gold in the cell pellet from the cell uptake value (174.68 pg/cell) and the number of cells in the pellet (2.5 million) to be 0.44 mg. Since the volume of the pellet was 10 µL, we calculated the concentration of gold in the pellet to be 221.7 mM. The attenuation change relative to the concentration of gold was therefore approximately 9.65 HU/mM of Au. This attenuation per concentration of gold value is close to those reported previously in the literature when using similar CT scanners.[52]

For the purpose of labeling monocytes, similar values of gold uptake were seen with 15 nm 11-MUA, 50 nm PCOOH, and 75 nm PCOOH AuNP. Both types of coatings have functional carboxylic acid end groups with strong negative surface charge. Previous research has shown that anionic surface charges may lead to favorable protein corona formation for uptake by preferential binding of Apolipoprotein H (ApoH) compared to positively charged particles.[53] The increased presence of ApoH on nanoparticles showed increased uptake in human mesenchymal stem cells compared to other highly abundant proteins composing the corona. Considering synthetic efficiency, 15 nm AuNP are easier to produce on a large scale (performing seeded growth to form 50-75 nm AuNP adds another synthetic step which we have found challenging to scale up). The scalability of a synthesis is important feature for future translation, an issue that few studies have sought to address.[54] Additionally, the low cost of the 11-MUA ligand ($13.14/g, Sigma-Aldrich, St. Louis, MO) compared to the ligand PCOOH ($1400/g, Creative PEGworks, Chapel Hill, NC) reinforces the justification for use of 15 nm 11-MUA coated AuNP for future monocyte labeling studies.

3.6 Conclusion

In this study, we explored the effect of size and surface coating on AuNP biocompatibility and uptake in monocytes. We synthesized AuNP ranging in diameter from 15 to 150 nm and examined both short carbon chain ligands and PEG-2000 functionalized ligands. The majority of these formulations had no adverse effect on cell viability except 150 nm AuNP coated with charged PEG ligands. We found that small AuNP coated with short carboxylic acid ligands were taken up extensively. We also observed a complex effect of diameter for PCOOH coated AuNP, with high uptake

values at the intermediate sizes of 50 and 75 nm but lower uptake for smaller and larger diameters. Additionally, TEM and CT scans of monocytes incubated with these formulations showed similar patterns of high uptake for 50 and 75 nm PCOOH AuNP. Gold uptake values at 50 and 75 nm for PCOOH AuNP were similar to values seen for 15 nm 11-MUA particles. Therefore in the following chapter, we evaluate 15 nm gold nanoparticles as an effective monocyte label and track these labeled cells in a mouse model of atherosclerosis.

3.7 References

1. Zhang, L. J.; Wu, S. Y.; Wang, J.; Lu, Y.; Zhang, Z. L.; Jiang, S. S.; Zhou, C. S.; Lu, G. M., Diagnostic accuracy of dual-source CT coronary angiography: The effect of average heart rate, heart rate variability, and calcium score in a clinical perspective. *Acta Radiol* **2010,** *51* (7), 727-740.

2. Cademartiri, F.; Maffei, E.; Palumbo, A. A.; Malago, R.; La Grutta, L.; Meijboom, W. B.; Aldrovandi, A.; Fusaro, M.; Vignali, L.; Menozzi, A., et al., Influence of intra-coronary enhancement on diagnostic accuracy with 64-slice CT coronary angiography. *Eur Radiol* **2008,** *18* (3), 576-583.

3. Passlick, B.; Flieger, D.; Ziegler-Heitbrock, H. W., Identification and characterization of a novel monocyte subpopulation in human peripheral blood. *Blood* **1989,** *74* (7), 2527-2534.

4. Piccini, D.; Littmann, A.; Nielles-Vallespin, S.; Zenge, M. O., Respiratory self-navigation for whole-heart bright-blood coronary MRI: methods for robust isolation and automatic segmentation of the blood pool. *Magn Reson Med* **2012,** *68* (2), 571-579.

5. Heit, B.; Jones, G.; Knight, D.; Antony, J. M.; Gill, M. J.; Brown, C.; Power, C.; Kubes, P., HIV and other lentiviral infections cause defects in neutrophil chemotaxis, recruitment, and cell structure: immunorestorative effects of granulocyte-macrophage colony-stimulating factor. *J Immunol* **2006,** *177* (9), 6405-6414.

6. Meir, R.; Shamalov, K.; Betzer, O.; Motiei, M.; Horovitz-Fried, M.; Yehuda, R.; Popovtzer, A.; Popovtzer, R.; Cohen, C. J., Nanomedicine for Cancer Immunotherapy: Tracking Cancer-Specific T-Cells in Vivo with Gold Nanoparticles and CT Imaging. *ACS Nano* **2015,** *9* (6), 6363-6372.

7. Ahrens, E. T.; Bulte, J. W., Tracking immune cells in vivo using magnetic resonance imaging. *Nat Rev Immunol* **2013,** *13* (10), 755-763.

8. Gerrity, R. G., The role of the monocyte in atherogenesis: II. Migration of foam cells from atherosclerotic lesions. *Am J Pathol* **1981,** *103* (2), 191-200.

9. Miller, C. D.; Litt, H. I.; Askew, K.; Entrikin, D.; Carr, J. J.; Chang, A. M.; Kilkenny, J.; Weisenthal, B.; Hollander, J. E., Implications of 25% to 50% coronary stenosis with cardiac computed tomographic angiography in ED patients. *Am J Emerg Med* **2012,** *30* (4), 597-605.

10. Naha, P. C.; Lau, K. C.; Hsu, J. C.; Hajfathalian, M.; Mian, S.; Chhour, P.; Uppuluri, L.; McDonald, E. S.; Maidment, A. D.; Cormode, D. P., Gold silver alloy nanoparticles (GSAN): an imaging probe for breast cancer screening with dual-energy mammography or computed tomography. *Nanoscale* **2016,** *8* (28), 13740-13754.

11. Astolfo, A.; Schultke, E.; Menk, R. H.; Kirch, R. D.; Juurlink, B. H.; Hall, C.; Harsan, L. A.; Stebel, M.; Barbetta, D.; Tromba, G., et al., In vivo visualization of gold-loaded cells in mice using x-ray computed tomography. *Nanomedicine* **2013,** *9* (2), 284-292.

12. Meir, R.; Motiei, M.; Popovtzer, R., Gold nanoparticles for in vivo cell tracking. *Nanomedicine (Lond)* **2014,** *9* (13), 2059-2069.

13. Chhour, P.; Naha, P. C.; O'Neill, S. M.; Litt, H. I.; Reilly, M. P.; Ferrari, V. A.; Cormode, D. P., Labeling monocytes with gold nanoparticles to track their recruitment in atherosclerosis with computed tomography. *Biomaterials* **2016,** *87*, 93-103.

14. Cormode, D. P.; Naha, P. C.; Fayad, Z. A., Nanoparticle contrast agents for computed tomography: a focus on micelles. *Contrast Media Mol Imaging* **2014,** *9* (1), 37-52.

15. Bardo, D. M.; Brown, P., Cardiac multidetector computed tomography: basic physics of image acquisition and clinical applications. *Curr Cardiol Rev* **2008,** *4* (3), 231-243.

16. Chang, A. M.; Ginty, C. T.; Litt, H. I.; Hollander, J. E., Coronary artery disease progression in patients without significant stenosis on coronary computed tomographic angiography. *Am J Emerg Med* **2012,** *30* (9), 2015-2020.

17. Betzer, O.; Shwartz, A.; Motiei, M.; Kazimirsky, G.; Gispan, I.; Damti, E.; Brodie, C.; Yadid, G.; Popovtzer, R., Nanoparticle-based CT imaging technique for longitudinal and quantitative stem cell tracking within the brain: application in neuropsychiatric disorders. *ACS Nano* **2014,** *8* (9), 9274-9285.

18. Astolfo, A.; Arfelli, F.; Schultke, E.; James, S.; Mancini, L.; Menk, R. H., A detailed study of gold-nanoparticle loaded cells using X-ray based techniques for cell-tracking applications with single-cell sensitivity. *Nanoscale* **2013,** *5* (8), 3337-3345.

19. Schultke, E.; Menk, R.; Pinzer, B.; Astolfo, A.; Stampanoni, M.; Arfelli, F.; Harsan, L. A.; Nikkhah, G., Single-cell resolution in high-resolution synchrotron X-ray CT imaging with gold nanoparticles. *J Synchrotron Radiat* **2014,** *21* (Pt 1), 242-250.

20. Cormode, D. P.; Roessl, E.; Thran, A.; Skajaa, T.; Gordon, R. E.; Schlomka, J. P.; Fuster, V.; Fisher, E. A.; Mulder, W. J.; Proksa, R., et al., Atherosclerotic plaque composition: analysis with multicolor CT and targeted gold nanoparticles. *Radiology* **2010,** *256* (3), 774-782.

21. Au, J. T.; Craig, G.; Longo, V.; Zanzonico, P.; Mason, M.; Fong, Y.; Allen, P. J., Gold nanoparticles provide bright long-lasting vascular contrast for CT imaging. *AJR Am J Roentgenol* **2013,** *200* (6), 1347-1351.

22. Lee, N.; Choi, S. H.; Hyeon, T., Nano-sized CT contrast agents. *Adv Mater* **2013,** *25* (19), 2641-2660.

23. Albanese, A.; Tang, P. S.; Chan, W. C., The effect of nanoparticle size, shape, and surface chemistry on biological systems. *Annu Rev Biomed Eng* **2012,** *14*, 1-16.

24. Mieszawska, A. J.; Mulder, W. J.; Fayad, Z. A.; Cormode, D. P., Multifunctional gold nanoparticles for diagnosis and therapy of disease. *Mol Pharm* **2013,** *10* (3), 831-847.

25. Coradeghini, R.; Gioria, S.; Garcia, C. P.; Nativo, P.; Franchini, F.; Gilliland, D.; Ponti, J.; Rossi, F., Size-dependent toxicity and cell interaction mechanisms of gold nanoparticles on mouse fibroblasts. *Toxicol Lett* **2013,** *217* (3), 205-216.

26. Naha, P. C.; Chhour, P.; Cormode, D. P., Systematic in vitro toxicological screening of gold nanoparticles designed for nanomedicine applications. *Toxicol In Vitro* **2015,** *29* (7), 1445-1453.

27. Cai, H.; Yao, P., Gold nanoparticles with different amino acid surfaces: Serum albumin adsorption, intracellular uptake and cytotoxicity. *Colloids Surf B Biointerfaces* **2014,** *123*, 900-906.

28. Menke, J.; Kowalski, J., Diagnostic accuracy and utility of coronary CT angiography with consideration of unevaluable results: A systematic review and multivariate Bayesian random-effects meta-analysis with intention to diagnose. *Eur Radiol* **2016,** *26* (2), 451-458.

29. Robbins, C. S.; Hilgendorf, I.; Weber, G. F.; Theurl, I.; Iwamoto, Y.; Figueiredo, J. L.; Gorbatov, R.; Sukhova, G. K.; Gerhardt, L. M.; Smyth, D., et al., Local proliferation dominates lesional macrophage accumulation in atherosclerosis. *Nat Med* **2013,** *19* (9), 1166-1172.

30. Swirski, F. K.; Libby, P.; Aikawa, E.; Alcaide, P.; Luscinskas, F. W.; Weissleder, R.; Pittet, M. J., Ly-6Chi monocytes dominate hypercholesterolemia-associated monocytosis and give rise to macrophages in atheromata. *J Clin Invest* **2007,** *117* (1), 195-205.

31. Swirski, F. K.; Pittet, M. J.; Kircher, M. F.; Aikawa, E.; Jaffer, F. A.; Libby, P.; Weissleder, R., Monocyte accumulation in mouse atherogenesis is progressive and proportional to extent of disease. *Proc Natl Acad Sci U S A* **2006,** *103* (27), 10340-10345.

32. Gorenoi, V.; Schonermark, M. P.; Hagen, A., CT coronary angiography vs. invasive coronary angiography in CHD. *GMS Health Technol Assess* **2012,** *8*, Doc02.

33. Frens, G., Controlled nucleation for the regulation of the particle size in monodisperse gold suspensions. *Nat Phys Sci* **1973,** (241), 22-22.

34. Turkevich, J.; Stevenson, P.; Hillier, J., A study of the nucleation and growth processes in the synthesis of colloidal gold. *Discuss. Faraday Soc.* **1951,** *11*, 55-75.

35. Perrault, S. D.; Chan, W. C., Synthesis and surface modification of highly monodispersed, spherical gold nanoparticles of 50-200 nm. *J Am Chem Soc* **2009,** *131* (47), 17042-17043.

36. Takaoka, H.; Funabashi, N.; Uehara, M.; Fujimoto, Y.; Kobayashi, Y., Diagnostic accuracy of coronary 320 slice CT angiography using retrospective electrocardiogram gated acquisition compared with virtual prospective electrocardiogram gated acquisition with and without padding. *Int J Cardiol* **2013,** *168* (3), 2811-2815.

37. Simpson, C. A.; Agrawal, A. C.; Balinski, A.; Harkness, K. M.; Cliffel, D. E., Short-chain PEG mixed monolayer protected gold clusters increase clearance and red blood cell counts. *ACS Nano* **2011,** *5* (5), 3577-3584.

38. Kim, D.; Park, S.; Lee, J. H.; Jeong, Y. Y.; Jon, S., Antibiofouling polymer-coated gold nanoparticles as a contrast agent for in vivo X-ray computed tomography imaging. *J Am Chem Soc* **2007,** *129* (24), 7661-7665.

39. Neefjes, L. A.; Rossi, A.; Genders, T. S.; Nieman, K.; Papadopoulou, S. L.; Dharampal, A. S.; Schultz, C. J.; Weustink, A. C.; Dijkshoorn, M. L.; Ten Kate, G. J., et al., Diagnostic accuracy of 128-slice dual-source CT coronary angiography: a randomized comparison of different acquisition protocols. *Eur Radiol* **2013,** *23* (3), 614-622.

40. Renker, M.; Geyer, L. L.; Krazinski, A. W.; Silverman, J. R.; Ebersberger, U.; Schoepf, U. J., Iterative image reconstruction: a realistic dose-saving method in cardiac CT imaging? *Expert Rev Cardiovasc Ther* **2013,** *11* (4), 403-409.

41. Ma, X.; Wu, Y.; Jin, S.; Tian, Y.; Zhang, X.; Zhao, Y.; Yu, L.; Liang, X. J., Gold nanoparticles induce autophagosome accumulation through size-dependent nanoparticle uptake and lysosome impairment. *ACS Nano* **2011,** *5* (11), 8629-8639.

42. Juurlink, B. H.; Devon, R. M., Colloidal gold as a permanent marker of cells. *Experientia* **1991,** *47* (1), 75-77.

43. Goodman, C. M.; McCusker, C. D.; Yilmaz, T.; Rotello, V. M., Toxicity of gold nanoparticles functionalized with cationic and anionic side chains. *Bioconjug Chem* **2004,** *15* (4), 897-900.

44. Nakazato, R.; Arsanjani, R.; Shalev, A.; Leipsic, J. A.; Gransar, H.; Lin, F. Y.; Gomez, M.; Berman, D. S.; Min, J. K., Diagnostic Accuracy, Image Quality, and Patient Comfort for Coronary CT Angiography Performed Using Iso-Osmolar versus Low-Osmolar Iodinated Contrast: A Prospective International Multicenter Randomized Controlled Trial. *Acad Radiol* **2016,** *23* (6), 743-751.

45. Chithrani, B. D.; Chan, W. C., Elucidating the mechanism of cellular uptake and removal of protein-coated gold nanoparticles of different sizes and shapes. *Nano Lett* **2007,** *7* (6), 1542-1550.

46. Cho, Y. J.; Schoepf, U. J.; Silverman, J. R.; Krazinski, A. W.; Canstein, C.; Deak, Z.; Grimm, J.; Geyer, L. L., Iterative image reconstruction techniques: cardiothoracic computed tomography applications. *J Thorac Imaging* **2014,** *29* (4), 198-208.

47. Jokerst, J. V.; Lobovkina, T.; Zare, R. N.; Gambhir, S. S., Nanoparticle PEGylation for imaging and therapy. *Nanomedicine (Lond)* **2011,** *6* (4), 715-728.

48. Iyengar, S. S.; Morgan-Hughes, G.; Ukoumunne, O.; Clayton, B.; Davies, E. J.; Nikolaou, V.; Hyde, C. J.; Shore, A. C.; Roobottom, C. A., Diagnostic accuracy of high-definition CT coronary angiography in high-risk patients. *Clin Radiol* **2016,** *71* (2), 151-158.

49. Chithrani, B. D.; Ghazani, A. A.; Chan, W. C., Determining the size and shape dependence of gold nanoparticle uptake into mammalian cells. *Nano Lett* **2006,** *6* (4), 662-668.

50. Agudelo, C. A.; Tachibana, Y.; Hurtado, A. F.; Ose, T.; Iida, H.; Yamaoka, T., The use of magnetic resonance cell tracking to monitor endothelial progenitor cells in a rat hindlimb ischemic model. *Biomaterials* **2012,** *33* (8), 2439-2448.

51. Goldbergova, M. P.; Parenica, J.; Jarkovsky, J.; Kala, P.; Poloczek, M.; Manousek, J.; Kluz, K.; Kubkova, L.; Littnerova, S.; Tesak, M., et al., The association between levels of tissue inhibitor of metalloproteinase-1 with acute heart failure and left ventricular dysfunction in patients with ST elevation myocardial infarction treated by primary percutaneous coronary intervention. *Genet Test Mol Biomarkers* **2012,** *16* (10), 1172-1178.

52. Hofmann, M.; Wollert, K. C.; Meyer, G. P.; Menke, A.; Arseniev, L.; Hertenstein, B.; Ganser, A.; Knapp, W. H.; Drexler, H., Monitoring of bone marrow cell homing into the infarcted human myocardium. *Circulation* **2005,** *111* (17), 2198-2202.

53. Ritz, S.; Schottler, S.; Kotman, N.; Baier, G.; Musyanovych, A.; Kuharev, J.; Landfester, K.; Schild, H.; Jahn, O.; Tenzer, S., et al., Protein corona of nanoparticles: distinct proteins regulate the cellular uptake. *Biomacromolecules* **2015,** *16* (4), 1311-1321.

54. Kim, Y. J.; Huh, Y. M.; Choe, K. O.; Choi, B. W.; Choi, E. J.; Jang, Y.; Lee, J. M.; Suh, J. S., In vivo magnetic resonance imaging of injected mesenchymal stem cells in rat myocardial infarction; simultaneous cell tracking and left ventricular function measurement. *Int J Cardiovasc Imaging* **2009,** *25 Suppl 1*, 99-109.

Chapter 4: Labeling of monocytes for CT cell tracking to atherosclerotic plaques

4.1 Abstract

Monocytes are actively recruited from the circulation into developing atherosclerotic plaques. In the plaque, monocytes differentiate into macrophages and eventually form foam cells. Continued accumulation of foam cells can lead to plaque rupture and subsequent myocardial infarction. X-ray computed tomography (CT) is the best modality to image the coronary arteries non-invasively, therefore we have sought to track the accumulation of monocytes into atherosclerotic plaques using CT. Gold nanoparticles were synthesized and stabilized with a variety of ligands. Selected formulations were incubated with an immortalized monocyte cell line *in vitro* and evaluated for cytotoxicity, effects on cytokine release, and cell uptake. These data identified a lead formulation, 11-MUA capped gold nanoparticles, to test for labeling primary monocytes. The formulation did not the affect the viability or cytokine release of primary monocytes and was highly taken up by these cells. Gold labeled primary monocytes were injected into apolipoprotein E deficient mice kept on Western diet for 10 weeks. Imaging was done with a microCT scanner. A significant increase in attenuation was measured in the aorta of mice receiving the gold labeled cells as compared to control animals. Following the experiment, the biodistribution of gold was evaluated in major organs. Additionally, plaques were sectioned and examined with electron microscopy. The results showed that gold nanoparticles were present inside monocytes located within plaques. This study demonstrates the feasibility of using gold

nanoparticles as effective cell labeling contrast agents for non-invasive imaging of monocyte accumulation within plaques with CT.

4.2 Introduction

Cardiovascular disease is the leading cause of death in the United States, accounting for 1 in every 3 deaths.[1] The majority of these deaths arise from the development of atherosclerosis in the coronary arteries, where rupture of vulnerable plaques can potentially lead to thrombus formation and myocardial infarction. Over the last decade, the role of inflammation in atherosclerosis has become a prominent point of study in progression of the disease.[2]

After the initial development of inflammation in the arterial wall, monocytes are actively recruited from the circulation into the arterial wall. In the intima, monocytes differentiate into macrophages and eventually foam cells after engulfing low density lipoproteins (LDL).[3] These foam cells release cytokines and enzymes that lead to growth and destabilization of the plaque over time.[4] Continued recruitment of monocytes and subsequent accumulation of foam cells increase the likelihood of plaque rupture and clinical manifestations of atherosclerosis. Monocyte recruitment is a possible drug target for atherosclerosis regulation.[5] Studies have found that targeting the chemokine receptors on monocytes reduces overall plaque progression.[6-8] The accumulation of monocytes has been found to correlate to the progression and severity of atherosclerosis.[9] These studies typically involve destructive processes to analyze monocyte population in plaques preventing the study of multiple time points in the same animal. With non-invasive detection, monocyte accumulation can be rapidly assessed, informing the direction of the study before its end. This information can be revealing in clinical trials, where imaging may demonstrate the effectiveness or lack of effectiveness of drug therapies without invasive measures or waiting for patient mortality outcomes.[10]

CT is one of the best and most frequently used modalities to image the coronary arteries non-invasively in patients.[11] Modern CT scanners allow for fast, high resolution image acquisition, reducing common cardiac and respiratory motion artifacts when imaging the coronary arteries.[12] With increasing interest in cell imaging, the use of x-ray CT is an emerging modality in cell tracking applications. Astolfo *et al.* and Menk *et al.* performed detailed analysis of gold nanoparticle uptake in cells, as well in vivo detection and proliferation of gold labeled tumor cells in rat brain tumor models.[13-14] Moreover, recent studies utilizing synchrotron radiation sources for x-rays, have been able image gold nanoparticle labeled cells with single cell resolution in *ex vivo* and *in vitro* samples.[15-16] Of the few studies regarding monocyte tracking, SPECT and MRI modalities were used.[17-18] SPECT and MRI face challenges due to chest and heart motion when imaging the coronary arteries.[19] Therefore, we sought to develop a technique to monitor the monocyte accumulation in atherosclerotic plaques non-invasively through computed tomography.

Gold nanoparticles (AuNP) have been explored for biomedical applications due to the synthetic control over size, shape and coating, their high biocompatibility and their unique physical properties.[20] This allows the development of AuNP that have specific properties tailored for given biomedical applications. For instance, the addition of poly(ethylene glycol) (PEG) coatings to particles can be used to increase *in vivo* circulation time by avoiding uptake by cells of the reticuloendothelial system.[21] AuNP are popular as experimental CT contrast agents, as they attenuate x-rays strongly, as well as the afore-mentioned characteristics of biocompatibility and control over size and surface functionality.[22-24] AuNP have been shown to be effective as both blood pool and targeted contrast agents for CT.[25-28]

In this study, we demonstrate the use of AuNP to label monocytes and track their migration into atherosclerotic plaques non-invasively using CT. We synthesized AuNP 15 nm in diameter and performed ligand exchange with a variety of ligands to create a library of AuNP. These particles were characterized with dynamic light scattering (DLS), zeta potential, and transmission electron microscopy (TEM). After characterization, AuNP were evaluated *in vitro* for the effects on cytotoxicity, cytokine production, and cell uptake with monocytes. A lead formulation was then evaluated *in vitro* with primary monocytes isolated from spleens. Lastly, atherosclerotic mice were injected with AuNP labeled monocytes and scanned with CT before injection and days 3, 4, and 5 post injection. The CT scans were analyzed for intensity. Aortic plaques were excised and examined with TEM for the presence of gold labeled monocytes.

4.3 Materials and methods

4.3.1 Materials

All chemicals were of analytical grade and were purchased from Sigma Aldrich (St. Louis, MO). A monocyte cell line, RAW 264.7, was purchased from ATCC (Manassas, VA). Dubecco's Modified Eagle Medium (DMEM) and RPMI-1640 supplemented with 10% fetal bovine serum and 1% penicillin/streptomycin (10000 units/Ml, 10000 µg/mL) were purchased from Cellgro, Corning (Manassas, VA). LIVE/DEAD assay and ELISA kits were purchased from Life Technologies Invitrogen (Grand Island, NY). All mice were acquired from Jackson Laboratory, Bar Harbor, ME.

4.3.2 Gold synthesis

Citrate capped gold nanoparticles were synthesized using the Turkevich method.[29] Briefly, 85 mg of gold(III) chloride hydrate was dissolved in 250 mL of ultrapure water (Milli-Q, EMD Millipore, Billerica MA). The gold solution was heated to a boil. 25 mL of a 38.8 mM sodium citrate solution was then added, producing citrate coated gold nanoparticles. The solution was refluxed for 15 minutes and allowed to cool to room temperature. For ligand exchange, capping ligands were added to the solution for a final concentration of 0.047 mM in the gold solution. For instance, 2.6 mg of 11-mercaptoundecanoic acid (MW 218.36) was dissolved in 1 ml of ethanol and added into the gold solution to stir overnight. The full library of ligands examined can be found in Figure 4.1. After exchange, the particles were spun at 8.5 krcf for 3 hours to pellet the particles. The pellets were collected into 1.5 ml micro-centrifuge tubes and washed twice with ultrapure water by centrifuging at 8.5 krcf for 45 minutes. The AuNP were then filtered through a 0.45 μm syringe filter (EMD Millipore, Billerica MA) in a biosafety cabinet for sterilization.

Ligands	Structure	Stability	Ligands	Structure	Stability
11-mercaptoundecanoic acid	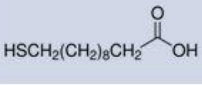	Y 	Poly(ethyleneimine)	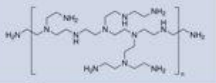	Y 
Meso-2,3-Dimercaptosuccinic acid	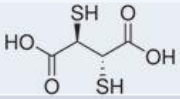	N 	Poly L-lysine	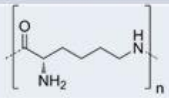	N 
Cystamine	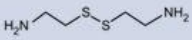	N 	11-mercaptoundecyl-tetra(ethylene glycol)		Y 
Cysteine	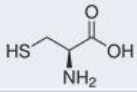	N 	11-amino-1-undecanethiol hydrochloride	$HSCH_2(CH_2)_9CH_2NH_2$ • HCl	N 
4-mercapto-1-butanol		Y 	6-mercaptohexanoic acid	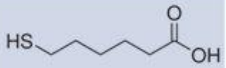	N 
3-mercaptopropionic acid	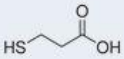	N 	16-mercaptohexadecanoic acid	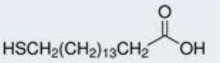	Y 
Poly(ethylene glycol) methyl ether thiol 1kDa	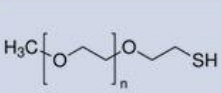	Y 	11-mercapto-1-undecanol	$HSCH_2(CH_2)_9CH_2OH$	N 
Spermine tetrahydrochloride	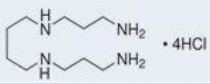	N 	2-mercaptoethanol	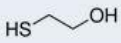	Y 
Poly(bis(4-carboxyphenoxy) phosphazene disodium	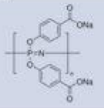	N 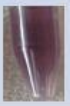			

Figure 4.1 Library of capping ligands.

Ligand library explored for AuNP stability. Chemical structures and stability determination shown for each ligand.

4.3.3 Particle characterization

For electron microscopy, AuNP samples were drop casted onto Formvar carbon copper grids with 200 mesh (Electron Microscopy Sciences, Hatfield, PA). Samples were exposed to air for 30 mins and excess solution was blotted away with filter paper. The

grids were viewed with an FEI Tecnai T12 electron microscope at 120 kV. Dynamic light scattering and zeta potential analysis was performed with a Nano ZS-90 Zetasizer. Stability was tested by diluting 10 µL sample of AuNP into 1 mL of DPBS and 1 mL of cell media.

4.3.4 In vitro viability assessment

The interaction of stable AuNP formulations with monocytes was evaluated using RAW 264.7 and isolated primary monocytes. The LIVE/DEAD assay was used to assess cytotoxicity. Briefly, RAW 264.7 cells were cultured in 20 mm diameter glass bottom dishes at 7.0 x 10^5 cells per well with DMEM supplemented with 10% FBS and 1% penicillin/streptomycin (PS). After 24 hours of incubation, monocytes were treated with AuNP formulations for an additional 24 hours. After treatment, cells were washed 2x with DPBS and incubated with 400 µL of LIVE/DEAD cocktail (2 ml DPBS, 2 µL stock Ethidium-1 homodimer, 0.5 µL stock Calcein AM and 0.5 µL 3.2 mM Hoechst 33342). Primary isolated monocytes were prepared similarly but cultured using RPMI-1640 supplemented with 10% FBS and 1% PS. Cells were imaged with Nikon Eclipse Ti-U fluorescence microscope using DAPI (Ex: 359, Em: 461 nm), FITC (Ex: 495, Em: 519 nm), and Texas Red (Ex: 595, Em: 613 nm) filters. Four images were taken per well for each channel. A custom MATLAB (MathWorks, Natick, MA) program was used to count the number of cells for the Hoechst, Ethidium-1 homodimer, and Calcein AM stain for each sample. The ratio of living cells to total number of cells was used to determine the viability percentage.

4.3.5 In vitro cytokine expression

Monocyte cytokine expression of TNF-α and lL-6 was evaluated using an ELISA kit from Life Technologies, (Frederick, MD). First, monocytes were cultured in 96 well plates at 1.0 x 10^5 cells per well for 24 hours. Immortalized monocytes were then treated with 0.5 mg/ml of various AuNP formulations for 24 hours (note: all nanoparticle concentrations are given as mg/ml of gold). Primary monocytes were treated with concentrations of 0.1, 0.25, and 0.5 mg/ml of 11-MUA AuNP. The cells were then washed twice with DPBS to remove remaining free AuNP. Afterwards cell media in each well was replaced with 100 µL of cell media containing 100 ng/mL of lipopolysaccharides (LPS) for 3 hours or replaced with new media for non-activated samples. The media was then collected for use in the ELISA, which was performed according to kit instructions.

4.3.6 Cell uptake evaluation

The uptake of AuNP was measured using both a direct method (analytical determination of gold content) and an indirect method (CT imaging of cell pellets). For both methods, cells were cultured onto 6-well plates at 2.0 x 10^6 cells per well for 24 hours. The cells were treated with varying concentrations of AuNP formulations for 24 hours. The cells were then washed twice with DPBS and collected. For direct measurements, the cells were dissolved in aqua regia (3 parts hydrochloric acid, 1 part nitric acid) for 15 mins. The gold content of these samples were measured using inductively coupled plasma-optical emission spectroscopy (ICP-OES) on a Spectro Genesis ICP (SPECTRO Analytical Instruments GmbH, Boschstr, Germany). Gold content was normalized by the number of cells in each sample to express the value as gold per cell.

For CT measurements, after AuNP treatment, the cells were collected and fixed in 4% paraformaldehyde. The cells were allowed to loosely settle and then scanned using a clinical CT scanner (Siemens Definition DS 64-slice) at 100 kVp, 440 mA, 512x512 matrix, 37x37 cm FoV, a slice thickness of 0.6 cm and reconstructed using kernel B30f. Intensities in the scan were measured in 3 sequential sections using ROI measurements and averaged for an intensity measurement using OsiriX v.3.7.1 64-bit software.

4.3.7 Primary monocyte cell dispersion scans

Primary monocytes were cultured for 24 hours after isolation and then subsequently treated with 0.5 mg/ml of 11-MUA AuNP. After 24 hours, the cells were washed x2 with DPBS and resuspended into increasing concentrations of 0, 100 k, 250 k, 500 k, 1.0 M, 2.5 M, and 5.0 M cells/ml in 100 µl of DPBS and then 100 µl of 1% agarose. The agarose was heated prior to addition and then cooled on ice for 15 minutes. The suspensions were then scanned with microCT scanner (Imtek Inc, 80 kVP, 500 µA). The scans were quantified using OsiriX v3.7.1 with 64-bit software.

4.3.8 Transmission electron microscopy of tissue

RAW 264.7 cells and aorta samples from treated ApoE-/- mice were prepared for TEM imaging using standard preparation techniques.[30] Cells and tissue were fixed in 2% PFA and 2.5% glutaraldehyde before staining and embedding. Samples were cut into 60 nm thick sections and mounted onto grids before viewing with a JEOL 1010 Electron Microscope at 80 kV.

4.3.9 Primary monocyte isolation

Spleens from C57BL/6 donor mice were used as the source for primary monocytes. Mice were anesthetized with isoflurane and then euthanized. The chest cavity was opened and mice were perfused through the left ventricle with 10 mL of DPBS before removal of the spleen. After excision, the spleen was mechanically homogenized using the plunger of a 1 mL syringe in 1 mL of Hank's balanced salt solution (HBSS). The resulting cell slurry was filtered through a 70 µm filter and spun at 250 rcf for 5 mins to pellet the cells. The pellet was then re-suspended in 250 µL of RBC lysis buffer for 1 min on ice. Afterwards, HBSS supplemented with 0.6% bovine serum albumin (BSA) and 0.3 mM EDTA was added to the cells for a total volume of 10 mL. The cell solution was centrifuged at 250 rcf for 5 mins and re-suspended with HBSS+ BSA. This step was repeated twice. The cell suspension was then incubated with anti-CD11b magnetic microbeads (Mitlenyi Biotech, 140-049-601) for 30 mins at 4°C. After incubation, the suspension was washed with eluting buffer (DPBS, 0.5% BSA, 2mM EDTA). The cell suspension was then passed through a LS separation column (Miltenyi Biotech, 130-042-401) in the presence of a strong magnet to retain only CD11b+ cells in the column. Afterwards, the column is removed from the magnet and 5 mL of eluting buffer is used to remove the cells from the column. The cells were eluted through two sequential LS columns for increased purity. The resulting solution was spun at 250 rcf for 5 mins and re-suspended with RPMI medium 1640 supplemented with 10% FBS and 1% penicillin/streptomycin for cell culture.

4.3.10 Flow cytometry

The purity of the resulting cell suspension was analyzed using flow cytometry. Cells were incubated with Fc blocking agent for 15 minutes. After blocking, cells were incubated with markers for CD11b-PE Cy7, Ter119-PE, CD3-APCeF780, CD19-PerCP Cy5.5 for 30 mins on ice. Flow cytometry were performed on a BD FACSCanto System (BD Sciences, San Jose, CA). Fluorescence minus one solutions and compensation beads for each fluorophore were used for controls.

4.3.11 Animals

Six week old male apolipoprotein E (ApoE) deficient mice (B6.129P2-ApoE$^{tm1UnC/J}$) were fed western chow diet (Research Diets Inc, New Brunswick, NJ) for 10 weeks to establish early atherosclerosis before use. Age-matched male C57BL/6 were kept on regular chow diet for the duration of the experiment as controls. All experimental protocols were approved by University Laboratory Animal Resources in conjunction with the Institutional Animal Care and Use Committee at University of Pennsylvania.

4.3.12 In vivo monocyte imaging

The treated group (AtT, n=8) received AuNP labeled monocytes following the procedure below. Briefly, primary monocytes isolated through magnetic sorting as described above were cultured for 24 hours before gold labeling. The cells were then treated with 0.5 mg/ml of 11-MUA AuNP for an additional 24 hours. The cells were washed twice with DPBS and collected. After resuspension in 250 µl of DPBS, 1.0 x 10^6 cells were injected intravenously into the ApoE deficient mouse model. The animals

were scanned with a microCT II scanner (Imtek Inc, 80 kVp, 500 µA, 512x512 matrix, 100 µm slice thickness) pre-injection and on day 3, 4, and 5 post-injection. Wild type mice receiving gold labeled monocytes following a similar procedure were used as controls (WdT, n=9). Additionally, atherosclerotic mice receiving non labeled monocytes were also used as a control group (AtN, n=8). CT scans were analyzed using OsiriX software. For aorta measurements, 3 sequential ROI were measured in the ascending aorta and averaged for a final attenuation value. The location of the aorta was identified by comparing the CT images with scans from a separate mouse experiment using a CT blood pool contrast agent. Identical ROI were used for each day for each mouse. The image sets from different days were matched for each animal using the spine and ribcage as markers.

4.3.13 Ex-vivo and biodistribution

After the final scan, mice were euthanized and dissected for biodistribution. Tissue including the heart, lungs, spleen, kidney, and liver were fixed in 4% PFA after excision. For biodistribution, tissue was dissolved in 500 µL of HNO_3 for 18 hours at 60°C. Afterwards, 300 µL of HCl was added and incubated at 60°C for an additional hour. The resulting solution was spun at 300 rcf for 10 mins for remove cell debris. The samples were analyzed using ICP-OES for measurement of gold content.

4.3.14 Statistics

Statistical analysis was performed with guidance from the Center for Clinical Epidemiology and Biostatistics at the University of Pennsylvania. A linear mixed effect model was used to analyze intensities from *in vivo* scans. Each mouse was assumed to

have a unique intercept and inputted into the model as a random effect to control for baseline differences between mice. Attenuation measurements were used as the dependent variable and each day as the independent variable in the model. Analysis was performed using Stata 13.1 (64-bit, College Station TX).

4.4 Results

4.4.1 Gold nanoparticle synthesis and characterization

The Turkevich method of synthesizing gold nanoparticles was used to produce citrate coated gold nanospheres (Figure 4.2a).[29] For additional stability in biological media, a library of thiol-ligands was used to displace the citrate ligands of the AuNP (Figure 4.1). Stability for each AuNP formulation was evaluated with Dulbecco's Phosphate Buffered Saline (DPBS). When suspended in a salt based solution, stable gold nanoparticles of this size appear as a deep red solution while non-stable gold particles aggregate causing the solution to change to a blue-black color. We identified the following 5 stable coatings which we tested further: 11-mercaptoundecanoic acid (11-MUA), 16-mecaptohexadecanoic acid (16-MHA), poly(ethyleneimine) (PEI), 4-mercapto-1-butanol (4-MB), and 11-mercaptoundecyl-tetra(ethylene gycol) (MTEG). These ligands give the nanoparticles several different surface functionalities, which could influence cellular interactions including cell uptake and cytotoxicity.

TEM was used to observe the particle size and shape (Figure 4.2b). TEM revealed monodispersed spheres of 14.6 ± 1.5 nm in average diameter. DLS and zeta potential were performed to characterize hydrodynamic diameters and surface charges (Table 4.1). The hydrodynamic diameter of the particles seemed to relate to the size of

the ligand used to stabilize the particle, *i.e* the shortest ligand 4-MB displayed the smallest hydrodynamic diameter, although it seems likely that for the PEI and MTEG coated AuNP that there is some degree of aggregation of cores. The zeta potential results showed that carboxylic acid ligands (11-MUA, 16-MHA) and alcohol ligands (4-MB) had negative surface potentials, as expected. Additionally, AuNP coated with PEI, which has many amine groups, had a positive surface potential. AuNP that were coated with MTEG, which has a methoxy group at the distal end, had a nearly neutral charge.

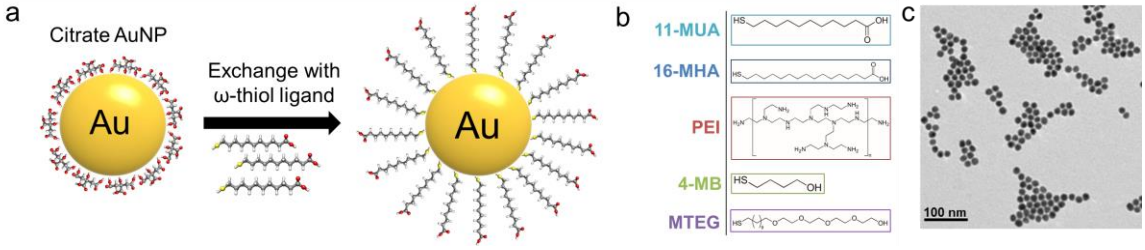

Figure 4.2 AuNP synthesis, coating and characterization.

(a) Schematic of ligand exchange for citrate capped gold nanoparticles. (b) Chemical structures of 5 formulations further used in experiments. (c) TEM image of 11-MUA capped AuNP.

Table 4.1 Characterization of selected AuNP formulations.

Surface Formulation	DLS Diameter (nm)	Surface Charge (eV)	UV Absorption (nm)
11-MUA	31.5	-36.8	525.36
16-MHA	52.2	-36.2	529.12
4-MB	25.9	-35	523.7
PEI	91.83	+45.4	528.9
MTEG	111.9	-2.1	528.17

4.4.2 In vitro evaluation of selected AuNP formulations

Following selection of AuNP formulations, we examined the interaction of these particles with a monocyte cell line, RAW 264.7. The viability of the cells after the treatment with AuNP formulations was examined using the LIVE/DEAD assay. Each formulation was assessed at several concentrations (0.025, 0.05, 0.1, 0.5, and 1.0 mg/ml of Au) for 24 hours. The ratio of living cells to total cells was determined via automatic counting by a custom MATLAB program. The results shown in Figure 4.3a demonstrate high biocompatibility for each formulation at the concentrations examined except for PEI. Due to being a polycation, PEI has been widely used as a transfection agent in gene therapy applications, but it is known that PEI can cause toxicity.[31]

We next assessed if the uptake of AuNP would affect monocyte function in an inflammatory role. Circulating monocytes produce pro-inflammatory cytokines such as TNF-α, and IL-6 after activation.[32] We therefore evaluated the cytokine release of TNF-α and IL-6 from monocytes after 0.5 mg/ml treatment of each AuNP formulation and activation with lipopolysaccharides (LPS). The AuNP formulations did not appear to disrupt cytokine release for 11-MUA, 16-MHA, and MTEG. However, the 4-MB formulation was found to decrease the cytokine release of TNF-α, but not IL-6. PEI

coated AuNP, on the other hand, were found to decrease the release of IL-6, but not TNF-α. Expression of TNF-α and IL-6 for AuNP treated monocytes was relatively similar to non-treated cells.

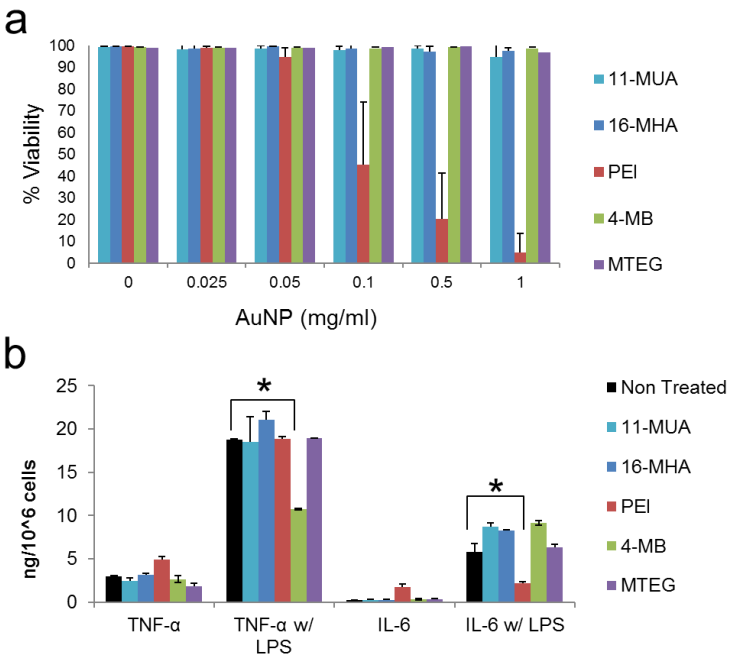

Figure 4.3 Effects of AuNP on the viability and cytokine release of monocytes.
(a) Viability of monocytes after treatment with different AuNP formulations at increasing concentrations. Viability % expressed as the ratio of living cells to total cells in the well. (b) Results from ELISA for TNF-α and IL-6 release after treatment (0.5 mg/ml) with different AuNP formulations. LPS groups were treated with LPS for 3 hours after gold treatment. ***** $P<0.05$ compared to samples not treated with AuNP. (Student's t-test)

Previous studies have demonstrated that size, shape, and surface functionality of the AuNP can significantly affect the amount of uptake into the cells.[33-34] While each of our formulations are spherical in shape, the different surface ligands resulted in altered

hydrodynamic sizes and surface properties of the particle. After treating with AuNP, monocytes were found to take up the AuNP into vesicles, likely to be lysosomes. Figure 4.4a shows TEM images of sections of monocytes that had been incubated with 11-MUA. The uptake of these gold particles may be *via* phagocytosis as found in other gold cell labeling studies.[35]

We studied the amount of AuNP uptake by monocytes for each formulation by examining CT contrast generation. Each formulation was incubated at three concentrations (0.1, 0.25, 0.5 mg/ml) for 24 hours. After treatment, cells were collected and scanned using a clinical CT scanner. The scans show an observable increase in CT attenuation dependent on the treatment concentration for our formulations (Figure 4.4b). The attenuation was quantified by measuring the intensity of the pellets. The attenuation of 11-MUA, 16-MHA, and 4-MB increased proportionally with treatment concentration of AuNP. It is important to note that the images seen in Figure 4.4b are not saturated, but some pixels are very bright due to the CT windowing scale used. All attenuation values in these experiments were well below the maximum CT attenuation values handled by this clinical system (3000 HU).[22] The attenuation for the PEI formulation was not dependent on the concentration of gold, likely due to the toxicity seen in Figure 4.3a. Interestingly, 11-MUA displayed significantly higher attenuation than 16-MHA despite both ligands having carboxylic acid functional groups. The size difference in hydrodynamic diameter (Table 4.1) may account for the difference in gold uptake between the formulations. The MTEG formulation was found to have the lowest uptake, which was not surprising since ethylene glycol based ligands are known to reduce nanoparticle uptake by the mononuclear phagocytosis system.[36] The results show that formulations of 11-MUA and 4-MB displayed the highest CT attenuation and therefore

AuNP uptake (Figure 4.4c). From the DLS and zeta potential results, both formulations 4-MB and 11-MUA have relatively low hydrodynamic diameters and strong negative surface charge suggesting that these particle properties may encourage high AuNP uptake.[37] Taking together all the results from these *in vitro* experiments, we chose to move forward with 11-MUA as our lead formulation as it displayed low cytotoxicity, no disruption of cytokine release, and high uptake in monocytes.

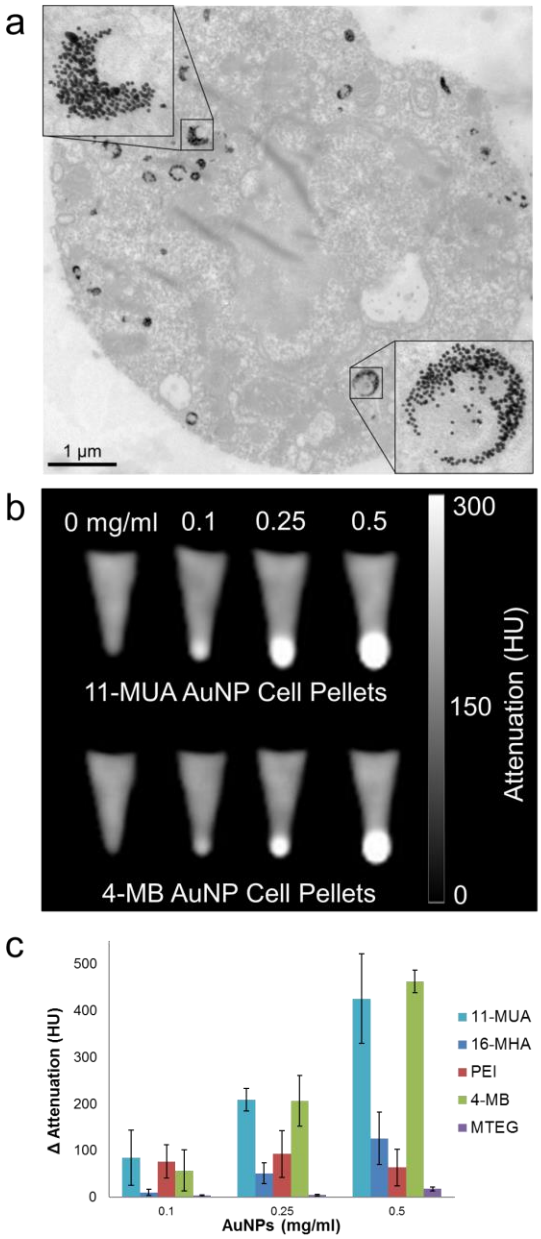

Figure 4.4 Uptake of AuNP in monocytes.

(a) TEM image of a RAW 264.7 monocyte cell after 24 hr incubation with 11-MUA AuNP. (b) CT images of pellets of 11-MUA and 4-MB AuNP treated monocytes at increasing concentrations. (c) Quantification of intensities from CT scans for each formulation.

4.4.3 In vitro evaluation of 11-MUA coated AuNP with primary monocytes

We first isolated primary monocytes from donor C57BL/6 mice. Others have shown the spleen to be a large reservoir of monocytes that are nearly identical in subtype and behavior to circulating blood monocytes.[38] Purified monocytes isolated from the spleen of donor mice were examined with flow cytometry. Cells were incubated with cocktail of antibodies consisting of CD11b-PE Cy7, Ter119-PE, CD3-APCeF780, and CD19-PerCP Cy5.5. The enriched monocyte population contained 99.3% of CD11b+ (monocyte marker), CD19- (B-cell marker), CD3- (T-cell marker) cells in the suspension (Figure 4.5).

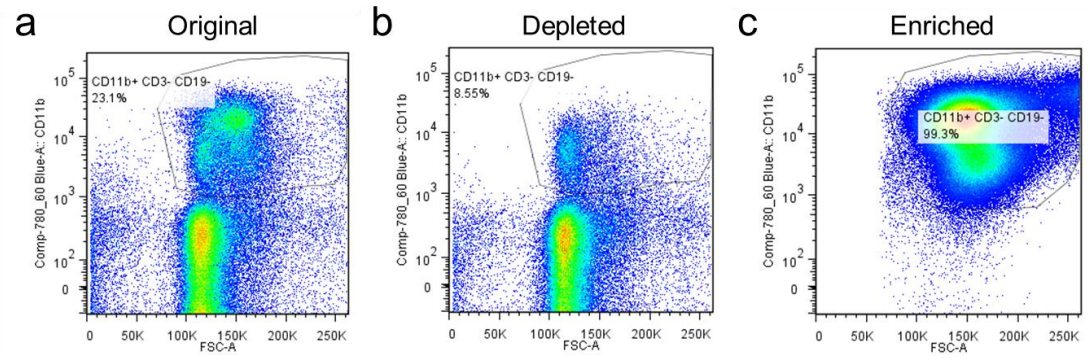

Figure 4.5 Flow cytometry for primary monocytes.

Flow cytometry of cell suspension from spleen. Purity determined by population of CD11b+, CD3-, and CD19- cells. (a) Original population of cell suspension. (b) Depleted cell population from magnetic cell sorting. (c) Enriched population from magnetic cell sorting.

We examined these primary monocytes in a method similar to the immortalized monocyte cell line. The primary monocytes were treated with 11-MUA AuNP and

evaluated for cytotoxicity and cytokine release of TNF-α. Additionally, the uptake of AuNP was directly quantified using ICP-OES and compared to the uptake of the immortalized cell line. The results show that 11-MUA AuNP treatments up to 1.0 mg/ml did not decrease cell viability of cultured primary monocytes (Figure 4.6a). Similarly, the uptake of 11-MUA AuNP did not significantly alter the release of TNF-α after activation with LPS as seen in Figure 4.6b. In much the same way, the uptake of 11-MUA AuNP did not significantly alter the release of TNF-α after activation with LPS as seen in Figure 4.6b. The TNF-α release for monocytes without LPS activation was found to be at similar low levels for non-treated and 11-MUA treated cells. These results confirm that the primary monocytes were not activated during the isolation, culturing, and gold labeling procedures. Comparable results were found with the monocyte cell line, RAW 264.7. The quantified cell uptake of AuNP was comparable between the primary monocytes and the cell line. The uptake of AuNP in primary monocytes after 24 hours of 0.5 mg/ml 11-MUA AuNP incubation was found to be 127 pg/cell (Figure 4.6c). These data demonstrated that the uptake of 11-MUA AuNP did not impact the behavior of the primary monocytes during the *ex-vivo* labeling process.

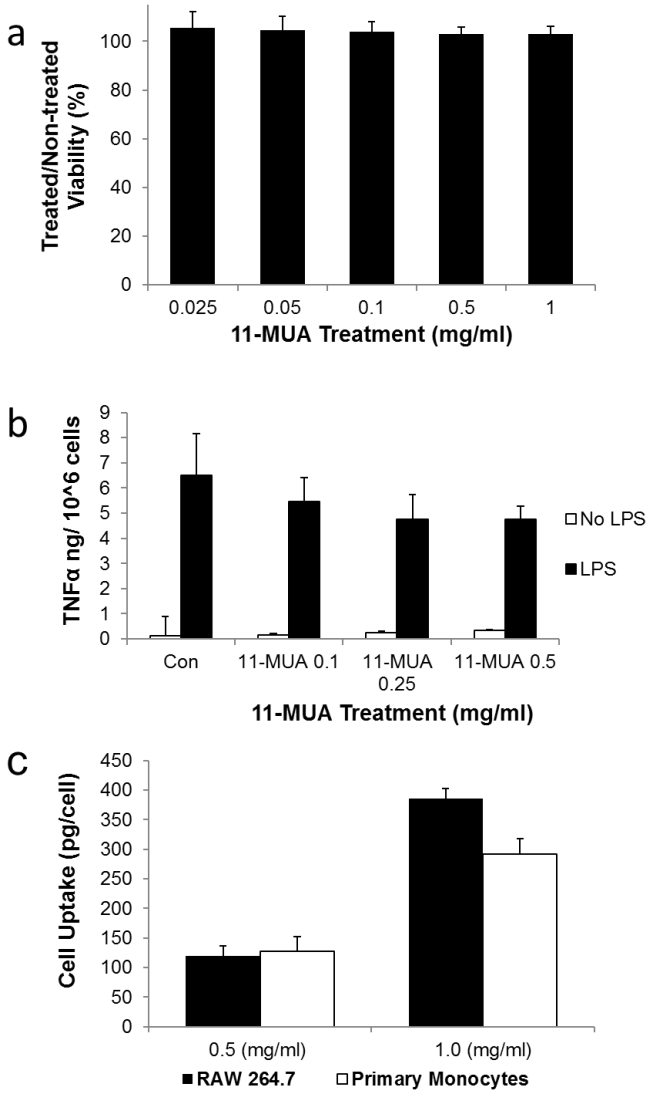

Figure 4.6 Effects of 11-MUA coated AuNP on primary monocytes.

Mouse monocytes from the spleen were cultured and evaluated *in vitro* for (a) viability using LIVE/DEAD assay, (b) TNF-α release using ELISA, and (c) AuNP cell uptake using ICP-OES for primary monocytes compared to the cell line.

4.4.4 In vivo detection of gold labeled monocytes

Having established a method for labeling monocytes with AuNP without affecting cell viability or cytokine production, we proceeded to track the recruitment of these labeled monocytes in a mouse model of atherosclerosis *via* CT imaging. ApoE deficient mice were kept on a Western diet for 10 weeks to promote the development of aortic plaques. To track the recruitment of monocytes, primary monocytes were cultured and labeled *ex-vivo* with 11-MUA AuNP a day before intravenous injection of these cells. The timeline of the experiment is shown in Figure 4.7. The mice were scanned with CT (Imtek, Inc, 80kVp, 500 µA) before I.V. injection and on days 3, 4, and 5 post-injection. The groups consisted of atherosclerotic mice receiving gold labeled monocytes (AtT), atherosclerotic mice receiving non-labeled monocytes (AtN) and wild-type mice receiving gold labeled monocytes (WdT).

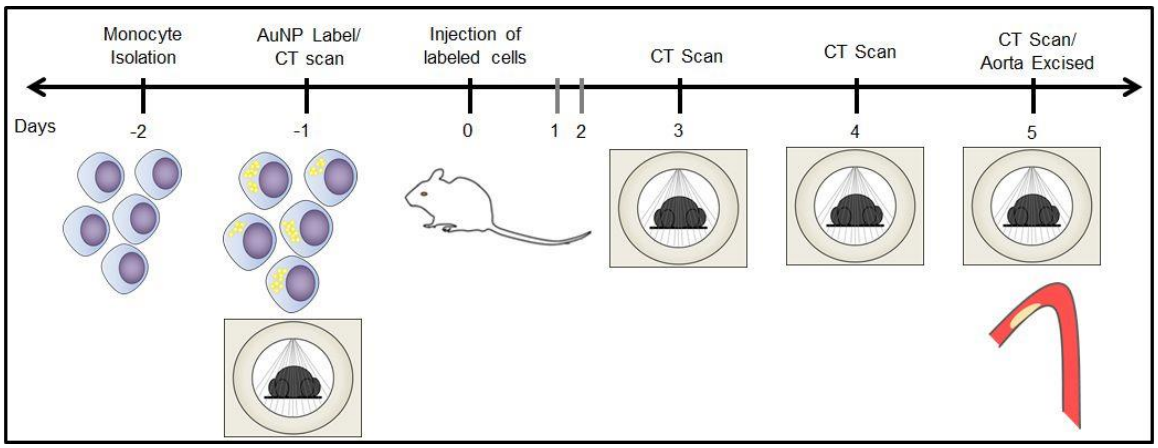

Figure 4.7 In vivo experiment timeline**.**

Experimental timeline for CT scanning of *ex-vivo* labeled monocytes injected I.V. into atherosclerotic mice.

Figure 4.8 shows images of an atherosclerotic mouse that received AuNP labeled monocytes for day 0 and day 5 scans; attenuation was seen to increase in the aorta over time as compared to the day 0 scan. The AtT group (atherosclerotic mice receiving AuNP labeled monocytes) showed a continual increase in attenuation over time resulting in a final 15.3 HU difference on day 5 as compared to the pre-injection scan (Figure 4.8c). The increase for the AtN group (atherosclerotic mice receiving non-labeled monocytes) animals was much less. The WdT group (wild type mice receiving gold AuNP monocytes) attenuation values varied across acquisitions with no significant increase. Due to the heterogeneity of developing atherosclerosis, a linear mixed effects statistical model was used to account for disease variation among animals over time. Accounting for the attenuation values obtained each day (day 1 through 5) and random effects, we found a statistically significant increase in attenuation for the AtT group ($p=0.002$) of 15.3 HU. In comparison, the WdT ($p=0.305$) and the AtN ($p=0.251$) models showed no significant change in attenuation over time. This increase in attenuation in our AtT animals suggests that the recruitment of AuNP labeled monocytes can be detected by CT imaging. While the change in attenuation in the AtN group was not statistically significant, there may be small increases in the attenuation of the plaque during the 5 days of the experiment due to disease progression.

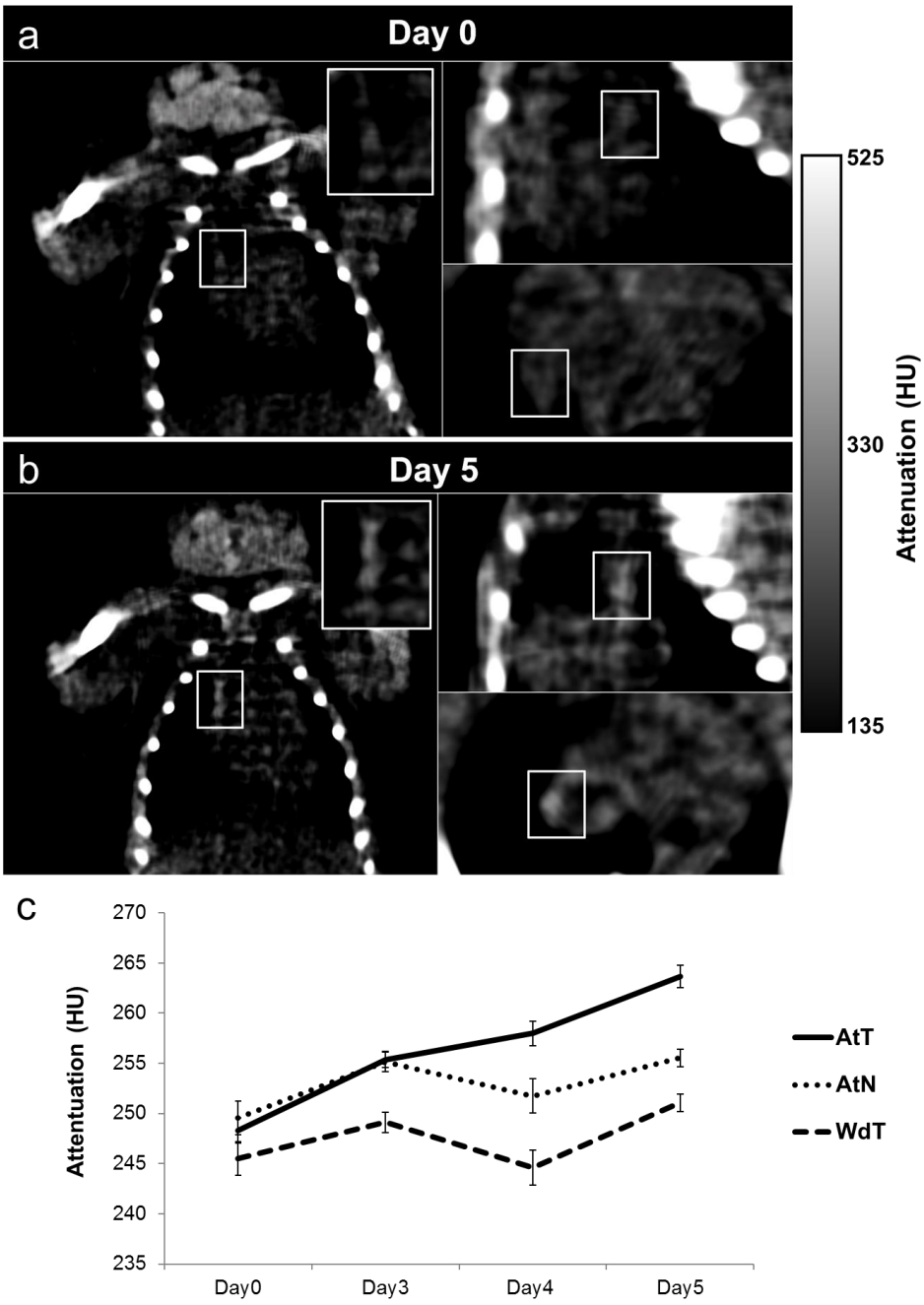

Figure 4.8 In vivo attenuation of gold labeled monocytes.

CT scans of an atherosclerotic mouse injected with gold labeled monocytes (AtT) for (a) day 0 and (b) day 5. White boxes indicated aortic region of interest. Attenuation

increases in the aorta over 5 days as compared to the pre-injection scan. (c) Graph plotting the average intensities in the aorta of mice in CT scans over time.

For an estimation of the number of gold labeled cells in the plaque, a standard curve of attenuation versus gold labeled cells per unit volume was generated. Primary monocytes were treated with 0.5 mg/ml of 11-MUA AuNP for 24 hours and resuspended in an agarose gel at increasing concentrations. The cell concentrations were scanned with microCT scanner (Imtek Inc., 80 kVp, 500 μA) and quantified (Figure 4.9). Using this standard curve, the change in attenuation of 15.3 HU in the AtT treated group correlated to be approximately 15 gold labeled cells/voxel in the plaque. The true number of gold labeled cells in the plaque would vary depending on plaque size but we believe this to be a reasonable estimation.

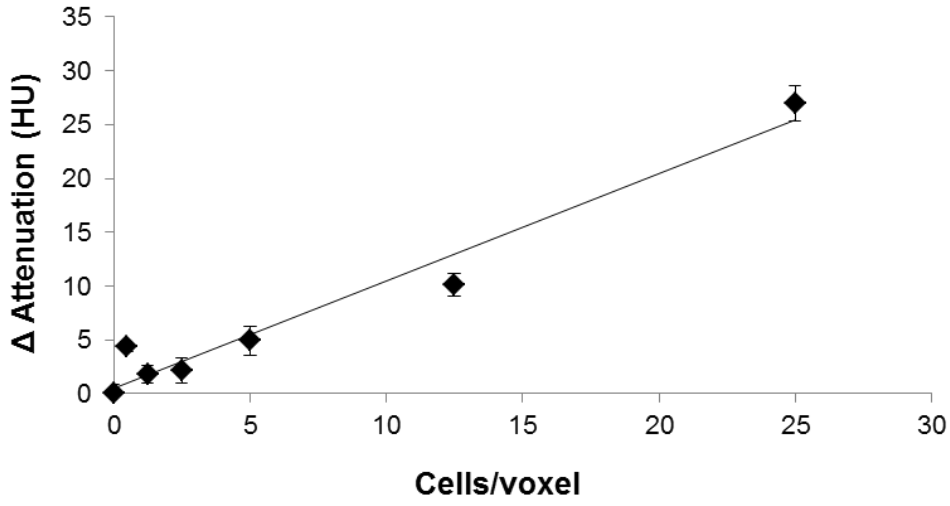

Figure 4.9 Quantification of gold labeled cells.

Standard curve of attenuation versus cells per voxel (isotropic voxel size 0.1 mm). Quantification of attenuation for gold labeled primary monocyte, values normalized to attenuation at 0 cells/voxel.

4.4.5 Biodistribution of AuNP

At the end of the experiment, animals were sacrificed and organs excised for biodistribution. The gold content in the tissue was analyzed using ICP-OES to measure the distribution after 5 days post injection. Figure 4.10 shows high gold uptake in the spleen and liver, which are organs that typically host large numbers of monocytes and monocyte derived cells. Swirski *et al.,* showed similarly high uptake of labeled monocytes in the spleen 5 days after intravenous injection.[9]

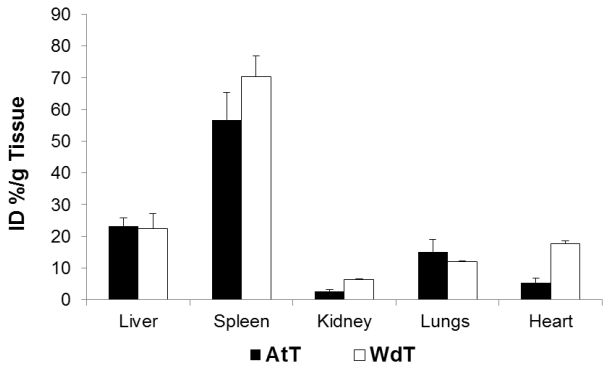

Figure 4.10 Biodistribution of gold from in vivo experiments.

Gold content of tissue analyzed by ICP-OES at 5 days post injection of the atherosclerotic and wild type mice receiving AuNP labeled monocytes.

4.4.6 Ex-vivo analysis of atherosclerotic plaques

The aortas of AtT mice (received AuNP labeled monocytes) were sectioned through the atherosclerotic plaque and examined with TEM. AuNP were found in monocytes that were located in the atherosclerotic plaque (Figure 4.11). This indicates that the attenuation increase seen in the *in vivo* CT scans is due to recruitment of the AuNP labeled monocytes into the plaques.

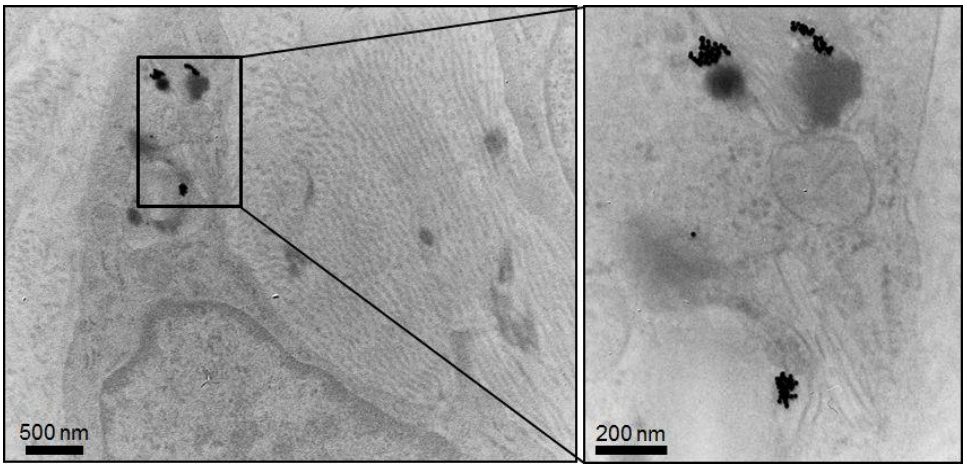

Figure 4.11 AuNP labeled cells in aortic sections.

Excised aortas from atherosclerotic mice receiving AuNP labeled monocytes were sectioned through the plaque and examined with TEM for localization of gold nanoparticles.

4.5 Discussion

In this study, we demonstrate the successful labeling of monocytes with AuNP of varying formulations. Each ligand conferred a distinct combination of particle parameters including hydrodynamic diameter, surface potential and chemical functionality (Table 4.1). Formulations of 4-MB and 11-MUA, which have similar diameters and negative surface potential, were found to have low cytotoxicity and the highest monocyte uptake.[37] Previous reports have shown that anionic AuNP exhibit less toxicity as compared to cationic nanoparticles.[39] The authors suggest that positively charged particles may directly diffuse through the plasma membrane, disrupting the lipid bilayer causing cytotoxicity. Additionally, our incubation of monocytes with AuNP occurs in media with serum. Studies have shown that the makeup of the protein corona surrounding the particle could be responsible for differences in cellular uptake.[40-41] It is likely that 4-MB and 11-MUA AuNP formulations form a protein corona preferential for cell uptake as compared to other our examined ligands. We found uptake of 127 pg Au/cell in our *in vitro* incubations performed with 0.5 mg Au/ml in the cell culture media. This is comparable to previous work since Menk *et al*. reported uptake of 33-36 pg Au/cell for incubations performed with 0.052 mg Au/ml, a ten-fold lower concentration than in our experiments, over a similar timeframe.[14] Furthermore, others have loaded cells with iron oxide nanoparticles up to a weight of 39 pg Fe/cell. Adjusting for the

differing densities of gold and iron oxide, this would be equivalent to 209.9 pg Au/cell.[42-43]

We found that the migration of these labeled monocytes to atherosclerotic plaques could be observed and measured with CT. We believe this is the first study to non-invasively track monocyte recruitment into atherosclerotic plaques using computed tomography. For plaque imaging, a number of targets have been previously studied with MRI, PET, SPECT, and NIRF. Researchers have successfully imaged cell-adhesion molecules, lipoproteins, ECM, proteases, and angiogenesis in plaques.[44] Studies looking to image inflammatory cells primarily focus on macrophage presence in the plaque.[45-47] Due to the insensitivity of contrast agents in CT, few imaging studies of plaque use x-ray computed tomography as the sole means of imaging. Researchers have previously demonstrated the in vivo detection of macrophages in atherosclerotic plaques with CT by using an iodinated agent,[48] PEGylated nanoparticles[49] and gold core lipoproteins.[27-28] High macrophage content atherosclerotic plaque is a potential indicator of imminent risk of plaque rupture.[50] In the present study, we sought to track the process of monocyte recruitment, which has been found to be informative of disease progression. A study by Robbins *et al.* found that monocyte recruitment is a significant source of the macrophage population in early plaques while the macrophage populations in established are due to *in-situ* proliferation.[51] Therefore, the detection of monocyte recruitment into the plaque could be an early marker for patients at risk of development of cardiovascular disease.

Our study presented here looks at the important process of monocyte recruitment in early stage atherosclerosis utilizing CT. This technique can improve the study of monocyte recruitment and help elucidate monocyte role in atherosclerosis progression and/or regression. Additionally, this technique may help assess new atherosclerotic

interventions that target monocytes and plaque inflammation. However, CT sensitivity to contrast agents has been a significant obstacle in the further development of this method. The present study demonstrated increased intensity in the aorta (Δ 15.3 HU) as compared to pre-scan values. This attenuation change is on par with similar studies in the field. For instance, Hyafil *et al*. reported a change of 13.3 HU in the atherosclerotic plaques of rabbits intravenously injected with iodinated nanoparticles designed to target macrophages.[48] Similarly, Eck *et al.*, injected anti-CD4 gold nanoparticles intravenously to target lymph in-vivo and found an attenuation change of 20 HU at 1 hr and 25 HU at 48 hrs for 28 nm gold nanoparticles.[52] However, for our study, an increase in sensitivity and overall attenuation change would be required to discern small reductions of monocyte uptake (e.g. <30%). A recent study by Betzer *et al.,* presented the use of a "CT ruler" to approximate the number of gold labeled cells in a tissue non-invasively.[53] However, the high attenuation required for this method was achieved by directly injecting the gold labeled cells at the site of interest. In our study, increasing the signal from our cells may be achieved by further optimizing the method. By increasing the number of injected gold label monocytes, we hypothesize a higher intensity in our scans is possible; however in this approach, injecting more monocytes than are physiologically present in the circulation may significantly alter the response of the animal to these cells. Instead, increasing the amount of gold per cell may be the ideal strategy to increase CT contrast in the images without increasing the number of injected cells. Translation of nanoparticle-facilitated cell tracking to clinical scanners would be beneficial, due to the lower image noise in clinical scanners as compared with preclinical scanners.[54] Lower image noise improves signal-to-noise ratios and hence improves sensitivity.

An alternative solution to achieve higher intensities may be to purify the monocyte subtype further. In the current study, monocytes are isolated by the expression of CD11b marker, a conserved monocytes marker across many subtypes.[55] In mice, the "inflammatory" Ly6C^{Hi} monocyte subtype has been described as the dominant subtype for migration in early atherosclerotic plaques as compared to the "resident" monocyte, Ly6C^{Lo}.[56-57] Hence, we may improve the overall recruitment of our gold labeled monocytes by further purifying our isolated monocytes for CD11b+, Ly6C^{Hi} subtype in future studies.

In this cell tracking study, isolated monocytes are labeled *ex-vivo* before injection as opposed to labeling *in-situ*. The emergence of adoptive cell therapies as successful clinical therapies reinforces the need for methods of cell tracking *ex-vivo* cultured cells.[58] Cell tracking using *ex-vivo* labeled cells with CT has been demonstrated with a number of applications including T-cell labeling for cancer, C6 glioma cells for brain tumor models, olfactory ensheathing cells for spinal compression injury models and pancreatic islets labeling for diabetes.[14, 59-63] *In-situ* labeling, where nanoparticles are injected into animals and cells take up the nanoparticles *in vivo*, is more straightforward and simpler to implement clinically.[64-65] However, *in-situ* labeling may result in labeling a variety of cells, such as macrophages and monocytes resident within the plaque, as well as circulating monocytes, confounding results from imaging. In the future, we will explore ways to adapt our current approach for *in-situ* labeling and compare the results.

4.6 Conclusion

In this study, we screened AuNP formulations for effective uptake in monocytes without disruption of viability or inflammatory function. We identified a lead formulation

with these characteristics, which was confirmed with primary monocytes. These labeled monocytes were intravenously injected and monitored for recruitment into atherosclerotic plaques using x-ray computed tomography. We found an increase in the attenuation in the aorta, post injection of these labeled cells. We confirmed the presence of these labeled monocytes in the plaque through the use of TEM. This study demonstrates the feasibility of tracking labeled monocytes with CT. Further studies are required to optimize the detection of these cells for quantification of monocyte accumulation in the plaque. Increased sensitivity will allow for examination of monocyte recruitment in the presence of emerging atherosclerosis therapies.

While we demonstrated that detection of gold labeled monocytes recruited to atherosclerosis is achievable, further experimental refinement is needed to be utilized as research tool. However, we believe this study continues to expand the use of CT as a cell tracking modality. The use of gold nanoparticles to track monocytes and other cells in other disease applications is possible. In the following chapter, we indicate future directions for the work and discuss expanded biomedical applications for gold labeling of cells for cell tracking.

4.7 References

1. Mozaffarian, D.; Benjamin, E. J.; Go, A. S.; Arnett, D. K.; Blaha, M. J.; Cushman, M.; de Ferranti, S.; Despres, J.; Fullerton, H. J.; Howard, V. J., et al., Heart Disease and Stroke Statistics-2015 Update: A Report From the American Heart Association. *Circulation* **2014**.

2. Libby, P.; Ridker, P. M.; Maseri, A., Inflammation and atherosclerosis. *Circulation* **2002,** *105* (9), 1135-1143.

3. Libby, P., Inflammation in atherosclerosis. *Nature* **2002,** *420* (6917), 868-874.

4. Moreno, P. R.; Falk, E.; Palacios, I. F.; Newell, J. B.; Fuster, V.; Fallon, J. T., Macrophage infiltration in acute coronary syndromes. Implications for plaque rupture. *Circulation* **1994,** *90* (2), 775-778.

5. Ley, K.; Miller, Y. I.; Hedrick, C. C., Monocyte and macrophage dynamics during atherogenesis. *Arterioscler Thromb Vasc Biol* **2011,** *31* (7), 1506-1516.

6. Boisvert, W. A.; Rose, D. M.; Johnson, K. A.; Fuentes, M. E.; Lira, S. A.; Curtiss, L. K.; Terkeltaub, R. A., Up-regulated expression of the CXCR2 ligand KC/GRO-alpha in atherosclerotic lesions plays a central role in macrophage accumulation and lesion progression. *Am J Pathol* **2006,** *168* (4), 1385-1395.

7. Boring, L.; Gosling, J.; Cleary, M.; Charo, I. F., Decreased lesion formation in CCR2-/- mice reveals a role for chemokines in the initiation of atherosclerosis. *Nature* **1998,** *394* (6696), 894-897.

8. Combadiere, C.; Potteaux, S.; Rodero, M.; Simon, T.; Pezard, A.; Esposito, B.; Merval, R.; Proudfoot, A.; Tedgui, A.; Mallat, Z., Combined inhibition of CCL2, CX3CR1, and CCR5 abrogates Ly6C(hi) and Ly6C(lo) monocytosis and almost abolishes atherosclerosis in hypercholesterolemic mice. *Circulation* **2008,** *117* (13), 1649-1657.

9. Swirski, F. K.; Pittet, M. J.; Kircher, M. F.; Aikawa, E.; Jaffer, F. A.; Libby, P.; Weissleder, R., Monocyte accumulation in mouse atherogenesis is progressive and proportional to extent of disease. *Proc Natl Acad Sci U S A* **2006,** *103* (27), 10340-10345.

10. Fayad, Z. A.; Mani, V.; Woodward, M.; Kallend, D.; Abt, M.; Burgess, T.; Fuster, V.; Ballantyne, C. M.; Stein, E. A.; Tardif, J. C., et al., Safety and efficacy of dalcetrapib on atherosclerotic disease using novel non-invasive multimodality imaging (dal-PLAQUE): a randomised clinical trial. *Lancet* **2011,** *378* (9802), 1547-1559.

11. Mowatt, G.; Cummins, E.; Waugh, N.; Walker, S.; Cook, J.; Jia, X.; Hillis, G. S.; Fraser, C., Systematic review of the clinical effectiveness and cost-effectiveness of 64-slice or higher computed tomography angiography as an alternative to invasive coronary angiography in the investigation of coronary artery disease. *Health Technol Assess* **2008,** *12* (17), iii-iv, ix-143.

12. Sandfort, V.; Lima, J. A.; Bluemke, D. A., Noninvasive Imaging of Atherosclerotic Plaque Progression: Status of Coronary Computed Tomography Angiography. *Circ Cardiovasc Imaging* **2015,** *8* (7).

13. Astolfo, A.; Schultke, E.; Menk, R. H.; Kirch, R. D.; Juurlink, B. H.; Hall, C.; Harsan, L. A.; Stebel, M.; Barbetta, D.; Tromba, G., et al., In vivo visualization of gold-loaded cells in mice using x-ray computed tomography. *Nanomedicine* **2013,** *9* (2), 284-292.

14. Menk, R. H.; Schultke, E.; Hall, C.; Arfelli, F.; Astolfo, A.; Rigon, L.; Round, A.; Ataelmannan, K.; MacDonald, S. R.; Juurlink, B. H., Gold nanoparticle labeling of cells is a sensitive method to investigate cell distribution and migration in animal models of human disease. *Nanomedicine* **2011,** *7* (5), 647-654.

15. Astolfo, A.; Arfelli, F.; Schultke, E.; James, S.; Mancini, L.; Menk, R. H., A detailed study of gold-nanoparticle loaded cells using X-ray based techniques for cell-tracking applications with single-cell sensitivity. *Nanoscale* **2013,** *5* (8), 3337-3345.

16. Schultke, E.; Menk, R.; Pinzer, B.; Astolfo, A.; Stampanoni, M.; Arfelli, F.; Harsan, L. A.; Nikkhah, G., Single-cell resolution in high-resolution synchrotron X-ray CT imaging with gold nanoparticles. *J Synchrotron Radiat* **2014,** *21* (Pt 1), 242-250.

17. Kircher, M. F.; Grimm, J.; Swirski, F. K.; Libby, P.; Gerszten, R. E.; Allport, J. R.; Weissleder, R., Noninvasive in vivo imaging of monocyte trafficking to atherosclerotic lesions. *Circulation* **2008,** *117* (3), 388-395.

18. Ye, Y. X.; Basse-Lusebrink, T. C.; Arias-Loza, P. A.; Kocoski, V.; Kampf, T.; Gan, Q.; Bauer, E.; Sparka, S.; Helluy, X.; Hu, K., et al., Monitoring of monocyte recruitment in reperfused myocardial infarction with intramyocardial hemorrhage and microvascular obstruction by combined fluorine 19 and proton cardiac magnetic resonance imaging. *Circulation* **2013,** *128* (17), 1878-1888.

19. Ishida, M.; Sakuma, H., Magnetic resonance of coronary arteries: assessment of luminal narrowing and blood flow in the coronary arteries. *J Thorac Imaging* **2014,** *29* (3), 155-162.

20. Mieszawska, A. J.; Mulder, W. J.; Fayad, Z. A.; Cormode, D. P., Multifunctional gold nanoparticles for diagnosis and therapy of disease. *Mol Pharm* **2013,** *10* (3), 831-847.

21. Simpson, C. A.; Agrawal, A. C.; Balinski, A.; Harkness, K. M.; Cliffel, D. E., Short-chain PEG mixed monolayer protected gold clusters increase clearance and red blood cell counts. *ACS Nano* **2011,** *5* (5), 3577-3584.

22. Galper, M. W.; Saung, M. T.; Fuster, V.; Roessl, E.; Thran, A.; Proksa, R.; Fayad, Z. A.; Cormode, D. P., Effect of computed tomography scanning parameters on gold nanoparticle and iodine contrast. *Invest Radiol* **2012,** *47* (8), 475-481.

23. Naha, P. C.; Chhour, P.; Cormode, D. P., Systematic in vitro toxicological screening of gold nanoparticles designed for nanomedicine applications. *Toxicol In Vitro* **2015,** *29* (7), 1445-1453.

24. Cormode, D. P.; Naha, P. C.; Fayad, Z. A., Nanoparticle contrast agents for computed tomography: a focus on micelles. *Contrast Media Mol Imaging* **2014,** *9* (1), 37-52.

25. Au, J. T.; Craig, G.; Longo, V.; Zanzonico, P.; Mason, M.; Fong, Y.; Allen, P. J., Gold nanoparticles provide bright long-lasting vascular contrast for CT imaging. *AJR Am J Roentgenol* **2013,** *200* (6), 1347-1351.

26. Cai, Q. Y.; Kim, S. H.; Choi, K. S.; Kim, S. Y.; Byun, S. J.; Kim, K. W.; Park, S. H.; Juhng, S. K.; Yoon, K. H., Colloidal gold nanoparticles as a blood-pool contrast agent for X-ray computed tomography in mice. *Invest Radiol* **2007,** *42* (12), 797-806.

27. Cormode, D. P.; Roessl, E.; Thran, A.; Skajaa, T.; Gordon, R. E.; Schlomka, J. P.; Fuster, V.; Fisher, E. A.; Mulder, W. J.; Proksa, R., et al., Atherosclerotic plaque composition: analysis with multicolor CT and targeted gold nanoparticles. *Radiology* **2010,** *256* (3), 774-782.

28. Cormode, D. P.; Skajaa, T.; van Schooneveld, M. M.; Koole, R.; Jarzyna, P.; Lobatto, M. E.; Calcagno, C.; Barazza, A.; Gordon, R. E.; Zanzonico, P., et al., Nanocrystal core high-density lipoproteins: a multimodality contrast agent platform. *Nano Lett* **2008,** *8* (11), 3715-3723.

29. Turkevich, J.; Stevenson, P.; Hillier, J., A study of the nucleation and growth processes in the synthesis of colloidal gold. *Discuss. Faraday Soc.* **1951,** *11*, 55-75.

30. Horak, D.; Babic, M.; Jendelova, P.; Herynek, V.; Trchova, M.; Pientka, Z.; Pollert, E.; Hajek, M.; Sykova, E., D-mannose-modified iron oxide nanoparticles for stem cell labeling. *Bioconjug Chem* **2007,** *18* (3), 635-644.

31. Moghimi, S. M.; Symonds, P.; Murray, J. C.; Hunter, A. C.; Debska, G.; Szewczyk, A., A two-stage poly(ethylenimine)-mediated cytotoxicity: implications for gene transfer/therapy. *Mol Ther* **2005,** *11* (6), 990-995.

32. Ghattas, A.; Griffiths, H. R.; Devitt, A.; Lip, G. Y.; Shantsila, E., Monocytes in coronary artery disease and atherosclerosis: where are we now? *J Am Coll Cardiol* **2013,** *62* (17), 1541-1551.

33. Dreaden, E. C.; Austin, L. A.; Mackey, M. A.; El-Sayed, M. A., Size matters: gold nanoparticles in targeted cancer drug delivery. *Ther Deliv* **2012,** *3* (4), 457-478.

34. Ma, X.; Wu, Y.; Jin, S.; Tian, Y.; Zhang, X.; Zhao, Y.; Yu, L.; Liang, X. J., Gold nanoparticles induce autophagosome accumulation through size-dependent nanoparticle uptake and lysosome impairment. *ACS Nano* **2011,** *5* (11), 8629-8639.

35. Juurlink, B. H.; Devon, R. M., Colloidal gold as a permanent marker of cells. *Experientia* **1991,** *47* (1), 75-77.

36. Jokerst, J. V.; Lobovkina, T.; Zare, R. N.; Gambhir, S. S., Nanoparticle PEGylation for imaging and therapy. *Nanomedicine (Lond)* **2011,** *6* (4), 715-728.

37. Giljohann, D. A.; Seferos, D. S.; Patel, P. C.; Millstone, J. E.; Rosi, N. L.; Mirkin, C. A., Oligonucleotide loading determines cellular uptake of DNA-modified gold nanoparticles. *Nano Lett* **2007,** *7* (12), 3818-3821.

38. Swirski, F. K.; Nahrendorf, M.; Etzrodt, M.; Wildgruber, M.; Cortez-Retamozo, V.; Panizzi, P.; Figueiredo, J. L.; Kohler, R. H.; Chudnovskiy, A.; Waterman, P., et al., Identification of splenic reservoir monocytes and their deployment to inflammatory sites. *Science* **2009,** *325* (5940), 612-616.

39. Goodman, C. M.; McCusker, C. D.; Yilmaz, T.; Rotello, V. M., Toxicity of gold nanoparticles functionalized with cationic and anionic side chains. *Bioconjug Chem* **2004,** *15* (4), 897-900.

40. Ritz, S.; Schottler, S.; Kotman, N.; Baier, G.; Musyanovych, A.; Kuharev, J.; Landfester, K.; Schild, H.; Jahn, O.; Tenzer, S., et al., Protein corona of nanoparticles: distinct proteins regulate the cellular uptake. *Biomacromolecules* **2015,** *16* (4), 1311-1321.

41. Chithrani, B. D.; Chan, W. C., Elucidating the mechanism of cellular uptake and removal of protein-coated gold nanoparticles of different sizes and shapes. *Nano Lett* **2007,** *7* (6), 1542-1550.

42. Bohmer, N.; Jordan, A., Caveolin-1 and CDC42 mediated endocytosis of silica-coated iron oxide nanoparticles in HeLa cells. *Beilstein J Nanotechnol* **2015,** *6*, 167-176.

43. Wuerfel, E.; Smyth, M.; Millward, J. M.; Schellenberger, E.; Glumm, J.; Prozorovski, T.; Aktas, O.; Schulze-Topphoff, U.; Schnorr, J.; Wagner, S., et al., Electrostatically Stabilized Magnetic Nanoparticles - An Optimized Protocol to Label Murine T Cells for in vivo MRI. *Front Neurol* **2011,** *2*, 72.

44. Choudhury, R. P.; Fuster, V.; Fayad, Z. A., Molecular, cellular and functional imaging of atherothrombosis. *Nat Rev Drug Discov* **2004,** *3* (11), 913-925.

45. Mulder, W. J. M.; Strijkers, G. J.; Briley-Saboe, K. C.; Frias, J. C.; Aguinaldo, J. G. S.; Vucic, E.; Amirbekian, V.; Tang, C.; Chin, P. T. K.; Nicolay, K., et al., Molecular

imaging of macrophages in antherosclerotic plaques using bimodal PEG-micelles. *Magn Reson Med* **2007,** *58* (6), 1164-1170.

46. Amirbekian, V.; Lipinski, M. J.; Briley-Saebo, K. C.; Amirbekian, S.; Aguinaldo, J. G. S.; Weinreb, D. B.; Vucic, E.; Frias, J. C.; Hyafil, F.; Mani, V., et al., Detecting and assessing macrophages in vivo to evaluate atherosclerosis noninvasively using molecular MRI. *Proc Natl Acad Sci USA* **2007,** *104* (3), 961-966.

47. Hyafil, F.; Laissy, J. P.; Mazighi, M.; Tchetche, D.; Louedec, L.; Adle-Biassette, H.; Chillon, S.; Henin, D.; Jacob, M. P.; Letourneur, D., et al., Ferumoxtran-10-enhanced MRI of the hypercholesterolemic rabbit aorta: relationship between signal loss and macrophage infiltration. *Arterioscler Thromb Vasc Biol* **2006,** *26* (1), 176-181.

48. Hyafil, F.; Cornily, J. C.; Feig, J. E.; Gordon, R.; Vucic, E.; Amirbekian, V.; Fisher, E. A.; Fuster, V.; Feldman, L. J.; Fayad, Z. A., Noninvasive detection of macrophages using a nanoparticulate contrast agent for computed tomography. *Nat Med* **2007,** *13* (5), 636-641.

49. Qin, J.; Peng, C.; Zhao, B.; Ye, K.; Yuan, F.; Peng, Z.; Yang, X.; Huang, L.; Jiang, M.; Zhao, Q., et al., Noninvasive detection of macrophages in atherosclerotic lesions by computed tomography enhanced with PEGylated gold nanoparticles. *Int J Nanomedicine* **2014,** *9*, 5575-5590.

50. Naghavi, M.; Libby, P.; Falk, E.; Casscells, S. W.; Litovsky, S.; Rumberger, J.; Badimon, J. J.; Stefanadis, C.; Moreno, P.; Pasterkamp, G., et al., From vulnerable plaque to vulnerable patient: a call for new definitions and risk assessment strategies: Part I. *Circulation* **2003,** *108* (14), 1664-1672.

51. Robbins, C. S.; Hilgendorf, I.; Weber, G. F.; Theurl, I.; Iwamoto, Y.; Figueiredo, J. L.; Gorbatov, R.; Sukhova, G. K.; Gerhardt, L. M.; Smyth, D., et al., Local proliferation

dominates lesional macrophage accumulation in atherosclerosis. *Nat Med* **2013,** *19* (9), 1166-1172.

52. Eck, W.; Nicholson, A. I.; Zentgraf, H.; Semmler, W.; Bartling, S., Anti-CD4-targeted gold nanoparticles induce specific contrast enhancement of peripheral lymph nodes in X-ray computed tomography of live mice. *Nano Lett* **2010,** *10* (7), 2318-2322.

53. Betzer, O.; Shwartz, A.; Motiei, M.; Kazimirsky, G.; Gispan, I.; Damti, E.; Brodie, C.; Yadid, G.; Popovtzer, R., Nanoparticle-based CT imaging technique for longitudinal and quantitative stem cell tracking within the brain: application in neuropsychiatric disorders. *ACS Nano* **2014,** *8* (9), 9274-9285.

54. Halpern, E. J.; Gingold, E. L.; White, H.; Read, K., Evaluation of coronary artery image quality with knowledge-based iterative model reconstruction. *Acad Radiol* **2014,** *21* (6), 805-811.

55. Gordon, S.; Taylor, P. R., Monocyte and macrophage heterogeneity. *Nat Rev Immunol* **2005,** *5* (12), 953-964.

56. Swirski, F. K.; Libby, P.; Aikawa, E.; Alcaide, P.; Luscinskas, F. W.; Weissleder, R.; Pittet, M. J., Ly-6Chi monocytes dominate hypercholesterolemia-associated monocytosis and give rise to macrophages in atheromata. *J Clin Invest* **2007,** *117* (1), 195-205.

57. Hilgendorf, I.; Swirski, F. K.; Robbins, C. S., Monocyte fate in atherosclerosis. *Arterioscler Thromb Vasc Biol* **2015,** *35* (2), 272-279.

58. June, C. H.; Riddell, S. R.; Schumacher, T. N., Adoptive cellular therapy: a race to the finish line. *Sci Transl Med* **2015,** *7* (280), 280ps287.

59. Meir, R.; Shamalov, K.; Betzer, O.; Motiei, M.; Horovitz-Fried, M.; Yehuda, R.; Popovtzer, A.; Popovtzer, R.; Cohen, C. J., Nanomedicine for Cancer Immunotherapy:

Tracking Cancer-Specific T-Cells in Vivo with Gold Nanoparticles and CT Imaging. *ACS Nano* **2015,** *9* (6), 6363-6372.

60. Arifin, D. R.; Manek, S.; Call, E.; Arepally, A.; Bulte, J. W., Microcapsules with intrinsic barium radiopacity for immunoprotection and X-ray/CT imaging of pancreatic islet cells. *Biomaterials* **2012,** *33* (18), 4681-4689.

61. Hall, C.; Sturm, E.; Schultke, E.; Arfelli, F.; Menk, R. H.; Astolfo, A.; Juurlink, B. H. J., Progress in Cell Marking for Synchrotron X-ray Computed Tomography. *AIP Conf Proc* **2010,** *1266* (1), 51-56.

62. Hall, C. J.; Schultke, E.; Rigon, L.; Ataelmannan, K.; Rigley, S.; Menk, R.; Arfelli, F.; Tromba, G.; Pearson, S.; Wilkinson, S., et al., Synchrotron-based in vivo tracking of implanted mammalian cells. *Eur J Radiol* **2008,** *68* (3 Suppl), S156-159.

63. Rigley, S.; Rigon, L.; Ataelmannan, K.; Chapman, D.; Doucette, R.; Griebel, R.; Juurlink, B.; Arfelli, F.; Menk, R. H.; Tromba, G., et al., Absorption edge subtraction imaging for volumetric measurement in an animal model of malignant brain tumor. *Nucl Instr Meth Phys Res A* **2005,** *548* (1–2), 88-93.

64. Khurana, A.; Nejadnik, H.; Gawande, R.; Lin, G.; Lee, S.; Messing, S.; Castaneda, R.; Derugin, N.; Pisani, L.; Lue, T. F., et al., Intravenous ferumoxytol allows noninvasive MR imaging monitoring of macrophage migration into stem cell transplants. *Radiology* **2012,** *264* (3), 803-811.

65. Naresh, N. K.; Xu, Y.; Klibanov, A. L.; Vandsburger, M. H.; Meyer, C. H.; Leor, J.; Kramer, C. M.; French, B. A.; Epstein, F. H., Monocyte and/or macrophage infiltration of heart after myocardial infarction: MR imaging by using T1-shortening liposomes. *Radiology* **2012,** *264* (2), 428-435.

Chapter 5: Discussion and future directions

5.1 Overall discussion

5.1.1 Overview

In the work presented herein, we hypothesized that we could track monocyte migration with x-ray computed tomography (CT) through the use of gold nanoparticle constructs as labels. Cell tracking tools have become increasingly desired due to the ability to track cells that have been delivered from an external source. These tools are able to provide near real time information about cell location, migration, and viability. We sought to develop gold nanoparticles (AuNP) agents that could label monocytes and monitor their recruitment into atherosclerotic plaques.

We first explored using polyphosphazene polymers to create nanospheres with AuNP loaded into the core as discussed in Chapter 2. We also assessed the controlled localization of nanoparticles onto the surface of the nanospheres. We found substantial uptake of these nanospheres both for core-loaded and surface-loaded variants allowing for CT imaging of gold labeled monocytes in addition to drug delivery with surface-loaded particles. However, we found that high levels of uptake of core-loaded nanospheres negatively affected monocyte viability and cytokine release. Because CT requires high payloads of gold for contrast production, we explored alternative AuNP formulations for improved biocompatibility with high monocyte uptake.

In chapter 3, we examined a range of AuNP sizes (15 to 150 nm) and various surface ligands, totaling 44 distinct AuNP formulations. We sought to explore the relationship between size and surface ligand in the application of monocyte labeling.

AuNP formulations were examined for cytotoxicity and uptake by monocytes. Only the largest size, 150 nm AuNP, with polyethylene glycol (PEG) surface ligands were cytotoxic. We found the relationship between size and uptake to be specific for each surface ligand. High uptake in monocytes was seen with small (15, 25 nm) particles coated in short chain carboxylic acids. We also found a complex relationship between size and uptake for PEG-carboxylic acid coated (PEG-COOH) AuNP. High uptake in monocytes was found for intermediate sizes (50, 75 nm), but relatively low uptake at smaller and larger sizes. With synthetic efficiency and cost advantages for 15 nm particles, we choose to further proceed with this size to evaluate monocyte labeling for CT cell tracking in atherosclerosis.

With a focus on 15 nm diameter AuNP, we examined their potential as cell tracking agents for labeling monocytes. We examined an expanded library of surface ligands for stability and selected five ligands to evaluate with monocytes. Of these ligands, AuNP coated with 11-mercaptoundecanoic acid (11-MUA) did not affect monocyte viability or cytokine release, and were highly taken up by these cells (in both a monocyte cell line and primary monocytes). Therefore, we used this formulation to label primary monocytes and deliver the cells to mice with early atherosclerotic lesions. Using CT, we were able to detect a significant increase in x-ray attenuation in aortic plaques after 5 days. Sections through the aortic plaque showed the presence of gold labeled cells, reaffirming the migration to gold labeled monocytes to the plaque.

While this work demonstrated the feasibility of using AuNP constructs to track monocyte recruitment in atherosclerosis, further development is needed to improve this tool for expanded applications in monocyte tracking. Here, we discuss factors involved in the uptake and cytotoxicity seen with some AuNP formulations. We also discuss

strategies for improving monocyte detection in the atherosclerosis model and expanded uses for monocyte cell tracking. Last, we explain the barriers that need to be overcome to translate such a technology into the clinic.

5.1.2 Uptake and toxicity

One of the key features of the work presented here is the interaction between nanoparticles and cells. Specifically, the interaction between monocytes and each gold nanostructure investigated led to differing uptake and/or effects on monocyte viability/function. The work explored different structures (i.e. free and polymer nanosphere encapsulated AuNP), AuNP of differing sizes (15 to 150 nm) and a variety of gold nanoparticle surface chemistries.

In the work presented in Chapter 3, the highest uptake values in the monocyte cell line were seen with short chain carboxylic coated (11-mercaptoundecanoic acid, 11-MUA; 16-mercaptohexadecanoic acid, 16-MHA) 15 nm AuNP and intermediate sized AuNP (50, 75 nm) coated with a PEG carboxylic acid. Both the coating and size play a role in the gold uptake of the monocytes. Chithrani *et al.* also reported a size dependency of cellular AuNP uptake, with 50 nm particles being taken up to the greatest extent. In that study, the AuNP were citrate coated and uptake was examined in HeLa cells.[1-2] Other studies have also shown intermediate sized (~50 nm) AuNP to have highest cellular uptake.[3] A number of studies have sought to explain this observation. Jiang *et al.* and Chithrani *et al.* hypothesized that there is an optimal size for receptor mediated uptake of nanoparticles.[3-4] Receptor mediated uptake relies on binding of surface receptors on the cell and then “wrapping” around the bound material through invagination.[5-6] These works hypothesized that, with receptor mediated endocytosis as

the uptake route, particles (with surface adsorbed proteins) interact with surface receptors of the cell. With activation of those surface receptors, the cells “wrap” around the nanoparticle through invagination and internalize the particle. In this mechanism, smaller nanoparticles (less than 40 nm), due to low surface ligand density, do not bind to the cell surface for a long enough duration for this process to occur frequently. Conversely, larger nanoparticles (less than 70 nm) bind efficiently, but their large size presents challenges for the cell to wrap around the nanoparticle and therefore are not taken up extensively. However, intermediate sized nanoparticles (i.e. around 50 nm) have strong enough binding kinetics and their size allows for successful internalization.

This mechanism may explain the uptake profile seen with our differently sized nanoparticles. Phagocytosis, the likely uptake route of AuNP in our study, operates in a similar manner to receptor-mediated endocytosis, with binding of surface receptors and invagination for internalization of the nanoparticle. Monocytes have a family of toll-like receptors (TLR4, TLR2, TLR8) used to recognize foreign materials for phagocytosis.[7] In Chapter 3, AuNP above 25 nm in size and coated with 11-MUA aggregated severely in serum-containing media. It is likely that 15 nm 11-MUA AuNP also aggregate in serum-containing media to a certain extent, forming aggregates of an intermediate size that allow for very high uptake. This may explain why coatings that minimize aggregation such as the PEG-COOH coating result in high uptake at intermediate AuNP sizes, but low uptake at small sizes.

In addition to the size of the nanoparticles, surface ligands also play a large role in defining the biological interaction between nanoparticles and cells. Surface ligands provide stability and a surface charge (neutral, positive, negative) to the particle depending on the chemical groups of the ligand. Mammalian cells, due to the

phospholipid bi-layer, are typically negative in charge. Hence for cellular uptake, research has focused on the use of positively charged coating for preferential electrostatic interaction.[8] However, some researchers have shown cellular uptake with anionic nanoparticles to be greater than cationic nanoparticles in the same system.[9-11] This effect has been noted in greater frequency with phagocytic cells than non-phagocytic mammalian cells.[12-13] While intuitively, negatively charged nanoparticles should be repulsed by negatively charged cell membranes, researchers have shown that the adsorption of serum proteins onto the surface of the membrane drastically affects the interaction between the cell and nanoparticle.[14] In the 2006 study by Chithrani *et al.*, after incubation in serum, negatively charged AuNP were found to contain amine groups through Fourier transform infrared spectroscopy.[2] The authors attribute this finding to the amine groups contained in amino acids. Ritz *el al.* took a further step by identifying the serum proteins that adhered to polystyrene (PS) nanoparticles functionalized with different chemical groups.[15] The study evaluated a variety of surface coatings including carboxylic acids (PS-COOH), amine (PS-NH_2), or sulfates (PS-SO_3), with each nanoparticle approximately 100 nm in diameter. Apolipoproteins were found to adsorb onto all of these nanoparticles, however some proteins were found to significantly adsorb to specific formulations. For PS-COOH nanoparticles (carboxylic functional group), a significant increase in the presence of apolipoprotein-H was shown to increase the uptake of these particles with human mesenchymal stem cells. Our work presented here found highest uptake with carboxylic acid coated AuNP. Adsorption of serum proteins that aid in uptake in combination with the optimal size for uptake may explain why the highest uptake in monocytes were seen with those specific formulations. Examination of the composition of the protein corona of these nanoparticles and

consequent determination of their mechanism of uptake could be the topic of future work.

In the work presented here, some AuNP formulations exhibited cytotoxic effects at high concentrations. A number of studies have sought to elucidate the mechanisms behind the toxicities of various AuNP formulations since gold is typically described as bio-inert. The generation of reactive oxygen species (ROS) has previously been shown to be responsible for the observed cytotoxicity with nanoparticles.[16-17] A study by Chuang *et al.*, investigated the cytotoxicity of citrate capped gold nanorods (10 x 39 nm, 10 x 41 nm, 10 x 45 nm) at different concentrations in multiple mammalian cell lines.[18] The group found different mechanisms of cytotoxicity based on the cell type. For instance, these gold nanorods delayed the cell cycle for lung epithelial (A549) cells but induced apoptosis in gastric adenocarcinoma cells (AGS). These gold nanorods also increased the generation of ROS in AGS cells. However, the authors suggested that the observed increase in ROS did not induce apoptosis due to low response of anti-oxidative proteins. Another study utilizing 20 nm carboxyl-polysytrene particles demonstrated that negative nanoparticles were able to induce apoptosis and necrosis in the absence of reactive oxygen species.[19] A study by Chueh *et al.* also demonstrated that cytotoxicity of AuNP (citrate capped nanorods, 10 x 40 nm) may be dependent on the cell type.[20] After incubation with AuNP, kidney epithelial cells were found to undergo apoptosis mediated through inhibition of enzyme activity. In lung fibroblasts, arrestment of cell cycle and damage to DNA mechanisms were likely causes of cytotoxicity. Embryonic fibroblasts were found to undergo autophagy, a form of programmed cell death. Other studies have reported different mechanisms of cytotoxicity in the presence of AuNP in other cell systems.[21-23]

In this thesis, monocyte toxicity was observed with AuNP into loaded PCPP nanospheres (Chapter 2), large AuNP (Chapter 3), and PEI coated AuNP (Chapter 4). Taking into account the studies mentioned above, toxicity in instances of high uptake of AuNP may be due to arrest of cell cycle leading to apoptosis. Therefore, the toxicity we observed with AuNP loaded PCPP nanospheres and large AuNP may be due to this reason. More studies evaluating apoptosis with those formulations would be necessary to confirm this hypothesis. However, toxicity with PEI coated AuNP are likely due to the positively charged amine groups on the PEI coating. Previous reports have indicated that the high positive charge of PEI can cause toxicity at even low concentrations.[24-25]

5.1.3 Increasing sensitivity of monocyte detection

In this thesis, we systemically delivered gold labeled monocytes and after 5 days were able to detect a significant increase in CT attenuation in the region of the aorta. This increase was attributed to the migration of gold labeled monocytes from circulation to the plaque. Ex-vivo sectioning and transmission electron microscopy of the plaque revealed the presence of gold labeled cells. The change in attenuation over 5 days was 15.3 HU on average. This value is comparable to *in vivo* detection with CT contrast agents seen in other studies.[26-27] However, to be able to detect the effects of genes or drugs on modulating monocyte recruitment would likely necessitate higher changes in attenuation.

In Chapter 4, in vivo experiments were carried out using 1×10^6 labeled primary monocytes that were injected intravenously. Increasing the number of gold labeled cells for delivery may be an avenue to increase the amount of monocytes recruited to the

plaques. In preliminary studies, we trialed a 5-fold (5 x 10^6) delivery of gold labeled monocytes to apolipoprotein deficient (ApoE -/-) mice on a western diet for 10 weeks (AtT). The control groups were wild type mice injected with gold labeled monocytes (WdT) and atherosclerotic mice injected with non-labeled monocytes (AtN). Similar to the experiment in Chapter 4, the mice were CT scanned at 3, 4, and 5 days post injection. The results in Figure 5.1a show an attenuation change of 33.6 HU for the AtT group which was found to be significant ($p < .002$). Therefore, a significant increase in CT attenuation was achievable with an increase in the number of delivered gold labeled monocytes. The CT attenuation for atherosclerotic mice receiving 5 x 10^6 compared to receiving 1 x10^6 gold labeled monoyctes were also found to be significant. The biodistribution of this dose of gold labeled monocytes was similar 1 x 10^6 monocytes, with high accumulation of gold per tissue weight in the spleen (Figure 5.1b). However, mice have approximately 1 x 10^6 monocytes in blood circulation and the delivery of 5 x 10^6 monocytes may have unintended biological consequences that would require further evaluation.

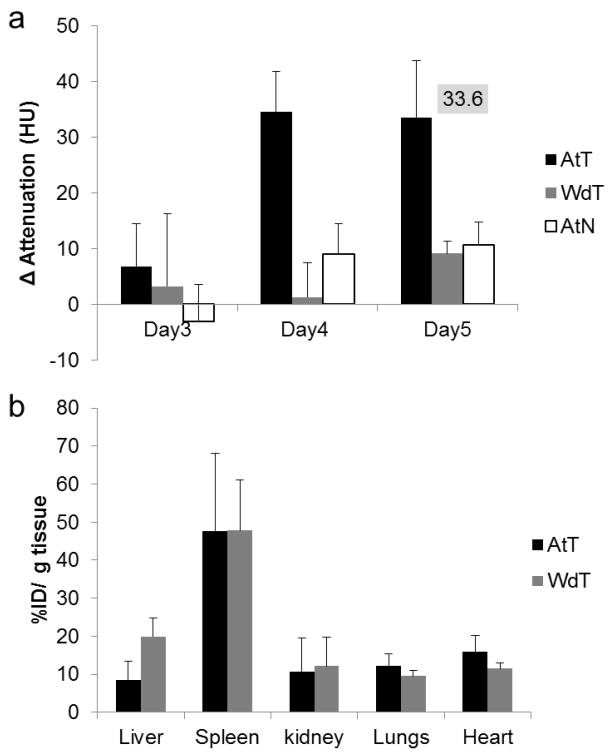

Figure 5.1 Changes in aorta attenuation and biodistribution arising from injections of 5 x 10^6 AuNP labeled monocytes.

Atherosclerotic mice defined as ApoE-/- mice kept on western diet for 10 weeks. (a) Atherosclerotic mice receiving gold labeled monocytes (AtT, n=4) show higher attenuation in aortic plaques after 5 days as compared to wild-type mice receiving gold labeled monocytes (WdT, n=3) and atherosclerotic mice receiving non-labeled monocytes (AtN, n=3). (b) Biodistribution of gold labeled monocytes in organs.

Another approach to increase the CT attenuation in the scans is to increase the number of recruited gold labeled monocytes to the plaques. In the current study, primary monocytes were isolated based on the surface marker CD11b, a conserved monocyte marker for all monocyte subtypes.[28] As mentioned in Chapter 1, there are two distinct monocyte populations conserved across species. In humans, classical “inflammatory”

monocytes are described by the presence of $CD14^+$ $CD16^-$ $CCR2^+$ $CX3CR1^-$ surface markers.[29] These monocytes have phagocytic properties and known to migrate from the circulation to inflamed tissue. The other "resident" monocyte is identified by $CD14^-$ $CD16^+$ $CCR2^-$ $CX3CR1^+$ surface markers and participate more frequently in wound healing.[30] In mice, inflammatory monocytes can be identified by $Ly6C^+$ and resident monocytes by $Ly6C^-$ markers.[31] In our studies, primary monocytes were isolated from spleens of donor mice. Swirski *et al.* analyzed the population of monocytes in the spleen, indicating that nearly 50% of the monocytes in the spleen were $Ly6C^+$.[32] By further purifying primary monocytes for the $Ly6C^+$ marker, we could isolate inflammatory monocytes for gold labeling. Injecting only inflammatory monocytes may increase the amount of gold labeled monocytes recruited to atherosclerotic plaques.

In addition to experimental changes, advances in CT technology are likely to improve the detection of gold labeled monocytes for atherosclerosis. Photon-counting CT presents the opportunity to use the k-edge of gold to improve detection of gold labeled cells.[33] This may also allow for better delineation between surrounding soft tissue and gold labeled cells in CT scans.[34-35] Advances in reconstruction methods are also likely to improve detection of gold labeled cells with improved signal to noise (SNR) in CT images. The development of iterative reconstruction methods have shown improved SNR as compared to traditional back filtered projection algorithms.[36] Iterative reconstruction may also improve detection of contrast agents in CT scans.[37] Together, the advances in CT technology are likely to improve the technology of cell tracking with CT.

5.1.4 Modulation of monocyte recruitment

With improvement to the detection of monocytes *in vivo,* we hypothesize that the technique can be used to both further assess mechanisms behind monocyte recruitment and therapies aimed at decreasing monocyte recruitment. As described in Chapter 1, monocytes play a crucial role in the progression of atherosclerosis through continued recruitment to developing plaques. Monocyte recruitment involves a number of processes including increased expression of adhesion molecules on endothelial cells and chemokine gradients for transmigration. In the intima, monocytes differentiate in macrophages and then foam cells, leading to the production of enzymes and cytokines that promote plaque rupture. Due to the pivotal roles of monocytes and macrophages in plaque progression, there has been significant interest in developing therapies that target their recruitment and atherogenic functions.

In mice, a number of studies have sought to examine the impact of plaque burden after the knocking down or therapeutically reducing the expression of key cell adhesion molecules (VCAM, ICAM, P-selectin).[38-41] For instance, Cybulsky *et al.* generated an VCAM-1 knockdown mice model to evaluate plaque formation.[42] The group observed a significant decrease in plaque formation in the whole aorta and arch (lesion area decreased by 31% and 45%, respectively) as compared mice expressing VCAM-1. The group also noted an increase in overall circulating leukocytes, including increased levels of circulating blood monocytes as compared to controls. Taken together, the authors suggested that increased blood monocytes indicate less lesional migration and therefore less plaque progression. With the development of cell tracking for monocytes, the study may have been able to confirm and quantify the reduction of monocyte recruitment in VCAM-1 knockdown mice. Interestingly in the study, the

authors show that knock down of both ICAM-1 and VCAM-1 produced similar reductions of plaque size to VCAM-1 knockdown alone. With comparing the significance of ICAM-1 versus VCAM-1 in plaque formation, the ability to quantify monocyte recruitment to plaques in each case could help elucidate the importance of each.

With the success of VCAM-1 inhibition seen in mice, researchers have explored VCAM inhibitors as possible therapeutics for coronary artery disease.[43-44] Specifically, groups have shown that natural antioxidants are able to inhibit VCAM-1 expression.[43] The anti-oxidant Succinobucol (AGI-1067) was investigated in a double-blind placebo trial for patients with acute coronary syndrome.[45] In the study, 6144 patients with either a recent myocardial infarction or unstable angina were split into Succinobucol receiving and placebo groups. However, no significant improvements were identified in the primary endpoints of severe cardiovascular events including death over 2 years. We believe that cell tracking techniques such as those demonstrated in this thesis could quickly determine the effectiveness of proposed drugs. In this study, monitoring monocyte migration over time *in vivo* may have demonstrated the drug's effectiveness or non-effectiveness on monocyte recruitment to plaques as a VCAM-1 inhibitor before launching a lengthy and costly primary outcome study.

Researchers continue to probe stages of monocyte recruitment to plaques as a possible therapeutic target for atherosclerosis. A number of pre-clinical studies have demonstrated the reduction of plaque formation in decreased expression of chemokine receptors responsible for monocyte migration through plaques (CCR2, CX3CR1, CCR5).[46-49] Similarly, clinical trials have explored inhibitors of these chemokine receptors as potential targets for plaque development. In a study with 243 patients, groups received either MLN1202 (monoclonal anti-body inhibitor of CCR2 binding to MCP-1) or

placebo.[50] The study showed reduced concentrations of serum C-reactive protein in the serum for treatment groups. C-reactive protein is a marker of inflammation and is positively correlated to the progression of atherosclerosis. The study also found a decrease in circulating monocytes with administration of MLN1202. The authors suggest reduced emigration of monocytes from the bone marrow as the cause of this result but no confirmatory data is shown. However, with real time monocyte tracking, the authors would be able to confirm their hypothesis and possibility determine if MLN1202 reduces monocyte recruitment to plaques.

In the monocyte recruitment pathway, additional potential targets continue to emerge as areas of interest. Studies have explored the effects of inhibiting transmigration targets such as junctional adhesion molecules (JAM-A) and connexins.[51-53] Monocyte-platelet interactions and macrophage migration inhibitory factor have also been explored as possible drug targets.[54-57] These studies aim to interfere with the monocyte recruitment process, but not directly observe or quantify monocyte recruitment. The monocyte cell tracking tool demonstrated in this thesis could enhance similar studies in the future via observation of monocyte localization and migration.

5.1.5 Barriers to translation

Cell tracking presents an opportunity to observe cell migration in a variety of cell based therapies. Currently, the state of cell tracking tools remains investigative with the technology under development in a breadth of applications.[58] While our technology of monocyte cell tracking with CT is in the early stages of preclinical examination, the capacity of translation into a clinical tool stands as a possibility. As mentioned in this

chapter, monocyte cell tracking could be used to assess mechanisms of monocyte recruitment or evaluate novel therapeutics targeting the recruitment pathway. In the work presented, we demonstrated the feasibility of isolating monocytes with high purity from donor animals. The cells were labeled with AuNP *ex-vivo* and delivered intravenously to atherosclerotic mice. The mice were then scanned with a preclinical CT scanner and monocytes localized to the plaques in the aorta were visualized. With the advances in clinical CT scanners and clinical cell transfer technologies, adapting our work with monocyte cell tracking to a clinical setting is a possibility.

In our studies, murine atherosclerotic plaques were visualized within the aorta using a pre-clinical scanner at 80 kVp and reconstructed at 100 µm spatial resolution (isotropic voxel). Modern clinical scanners are capable of spatial resolutions between 350 and 500 µm.[59] For translation of our technology, monocyte recruitment would likely be observed for plaque burden in the human coronary arteries. Current CT scanners are capable of resolving the coronary arteries and assessing plaque burden, therefore spatial detection of gold labeled cells in the human coronary arteries appears feasible. Additionally, clinical CT scanners are capable operating at higher energies (100 kV, 120 kV, 140 kV), which would result in greater contrast since gold's k-edge (80 keV) is within those spectra, and likely improving detection of gold labeled cells with clinical CT scanners.[60]

In a study by Dey *et al.*, the plaque burden in the human coronary arteries were quantified in patients with stable plaques and acute coronary syndrome.[45] Plaque volume was similar in both groups, 332.8 vs 334.3 mm^3, respectively. For comparison, the average volume of plaques measured in mouse aortas was 107.1 mm^3 based on estimations from our CT scans. In our mice, the average change in attenuation in the

plaque was 15.3 HU. From our *in vitro* cell dispersions from Chapter 4, we correlated this attenuation to approximately 15 cells/voxel (0.1 mm isotropic voxel). With approximation of plaque size in the mice (107.1 mm^3), we estimate that a change of 15.3 HU correlates to 1.07 x 10^3 gold labeled monocytes in the plaque. Theoretically for human coronary plaques, a similar change in attenuation measurement would require recruitment of 3.32 x 10^3 gold labeled monocytes based on coronary plaque volume (332.8 mm^3).

A significant barrier in the translation of this technology would be the isolation of monocytes from the patient for labeling. In our study, 1.0 x 10^6 gold labeled monocytes were delivered intravenously and localized to aortic plaques in mice. In mice, approximately 1.0 x 10^6 monocytes are present in circulation.[61] In humans, the number of circulating monocytes range from 1.0 to 5.0 x 10^9 cells.[62] For similar ratios as our mice experiments, a cell delivery of 1.0 x 10^9 gold labeled monocytes may prove challenging. However, with recent advancements in cell therapeutics, isolating and purifying this magnitude of cells (10^9) has been demonstrated.[63-64] Currently, dendritic cells are being explored as clinical cell treatments for a number of diseases including cancer.[65-67] The process of acquiring dendritic cells for cell therapy begins with the isolation of monocytes from patients through a process of leukapheresis.[68-69] This process involves collecting blood continuously, filtering out desired cells, and returning the remaining constituents to the patient. Recent technology developments utilizing elutriation for purification have yielded 10^9 monocytes in highly purified populations.[70] The technologies show that acquiring monocytes from patients for *ex-vivo* labeling is achievable.

After acquiring cells from the patient, the process of *ex-vivo* labeling with AuNP could face challenges involving the cost of gold and scaled up manufacturing. For our

current labeling experiments, we used a ratio of 0.5 mg of AuNP for 1 x 10^6 cells (0.5 mg:1 million cells). To label 1.0 x 10^9 cells under the same conditions, 500 mg of AuNP would be required. Previously in our lab, we have synthesized large batches of AuNP through the Turkevich method (1280 mg gold chloride trihydrate, $HAuCl_4$). With 20% efficiency from $HAuCl_4$ to purified and capped AuNP, we can achieve approximately 250 mg of AuNP in a single batch. However, each batch requires 3 days to complete. As of this writing, the cost of $HAuCl_4$ is $1600 USD for 25 g (Gold(III) chloride trihydrate, G4022-25G, Sigma-Aldrich, St. Louis, MO). Therefore, synthesis of AuNP for labeling of 1 x 10^9 cells, would require $HAuCl_4$ costing approximately $160 and 6 days to complete. These estimations are with the current procedures that would likely be refined for large scale manufacturing as a clinical tool. The process of *ex-vivo* labeling with AuNP for translation into the clinic appears feasible with these estimations.

With the current state of the CT scanners and technologies involved with adoptive cell therapies, our technology appears to be translatable into clinical tool. However, currently the cost and technical difficulty of the clinical procedures list above constrain the realistic translational of our technology into a clinical tool. These procedures continue to be reserved for experimental adoptive cell treatments and determining their efficacy *i.e.* T-CAR cell immuno-therapy and dendritic cell vaccines. With continued research and advancement, there may be a time where utility of monocyte cell tracking to investigate the efficacy of atherosclerotic drugs outweigh the challenges of these clinical procedures.

5.2 Future directions

5.2.1 Overview

The ability to track the location and migration of cells *in vivo* is an emerging tool of need, providing valuable information in the study of disease mechanisms and assessment of treatment effectiveness. In our work, the successful tracking of monocytes with CT opens a number of opportunities to not only study monocyte behavior, but the possibility of additional cells in different applications. Here I discuss future directions of the work and potential avenues for future projects. I will describe the potential use of monocyte tracking to study their role in myocardial infarction wound healing. I will examine alternative labeling strategies for monocytes and the potential applications for these approaches. Additionally, I discuss other cell types that would be interesting to track in atherosclerosis. Finally, I discuss the potential use of AuNP to track other cell types in other disease applications.

5.2.2 Myocardial infarction

Monocytes have several functional roles in the progression of coronary artery disease. In this thesis, we explored tracking the recruitment of monocytes to developing plaques. In addition, monocytes play a large role in wound healing after a myocardial infarct. Immediately following the infarct, monocytes are recruited from the circulation to the injured tissue. Evidence has shown that this recruitment period for wound healing consists of two overlapping phases.[71] The first phase is dominated by the recruitment of an inflammatory monocyte subset for phagocytosis and clearing of necrotic tissue, lasting for 1-4 days post infarction. From day 4 onwards, the anti-inflammatory monocyte

subset or “residential” monocytes are most present in the infarct. These monocytes are necessary for wound healing and tissue repair. This phenomenon was demonstrated in mice by Nahrendorf *et al.* with Ly-6c^{+} and Ly-6c^{-} monocyte subsets.[72] The authors suggest that this bi-phasic recruitment of monocytes is due to shifts in chemokine expression in the infarct tissue that favor each monocyte subtype at different times. The release of MCP-1 (CCR ligand) promotes Ly-6c^{+} monocyte recruitment initially and a subsequent shift to fractalkine (CX3CR1 ligand) release promotes Ly-6c^{-} monocyte recruitment. This bi-phasic monocyte recruitment has also been studied in human myocardial infarcts with CD14^{++}CD16^{-} (inflammatory) and CD14^{+}CD16^{+} (anti-inflammatory) monocytes subsets. The recruitment of monocytes in both phases are critical to proper wound healing as studies with increased inflammatory monocyte recruitment have shown poorer outcomes in left ventricular remodeling.[73-75] In our work, the development of monocyte cell tracking can be directly applied to studying monocyte recruitment after a myocardial infarction. There has been continued interest in developing cell tracking methods for cell therapy for myocardial infarction.[76]

In preliminary studies, we labeled primary monocytes with AuNP via *ex-vivo* incubation for 24 hours. Afterwards these cells were directly injected into the infarct region of mice post myocardial infarction. After 5 days, the hearts were excised and scanned with a microCT scanner. The results in Figure 5.2 show localized high CT attenuation areas in the infarct region indicating the persistence of gold labeled monocytes in the region. Further experiments could demonstrate the migratory process of gold labeled monocytes to infarct regions after intravenous delivery. With this development, monocyte tracking could potentially be used to study therapies that modulate monocyte recruitment and may alter wound healing outcomes in the infarct.

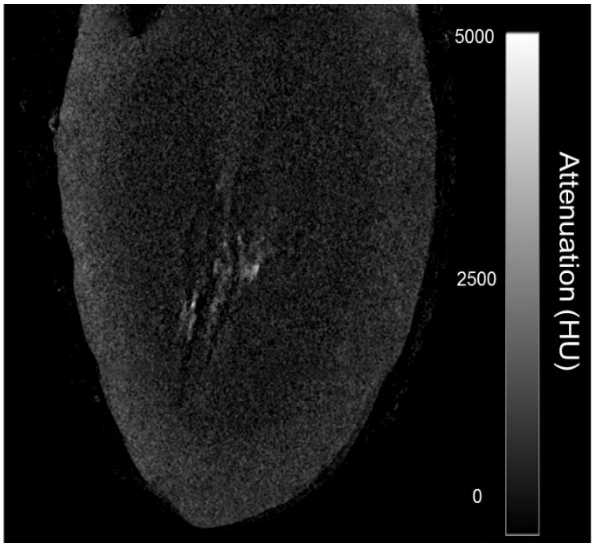

Figure 5.2 Gold labeled monocytes in myocardial infarct.
Monocytes were labeled with AuNP and directly injected into infarct region. Heart was excised 5 days post-injection and scanned with CT.

5.2.3 In-situ spleen labeling

In our studies, cells are isolated from the spleens of donor mice and labeled with AuNP *ex-vivo*. As mentioned, *ex-vivo* labeling remains a strategy that may procedurally translate clinically for adoptive cell therapies. However, this procedure requires the isolation of cells before labeling which can be technically challenging. A cell tracking agent that could label specific cells *in-situ* would be advantageous.

For monocyte labeling, we observed the high trafficking of AuNP to the spleen after intravenous delivery. The spleen has been shown as a major reservoir for monocytes containing as much as 50% of the total monocyte population.[32, 77] The monocytes are held in the red pulp with arterial access in the spleen. Studies have demonstrated that upon significant injury, monocytes in the spleen are deployed into circulation to address the wound.[78-79] A study by van der Laan *et al.*, studied the

recruitment of monocytes after myocardial infarction in humans.[80] The group found an abundance of $CD14^{+}CD16^{-}$ cells (markers for inflammatory monocytes) in the border zone during the inflammatory recruitment phase. During this inflammatory phase (>3 day post infarct), the authors also found a decrease in $CD14^{+}$ cells in the spleen and an increase in the blood circulation. Taken together, the results suggest that early after a myocardial infarction, monocytes are released into circulation and are recruited into the surrounding infarct region for repair.

We hypothesis a cell tracking method could be developed to label monocytes in the spleen before deployment to sites of inflammation. In preliminary studies, we intravenously injected AuNP coated with methoxy-poly(ethylene glycol) (AuNP-MPEG, 250 mg/kg) into wild type mice. The mice were scanned with CT over 48 hours after which they were dissected for biodistribution afterwards. The spleen was excised and monocytes were purified through magnetic labeling for CD11b similar to methods in Chapter 4. The monocytes were collected and ICP-OES was run to determine if AuNP were present in the isolated monocyte fraction.

In Figure 5.3a, CT images are shown of the abdomen and thorax acquired over a 48 hour period pre- and post-injection of AuNP. There is a significant increase in attenuation in the spleen over this time period. The scans also show initial increases in attenuation in the vasculature and heart, reflection the presence of the AuNP in the circulation. After 48 hours, the attenuation in the spleen remained high, indicating AuNP accumulation. This organ was excised and monocytes were isolated. We found higher gold uptake in the enriched monocyte population, as compared to the discarded cell fraction (Figure 5.3b). This indicates that AuNP from intravenous injection were taken up

by monocytes in the spleen. Figure 5.3c shows the biodistribution after 48 hours with AuNP taken up to the greatest extent by the liver.

The uptake of AuNP in our purified monocyte population indicates that labeling of monocytes in the spleen may be achievable. However, the uptake of approximately 4 pg/cell is considerably less than our *ex-vivo* labeling uptake values of 126 pg/cell. Further experiments on different AuNP formulations may be explored to improve uptake for the monocytes in the spleen. In this study, mPEG was used to provide long circulation for the AuNP; however mPEG is well known to minimize cell uptake, which may have contributed to low monocyte uptake values. Eventually, with adequate uptake in monocytes for detection, we envision pre-labeling monocytes in the spleen. Afterwards, we expect a significant injury leading to a strong inflammatory response will allow for detection of monocytes migrating from the spleen to the site of injury, as in the case of myocardial infarction. This cell tracking approach would open opportunities in studying monocyte response to various inflammation reactions, including the timing and magnitude of monocyte responses.

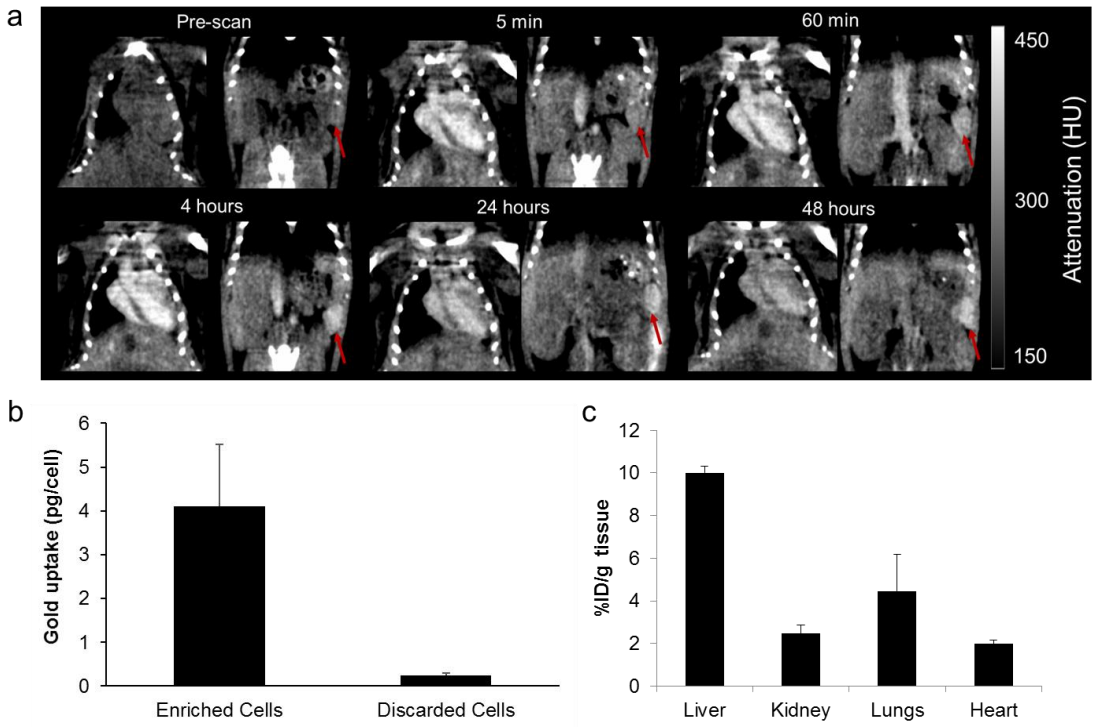

Figure 5.3 In-situ labeling of monocytes in the spleen.

Wild-type mice received intravenous injections of AuNP-mPEG (250 mg/kg). (a) CT scans of mice pre-injection, 5 minutes, 60 minutes, 4 hours, 24 hours, and 48 hours post injection. Red arrows indicate the location of spleen. (b) ICP-OES quantification of gold uptake in monocyte enriched populations versus discarded cell populations. (c) Biodistribution of AuNP-mPEG after 48 hours.

5.2.4 Alternative cell tracking for atherosclerosis

In our work, we focused on the role of monocytes in the progression of atherosclerosis. While monocyte recruitment contributes significantly to plaque progression, it is only one part of the inflammation story in atherosclerosis. A number of different cells, especially other leukocytes including neutrophils, dendritic cells, platelets

and T-cells, have been found contribute to plaque progression due to their association with inflammation.[81-82] Similar to monocytes, the increase in expression of cellular adhesion molecules on endothelial cells promotes the adherence and extravasation of leukocytes into the vessel wall. The work with monocyte tracking with CT could be expanded to other cells playing a role in atherosclerosis.

Neutrophils are essential to the innate immune system and typically are the "first responders" to acute injury sites. More recently, the role of neutrophils in chronic diseases have attracted attention due their ability to release a number of different cell modulators including various cytokines.[83-84] In atherosclerosis, neutrophil adherence and rolling relies on several chemokine receptors on their surface including CCR2, CXCR2 and CCR5.[85-86] Recent studies have shown that neutrophils play a role in recruiting monocytes to atherosclerotic lesions. In Cramp (neutrophil secreted protein) deficient mice, a reduction of early plaque formation was observed due to reduced monocytes recruitment.[87] Other neutrophil secreted factors including cathepsin G and α-defensins also have shown to play role in driving monocyte recruitment into plaques.[88-90] Neutrophils have also demonstrated compounding effects to atherosclerosis progression including increasing endothelial dysfunction at plaque prone sites and promoting foam cell formation of lesional macrophages.[91-92] Neutrophils represent a possible candidate for CT cell tracking to allow further elucidation of their role in plaque progression.

Along with monocytes, T-cells undergo recruitment to developing plaques through adherence to VCAM-1 and migration through CX3CR1 cell surface marker.[81] In the plaque, with exposure to abundant low density lipids, T-cells differentiate into T-1 helper cells (T_H1).[93] T_H1 cells have been shown to be atherogenic with release of pro-inflammatory cytokines including interferon-γ (IFN-γ), interleukin-12, and interleukin-

18.[94-96] Particularly, the release of IFN-γ can exacerbate plaque instability by further amplifying macrophage/foam cell release of degradation enzymes and proteases.[97-98] Also found in lesions were the presence of T-2 helper cells (T_H2) and T-17 helper cells (T_H17). However, the atherogenic or atheroprotective roles of these cells remain unclear.[99] More recently, the role of T-regulatory (T_{reg}) cells have become a point of investigation in atherosclerosis due to their auto-immunity protective properties. T_{reg} cells have been found to have several functions in atherosclerosis including inhibiting foam cell formation, inhibiting macrophage activation, and inhibiting atherogenic properties of T_H1 cells.[100-103] The effects of T_{reg} cells are mostly accomplished through the release of anti-inflammatory cytokines, interleukin-10 and transforming growth factor-β.[104-105] Inhibition of these cytokines has shown accelerated plaque progression.[106-107] Interestingly, T_{reg} cells are found in low concentrations in plaques as compared to other inflammatory diseases, implying a suppression of their presence under atherosclerotic disease conditions.[108-109] Therefore, there is considerable interest in utilizing T_{reg} cells as a potential cell therapy for atherosclerosis.[110-111] Studies enhancing migration of T_{reg} cells to atherosclerosis may greatly benefit from similar cell tracking tools developed in our work. Cell tracking may also help further elucidate the effects of T-helper cells by altering their plaque migratory properties.

5.2.5 Alternative CT cell tracking applications

X-ray computed tomography with high spatial and temporal resolution allows for imaging of the human coronary arteries and is therefore a preferred choice in developing cell tracking tools for the study of atherosclerosis. However, with advances in photon

counting CT, especially in material decomposition, the utility of cell tracking can be further expanded.

In a collaboration with Marlène Wiart from the Center for National Research (Lyon, France), we are exploring the use of our AuNP to track macrophages in the treatment of stroke. The work entails utilizing a gadolinium labeled scaffold to deliver AuNP labeled macrophages to the site of injury. The use of photon-counting CT allows for the discrimination between gold labeled macrophages and the gadolinium scaffold. This could provide information on cell migration from the scaffold to injured areas. While studies are still preliminary, the successful labeling of macrophages and their detection with photon-counting CT have been demonstrated (Figure 5.4).

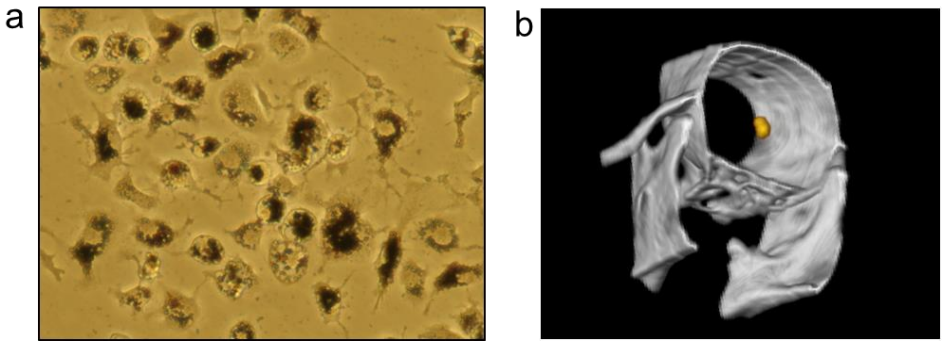

Figure 5.4 Gold labeling of macrophages for stroke cell therapies.
(a) Labeling of primary macrophages with AuNP. (b) Detection of gold labeling macrophages using single photon counting CT. 3D overlay of gold specific image (yellow) on a conventional CT image (greyscale) with an injection of AuNP labeled macrophages in the brain

5.3 Concluding remarks

The work of monocyte cell tracking for CT, the improvement of labeling techniques has the opportunity for this tool to be utilized to study atherosclerotic mechanisms and therapies. The work reported in this thesis is the initial steps in using CT cell tracking to study monocyte recruitment. Overall, I think this work is a significant development in the use of CT as a cell tracking method, which has been relatively unexplored compared to MRI and PET. Few studies have reported the use of CT for cell tracking, but with rapidly improving CT technology, I believe that this field will grow, especially with the use of photon counting CT and material decomposition. With further research, I envisage that cell tracking will emerge as a valuable tool for the development and implementation of clinical cell therapies.

5.4 References

1. Chithrani, D. B., Intracellular uptake, transport, and processing of gold nanostructures. *Mol Membr Biol* **2010,** *27* (7), 299-311.

2. Chithrani, B. D.; Ghazani, A. A.; Chan, W. C., Determining the size and shape dependence of gold nanoparticle uptake into mammalian cells. *Nano Lett* **2006,** *6* (4), 662-668.

3. Chithrani, B. D.; Chan, W. C., Elucidating the mechanism of cellular uptake and removal of protein-coated gold nanoparticles of different sizes and shapes. *Nano Lett* **2007,** *7* (6), 1542-1550.

4. Jiang, W.; Kim, B. Y.; Rutka, J. T.; Chan, W. C., Nanoparticle-mediated cellular response is size-dependent. *Nat Nanotechnol* **2008,** *3* (3), 145-150.

5. Gao, H.; Shi, W.; Freund, L. B., Mechanics of receptor-mediated endocytosis. *Proc Natl Acad Sci U S A* **2005,** *102* (27), 9469-9474.

6. Shi, W.; Wang, J.; Fan, X.; Gao, H., Size and shape effects on diffusion and absorption of colloidal particles near a partially absorbing sphere: implications for uptake of nanoparticles in animal cells. *Phys Rev E Stat Nonlin Soft Matter Phys* **2008,** *78* (6 Pt 1), 061914.

7. Dale, D. C.; Boxer, L.; Liles, W. C., The phagocytes: neutrophils and monocytes. *Blood* **2008,** *112* (4), 935-945.

8. Lee, K. D.; Nir, S.; Papahadjopoulos, D., Quantitative analysis of liposome-cell interactions in vitro: rate constants of binding and endocytosis with suspension and adherent J774 cells and human monocytes. *Biochemistry* **1993,** *32* (3), 889-899.

9. Jiang, X.; Musyanovych, A.; Rocker, C.; Landfester, K.; Mailander, V.; Nienhaus, G. U., Specific effects of surface carboxyl groups on anionic polystyrene particles in their interactions with mesenchymal stem cells. *Nanoscale* **2011,** *3* (5), 2028-2035.

10. Frohlich, E., The role of surface charge in cellular uptake and cytotoxicity of medical nanoparticles. *Int J Nanomedicine* **2012,** *7*, 5577-5591.

11. Jiang, X.; Dausend, J.; Hafner, M.; Musyanovych, A.; Rocker, C.; Landfester, K.; Mailander, V.; Nienhaus, G. U., Specific effects of surface amines on polystyrene nanoparticles in their interactions with mesenchymal stem cells. *Biomacromolecules* **2010,** *11* (3), 748-753.

12. Champion, J. A.; Walker, A.; Mitragotri, S., Role of particle size in phagocytosis of polymeric microspheres. *Pharm Res* **2008,** *25* (8), 1815-1821.

13. Lunov, O.; Syrovets, T.; Loos, C.; Beil, J.; Delacher, M.; Tron, K.; Nienhaus, G. U.; Musyanovych, A.; Mailander, V.; Landfester, K., et al., Differential uptake of functionalized polystyrene nanoparticles by human macrophages and a monocytic cell line. *ACS Nano* **2011,** *5* (3), 1657-1669.

14. Cai, H.; Yao, P., Gold nanoparticles with different amino acid surfaces: Serum albumin adsorption, intracellular uptake and cytotoxicity. *Colloids Surf B Biointerfaces* **2014,** *123*, 900-906.

15. Ritz, S.; Schottler, S.; Kotman, N.; Baier, G.; Musyanovych, A.; Kuharev, J.; Landfester, K.; Schild, H.; Jahn, O.; Tenzer, S., et al., Protein corona of nanoparticles: distinct proteins regulate the cellular uptake. *Biomacromolecules* **2015,** *16* (4), 1311-1321.

16. Ahmad, J.; Ahamed, M.; Akhtar, M. J.; Alrokayan, S. A.; Siddiqui, M. A.; Musarrat, J.; Al-Khedhairy, A. A., Apoptosis induction by silica nanoparticles mediated

through reactive oxygen species in human liver cell line HepG2. *Toxicol Appl Pharmacol* **2012,** *259* (2), 160-168.

17. Passagne, I.; Morille, M.; Rousset, M.; Pujalte, I.; L'Azou, B., Implication of oxidative stress in size-dependent toxicity of silica nanoparticles in kidney cells. *Toxicology* **2012,** *299* (2-3), 112-124.

18. Chuang, S. M.; Lee, Y. H.; Liang, R. Y.; Roam, G. D.; Zeng, Z. M.; Tu, H. F.; Wang, S. K.; Chueh, P. J., Extensive evaluations of the cytotoxic effects of gold nanoparticles. *Biochim Biophys Acta* **2013,** *1830* (10), 4960-4973.

19. Frohlich, E.; Samberger, C.; Kueznik, T.; Absenger, M.; Roblegg, E.; Zimmer, A.; Pieber, T. R., Cytotoxicity of nanoparticles independent from oxidative stress. *J Toxicol Sci* **2009,** *34* (4), 363-375.

20. Chueh, P. J.; Liang, R. Y.; Lee, Y. H.; Zeng, Z. M.; Chuang, S. M., Differential cytotoxic effects of gold nanoparticles in different mammalian cell lines. *J Hazard Mater* **2014,** *264*, 303-312.

21. Coradeghini, R.; Gioria, S.; Garcia, C. P.; Nativo, P.; Franchini, F.; Gilliland, D.; Ponti, J.; Rossi, F., Size-dependent toxicity and cell interaction mechanisms of gold nanoparticles on mouse fibroblasts. *Toxicol Lett* **2013,** *217* (3), 205-216.

22. Cui, W.; Li, J.; Zhang, Y.; Rong, H.; Lu, W.; Jiang, L., Effects of aggregation and the surface properties of gold nanoparticles on cytotoxicity and cell growth. *Nanomedicine* **2012,** *8* (1), 46-53.

23. Pan, Y.; Neuss, S.; Leifert, A.; Fischler, M.; Wen, F.; Simon, U.; Schmid, G.; Brandau, W.; Jahnen-Dechent, W., Size-dependent cytotoxicity of gold nanoparticles. *Small* **2007,** *3* (11), 1941-1949.

24. Moghimi, S. M.; Symonds, P.; Murray, J. C.; Hunter, A. C.; Debska, G.; Szewczyk, A., A two-stage poly(ethylenimine)-mediated cytotoxicity: implications for gene transfer/therapy. *Mol Ther* **2005,** *11* (6), 990-995.

25. Fischer, D.; Li, Y.; Ahlemeyer, B.; Krieglstein, J.; Kissel, T., In vitro cytotoxicity testing of polycations: influence of polymer structure on cell viability and hemolysis. *Biomaterials* **2003,** *24* (7), 1121-1131.

26. Hyafil, F.; Cornily, J. C.; Feig, J. E.; Gordon, R.; Vucic, E.; Amirbekian, V.; Fisher, E. A.; Fuster, V.; Feldman, L. J.; Fayad, Z. A., Noninvasive detection of macrophages using a nanoparticulate contrast agent for computed tomography. *Nat Med* **2007,** *13* (5), 636-641.

27. Eck, W.; Nicholson, A. I.; Zentgraf, H.; Semmler, W.; Bartling, S., Anti-CD4-targeted gold nanoparticles induce specific contrast enhancement of peripheral lymph nodes in X-ray computed tomography of live mice. *Nano Lett* **2010,** *10* (7), 2318-2322.

28. Gordon, S.; Taylor, P. R., Monocyte and macrophage heterogeneity. *Nat Rev Immunol* **2005,** *5* (12), 953-964.

29. Geissmann, F.; Jung, S.; Littman, D. R., Blood monocytes consist of two principal subsets with distinct migratory properties. *Immunity* **2003,** *19* (1), 71-82.

30. Passlick, B.; Flieger, D.; Ziegler-Heitbrock, H. W., Identification and characterization of a novel monocyte subpopulation in human peripheral blood. *Blood* **1989,** *74* (7), 2527-2534.

31. Yang, J.; Zhang, L.; Yu, C.; Yang, X. F.; Wang, H., Monocyte and macrophage differentiation: circulation inflammatory monocyte as biomarker for inflammatory diseases. *Biomark Res* **2014,** *2* (1), 1.

32. Swirski, F. K.; Nahrendorf, M.; Etzrodt, M.; Wildgruber, M.; Cortez-Retamozo, V.; Panizzi, P.; Figueiredo, J. L.; Kohler, R. H.; Chudnovskiy, A.; Waterman, P., et al., Identification of splenic reservoir monocytes and their deployment to inflammatory sites. *Science* **2009,** *325* (5940), 612-616.

33. Schirra, C. O.; Brendel, B.; Anastasio, M. A.; Roessl, E., Spectral CT: a technology primer for contrast agent development. *Contrast Media Mol Imaging* **2014,** *9* (1), 62-70.

34. Roessl, E.; Brendel, B.; Engel, K. J.; Schlomka, J. P.; Thran, A.; Proksa, R., Sensitivity of photon-counting based K-edge imaging in X-ray computed tomography. *IEEE Trans Med Imaging* **2011,** *30* (9), 1678-1690.

35. Cormode, D. P.; Roessl, E.; Thran, A.; Skajaa, T.; Gordon, R. E.; Schlomka, J. P.; Fuster, V.; Fisher, E. A.; Mulder, W. J.; Proksa, R., et al., Atherosclerotic plaque composition: analysis with multicolor CT and targeted gold nanoparticles. *Radiology* **2010,** *256* (3), 774-782.

36. Singh, S.; Khawaja, R. D.; Pourjabbar, S.; Padole, A.; Lira, D.; Kalra, M. K., Iterative image reconstruction and its role in cardiothoracic computed tomography. *J Thorac Imaging* **2013,** *28* (6), 355-367.

37. Bernstein, A. L.; Dhanantwari, A.; Jurcova, M.; Cheheltani, R.; Naha, P. C.; Ivanc, T.; Shefer, E.; Cormode, D. P., Improved sensitivity of computed tomography towards iodine and gold nanoparticle contrast agents via iterative reconstruction methods. *Sci Rep* **2016,** *6*, 26177.

38. Dansky, H. M.; Barlow, C. B.; Lominska, C.; Sikes, J. L.; Kao, C.; Weinsaft, J.; Cybulsky, M. I.; Smith, J. D., Adhesion of monocytes to arterial endothelium and

initiation of atherosclerosis are critically dependent on vascular cell adhesion molecule-1 gene dosage. *Arterioscler Thromb Vasc Biol* **2001,** *21* (10), 1662-1667.

39. Kumar, A.; Hoover, J. L.; Simmons, C. A.; Lindner, V.; Shebuski, R. J., Remodeling and neointimal formation in the carotid artery of normal and P-selectin-deficient mice. *Circulation* **1997,** *96* (12), 4333-4342.

40. Nageh, M. F.; Sandberg, E. T.; Marotti, K. R.; Lin, A. H.; Melchior, E. P.; Bullard, D. C.; Beaudet, A. L., Deficiency of inflammatory cell adhesion molecules protects against atherosclerosis in mice. *Arterioscler Thromb Vasc Biol* **1997,** *17* (8), 1517-1520.

41. Patel, S. S.; Thiagarajan, R.; Willerson, J. T.; Yeh, E. T., Inhibition of alpha4 integrin and ICAM-1 markedly attenuate macrophage homing to atherosclerotic plaques in ApoE-deficient mice. *Circulation* **1998,** *97* (1), 75-81.

42. Cybulsky, M. I.; Iiyama, K.; Li, H.; Zhu, S.; Chen, M.; Iiyama, M.; Davis, V.; Gutierrez-Ramos, J. C.; Connelly, P. W.; Milstone, D. S., A major role for VCAM-1, but not ICAM-1, in early atherosclerosis. *J Clin Invest* **2001,** *107* (10), 1255-1262.

43. Schreiner, E. P.; Kern, M.; Steck, A.; Foster, C. A., Synthesis of ether analogues derived from HUN-7293 and evaluation as inhibitors of VCAM-1 expression. *Bioorg Med Chem Lett* **2004,** *14* (19), 5003-5006.

44. Besemer, J.; Harant, H.; Wang, S.; Oberhauser, B.; Marquardt, K.; Foster, C. A.; Schreiner, E. P.; de Vries, J. E.; Dascher-Nadel, C.; Lindley, I. J., Selective inhibition of cotranslational translocation of vascular cell adhesion molecule 1. *Nature* **2005,** *436* (7048), 290-293.

45. Dey, D.; Achenbach, S.; Schuhbaeck, A.; Pflederer, T.; Nakazato, R.; Slomka, P. J.; Berman, D. S.; Marwan, M., Comparison of quantitative atherosclerotic plaque

burden from coronary CT angiography in patients with first acute coronary syndrome and stable coronary artery disease. *J Cardiovasc Comput Tomogr* **2014,** *8* (5), 368-374.

46. Boring, L.; Gosling, J.; Cleary, M.; Charo, I. F., Decreased lesion formation in CCR2-/- mice reveals a role for chemokines in the initiation of atherosclerosis. *Nature* **1998,** *394* (6696), 894-897.

47. Combadiere, C.; Potteaux, S.; Gao, J. L.; Esposito, B.; Casanova, S.; Lee, E. J.; Debre, P.; Tedgui, A.; Murphy, P. M.; Mallat, Z., Decreased atherosclerotic lesion formation in CX3CR1/apolipoprotein E double knockout mice. *Circulation* **2003,** *107* (7), 1009-1016.

48. Combadiere, C.; Potteaux, S.; Rodero, M.; Simon, T.; Pezard, A.; Esposito, B.; Merval, R.; Proudfoot, A.; Tedgui, A.; Mallat, Z., Combined inhibition of CCL2, CX3CR1, and CCR5 abrogates Ly6C(hi) and Ly6C(lo) monocytosis and almost abolishes atherosclerosis in hypercholesterolemic mice. *Circulation* **2008,** *117* (13), 1649-1657.

49. Tacke, F.; Alvarez, D.; Kaplan, T. J.; Jakubzick, C.; Spanbroek, R.; Llodra, J.; Garin, A.; Liu, J.; Mack, M.; van Rooijen, N., et al., Monocyte subsets differentially employ CCR2, CCR5, and CX3CR1 to accumulate within atherosclerotic plaques. *J Clin Invest* **2007,** *117* (1), 185-194.

50. Gilbert, J.; Lekstrom-Himes, J.; Donaldson, D.; Lee, Y.; Hu, M.; Xu, J.; Wyant, T.; Davidson, M.; Group, M. L. N. S., Effect of CC chemokine receptor 2 CCR2 blockade on serum C-reactive protein in individuals at atherosclerotic risk and with a single nucleotide polymorphism of the monocyte chemoattractant protein-1 promoter region. *Am J Cardiol* **2011,** *107* (6), 906-911.

51. Kwak, B. R.; Veillard, N.; Pelli, G.; Mulhaupt, F.; James, R. W.; Chanson, M.; Mach, F., Reduced connexin43 expression inhibits atherosclerotic lesion formation in low-density lipoprotein receptor-deficient mice. *Circulation* **2003,** *107* (7), 1033-1039.

52. Ostermann, G.; Fraemohs, L.; Baltus, T.; Schober, A.; Lietz, M.; Zernecke, A.; Liehn, E. A.; Weber, C., Involvement of JAM-A in mononuclear cell recruitment on inflamed or atherosclerotic endothelium: inhibition by soluble JAM-A. *Arterioscler Thromb Vasc Biol* **2005,** *25* (4), 729-735.

53. Zernecke, A.; Liehn, E. A.; Fraemohs, L.; von Hundelshausen, P.; Koenen, R. R.; Corada, M.; Dejana, E.; Weber, C., Importance of junctional adhesion molecule-A for neointimal lesion formation and infiltration in atherosclerosis-prone mice. *Arterioscler Thromb Vasc Biol* **2006,** *26* (2), e10-13.

54. Afek, A.; Kogan, E.; Maysel-Auslender, S.; Mor, A.; Regev, E.; Rubinstein, A.; Keren, G.; George, J., Clopidogrel attenuates atheroma formation and induces a stable plaque phenotype in apolipoprotein E knockout mice. *Microvasc Res* **2009,** *77* (3), 364-369.

55. da Costa Martins, P.; van den Berk, N.; Ulfman, L. H.; Koenderman, L.; Hordijk, P. L.; Zwaginga, J. J., Platelet-monocyte complexes support monocyte adhesion to endothelium by enhancing secondary tethering and cluster formation. *Arterioscler Thromb Vasc Biol* **2004,** *24* (1), 193-199.

56. Pan, J. H.; Sukhova, G. K.; Yang, J. T.; Wang, B.; Xie, T.; Fu, H.; Zhang, Y.; Satoskar, A. R.; David, J. R.; Metz, C. N., et al., Macrophage migration inhibitory factor deficiency impairs atherosclerosis in low-density lipoprotein receptor-deficient mice. *Circulation* **2004,** *109* (25), 3149-3153.

57. Schober, A.; Bernhagen, J.; Thiele, M.; Zeiffer, U.; Knarren, S.; Roller, M.; Bucala, R.; Weber, C., Stabilization of atherosclerotic plaques by blockade of macrophage migration inhibitory factor after vascular injury in apolipoprotein E-deficient mice. *Circulation* **2004,** *109* (3), 380-385.

58. Ngen, E. J.; Artemov, D., Advances in Monitoring Cell-Based Therapies with Magnetic Resonance Imaging: Future Perspectives. *Int J Mol Sci* **2017,** *18* (1).

59. Otero, H. J.; Steigner, M. L.; Rybicki, F. J., The "post-64" era of coronary CT angiography: understanding new technology from physical principles. *Radiol Clin North Am* **2009,** *47* (1), 79-90.

60. Galper, M. W.; Saung, M. T.; Fuster, V.; Roessl, E.; Thran, A.; Proksa, R.; Fayad, Z. A.; Cormode, D. P., Effect of computed tomography scanning parameters on gold nanoparticle and iodine contrast. *Invest Radiol* **2012,** *47* (8), 475-481.

61. Nemzek, J. A.; Bolgos, G. L.; Williams, B. A.; Remick, D. G., Differences in normal values for murine white blood cell counts and other hematological parameters based on sampling site. *Inflamm Res* **2001,** *50* (10), 523-527.

62. Johnson, W. D., Jr.; Mei, B.; Cohn, Z. A., The separation, long-term cultivation, and maturation of the human monocyte. *J Exp Med* **1977,** *146* (6), 1613-1626.

63. Fesnak, A.; Lin, C.; Siegel, D. L.; Maus, M. V., CAR-T Cell Therapies From the Transfusion Medicine Perspective. *Transfus Med Rev* **2016,** *30* (3), 139-145.

64. Krug, C.; Wiesinger, M.; Abken, H.; Schuler-Thurner, B.; Schuler, G.; Dorrie, J.; Schaft, N., A GMP-compliant protocol to expand and transfect cancer patient T cells with mRNA encoding a tumor-specific chimeric antigen receptor. *Cancer Immunol Immunother* **2014,** *63* (10), 999-1008.

65. Coelho, A. V.; de Moura, R. R.; Kamada, A. J.; da Silva, R. C.; Guimaraes, R. L.; Brandao, L. A.; de Alencar, L. C.; Crovella, S., Dendritic Cell-Based Immunotherapies to Fight HIV: How Far from a Success Story? A Systematic Review and Meta-Analysis. *Int J Mol Sci* **2016,** *17* (12).

66. Fujii, S.; Takayama, T.; Asakura, M.; Aki, K.; Fujimoto, K.; Shimizu, K., Dendritic cell-based cancer immunotherapies. *Arch Immunol Ther Exp (Warsz)* **2009,** *57* (3), 189-198.

67. Matsue, H.; Morita, A.; Matsue, K.; Takashima, A., New technologies toward dendritic cell-based cancer immunotherapies. *J Dermatol* **1999,** *26* (11), 757-763.

68. Cao, H.; Verge, V.; Baron, C.; Martinache, C.; Leon, A.; Scholl, S.; Gorin, N. C.; Salamero, J.; Assari, S.; Bernard, J., et al., In vitro generation of dendritic cells from human blood monocytes in experimental conditions compatible for in vivo cell therapy. *J Hematother Stem Cell Res* **2000,** *9* (2), 183-194.

69. Pullarkat, V.; Lau, R.; Lee, S. M.; Bender, J. G.; Weber, J. S., Large-scale monocyte enrichment coupled with a closed culture system for the generation of human dendritic cells. *J Immunol Methods* **2002,** *267* (2), 173-183.

70. Perseghin, P.; D'Amico, G.; Dander, E.; Gaipa, G.; Dassi, M.; Biagi, E.; Biondi, A., Isolation of monocytes from leukapheretic products for large-scale GMP-grade generation of cytomegalovirus-specific T-cell lines by means of an automated elutriation device. *Transfusion* **2008,** *48* (8), 1644-1649.

71. Nahrendorf, M.; Pittet, M. J.; Swirski, F. K., Monocytes: protagonists of infarct inflammation and repair after myocardial infarction. *Circulation* **2010,** *121* (22), 2437-2445.

72. Nahrendorf, M.; Swirski, F. K.; Aikawa, E.; Stangenberg, L.; Wurdinger, T.; Figueiredo, J. L.; Libby, P.; Weissleder, R.; Pittet, M. J., The healing myocardium sequentially mobilizes two monocyte subsets with divergent and complementary functions. *J Exp Med* **2007,** *204* (12), 3037-3047.

73. Bouchentouf, M.; Paradis, P.; Forner, K. A.; Cuerquis, J.; Boivin, M. N.; Zheng, J.; Boulassel, M. R.; Routy, J. P.; Schiffrin, E. L.; Galipeau, J., Monocyte derivatives promote angiogenesis and myocyte survival in a model of myocardial infarction. *Cell Transplant* **2010,** *19* (4), 369-386.

74. Panizzi, P.; Swirski, F. K.; Figueiredo, J. L.; Waterman, P.; Sosnovik, D. E.; Aikawa, E.; Libby, P.; Pittet, M.; Weissleder, R.; Nahrendorf, M., Impaired infarct healing in atherosclerotic mice with Ly-6C(hi) monocytosis. *J Am Coll Cardiol* **2010,** *55* (15), 1629-1638.

75. van Amerongen, M. J.; Harmsen, M. C.; van Rooijen, N.; Petersen, A. H.; van Luyn, M. J., Macrophage depletion impairs wound healing and increases left ventricular remodeling after myocardial injury in mice. *Am J Pathol* **2007,** *170* (3), 818-829.

76. Wei, H.; Ooi, T. H.; Tan, G.; Lim, S. Y.; Qian, L.; Wong, P.; Shim, W., Cell delivery and tracking in post-myocardial infarction cardiac stem cell therapy: an introduction for clinical researchers. *Heart Fail Rev* **2010,** *15* (1), 1-14.

77. Hey, Y. Y.; Tan, J. K.; O'Neill, H. C., Redefining Myeloid Cell Subsets in Murine Spleen. *Front Immunol* **2015,** *6*, 652.

78. Seifert, H. A.; Hall, A. A.; Chapman, C. B.; Collier, L. A.; Willing, A. E.; Pennypacker, K. R., A transient decrease in spleen size following stroke corresponds to splenocyte release into systemic circulation. *J Neuroimmune Pharmacol* **2012,** *7* (4), 1017-1024.

79. Wu, W.; Zhang, J.; Yang, W.; Hu, B.; Fallon, M. B., Role of splenic reservoir monocytes in pulmonary vascular monocyte accumulation in experimental hepatopulmonary syndrome. *J Gastroenterol Hepatol* **2016,** *31* (11), 1888-1894.

80. van der Laan, A. M.; Ter Horst, E. N.; Delewi, R.; Begieneman, M. P.; Krijnen, P. A.; Hirsch, A.; Lavaei, M.; Nahrendorf, M.; Horrevoets, A. J.; Niessen, H. W., et al., Monocyte subset accumulation in the human heart following acute myocardial infarction and the role of the spleen as monocyte reservoir. *Eur Heart J* **2014,** *35* (6), 376-385.

81. Libby, P., Inflammation in atherosclerosis. *Nature* **2002,** *420* (6917), 868-874.

82. Libby, P.; Lichtman, A. H.; Hansson, G. K., Immune effector mechanisms implicated in atherosclerosis: from mice to humans. *Immunity* **2013,** *38* (6), 1092-1104.

83. Drechsler, M.; Doring, Y.; Megens, R. T.; Soehnlein, O., Neutrophilic granulocytes - promiscuous accelerators of atherosclerosis. *Thromb Haemost* **2011,** *106* (5), 839-848.

84. Mocsai, A., Diverse novel functions of neutrophils in immunity, inflammation, and beyond. *J Exp Med* **2013,** *210* (7), 1283-1299.

85. de Jager, S. C.; Bongaerts, B. W.; Weber, M.; Kraaijeveld, A. O.; Rousch, M.; Dimmeler, S.; van Dieijen-Visser, M. P.; Cleutjens, K. B.; Nelemans, P. J.; van Berkel, T. J., et al., Chemokines CCL3/MIP1alpha, CCL5/RANTES and CCL18/PARC are independent risk predictors of short-term mortality in patients with acute coronary syndromes. *PLoS One* **2012,** *7* (9), e45804.

86. Nencioni, A.; da Silva, R. F.; Fraga-Silva, R. A.; Steffens, S.; Fabre, M.; Bauer, I.; Caffa, I.; Magnone, M.; Sociali, G.; Quercioli, A., et al., Nicotinamide phosphoribosyltransferase inhibition reduces intraplaque CXCL1 production and

associated neutrophil infiltration in atherosclerotic mice. *Thromb Haemost* **2014,** *111* (2), 308-322.

87. Doring, Y.; Drechsler, M.; Wantha, S.; Kemmerich, K.; Lievens, D.; Vijayan, S.; Gallo, R. L.; Weber, C.; Soehnlein, O., Lack of neutrophil-derived CRAMP reduces atherosclerosis in mice. *Circ Res* **2012,** *110* (8), 1052-1056.

88. Chertov, O.; Ueda, H.; Xu, L. L.; Tani, K.; Murphy, W. J.; Wang, J. M.; Howard, O. M.; Sayers, T. J.; Oppenheim, J. J., Identification of human neutrophil-derived cathepsin G and azurocidin/CAP37 as chemoattractants for mononuclear cells and neutrophils. *J Exp Med* **1997,** *186* (5), 739-747.

89. Chertov, O.; Michiel, D. F.; Xu, L.; Wang, J. M.; Tani, K.; Murphy, W. J.; Longo, D. L.; Taub, D. D.; Oppenheim, J. J., Identification of defensin-1, defensin-2, and CAP37/azurocidin as T-cell chemoattractant proteins released from interleukin-8-stimulated neutrophils. *J Biol Chem* **1996,** *271* (6), 2935-2940.

90. Sun, R.; Iribarren, P.; Zhang, N.; Zhou, Y.; Gong, W.; Cho, E. H.; Lockett, S.; Chertov, O.; Bednar, F.; Rogers, T. J., et al., Identification of neutrophil granule protein cathepsin G as a novel chemotactic agonist for the G protein-coupled formyl peptide receptor. *J Immunol* **2004,** *173* (1), 428-436.

91. Hartwig, H.; Silvestre Roig, C.; Daemen, M.; Lutgens, E.; Soehnlein, O., Neutrophils in atherosclerosis. A brief overview. *Hamostaseologie* **2015,** *35* (2), 121-127.

92. Soehnlein, O., Multiple roles for neutrophils in atherosclerosis. *Circ Res* **2012,** *110* (6), 875-888.

93. Stemme, S.; Faber, B.; Holm, J.; Wiklund, O.; Witztum, J. L.; Hansson, G. K., T lymphocytes from human atherosclerotic plaques recognize oxidized low density lipoprotein. *Proc Natl Acad Sci U S A* **1995,** *92* (9), 3893-3897.

94. Lee, T. S.; Yen, H. C.; Pan, C. C.; Chau, L. Y., The role of interleukin 12 in the development of atherosclerosis in ApoE-deficient mice. *Arterioscler Thromb Vasc Biol* **1999,** *19* (3), 734-742.

95. Whitman, S. C.; Ravisankar, P.; Daugherty, A., Interleukin-18 enhances atherosclerosis in apolipoprotein E(-/-) mice through release of interferon-gamma. *Circ Res* **2002,** *90* (2), E34-38.

96. Whitman, S. C.; Ravisankar, P.; Elam, H.; Daugherty, A., Exogenous interferon-gamma enhances atherosclerosis in apolipoprotein E-/- mice. *Am J Pathol* **2000,** *157* (6), 1819-1824.

97. Tedgui, A.; Mallat, Z., Cytokines in atherosclerosis: pathogenic and regulatory pathways. *Physiol Rev* **2006,** *86* (2), 515-581.

98. Gupta, S.; Pablo, A. M.; Jiang, X.; Wang, N.; Tall, A. R.; Schindler, C., IFN-gamma potentiates atherosclerosis in ApoE knock-out mice. *J Clin Invest* **1997,** *99* (11), 2752-2761.

99. Lahoute, C.; Herbin, O.; Mallat, Z.; Tedgui, A., Adaptive immunity in atherosclerosis: mechanisms and future therapeutic targets. *Nat Rev Cardiol* **2011,** *8* (6), 348-358.

100. von Boehmer, H.; Daniel, C., Therapeutic opportunities for manipulating T(Reg) cells in autoimmunity and cancer. *Nat Rev Drug Discov* **2013,** *12* (1), 51-63.

101. Foks, A. C.; Lichtman, A. H.; Kuiper, J., Treating atherosclerosis with regulatory T cells. *Arterioscler Thromb Vasc Biol* **2015,** *35* (2), 280-287.

102. Lin, J.; Li, M.; Wang, Z.; He, S.; Ma, X.; Li, D., The role of CD4+CD25+ regulatory T cells in macrophage-derived foam-cell formation. *J Lipid Res* **2010,** *51* (5), 1208-1217.

103. Tiemessen, M. M.; Jagger, A. L.; Evans, H. G.; van Herwijnen, M. J.; John, S.; Taams, L. S., CD4+CD25+Foxp3+ regulatory T cells induce alternative activation of human monocytes/macrophages. *Proc Natl Acad Sci U S A* **2007,** *104* (49), 19446-19451.

104. George, J.; Schwartzenberg, S.; Medvedovsky, D.; Jonas, M.; Charach, G.; Afek, A.; Shamiss, A., Regulatory T cells and IL-10 levels are reduced in patients with vulnerable coronary plaques. *Atherosclerosis* **2012,** *222* (2), 519-523.

105. Robertson, A. K.; Rudling, M.; Zhou, X.; Gorelik, L.; Flavell, R. A.; Hansson, G. K., Disruption of TGF-beta signaling in T cells accelerates atherosclerosis. *J Clin Invest* **2003,** *112* (9), 1342-1350.

106. Pinderski Oslund, L. J.; Hedrick, C. C.; Olvera, T.; Hagenbaugh, A.; Territo, M.; Berliner, J. A.; Fyfe, A. I., Interleukin-10 blocks atherosclerotic events in vitro and in vivo. *Arterioscler Thromb Vasc Biol* **1999,** *19* (12), 2847-2853.

107. Mallat, Z.; Gojova, A.; Marchiol-Fournigault, C.; Esposito, B.; Kamate, C.; Merval, R.; Fradelizi, D.; Tedgui, A., Inhibition of transforming growth factor-beta signaling accelerates atherosclerosis and induces an unstable plaque phenotype in mice. *Circ Res* **2001,** *89* (10), 930-934.

108. Mor, A.; Planer, D.; Luboshits, G.; Afek, A.; Metzger, S.; Chajek-Shaul, T.; Keren, G.; George, J., Role of naturally occurring CD4+ CD25+ regulatory T cells in experimental atherosclerosis. *Arterioscler Thromb Vasc Biol* **2007,** *27* (4), 893-900.

109. Maganto-Garcia, E.; Tarrio, M. L.; Grabie, N.; Bu, D. X.; Lichtman, A. H., Dynamic changes in regulatory T cells are linked to levels of diet-induced hypercholesterolemia. *Circulation* **2011,** *124* (2), 185-195.

110. van Puijvelde, G. H.; van Es, T.; van Wanrooij, E. J.; Habets, K. L.; de Vos, P.; van der Zee, R.; van Eden, W.; van Berkel, T. J.; Kuiper, J., Induction of oral tolerance to HSP60 or an HSP60-peptide activates T cell regulation and reduces atherosclerosis. *Arterioscler Thromb Vasc Biol* **2007,** *27* (12), 2677-2683.

111. Ait-Oufella, H.; Salomon, B. L.; Potteaux, S.; Robertson, A. K.; Gourdy, P.; Zoll, J.; Merval, R.; Esposito, B.; Cohen, J. L.; Fisson, S., et al., Natural regulatory T cells control the development of atherosclerosis in mice. *Nat Med* **2006,** *12* (2), 178-180.

List of publications

(from Ph.D studies)

- Naha PC, Lau KC, Hsu JC, Hajfathalian M, Mian S, Chhour P, Uppulari L, MacDonald, ES, Maidment ADA, Cormode DP. (2016) Gold silver alloy nanoparticles (GSAN): an imaging probe for breast cancer screening with dual energy mammography or computed tomography. *Nanoscale*. 8, 13740-13754
- Chhour P, Kim J, Benardo B, Tovar A, Mian S, Litt HI, Ferrari VA, Cormode DP. (2016) Effect of gold nanoparticle size and coating on labeling monocytes for CT tracking. *Bioconjugate Chemisty.* 28(1), pp 260–269 **(Chapter 3)**
- Chhour P, Cheheltani R, Naha PC, Litt HI, Ferrari VA, Cormode DP. (2016) Nanoparticles for Cardiovascular Imaging with CT. Book Chapter in *Design and Applications of Nanoparticles in Biomedical Imaging.* Springer. ISBN 978-3-319-42169-8, pp 357-384. **(Chapter 1)**
- Cheheltani R, Ezzibdeh RM, Chhour P, Chandrika K, Jurcova M, Hsu JC, Blundell C, Litt HI, Ferrari VA, Allcock HA, Sehgal CM, Cormode DP. (2016) Tunable, biodegradable gold nanoparticles as contrast agents for computed tomography and photoacoustic imaging. *Biomaterials*. (102), 87-97. **(Chapter 2)**
- Chhour P, Naha PC, O'Neill SM, Litt HI, Reilly MP, Ferrari VA, Cormode DP. (2016) Labeling monocytes with gold nanoparticles to track their recruitment in atherosclerosis with computed tomography. *Biomaterials.* (87), 93-103*.* **(Chapter 4)**
- Chhour P, Naha PC, Cheheltani R, Benardo B, Mian S, Cormode DP. (2015) Gold nanoparticles for biomedical applications: synthesis and in vitro evaluation.

Book Chapter in *Nanomaterials in Pharmacology.* Springer Protocols. ISBN 978-1-4939-3121-7, pp 87-111

- Teraphongphom NT, Chhour P, Naha PC, Witschey WRT, Jablonowski L, Opasanont B, Cormode DP, Wheatley MA. (2015) Nanocrystal loaded polymeric microbubbles as contrast agents for multimodal imaging. *Langmuir.* 31(43): 11858-11867
- Naha PC, Chhour P, Cormode DP. (2015) Systematic in vitro toxicological screening of gold nanoparticles designed for nanomedicine applications. *Toxicology in Vitro.* 29(7):1445-1453
- Naha PC, Al-Zaki A, Hecht E, Chorny M, Chhour P, Blankemeyer E, Yates DM, Witschey WRT, Litt HI, Tsourkas A, Cormode DP. (2014) Dextran coated bismuth–iron oxide nanohybrid contrast agents for computed tomography and magnetic resonance imaging. *Journal of Materials Chemistry B.* 2, 8239-8248
- Chhour P, Gallo N, Cheheltani R, Williams D, Al-Zaki A, Paik T, Nichol JL, Tian Z, Naha PC, Witschey WRT, Allcock HR, Murray CB, Tsourkas A, Cormode DP. (2014) Nanodisco Balls: Control over Surface versus Core Loading of Diagnostically Active Nanocrystals into Polymer Nanoparticles. *ACS Nano*. 8 (9):9143–9153 **(Chapter 2)**